# INTEGRATION OF STATE-OF-ART TECHNIQUES FOR LANDSLIDE HAZARD ASSESSMENT AND FOR THE MITIGATION CAUSED BY THE SUBSEQUENT MULTIMODAL DISASTER

EDITED BY: Yih-Chin Tai, Norifumi Hotta, Chih-Yu Kuo, Marc-Henri Derron and Rou-Fei Chen

PUBLISHED IN: Frontiers in Earth Science

frontiers Research Topics

# frontiers



ISSN 1664-8714
ISBN 978-2-83250-185-6
DOI 10.3389/978-2-83250-185-6

## About Frontiers

Frontiers is more than just an open-access publisher of scholarly articles: it is a pioneering approach to the world of academia, radically improving the way scholarly research is managed. The grand vision of Frontiers is a world where all people have an equal opportunity to seek, share and generate knowledge. Frontiers provides immediate and permanent online open access to all its publications, but this alone is not enough to realize our grand goals.

## Frontiers Journal Series

The Frontiers Journal Series is a multi-tier and interdisciplinary set of open-access, online journals, promising a paradigm shift from the current review, selection and dissemination processes in academic publishing. All Frontiers journals are driven by researchers for researchers; therefore, they constitute a service to the scholarly community. At the same time, the Frontiers Journal Series operates on a revolutionary invention, the tiered publishing system, initially addressing specific communities of scholars, and gradually climbing up to broader public understanding, thus serving the interests of the lay society, too.

## Dedication to Quality

Each Frontiers article is a landmark of the highest quality, thanks to genuinely collaborative interactions between authors and review editors, who include some of the world's best academicians. Research must be certified by peers before entering a stream of knowledge that may eventually reach the public - and shape society; therefore, Frontiers only applies the most rigorous and unbiased reviews.
Frontiers revolutionizes research publishing by freely delivering the most outstanding research, evaluated with no bias from both the academic and social point of view. By applying the most advanced information technologies, Frontiers is catapulting scholarly publishing into a new generation.

## What are Frontiers Research Topics?

Frontiers Research Topics are very popular trademarks of the Frontiers Journals Series: they are collections of at least ten articles, all centered on a particular subject. With their unique mix of varied contributions from Original Research to Review Articles, Frontiers Research Topics unify the most influential researchers, the latest key findings and historical advances in a hot research area! Find out more on how to host your own Frontiers Research Topic or contribute to one as an author by contacting the Frontiers Editorial Office: frontiersin.org/about/contact

# INTEGRATION OF STATE-OF-ART TECHNIQUES FOR LANDSLIDE HAZARD ASSESSMENT AND FOR THE MITIGATION CAUSED BY THE SUBSEQUENT MULTIMODAL DISASTER

Topic Editors:
**Yih-Chin Tai,** National Cheng Kung University, Taiwan
**Norifumi Hotta,** The University of Tokyo, Japan
**Chih-Yu Kuo,** Academia Sinica, Taiwan
**Marc-Henri Derron,** Université de Lausanne, Switzerland
**Rou-Fei Chen,** National Taipei University of Technology, Taiwan

**Citation:** Tai, Y.-C., Hotta, N., Kuo, C.-Y., Derron, M.-H., Chen, R.-F., eds. (2022). Integration of State-of-art Techniques for Landslide Hazard Assessment and for the Mitigation Caused by the Subsequent Multimodal Disaster. Lausanne: Frontiers Media SA. doi: 10.3389/978-2-83250-185-6

# Table of Contents

frontiers | Frontiers in Earth Science

TYPE Editorial
PUBLISHED 29 August 2022
DOI 10.3389/feart.2022.979106



OPEN ACCESS

EDITED AND REVIEWED BY
Chong Xu,
Ministry of Emergency Management, China

*CORRESPONDENCE
Yih-Chin Tai,
yctai@ncku.edu.tw

SPECIALTY SECTION
This article was submitted to Geohazards and Georisks, a section of the journal Frontiers in Earth Science

RECEIVED 27 June 2022
ACCEPTED 02 August 2022
PUBLISHED 29 August 2022

CITATION
Tai Y-C, Kuo C-Y, Hotta N, Derron M-H and Chen R-F (2022), Editorial: Integration of state-of-art techniques for landslide hazard assessment and for mitigation caused by subsequent multimodal disaster.
*Front. Earth Sci.* 10:979106.
doi: 10.3389/feart.2022.979106



# Editorial: Integration of state-of-art techniques for landslide hazard assessment and for mitigation caused by subsequent multimodal disaster

Yih-Chin Tai[1]*, Chih-Yu Kuo[2], Norifmi Hotta[3], Marc-Henri Derron[4] and Rou-Fei Chen[5]

[1]Department of Hydraulic and Ocean Engineering, National Cheng Kung University, Tainan, Taiwan, [2]Center of Applied Sciences, Academia Sinica, Taipei, Taiwan, [3]Graduate School of Agricultural and Life Sciences, The University of Tokyo, Tokyo, Japan, [4]Institute of Earth Sciences, University of Lausanne, Lausanne, Switzerland, [5]Institute of Mineral Resources Engineering, National Taipei University of Technology, Taipei, Taiwan

KEYWORDS

**surface monitoring, landslide-prone area, multimodal disaster, risk assessment, disaster mitigation**

Editorial on the Research Topic
Integration of state-of-art techniques for landslide hazard assessment and the mitigation caused by the subsequent multimodal disaster

Landslides and their subsequent multimodal disasters are extremely destructive. A tragedic example is the large-scale Hsiaolin landslide, triggered by heavy rainfall during typhoon Morakot in 2009 in Taiwan. A huge volume of mass was released, forming a landslide dam in the downstream river course, while debris flows developing with the subsequent dam breach buried the Hsiaolin village. More than 470 people were killed in this multimodal disaster. The post-event investigation indicates that the size of the Hsiaolin landslide is of the conventional slow-moving landslide (land creeping). But, the high moving speed is as fast as a shallow landslide. The mysterious complexity and severe destruction received much engineering attention and scientific interest because such a multimodal disaster may take place worldwide. In Japan, the typhoon-triggered catastrophic landslides and debris flow have killed more than 73 people in 2011 (typhoon Talas); the tragedies of the mudslides at Oso (2014, United States) and Atami (2021, Japan), and the landslides triggered by the earthquake in Hokkaido (2018, Japan) were also mournful.

This Research Topic has attracted ten original research articles. All of them focus on hazard assessment and disaster mitigation, and they can be grouped into two themes: the first is related to the assessment of landslide activities, and the second is about the mitigation of sediment-related disasters. Because of the complex strata and the lack of detailed field data, exaggerated assumptions and approaches are applied to assessing the occurrence, the initiation as well as the

scale of a landslide. Kuo et al. focused on the temporal correlation between the motion of deep-seated creeping landslides and the water content in slopes, where the tank model was employed for calculating the water content. With the investigation of five deep-seated landslides, they illustrated that the occurrences of landslides could be estimated by their correlations with the phenomenological water storage index (WSI) of a given catchment, for which some WSI threshold was suggested.

To investigate the correlation between the landslide activity and the dynamic processes of the water saturation in the bedrock or colluvium, Tsai et al. employed the innovative technique of Electrical Resistivity Tomography (ERT) for the time-lapse monitoring. Although no substantial landslide was sensed in the ground, suspected small slide/deformation might have caused detectable variation in the electrical resistivity data, revealing its possible applicability of landslide alert systems. On the other hand, the stream conductivity is utilized to evaluate the activity of potential large-scale landslides in Tsai et al.. This approach is motivated by the suspicion that the conductivity of the spring water near the landslide-prone site increases once the ground surface moves. Sound agreement between the stream electronic conductivity and ground surface displacement was identified, implying the potential for engineering application. Considering fourteen geo-environmental factors, Ou et al. applied the IV-based logistic regression model (LRM) to regional-scale landslide hazard assessment and mapping. It also reveals that the cutting of the slope toe plays a crucial role in the slope stability, and the failure is mainly triggered by rainfall.

Based on the geomorphological concept, Ko et al. proposed the ellipse-referenced idealized curved surface (ER-ICS) to search and mimic the plausible failure surface of a landslide of sliding type for investigating the consequent flow paths when the failure takes place. Their approach does not request detailed field data, and the flexibility of the orientation of the reference ellipse reduces the complexity of constructing the plausible failure surfaces of a landslide-prone area in various scenarios. In Lee et al., the Material Point Method (MPM) was employed to investigate the rainfall-induced landslides, which can provide detailed information concerning the transition from failure initiation to the post-failure stage. In the experimental validation and parameter study, the ratio of rainfall intensity to hydraulic conductivity plays a vital role in distinguishing the cause when the slope failure is triggered by the rising groundwater (up-welling) or the water infiltration (downward). Coupling both the discrete element and finite element simulations, Feng et al. investigated the characteristics of seismic signals induced by rockfalls. These characteristics were validated against field tests, and crucial physical parameters on the seismic signals were identified.

The earthquake on 6 September 2018 in Hokkaido, Japan, has induced thousands of shallow landslides, carrying trees on the slope to the catchment and becoming large woody debris (LWD). Koi et al. examined the link of the hydraulic conditions to the LWD generation, the spatial distribution, and the relocation of the LWD to evaluate the risk of an LWD disaster. Although no significant movement of the deposited LWD was identified 2 years after the earthquake, LWD disasters could be estimated during rainfall events with return periods of more than 10 years. Lee et al. examined and reported the main damage types and deterioration characteristics of check dams in Korea. For condition assessment, ten and nine representative types of damage and deterioration were classified for concrete and stone check dams, respectively. A numerical index was proposed to evaluate the structure conditions and to ease the determination of the mitigation priorities of the check dams. Gong et al. demonstrated an engineering planning method for mitigating the debris flow hazard in scenic areas. Taking into account the requirements of coordinating the landscapes and the ecosystem, they proposed four modes for a systematic strategy against post-earthquake debris flow disasters.

Despite the exciting and valuable articles collected in this issue of Research Topic, the landslide hazard assessment and mitigation countermeasure are still clumsy. The link between detecting the critical conditions of occurrence, complex strata, hydrological conditions, etc., remains to be built for an efficient methodology with precise and accurate prediction/estimation. We see, at this level, the importance of more efforts and investments in this research topic. And we are looking forward to substantial progress with the fast-developing remote sensing techniques in the near future.

## Author contributions

Y-CT, C-YK, NH, M-HD, and R-FC edited the Research Topic "*Integration of state-of-art techniques for landslide hazard assessment and the mitigation caused by the subsequent multimodal disaster.*" All the authors listed have made a substantial direct and intellectual contribution to the work and approved it for publication.

## Acknowledgments

We thank all the authors for their contributions and the efforts of the reviewers and editorial staff to pull together this collection are sincerely acknowledged.

## Conflict of interest

The authors declare that the research was conducted in the absence of any commercial or financial relationships that could be construed as a potential conflict of interest.

## Publisher's note

frontiers in Earth Science

ORIGINAL RESEARCH
published: 27 April 2021
doi: 10.3389/feart.2021.648342

# Assessment of Landslide Hazard in Jiangxi Using Geo-information Technology

*Penghui Ou[1], Weicheng Wu[1]*, Yaozu Qin[1], Xiaoting Zhou[1], Wenchao Huangfu[1], Yang Zhang[1], Lifeng Xie[1], Xiaolan Huang[1], Xiao Fu[1], Jie Li[1], Jingheng Jiang[1], Ming Zhang[1], Yixuan Liu[1], Shanling Peng[1], Chongjian Shao[1], Yonghui Bai[1], Xiaofeng Zhang[2], Xiangtong Liu[3] and Wenheng Liu[1]*

[1] Key Laboratory of Digital Lands and Resources and Faculty of Earth Sciences, East China University of Technology, Nanchang, China, [2] School of Geophysics and Measurement-Control Technology, East China University of Technology, Nanchang, China, [3] Faculty of Geomatics, East China University of Technology, Nanchang, China

Landslides constitute a severe environmental problem in Jiangxi, China. This research was aimed at conducting landslide hazard assessment to provide technical support for disaster reduction and prevention action in the province. Fourteen geo-environmental factors, e.g., slope, elevation, road, river, fault, lithology, rainfall, and land cover types, were selected for this study. A test was made in two cases: (1) only based on the main linear features, e.g., main rivers and roads, and (2) with detailed complete linear features including all levels of roads and rivers. After buffering of the linear features, an information value (IV) analysis was applied to quantify the distribution of the observed landslides for each subset of the 14 factors. The results were inputted into the binary logistic regression model (LRM) for landslide risk modeling, taking the known landslide points as a training set (70% of the total 9,525 points). The calculated probability of a landslide was further classified into five grades with an interval of 0.2 for hazard mapping: very high (3.70%), high (4.05%), moderate (18.72%), low (27.17%), and stable zones (46.36%). The accuracy was evaluated by AUC [the area under the receiver operating characteristic (ROC) curve] vs. the validation set (30%, the remaining landslides). The final results show that with increasing the completeness of the linear features, the modeling reliability also significantly increased. We hence concluded that the tested methodology is capable of achieving the landslide hazard prediction at regional scale, and the results may provide technical support for geohazard reduction and prevention in the studied province.

**Keywords: landslide, information value analysis, logistic regression model, risk zoning, Jiangxi province**

OPEN ACCESS

***Edited by:***
*Norifumi Hotta,*
*The University of Tokyo, Japan*

***Reviewed by:***
*Qi Yao,*
*China Earthquake Networks Center, China*
*Joern Lauterjung,*
*Helmholtz Centre Potsdam, Germany*

***Correspondence:**
*Weicheng Wu*
*Wuwc030903@sina.com;*
*wuwch@ecut.edu.cn*

***Specialty section:***
*This article was submitted to Geohazards and Georisks, a section of the journal Frontiers in Earth Science*

***Received:*** *31 December 2020*
***Accepted:*** *26 February 2021*
***Published:*** *27 April 2021*

***Citation:***
*Ou P, Wu W, Qin Y, Zhou X, Huangfu W, Zhang Y, Xie L, Huang X, Fu X, Li J, Jiang J, Zhang M, Liu Y, Peng S, Shao C, Bai Y, Zhang X, Liu X and Liu W (2021) Assessment of Landslide Hazard in Jiangxi Using Geo-information Technology. Front. Earth Sci. 9:648342. doi: 10.3389/feart.2021.648342*

## INTRODUCTION

Landslides are a worldwide natural hazard, especially in Southern and Southeastern Asia including South China, and cause huge damages to human life and property, e.g., destroying houses, farmland, roads, and various infrastructures; killing livestock; and even amplifying existing disasters (Wu and Ai, 1995; Nadim et al., 2006; Assilzadeh et al., 2010; Froude and Petley, 2018).

It is of critical importance to conduct landslide risk prediction, zoning, and assessment to provide scientific advice and technical support for disaster prevention and early warning.

Actually, a large number of institutions and scientists have implemented projects or undertaken research to find solutions to the problem of landslide disasters, including landslide mechanism analysis, risk mapping, and assessment (Montgomery and Dietrich, 1994; Guzzetti et al., 1999; Aleotti and Chowdhury, 1999; Ayalew and Yamagishi, 2005; Ruff and Czurda, 2008; Fan et al., 2016; Arabameri et al., 2017; Zhang Y. et al., 2020)[1]. These authors have proposed different qualitative and quantitative assessment approaches by involving a set of indicators (Guzzetti et al., 1999; Corominas et al., 2014; Goetz et al., 2015; Furlani and Ninfo, 2015; Li et al., 2017; Zhu et al., 2019; Zhang Y. et al., 2020; see text footnote 1), and these studies laid a solid foundation for our landslide hazard assessment study in Jiangxi, which ranks number 2 in terms of geohazard occurrence frequency in China in 2019 (Zhang Y. et al., 2020).

Actually, landslides are the result of the interaction of multiple geo-environmental factors and human activity, including geological lithology, structure (e.g., fractural zones, faults, and joints), elevation, slope, aspect, river, regolith, soil, land cover, rainfall, roads, and housing development. Djukem et al. (2020) and Zhang Y. et al. (2020) have discussed and successfully applied these factors for landslide hazard assessment. Hence, these geo-environmental factors will be necessary and taken into account for achieving our purpose in this study.

Combining the knowledge of different disciplines can effectively improve the assessment accuracy of geohazards in practical applications (Kilburn and Pasuto, 2003). The assessment of landslide hazard refers to the prediction of the probability of its occurrence in a specific area by studying the combined effects of multiple geo-environmental factors (Tian et al., 2020; Zhang Y. et al., 2020; see text footnote 1). To achieve an assessment, two types of approaches, i.e., knowledge-driven and data-driven methods, are at present available. The knowledge-driven method relies on expert experience and knowledge. It is subject to certain subjectivity and uncertainty and suitable for areas with simple geo-environmental conditions or areas with limited data. This method is of limited assessment accuracy for areas with complex conditions and unknown landslide mechanisms. For the data-driven method, the landslide assessment factors are selected by quantitative analysis, and risk assessment is conducted by employing artificial intelligence approaches. Hence, theoretically and practically, the data-driven method seems to be more robust and reliable although more computing power is required (Zhang and Jiang, 2004; Zhang et al., 2017).

As a matter of fact, a number of scientists have made efforts on this research topic. For the time being, statistical analysis, especially machine learning (Wu et al., 2018), is the common approach for landslide hazard risk assessment, for example, the information value (IV) analysis (Gao et al., 2006; Chen et al., 2012; Sharma et al., 2015; Feng et al., 2016; Ren et al., 2018), the logistic regression model (LRM) (Carrara, 1983; Lee and Min, 2001; Ayalew and Yamagishi, 2005; Xing et al., 2004; Bai et al., 2010; Feng et al., 2016), artificial neural networks (ANNs) (Pradhan and Lee, 2007; Yilmaz, 2009; Lee et al., 2010; Feng et al., 2016; Kalantar et al., 2018), support vector machines (SVMs) (Yao et al., 2008; Peng et al., 2014; Kumar et al., 2017; Xia et al., 2018; Wang et al., 2019), and random forests (RFs) (Li et al., 2014; Kim et al., 2018; Dang et al., 2018; Zhang Y. et al., 2020; see text footnote 1). Recently, some authors have even attempted to employ a combination of LRM with IV analysis (Feng et al., 2016; Du et al., 2017; Fan et al., 2018; Zhang Q. et al., 2020) or LRM with certainty factor (CF) analysis (Yang et al., 2019; Zhang Q. et al., 2020) for achieving landslide risk assessment. Although these different techniques have been proven to be effective, there is no consensus on which technique and method are the best (Wang et al., 2005; Zhang, 2019). It can be seen from the above brief review that data-driven approaches, in particular, machine learning approaches, have great potential in geohazard risk prediction and assessment. Zhang (2019) and Zhao et al. (2019) noted that IV-based LRM is well capable of addressing the problem of binary variables (e.g., presence or absence of landslides) and has been applied to the assessment of landslide hazards.

In view of these, the objective of this study was to realize a landslide risk assessment by the combined approaches of IV and LRM in order to provide technical support for disaster reduction and prevention of the local authorities, taking Jiangxi, China, as an example. With more and more regional-scale studies on geohazard assessment being required to meet the need of Disaster Reduction and Prevention actions of governments, one may immediately think to use coarse-resolution data with major features of the geo-environmental factors for this purpose. Thus, one specific objective was to test the influence of data completeness and detailed extent on such regional-scale modeling and prediction and to check whether coarse-resolution data and major features alone are able to successfully achieve this task.

# MATERIALS AND METHODS

## Study Area

Jiangxi is a province located in Southeast China, extending from 24°29′14″N to 30°04′41″N in latitude and from 113°34′36″E to 118°28′58″E in longitude, covering an area of 166,900 km$^2$. Situated in the south of the middle reaches of the Yangtze River Watershed, the overall terrain of Jiangxi looks like a horseshoe-type or dustpan-type basin. The Poyang Lake basin is situated between the Yangtze River in the north and a series of NE- or NNE-striking mountain ranges such as Huaiyu and Baiji in the east, Wuyi in the southeast, Jiulian in the south, and Mufu, Jiuling, Wugong, Wangyang, and Zhuguang in the west. There are five main rivers, namely, Xinjiang and Raohe from the east, Fuhe and Ganjiang from the south, and Xiushui from the west, all flowing into the Poyang Lake and then joining the Yangtze River (**Figure 1**). Jiangxi belongs to the subtropical climate zone. Rainfall is abundant, and monsoon rain is predominant in spring and summer, in particular in June and July. The annual precipitation is more than 1,500 mm. The average annual temperature is about 16.3–19.5°C, generally increasing from 16.3

[1]Zhou, X., Wu, W., Lin, Z., Zhang, G., Chen, R., Song, Y., et al. (under review). Zonation of landslide susceptibility in Ruijin, Jiangxi, China. *Int. J. Environ. Res. Public Health* (2nd round review).

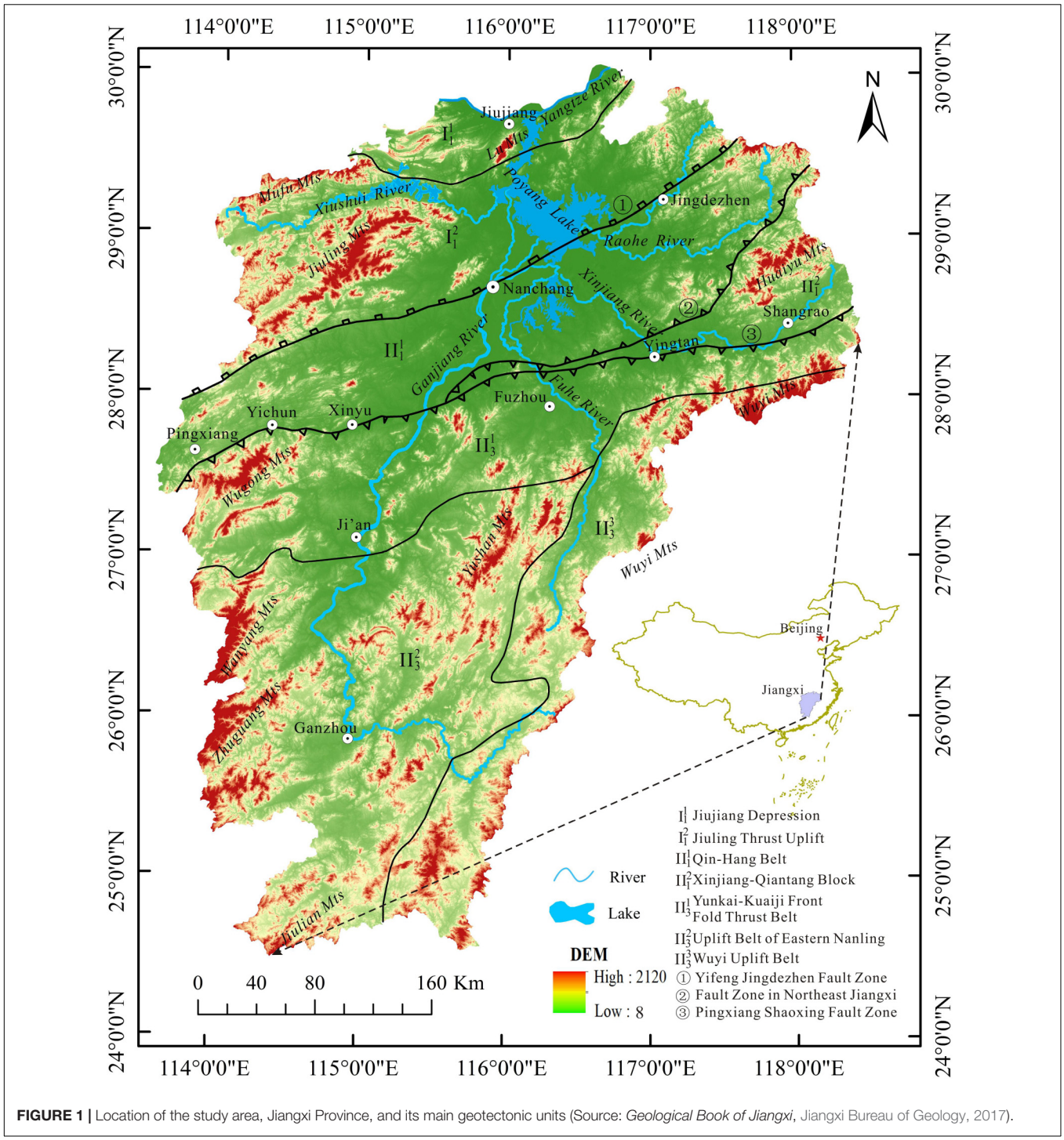


**FIGURE 1 |** Location of the study area, Jiangxi Province, and its main geotectonic units (Source: *Geological Book of Jiangxi*, Jiangxi Bureau of Geology, 2017).

to 17.5°C in the north to 19.0–19.5°C in the south. The northwest wind prevails in winter, and it is relatively cold. In summer, it is humid and hot with an average temperature of 24–29°C (and the extreme maximum temperature is more than 40.0°C because of the Pacific subtropical monsoon).

Geologically, as shown in **Figure 1**, Jiangxi crosses over two geotectonic units: Yangtze Plate in the north (I) and Cathaysia Massif (South China Plate) in the south ($II_3$) where the Qian-Hang Tectonic Belt ($II_1$) is the joint belt between the two plates (Yang, 2003). Though active faults are rarely observed nowadays, shaped by such geotectonic settings, the landform characterized by the mountains-basin pattern facilitates the occurrence of geohazards, especially landslides, in Jiangxi. Up to 2020, a total of 9,525 landslide taking place in the past decades were collected. The economic losses caused by geohazards are next to those by floods and droughts, and their casualties even exceed those of floods (Jiangxi Geological Disaster Emergency Center, 2014). Research on zoning of landslide susceptibility will hence help us

understand the overall situation of landslide disasters and provide technical support for decision making in hazard prediction, prevention, and early warning in the province.

## Data and Preprocessing

### Landslide Inventory Data

Apart from the field survey by ourselves in July–October 2019 and August 2020, the majority of the landslide data in Jiangxi were obtained from the Environmental Science Data Center, Institute of Geographical Sciences and Natural Resources Research (IGSNRR) of the Chinese Academy of Sciences (CAS). A total of 9,525 landslide points were made available for this research. The spatial distribution of these landslides is shown in **Figure 2**.

## Geo-Environmental Factors

Based on the field survey and general understanding of the landslide mechanism, the following geo-environmental

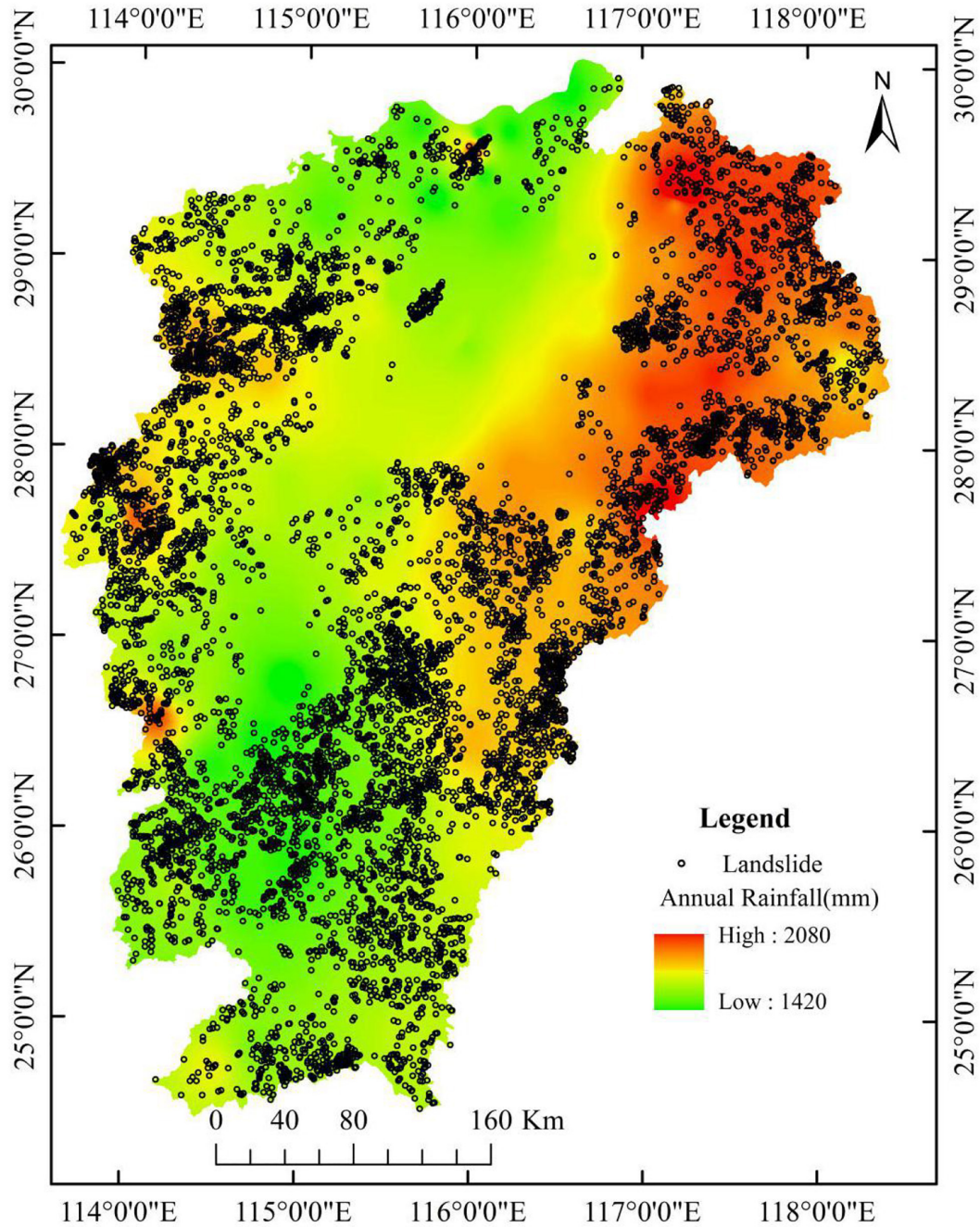


**FIGURE 2 |** Distribution map of landslide in Jiangxi in the context of annual rainfall.

parameters were utilized for risk assessment, e.g., slope; aspect; elevation derived from the digital elevation model (DEM); rainfall including mean annual rainfall; accumulated monthly rainfall of March–July, March–June, and May–July; roads; rivers; faults; lithologies of strata; normalized difference vegetation index (NDVI); and land cover (**Table 1**). These factors include both continuous and discrete data and are described as follows.

### *Slope*

The slope is an important factor in the occurrence of landslides which take place only when the slope reaches a certain degree. The geometric characteristics of the slope determine the stress distribution and hence the stability of the slope (Lan et al., 2002). Human activity such as road construction reduces the slope resistance and exacerbates instability (Yu, 2003). Derived from the DEM product ASTGTM (V003, 30 m), slope ranges from 0° to 75° in Jiangxi and is presented in **Figure 3A**.

### *Aspect*

The aspect is the normal direction of the slope surface projected on the horizontal plane. Jiangxi is situated to the north of the Tropic of Cancer. The southern slopes receive more solar radiation, leading to a higher temperature, bigger contrast in day–night temperature, and a stronger evapotranspiration than in the northern ones. Such difference in physiochemical conditions results in difference in vegetation development and weathering between the southern and northern slopes. Su (2006) noted that landslides occur more frequently in the southern slopes than in the northern ones. For this reason, the aspect information of Jiangxi was extracted from the DEM based on spatial analysis (**Figure 3B**) and used for landslide hazard assessment.

### *Relief Degree of Land Surface (RDLS)*

The RDLS is a parameter to recount surface morphology, one of the most important factors to determine the topographic conditions and to characterize the potential energy of surface erosion and material movement of the slope (Yin et al., 2010; Su et al., 2017). It is useful for quantitative analysis of landform and erosion degree of the regional surface (Guo et al., 2008). Based on the spatial analysis, the RDLS is calculated from the DEM with values ranging from 0 to 588 m (**Figure 3C**).

**TABLE 1 |** Data sources and data types of assessment factors.

| Basic data | Sources of data | Type of data or resolution |
|---|---|---|
| DEM | ASTGTM V003 30 m from NASA (www.earthdata.nasa.gov) | Raster (30 m) |
| Rainfall | China Meteorological Data Network (monthly rainfall data from 83 stations of 1980–2010, http://data.cma.cn) | Vector data (points) |
| Road, river | National Geomatics Center of China (http://ngcc.sbsm.gov.cn) | Vector data |
| Geological map (lithology, fault) | Coal Geological Bureau of Jiangxi Province (scale of 1:500,000) (www.jxmtdzj.gov.cn) | Vector data |
| NDVI | November MODIS Data from NASA (www.earthdata.nasa.gov) | Raster (250 m) |
| Land cover | Institute of Remote Sensing and Digital Earth, Chinese Academy of Sciences (www.radi.cas.cn) | Raster (30 m) |

### *Distance From the Linear Features: Roads, Rivers, and Faults*

The study area is situated in the south of the Yangtze River, composed a series of hills and mountains (see section "Study Area"), leading to the development of the five important rivers and their tributaries and subtributaries. They have been modifying the landscape and breaking up the rocks and, at the same time, generating instability of slopes and landslides. Generally, the closer to the river, the higher the slope instability and risk of landslide.

Faults are geological structures in which the rock blocks of the two sides are displaced against each other along the fractural surface, destroying the integrity of the rock formations. The development degree of joints of the geological bodies is often controlled by faulting. The occurrence of several geohazards is closely associated with faults, especially active faults (Huang and Li, 2009).

Road construction and other housing development engineering have led to slope cutting and destruction of the stability of slopes composed of rocks and soils. Hence, road networks and slope housing are a landslide indicator as well (Xu, 2005; Meten et al., 2015; Zhang Y. et al., 2020; see text footnote 1).

Linear features like roads (**Figure 3D**), rivers (**Figure 3E**), and faults (**Figure 3F**) have the same proximity effect; that is, the closer the slope to the linear feature, the higher the risk of landslide it may have. Moreover, scale may also play a role as the larger the scale of the faults, roads, and rivers, the stronger their impacts on the stability of the slope.

With a specific purpose to test the impacts of completeness of roads and rivers, we set up two groups of these two linear features for modeling: (1) main roads (highways and railways) and big rivers and their major tributaries and (2) main roads, secondary roads (provincial and county levels) and countryside roads, and big rivers with their major tributaries, subtributaries, and streams.

According to the field investigations undertaken in the period July–October 2019 and August 2020 and prior knowledge of experts, these features were largely divided into two scales: large and small. The large-scale main roads were categorized into buffers of 0–60, 60–120, 120–180, and >180 m, and the small secondary and countryside roads into 0–30, 30–60, 60–90, and >90 m. For the big rivers and faults (>10 km), buffer zones of 0–90, 90–180, 180–270, 270–360, 360–450, 450–540, and >540 m were derived, while for small rivers or subtributaries and faults (<10 km), smaller buffers of 0–30, 30–60, 90–120, 120–150, 150–180, and >180 m were generated.

### *Rainfall*

Rainfall is a salient triggering factor for landslides as it constitutes slope runoff, leading to soil erosion and lubrication of potential sliding surfaces. Rainfall may increase the load of rock and soil and reduce the resistance from underlying rocks. Usually, after a continuous rainfall reaches a certain threshold, landslides take place (Guzzetti et al., 2008). The distribution of heavy rainfall affects the concentration of landslides (Shan et al., 2004). Because

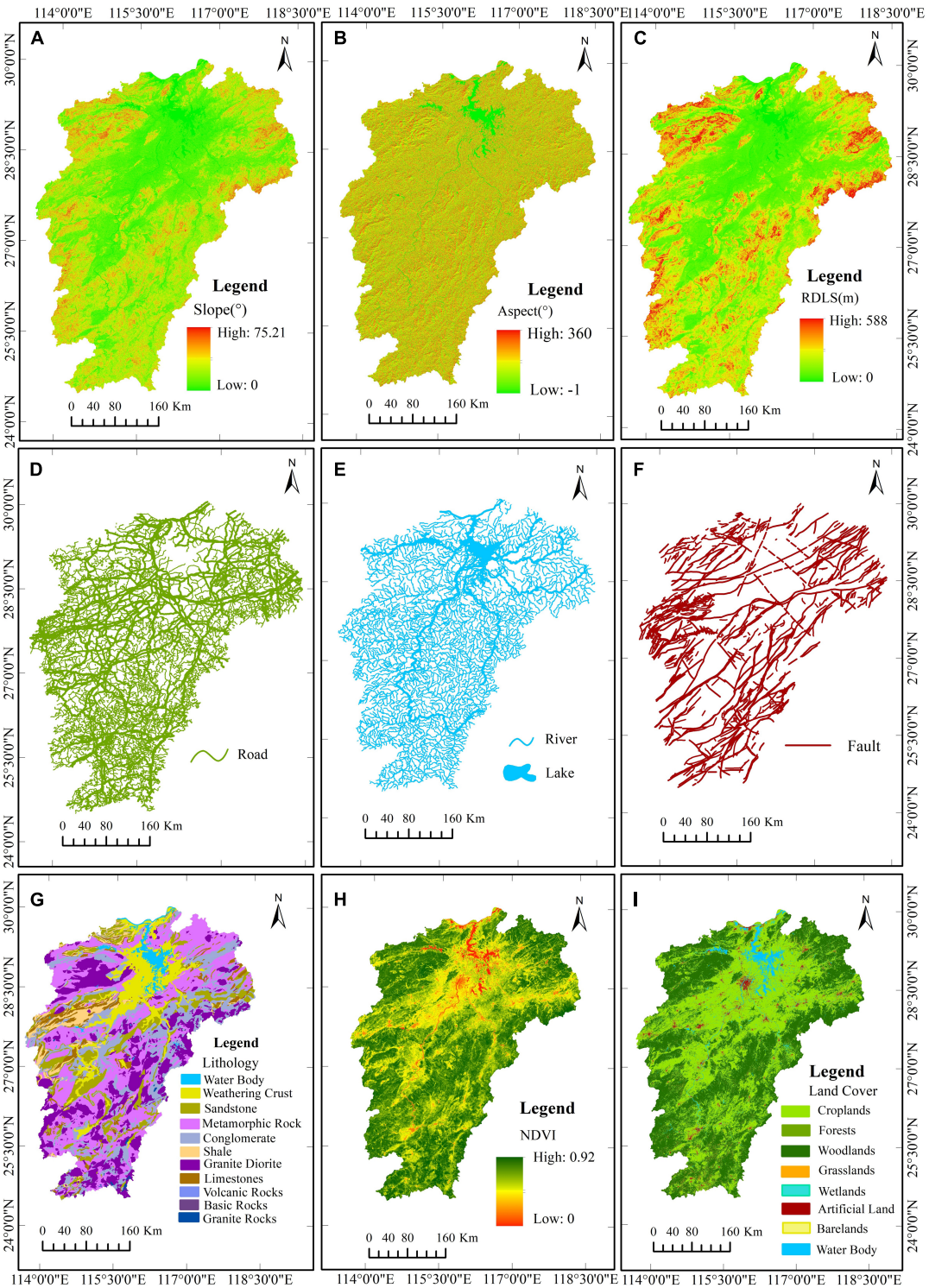


**FIGURE 3 |** Landslide proneness factors used in this research, taking the following as an example: **(A)** slope, **(B)** aspect, **(C)** RDLS, **(D)** roads, **(E)** rivers, **(F)** faults, **(G)** lithology, **(H)** NDVI, and **(I)** land cover.

of the subtropical monsoon climate, Jiangxi receives abundant rainfall and frequent heavy rains, which strongly provoke the occurrence of landslides. The annual rainfall in Jiangxi ranges from 1,361.6 to 2,037.4 mm (**Figure 2**). As landslides occur mainly in spring and early summer from March to July, especially from June to July, the mean annual rainfall and the mean

accumulated March–June, March–July, and May–July rainfall of the period 1981–2010 were produced for hazard analysis.

*Lithology of Strata*

Lithology plays a certain role in landslide events as it constitutes different resistances and degrees of propensity to this hazard (Yu, 2003). In addition, different lithologies may be weathered into different regoliths and soils. Lithological properties of the study area can be largely divided into weathering crust (including soil), sandstone, metamorphic rocks, conglomerate, shale, granodiorite, limestone, volcanic rocks, basic rocks, and granitic rocks (**Figure 3G**).

*NDVI*

The NDVI reflects the growth status and coverage of vegetation (Tucker, 1979). It is a widely used vegetation index for land cover characterization (Tucker, 1979; Huete et al., 1997; Walsh et al., 2001; Wu, 2014; Wu et al., 2016). The soil and water conservation effect of vegetation reduces surface runoff and soil erosion. At the same time, the biological weathering of vegetation also causes certain damage to rocks and soils (e.g., rock breakup process by plant rooting). Though it is not absolute, slopes with more abundant vegetation are more resistant to landslide than bare soils. Therefore, the occurrence of landslides is often related to vegetation coverage. The NDVI value was calculated from the November MODIS data from 2005 to 2010, and that below 0 (mostly water-bodies) was replaced by zero, and finally, its value ranges from 0 to 0.92 (**Figure 3H**).

*Land Cover*

Different types of land cover have different vegetation properties and different effects on surface water and soil conservation, which are associated with the slope surface stability, enforcing to a certain extent impacts on the occurrence of landslides. The main land cover types are croplands, grasslands, forests, woodlands, wetlands, artificial lands, barelands, and water bodies (**Figure 3I**).

# Methods

## IV Analysis

IV was used in the fields of geology and mineral prospecting in early times, converting the measured values reflecting various influencing factors into the IV. Later, some scholars transformed it into a bivariate statistical analysis, which can combine the subjective estimation of experts with objective data. The IV analysis is to analyze the possibility of landslides under similar conditions by counting the information of past landslides. Hence, Gao et al. (2006), Sharma et al. (2015), and Ren et al. (2018) considered that this IV represents regional stability.

Landslide information is calculated by the IV in each subset of the selected indicator. The IV of each factor is overlaid on each other to calculate the possibility of landslides in the study area. The greater the IV, the higher the possibility of a landslide or *vice versa* (Dai, 2013). The possibility of landslides can be evaluated by the amount of information or IV in the prediction process. The formula of the information model is shown as follows:

$$I\left(y, x_1, x_2, x_3, \cdots, x_n\right) = \ln \frac{P\left(y|x_1, x_2, x_3, \cdots, x_n\right)}{P\left(y\right)} \quad (1)$$

where $I$ is the IV, $P$ is the probability of landslide hazard occurrence for each evaluated indicator, and $P(y)$ denotes the probability of landslide occurrence in the normalized treatment area; $x_1$, $x_2$, $x_3$,... $x_n$ are the influencing factors of geohazards. Actually, the final form of Equation 1 can be further simplified and presented as follows:

$$I\left(y, x_1x_2x_3\cdots x_i\right) = \ln \frac{N_i/N}{S_i/S} \quad (2)$$

where $N$ is the total number of landslides (points or sites) in the study area; $N_i$ is the number of landslides in each subset of the given factor; $S$ is the total pixel number of assessment units in the study area; $S_i$ is the total pixel number of each subset of the given factor; and $I(y, x_1x_2x_3 \ldots x_i)$ is the IV of each factor contributing to the landslide hazard. IV can be both positive (favorable) and negative (unfavorable). Taking the geo-environmental factor slope as an example, we consider that a slope of $<3°$ is stable and is selected for non-risk sampling, subsetting started with 3° upward by an interval of 5° up to $>38°$, and IV was calculated using Equation 2 and is shown in **Table 2**.

## LRM

LRM is a non-linear statistical model in which the variables can be either continuous or discrete. In the assessment of geological hazards, the data combined with continuous and discrete variables are to be comprehensively processed (Nandi and Shakoor, 2010; Zhao et al., 2019). LRM has been widely used in land cover change estimation (Mertens and Lambin, 2000; Serneels and Lambin, 2001; Wu, 2003) and disaster prediction (Nandi and Shakoor, 2010; Zhao et al., 2019) and is able to reveal the relationship between the dependent variable, i.e., change or disaster occurrence (with 1 indicating that an event occurred and 0 indicating that no event occurred), and multiple independent variables, i.e., spatial determinants or hazard factors.

When the probability of an event is $P$ with a value range of (0, 1), the probability of the event not occurring is $1-P$. If $P$ is close to 0 or 1, it is difficult to capture its value, and thus, it is necessary to transform it into a logarithm function, i.e., $\ln(P) = \ln(P/1-P)$, which is called a logit transformation, in which

$$P = \frac{\exp(Z)}{1+\exp(Z)} \quad (3)$$

where

$$\mathrm{Z} = \alpha + \beta_1x_1 + \beta_2x_2 + \cdots + \beta_nx_n \quad (4)$$

$$P = \frac{\exp(\alpha + \beta_1x_1 + \cdots + \beta_nx_n)}{1+\exp(\alpha + \beta_1x_1 + \cdots + \beta_nx_n)} = \frac{1}{1+e^{-(\alpha+\beta_1x_1+\cdots+\beta_nx_n)}} \quad (5)$$

where $P$ is the probability of an event occurrence, $e$ the natural logarithm, $\alpha$ the intercept ($a$ constant), and $\beta_i$ ($i$ = 1, 2, 3, ..., $n$) the regression coefficient corresponding to the independent variable $x_i$ ($i$ = 1, 2, 3, ..., $n$). In our case, since the IV was calculated based on the subsets of each geo-environmental factor,

**TABLE 2 |** Information values (IVs) of different subsets of the geo-environmental factors contributing to landslides.

| Factors | Subsets | Subset area (%) | Number of landslides (%) | IV | Factors | Subsets | Subset area (%) | Number of landslides (%) | IV |
|---|---|---|---|---|---|---|---|---|---|
| Slope (°) | <3 | 15.20 | 3.36 | −1.51 | Rainfall (mm) | <1,500 | 3.68 | 3.57 | −0.03 |
| | 3–8 | 26.75 | 19.07 | −0.34 | | 1,500–1,550 | 11.93 | 10.77 | −0.10 |
| | 8–13 | 17.55 | 27.11 | 0.44 | | 1,550–1,600 | 17.31 | 14.81 | −0.16 |
| | 13–18 | 13.77 | 22.57 | 0.49 | | 1,600–1,650 | 16.81 | 14.73 | −0.13 |
| | 18–23 | 10.85 | 14.55 | 0.27 | | 1,650–1,700 | 12.60 | 12.09 | −0.04 |
| | 23–28 | 7.57 | 7.82 | 0.03 | | 1,700–1,750 | 10.88 | 9.80 | −0.10 |
| | 28–33 | 4.55 | 3.54 | −0.25 | | 1,750–1,800 | 9.44 | 10.98 | 0.15 |
| | 33–38 | 2.32 | 1.64 | −0.35 | | 1,800–1,850 | 8.68 | 8.79 | 0.01 |
| | >38 | 1.44 | 0.68 | −0.76 | | 1,850–1,900 | 6.13 | 10.46 | 0.53 |
| | | | | | | >1,900 | 2.52 | 3.99 | 0.46 |
| RDLS (m) | <30 | 25.78 | 1.50 | −2.84 | Road (m) | <30 | 26.39 | 1.49 | 2.87 |
| | 30–60 | 20.36 | 26.42 | 0.26 | | 30–60 | 19.59 | 1.47 | 2.59 |
| | 60–90 | 16.42 | 35.59 | 0.77 | | 60–90 | 12.21 | 1.46 | 2.12 |
| | 90–120 | 14.11 | 20.45 | 0.37 | | >90 | 34.72 | 91.49 | −0.97 |
| | 120–150 | 10.19 | 10.07 | −0.01 | | <60 | 3.06 | 1.41 | 0.78 |
| | 150–180 | 6.31 | 3.90 | −0.48 | | 60–120 | 2.51 | 1.36 | 0.61 |
| | 180–210 | 3.50 | 1.43 | −0.90 | | 120–180 | 1.52 | 1.32 | 0.14 |
| | >210 | 3.32 | 0.65 | −1.64 | | >180 | 34.72 | 91.49 | −0.97 |
| River buffer (m) | <30 | 1.29 | 2.61 | 0.70 | | <30 | 0.35 | 0.48 | 0.32 |
| | 30–60 | 1.29 | 2.93 | 0.82 | | 30–60 | 0.35 | 0.41 | 0.15 |
| | 60–90 | 1.28 | 2.90 | 0.81 | Fault buffer (m) | 60–90 | 0.35 | 0.42 | 0.18 |
| | 90–120 | 1.28 | 3.06 | 0.87 | | 90–120 | 0.35 | 0.63 | 0.59 |
| | 120–150 | 1.27 | 3.08 | 0.88 | | 120–150 | 0.35 | 0.26 | −0.32 |
| | 150–180 | 1.26 | 2.99 | 0.86 | | 150–180 | 0.35 | 0.42 | 0.18 |
| | >180 | 89.87 | 81.65 | −0.09 | | >180 | 96.62 | 95.42 | −0.01 |
| | <90 | 0.42 | 0.06 | −1.95 | | <90 | 0.21 | 0.39 | 0.61 |
| | 90–180 | 0.42 | 0.20 | −0.77 | | 90–180 | 0.21 | 0.38 | 0.57 |
| | 180–270 | 0.41 | 0.15 | −1.01 | | 180–270 | 0.21 | 0.26 | 0.18 |
| | 270–360 | 0.41 | 0.11 | −1.35 | | 270–360 | 0.21 | 0.33 | 0.44 |
| | 360–450 | 0.40 | 0.14 | −1.08 | | 360–450 | 0.21 | 0.39 | 0.59 |
| | 450–540 | 0.39 | 0.15 | −0.95 | | 450–540 | 0.21 | 0.23 | 0.05 |
| | >540 | 89.87 | 81.65 | −0.09 | | >540 | 96.62 | 95.42 | −0.01 |
| Litho. | Water body | 2.22 | 0 | 0 | Litho. | Weathering crust/soil | 10.02 | 0.63 | −2.77 |
| | Limestone | 4.50 | 4.38 | −0.03 | | Basic rocks | 0.03 | 0.08 | 0.79 |
| | Volcanic rocks | 0.01 | 0.02 | 0.86 | | Granodiorite | 18.26 | 29.33 | 0.47 |
| | Sandstone | 10.73 | 5.18 | −0.73 | | Shale | 3.86 | 3.21 | −0.18 |
| | Metamorphic rocks | 30.63 | 38.35 | 0.22 | | Conglomerate | 19.55 | 18.36 | −0.06 |
| | Granitic rocks | 0.17 | 0.48 | 1.02 | | | | | |

*Note: For rivers and faults, the parts left by small- and large-scale buffering, e.g., >180 and >540 m, or for roads, that is, >90 and >180 m, share the same percentage of subset area and number of landslides (%).*

hence, for the *i*th factor ($i = 1, 2, 3, \ldots, k$) and *j*th subset ($j = 1, 2, \ldots, n$), Equation 5 can be further specified as follows:

$$P = \frac{1}{1 + e^{-(\alpha+\beta_{11}x_{11}+\cdots+\beta_{nk}x_{nk})}} \quad (6)$$

where $P$ is the probability of landslide occurrence and $\beta_{ij}$ the regression coefficient of the variable $x_{ij}$ ($i = 1, 2, \ldots, n$, factor number; $j = 1, 2, \ldots, k$, the subset number of factor $i$), i.e., the IV of subset $ij$.

It is seen that the LRM is actually coupled with the IV analysis. This modeling is able to solve the problem of determining the weight of assessment factors and integrating different types of factor data. This may also reduce the influence of subjectiveness of a single model. The specific operation of model coupling is to get the IV of each subset of the geo-environmental factor through the IV analysis and then to input them into the LRM as independent variables to establish the regression equation in which the regression coefficient of each assessment factor is to be calculated (Zhang Q. et al., 2020).

## Modeling and Prediction of Landslide Hazard

For assessing the landslide hazards in Jiangxi, 14 geo-environmental factors were selected. The 9,525 landslide disaster points collected were randomly divided into a training set

(TS) and a validation set (VS) at a ratio of 7:3. Also non-landslide points were chosen from the relatively flat areas (such as cultivated land and urban areas) with a slope of <3° in terms of Miao et al. (2016) and Zhang Y. et al. (2020), and they were integrated into the TS and VS. The raster calculator within the spatial analysis tool of GIS was used to realize the superposition and calculation of IV for each geo-environmental factor.

### *Calculation of the IVs*

The landslides in the study area are mostly small and expressed in the form of points. The attribute values of the geo-environmental factors corresponding to each landslide point were extracted. In combination with division of the subsets, the IV of different subsets of each factor was calculated using Equation 2 as mentioned above, and the results are presented in **Table 2**, taking a part of factors as an example.

### *Correlation Test of the Assessment Factors*

To avoid the collinearity of the geo-environmental factors, a correlation analysis was performed. As shown in **Table 3**, the correlation among all the factors is less than 0.3, indicating that these factors and their division subsets are reasonable.

### *LRM*

All IVs of subsets of each geo-environmental factor were outputted in DBF format and then converted into an Excel file. Taking the attributes of landslides and non-landslide points in the TS as dependent variables and all predictive factors as independent variables, the binary LRM was realized within SPSS 25, a software package for statistical analysis.

Modeling was conducted in two cases: one with only the major linear features, e.g., big rivers, roads, and faults, and the other with both major and minor scales of linear features including also subtributaries of big rivers and streams, small roads (county level and commune level), and faults. The modeling results are presented in **Tables 4**, **5**.

### *Calculation of Landslide Risk*

The calculated regression coefficients (β) were inputted into Equation 5 to get the LRM:

$$\begin{cases} Y = 0.391x_1 + 0.497x_2 + 0.937x_3 + 0.628x_4 + 0.603x_5 \\ \quad +0.896x_6 + 0.126x_7 + 0.159x_8 - 0.263x_9 + 0.672x_{10} \\ \quad +0.465x_{11} + 0.392x_{12} + 0.742x_{13} + 0.294x_{14} - 0.041 \\ P = \dfrac{1}{1 + e^{-Y}} \end{cases} \tag{7}$$

where $x_1$ is the IVs of land cover, $x_2$ of lithology, $x_3$ of road, $x_4$ of river, $x_5$ of NDVI, $x_6$ of the mean annual rainfall, $x_7$ of May–July rainfall, $x_8$ of March–July rainfall, $x_9$ of March–June rainfall, $x_{10}$ of fault, $x_{11}$ of slope, $x_{12}$ of elevation, $x_{13}$ of RDLS, and $x_{14}$ of aspect. $P$ is the probability of landslide occurrence, with a value of 0–1. With the use of the raster calculator tool within GIS and Equation 5, the probability of landslide hazard in the study area was obtained.

## Landslide Hazard Mapping and Reliability Analysis

The obtained probability of the whole study area was divided into five hazard levels, i.e., stable (0–0.2), low (0.2–0.4), moderate (0.4–0.6), high (0.6–0.8), and very high (0.8–1).

Different approaches were used to analyze and compare the results of landslide hazard modeling. One was to check the rationality of the number distribution of the actual disaster points of each risk grades; the second was to assess the accuracy of hazard zoning through the receiver operating characteristic (ROC) curve, in which the latter is an effective method to assess the performance of classification algorithms. The area under the ROC curve (AUC) is the area between the ROC curve and the horizontal axis. The larger the AUC value, the better the prediction accuracy (Wang, 2013).

**TABLE 3 |** Correlation matrix of 14 geo-environmental factors.

| Factors | $x_1$ | $x_2$ | $x_3$ | $x_4$ | $x_5$ | $x_6$ | $x_7$ | $x_8$ | $x_9$ | $x_{10}$ | $x_{11}$ | $x_{12}$ | $x_{13}$ | $x_{14}$ |
|---|---|---|---|---|---|---|---|---|---|---|---|---|---|---|
| $x_1$ | 1 | | | | | | | | | | | | | |
| $x_2$ | 0.017 | 1 | | | | | | | | | | | | |
| $x_3$ | 0.017 | 0.067 | 1 | | | | | | | | | | | |
| $x_4$ | 0.005 | −0.023 | −0.007 | 1 | | | | | | | | | | |
| $x_5$ | −0.111 | 0.003 | 0.040 | −0.022 | 1 | | | | | | | | | |
| $x_6$ | −0.079 | −0.155 | 0.050 | −0.001 | 0.001 | 1 | | | | | | | | |
| $x_7$ | 0.016 | 0.022 | −0.030 | 0.011 | 0.026 | −0.145 | 1 | | | | | | | |
| $x_8$ | −0.005 | 0.007 | 0.032 | −0.032 | 0.023 | −0.370 | −0.301 | 1 | | | | | | |
| $x_9$ | −0.007 | −0.039 | −0.053 | 0.003 | −0.033 | −0.072 | −0.123 | −0.456 | 1 | | | | | |
| $x_{10}$ | 0.007 | 0.025 | 0.018 | −0.005 | 0.025 | −0.010 | 0.010 | 0.025 | −0.030 | 1 | | | | |
| $x_{11}$ | 0.000 | −0.029 | 0.121 | 0.075 | 0.054 | 0.015 | 0.004 | −0.370 | 0.020 | −0.017 | 1 | | | |
| $x_{12}$ | 0.012 | −0.080 | 0.038 | −0.003 | −0.050 | 0.026 | 0.129 | 0.021 | −0.049 | −0.026 | −0.073 | 1 | | |
| $x_{13}$ | 0.003 | −0.141 | 0.033 | −0.014 | −0.148 | −0.005 | −0.023 | −0.022 | −0.007 | −0.006 | −0.188 | −0.216 | 1 | |
| $x_{14}$ | −0.067 | 0.003 | −0.012 | −0.016 | 0.024 | −0.005 | −0.009 | 0.007 | −0.005 | 0.011 | −0.032 | 0.003 | 0.012 | 1 |

*Notes: $x_1$ is the land cover, $x_2$ lithology, $x_3$ road, $x_4$ river, $x_5$ NDVI, $x_6$ mean annual rainfall, $x_7$ May–July rainfall, $x_8$ March–July rainfall, $x_9$ March–June rainfall, $x_{10}$ fault, $x_{11}$ slope, $x_{12}$ elevation, $x_{13}$ RDLS, and $x_{14}$ aspect.*

**TABLE 4 |** Results of logistic regression modeling only with main linear features (Model 1).

| Factors | β | σ | *wals* | *df* | *sig* | *Exp(β)* |
|---|---|---|---|---|---|---|
| Lithology | 3.107 | 0.126 | 606.795 | 1 | 0.000 | 22.354 |
| RDLS | 2.859 | 0.092 | 970.230 | 1 | 0.000 | 17.436 |
| Land cover | 1.376 | 0.230 | 35.882 | 1 | 0.000 | 3.957 |
| NDVI | 1.266 | 0.089 | 200.888 | 1 | 0.000 | 3.547 |
| Aspect | 1.179 | 0.183 | 41.441 | 1 | 0.000 | 3.252 |
| Mean annual rainfall | 1.144 | 0.163 | 49.058 | 1 | 0.000 | 3.139 |
| May–July rainfall | 1.096 | 0.238 | 21.210 | 1 | 0.000 | 2.993 |
| Road | 1.023 | 0.084 | 148.019 | 1 | 0.000 | 2.782 |
| March–June rainfall | 0.881 | 0.165 | 28.630 | 1 | 0.000 | 2.412 |
| Elevation | 0.788 | 0.063 | 157.889 | 1 | 0.000 | 2.199 |
| River | 0.786 | 0.133 | 34.865 | 1 | 0.000 | 2.195 |
| Slope | 0.767 | 0.068 | 127.991 | 1 | 0.000 | 2.153 |
| Fault | 0.399 | 0.366 | 1.188 | 1 | 0.276 | 1.490 |
| March–July rainfall | −0.299 | 0.226 | 1.758 | 1 | 0.185 | 0.741 |
| Constant | −0.854 | 0.024 | 1,218.895 | 1 | 0.000 | 0.426 |

*Notes: β, regression coefficient of each factor in the model; σ, standard deviation; wals, chi-square value; df, degree of freedom; sig, significance; and Exp(β) is the odds ratio.*

**TABLE 5 |** Results of logistic regression modeling with complete linear features (Model 2).

| Factors | β | σ | *wals* | *df* | *sig* | *Exp(β)* |
|---|---|---|---|---|---|---|
| Road | 0.937 | 0.020 | 2,174.576 | 1 | 0.000 | 2.552 |
| Mean annual rainfall | 0.896 | 0.125 | 51.226 | 1 | 0.000 | 2.449 |
| Slope | 0.742 | 0.050 | 218.114 | 1 | 0.000 | 2.101 |
| Fault | 0.672 | 0.276 | 5.808 | 1 | 0.015 | 1.959 |
| River | 0.628 | 0.079 | 63.210 | 1 | 0.000 | 1.874 |
| NDVI | 0.603 | 0.037 | 258.861 | 1 | 0.000 | 1.828 |
| Lithology | 0.497 | 0.056 | 78.026 | 1 | 0.000 | 1.643 |
| RDLS | 0.465 | 0.034 | 191.772 | 1 | 0.000 | 1.592 |
| Elevation | 0.392 | 0.041 | 90.567 | 1 | 0.000 | 1.480 |
| Land cover | 0.391 | 0.107 | 51.226 | 1 | 0.000 | 1.479 |
| Aspect | 0.294 | 0.122 | 5.808 | 1 | 0.016 | 1.341 |
| March–July rainfall | 0.159 | 0.204 | 0.606 | 1 | 0.436 | 1.172 |
| May–July rainfall | 0.126 | 0.177 | 0.507 | 1 | 0.476 | 1.134 |
| March–June rainfall | −0.263 | 0.144 | 3.316 | 1 | 0.069 | 0.769 |
| Constant | −0.041 | 0.026 | 2.345 | 1 | 0.126 | 0.960 |

# RESULTS

Based on the above analysis and modeling, the results obtained are presented in this section.

## Landslide Hazard Models and Maps

**Tables 4**, **5** show the results of LRM for landslide hazard and the related coefficients of each geo-environmental factor. The β value represents the weight of each factor in a landslide event. The significance of each factor is judged by comparing the value of *wals* or *sig*. The larger the value of *wals* or the smaller the value of *sig*, the higher the significance (Liang and Cui, 2010). Clearly, in comparison with **Table 5**, the LRM of **Table 4** is something not logical as the roles of lithologies and RDLS are exaggerated and those of roads, rivers, and slopes are underestimated. There is more detail in the discussion.

The probability-based hazard zoning map based on the results from **Table 5** is shown in **Figure 4**, and from the statistics, it is known that stable, low, moderate, high, and very high hazardous areas take up respectively 76,282.21 $km^2$ (46.36%), 44,713.33 $km^2$ (27.17%), 30,802.22 $km^2$ (18.72%), 6,659.40 $km^2$ (4.05%), and 6,091.74 $km^2$ (3.70%).

From this risk map, we get to know that areas prone to landslide are those with a slope of 12–23°, within the scope of 150 m from the rivers and 100 m from the road and with an RDLS of 60–140 m, where annual rainfall is greater than 1,700 mm. In addition, landslides occur more frequently in low-altitude areas of mountainous and hilly slopes, where human activities are relatively intense.

## Reliability of the Risk Map

(1) Assessment of the risk maps from the LRM of **Tables 4**, **5** vs. the VS (field points not used for training) demonstrates a significant difference in prediction of the very high and high risk zones (**Tables 6**, **7**). These two zones from the LRM of **Table 4** (33.15%) are much larger than those from the LRM of **Table 5** (7.75%).

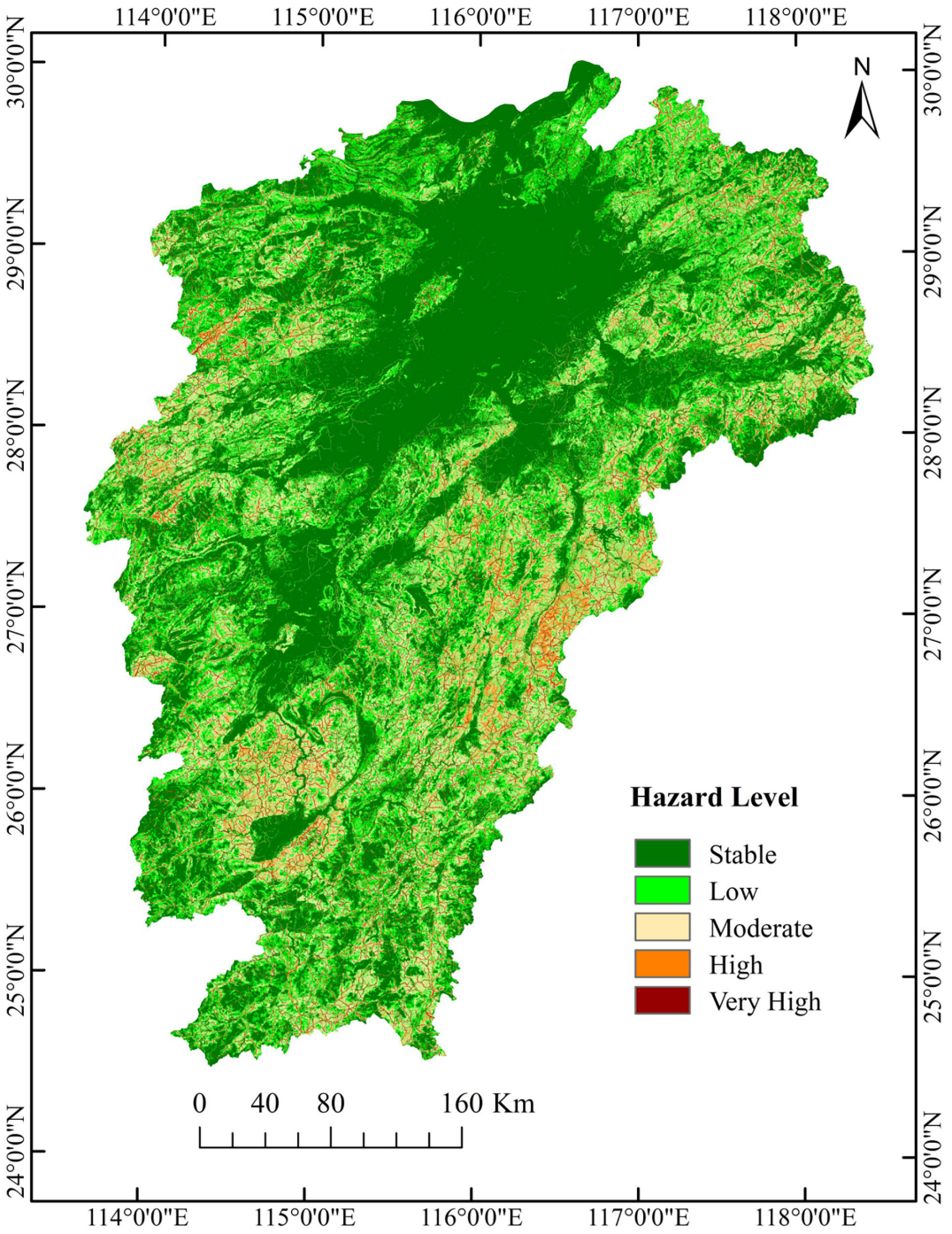


**FIGURE 4 |** Landslide hazard map of Jiangxi derived from a logistic regression model with complete linear features (**Table 5**).

The observed VS landslide points were projected into the different risk zones, and we found that a large proportion falls in the very high and high hazardous zones and that the stable zone has a little percentage. The corresponding ratio ($R_{ei}$) between the percentage of landslide points of the VS falling in each grade ($G_{ei}$) and the percentage of the area of each grade to the entire study area ($S_{ai}$) should have a clear increase (Tian et al., 2016) if the prediction is reliable. From the calculation results (**Tables 6**, **7A**), $R_{ei}(I) < R_{ei}(II) < R_{ei}(III) < R_{ei}(IV) < R_{ei}(V)$ meets these requirements, but **Table 7** from the LRM with complete linear features seems much better as very high and high risk zones are much narrower or, rather, more accurate than those from **Table 6**.

**TABLE 6 |** Distribution of the VS landslides in different hazard zones derived from Model 1 (**Table 4**).

| Hazard level | Number of VS | Proportion of VS ($G_{ei}$) | Zoning area (km$^2$) | Proportion of zone area ($S_{ai}$) | $R_{ei} = G_{ei}/S_{ai}$ |
|---|---|---|---|---|---|
| Stable | 179 | 6.26% | 74,371.59 | 45.20% | 0.14 |
| Low | 208 | 7.27% | 18,255.39 | 11.09% | 0.66 |
| Moderate | 343 | 11.99% | 17,373.03 | 10.56% | 1.14 |
| High | 614 | 21.47% | 21,273.36 | 12.93% | 1.66 |
| Very high | 1,516 | 53.01% | 33,275.63 | 20.22% | 2.62 |

**TABLE 7 |** Distribution of the landslides in different hazard zones derived from Model 2 (**Table 5**).

**(A) Validation set (VS: 30%)**

| Hazard level | Number of VS | Proportion of VS ($G_{ei}$) | Zoning area (km$^2$) | Proportion of zone area ($S_{ai}$) | $R_{ei} = G_{ei}/S_{ai}$ |
|---|---|---|---|---|---|
| Stable | 65 | 2.28% | 76,282.21 | 46.36% | 0.05 |
| Low | 310 | 10.85% | 44,713.33 | 27.17% | 0.40 |
| Moderate | 358 | 12.56% | 30,802.22 | 18.72% | 0.67 |
| High | 367 | 12.85% | 6,659.40 | 4.05% | 3.18 |
| Very high | 1,756 | 61.48% | 6,091.74 | 3.70% | 16.61 |

**(B) Training set (TS: 70%)**

| Hazard Level | Number of TS | Proportion of TS ($G_{ei}$) | Zoning area (km$^2$) | Proportion of zone area ($S_{ai}$) | $R_{ei} = G_{ei}/S_{ai}$ |
|---|---|---|---|---|---|
| Stable | 232 | 3.48% | 76,282.21 | 46.36% | 0.08 |
| Low | 694 | 10.41% | 44,713.33 | 27.17% | 0.38 |
| Moderate | 796 | 11.94% | 30,802.22 | 18.72% | 0.64 |
| High | 735 | 11.03% | 6,659.40 | 4.05% | 2.72 |
| Very high | 4,208 | 63.14% | 6,091.74 | 3.70% | 17.06 |

(2) The ROC curve is an efficient approach to assess the performance of classification algorithms. According to a series of different dichotomous methods, the curve is drawn with sensitivity as ordinate and 1 - specificity as abscissa, reflecting the restrictive relationship between sensitivity and 1 - specificity (Tian et al., 2016). The AUC is a standard used to measure the quality of the classification model. The AUC value is the area between the ROC curve and the horizontal axis. The larger the AUC value, the better the prediction accuracy (Wang, 2013). Based on the GIS interface, the landslide hazard map was sampled corresponding to the points in the VS, and the ROC curve and AUC value of the model are shown in **Figure 5**.

The AUC from LRM of **Table 5** is 0.863. The accuracy of the model is more than 86%, indicating that the IV-based LR modeling for landslide risk prediction and zoning allows us to achieve satisfactory results of high reliability, in particular with complete linear features.

# DISCUSSION

## Rationality of the IV-Based LRM Approach

The above research shows that the results of risk zoning are basically consistent with the distribution of the regional historical landslides. With a rather complete inventory of the landslide data, our approaches composed of IV analysis and LRM with complete linear features allowed us to achieve landslide risk prediction with high reliability with an accuracy of >86% against the VS. Actually, Du et al. (2017); Fan et al. (2018), Tian et al. (2020), and Zhang Q. et al. (2020) have conducted landslide susceptibility assessment at the local scale using similar approaches but with an accuracy of about 79–84%. We hence believe that the proposed methodology has improved the reasonableness for regional-scale studies, and it shall be extendable to other similar provincial and regional landslide risk assessments.

Actually, Tian et al. (2016) and Zhang (2019) have, respectively, employed CF-based LRM for landslide risk analysis in Guangdong and Shaanxi. Their results show that 57.99 and 60% of the field-observed landslides fall in the very high risk areas (22.15% of the total area, with an AUC of 0.782, and 10.03% of the total area with an AUC of 0.890, respectively). However, our analysis revealed that 74.33% of the landslides of the VS are located in the high and extremely high risk zones (7.75% of the total study area). This indicates that our analysis provides a more accurate prediction in locality of the potential hazards as we have used more geo-environmental factors and a better sampling scheme, e.g., division of the subsets, and used a higher-resolution DEM with more detailed factors.

Though rational weight assignment in terms of the propensity to landslide as applied by Chu (2012), Wang and Wang (2017), Zhang Y. et al. (2020), and see text footnote 1, appears plausible, a significant advantage of our approach lies in the fact that

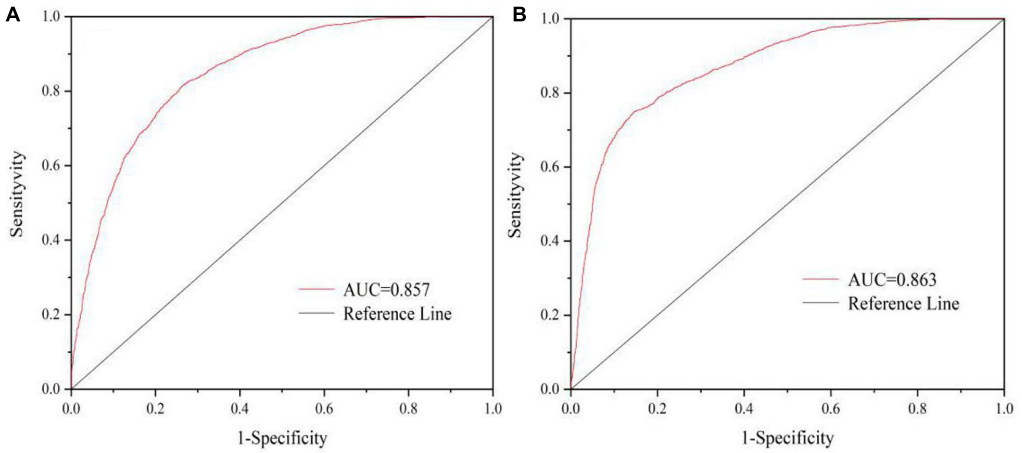


**FIGURE 5 |** Receiver operating characteristic (ROC) curve of the information value (IV)-based logistic regression (LR) modeling results: **(A)** with main linear features and **(B)** with complete linear features.

the combination of expert knowledge-driven and data-driven approaches avoids the subjective weight assignment to the geological strata and linear features after buffering. At the same time, the prior knowledge of experts obtained in the field is also considered important to achieve modeling and prediction with higher reasonableness.

## Importance of the Predictive Variables

The six most important independent variables revealed by LRM with complete linear features are roads, annual rainfall, slope, faults, river, and NDVI. These variables are more or less similar to those obtained by Zhang Y. et al. (2020) and see text footnote 1. For both local and provincial landslide hazard predictions, roads, rainfall, and slope are always the most important factors.

## Findings and Existing Difficulties

As previously expected, one finding is that given the same condition of other planar factors, the completeness of the linear features will be beneficial for a reliable prediction of landslide hazard. It is essential to use complete linear features, or rather, to use linear features that are as detailed as possible even for regional- and provincial-scale assessments. Coarse-resolution and major feature-based modeling and prediction may lead to a strong bias and even failure. This would be helpful for implementing the disaster reduction and prevention measures of governments.

Another surprising finding is that the slope of the most probable landslide occurrence in Jiangxi is low, about 3–23°, in which 83.3% of the total landslides have taken place (**Table 2**), much lower than the threshold of 28–35°, proposed for natural landslides by Fan et al. (2016). Zhang Y. et al. (2020) and (see text footnote 1) have also discovered a similar result. This may be due to (1) the uniformization of the realistic relief by the moderate resolution of DEM, 30 m, and the DEM-derived slope that is lower than the real one and (2) human activity, especially the development of the road network and urbanization through slope cutting, which has led to slope failure and reduced landslide slope threshold.

It is worth noting that while conducting IV analysis, we noted that area with a slope of $< 3°$ is also distributed with 3.36% of the total landslides (**Table 2**). This may result from the slope homogenization as mentioned above. Thence, for regional- and even national-scale landslide hazard assessments, coarser-resolution DEM (such as SRTM, 90 m) data are not recommended as they may hide most of the small-scale landslides (e.g., several tens to several hundreds of square meters in surface area).

Another problematic issue arising in our study is the utilization of the MODIS NDVI, with 250 m of resolution. This factor is not as important as DEM but clearly not ideal for representation of the greenness and coverage, in particular of forests and woodlands because of their heterogeneity. Nevertheless, for an often cloudy province, it is extremely difficult to obtain cloud-free November Landsat images of a 5-year period for such a large area. Hence, to use the MODIS NDVI was the only choice.

## Comparative Verification

Zhang Y. et al. (2020) and see text footnote 1 have taken advantage of the RF algorithm to assess the landslides in Guixi and Ruijin in Jiangxi, respectively. We compared our provincial/regional-scale IV-based LR modeling results with the local risk maps of Guixi and Ruijin and found a good agreement between the percentages of the observed landslides falling in the predicted high and very high risk zones. In Guixi, 81.69% of the total landslide points and 79.27% of the VS are distributed in the very high and high risk area (Zhang Y. et al., 2020), whereas see text footnote 1 illustrated that 92.67% of the total landslide points and 86.59% of the VS fall in these two zones in Ruijin. This means our risk modeling and prediction results for the Jiangxi Province are reliable and of practical value to provide technical support for disaster reduction and prevention in this province.

## CONCLUSION

In this paper, IV-based LRM for regional-scale landslide hazard mapping was applied to a complex disaster development and occurrence environment, namely the Jiangxi Province. The reliable results may provide technical support for landslide hazard reduction and prevention action at local- and provincial-scales.

One may think that it is enough to use large scale and the main linear features for regional-scale landslide risk modeling. However, this study reveals that it is essential to employ factors of all scales or as detailed as possible to achieve a reliable and accurate prediction.

From both local and regional/provincial-scale studies, it is uncovered that slope instability is mainly caused by road construction and housing development through slope cutting and triggered by rainfall. Hence, it is particularly important for engineers to select sites of stable geological and environmental conditions for road system development and urban planning to minimize the landslide risk. This is the precondition for a holistic and optimal design of infrastructures and urban planning, which is necessary for regional- or provincial-scale socioeconomic development.

## DATA AVAILABILITY STATEMENT

The raw data supporting the conclusions of this article will be made available upon reasonable request to the corresponding author (WW: wuwch@ecut.edu.cn), without undue reservation.

## AUTHOR CONTRIBUTIONS

PO, WW, and YQ: methodology. WW: software, validation, data curation, visualization, funding acquisition, supervision, and project dministration. PO, YQ, XZ, WH, and YZ: formal analysis. PO, XTZ, WH, YZ, JL, XF, JJ, MZ, and SP: investigation. PO, WW, YQ, CS, XZ, WH, YZ, LX, JL, XF, JJ, MZ, and XH: resources. PO, XTZ, WH, YZ, XL, YB, XFZ, and WL: writing—original draft preparation. PO and WW: writing—review and editing. All authors have read and agreed to the published version of the manuscript.

## FUNDING

This research was supported by the Start-up Fund for Scientific Research of the East China University of Technology (Grant No. DHTP2018001) and Jiangxi Talent Program (Grant No. 900/2120800004) granted to WW.

## ACKNOWLEDGMENTS

A part of the landslide inventory data was obtained from the Environmental Science Data Center, CAS, and the Geological Map of Jiangxi on the Scale of 1/500,000 was provided by the Coal Geological Bureau of Jiangxi Province. DEM (ASTGTMV003, 30 m) and MODIS NDVI data were obtained from NASA (www.earthdata.nasa.gov).

## REFERENCES

Aleotti, P., and Chowdhury, R. (1999). Landslide hazard assessment: summary review and new perspectives. *Bull. Eng. Geol. Environ.* 58, 21–44. doi: 10.1007/s100640050066

Arabameri, A., Pourghasemi, H. R., and Yamani, M. (2017). Applying different scenarios for landslide spatial modeling using computational intelligence methods. *Environ. Earth Sci.* 76:832. doi: 10.1007/s12665-017-7177-5

Assilzadeh, H., Levy, J. K., and Wang, X. (2010). Landslide catastrophes and disaster risk reduction: a GIS framework for landslide prevention and management. *Rem. Sens.* 2, 2259–2273. doi: 10.3390/rs2092259

Ayalew, L., and Yamagishi, H. (2005). The application of GIS-based logistic regression for landslide susceptibility mapping in the Kakuda-Yahiko Mountains, Central Japan. *Geomorphology* 65, 15–31. doi: 10.1016/j.geomorph.2004.06.010

Bai, S., Wang, J., Lue, G., Zhou, P., Hou, S., and Xu, S. (2010). GIS-based logistic regression for landslide susceptibility mapping of the Zhongxian segment in the Three Gorges area, China. *Geomorphology* 115, 23–31. doi: 10.1016/j.geomorph.2009.09.025

Carrara, A. (1983). Multivariate models for landslide hazard evaluation. *J. Int. Assoc. Math. Geol.* 15, 403–426. doi: 10.1007/BF01031290

Chen, V., Kervyn, M., Suh, C. E., Fontijn, K., Ernst, G. G. J., Marmol, M. A. D., et al. (2012). Ladslide susceptibility assessment in Limbe (SW Cameroon): a field calibrated seed cell and information value method. *Catena* 92, 83–98. doi: 10.1016/j.catena.2011.11.014

Chu, S. M. (2012). *The Weathering Factor Study on the Formation of Gully—type Debris flow—take Wenchuan earthquake as an Example(In Chinese with English abstract).* Master dissertation. Chengdu: Chengdu University of Technology.

Corominas, J., Westen, C. V., Frattini, P., Cascini, L., Malet, J. P., and Smith, J. T. (2014). Recommendations for the quantitative analysis of landslide risk. *Bull. Eng. Geol. Environ.* 73, 209–263. doi: 10.1007/s10064-013-0538-8

Dai, Y. (2013). *Study on the Method of Regional early Warning of Landslide in Three Gorges area Based on Information Model(In Chinese with English abstract).* Master dissertation. Beijing: Tsinghua University.

Dang, V. H., Dieu, T. B., Tran, X. L., and Hoang, N. D. (2018). Enhancing the accuracy of rainfall-induced landslide prediction along mountain roads with a gis-based random forest classifier. *Bull. Eng. Geol. Environ.* 78, 2835–2849. doi: 10.1007/s10064-018-1273-y

Djukem, W., Braun, A., Wouatong, A., Guedjeo, C., Dohmen, K., Wotchoko, P., et al. (2020). Effect of soil Geomechanical properties and Geo-environmental factors on landslide predisposition at mount Oku,Cameroon. *Int. J. Environ. Res. Public Health* 17:6795. doi: 10.3390/ijerph17186795

Du, G., Zhang, Y., Iqbai, J., Yang, Z., and Yao, X. (2017). Landslide susceptibility mapping using an integrated model of information value method and logistic regression in the Bailongjiang watershed, Gansu Province, China. *J. Mountain Sci.* 14, 249–268. doi: 10.1007/s11629-016-4126-9

Fan, L., Lehmann, P., and Or, D. (2016). Effects of soil spatial variability at the hillslope and catchment scales on characteristics of rainfall-induced landslides. *Water Resour. Res.* 52, 1781–1799. doi: 10.1002/2015WR017758

Fan, Z., Gou, X., Qin, M., Fan, Q., Yu, J., and Zhao, J. (2018). Information and logistic regression models based coupling analysis for susceptibility of geological hazards(In Chinese with English abstract). *J. Eng. Geol.* 26, 340–347. doi: 10.13544/j.cnki.jeg.2017-052

Feng, H., Zhou, A., Yu, J., Tang, X., Zheng, J., Chen, X., et al. (2016). A comparative study on plum-rain-triggered landslide susceptibility assessment models in west Zhejiang province(In Chinese with English abstract). *Earth Sci.* 41, 403–415. doi: 10.3799/dqkx.2016.032

Froude, M., and Petley, D. (2018). Global fatal landslide occurrence from 2004 to 2016. *Nat. Hazards Earth Syst. Sci.* 18, 2161–2181. doi: 10.5194/nhess-18-2161-2018

Furlani, S., and Ninfo, A. (2015). Is the present the key to the future? *Earth Sci. Rev.* 142, 38–46. doi: 10.1016/j.earscirev.2014.12.005

Gao, K., Cui, P., Zhao, C., Wei, F., and Gao, K. (2006). Landslide hazard evaluation of Wanzhou based on GIS information value method in the three gorges reservoir(In Chinese with English abstract). *Chin. J. Rock Mech. Eng.* 25, 991–996.

Goetz, J., Brenning, A., Petschko, H., and Leopold, P. (2015). Evaluating machine learning and statistical prediction techniques for landslide susceptibility modeling. *Comput. Geosci.* 81, 1–11. doi: 10.1016/j.cageo.2015.04.007

Guo, F., Yang, N., Meng, H., Zhang, Y., and Ye, B. (2008). Application of the relief amplitude and slope analysis to regional landslide hazard assessments(In Chinese with English abstract). *Geol. China* 35, 131–141.

Guzzetti, F., Carrara, A., Cardinali, M., and Reichenbach, P. (1999). Landslide hazard evaluation: a review of current techniques and their application in a multi-scale study, Central Italy. *Geomorphology* 31, 181–216. doi: 10.1016/S0169-555x(99)00078-1

Guzzetti, F., Peruccacci, S., Rossi, M., and Stark, C. P. (2008). The rainfall intensity-duration control of shallow landslides and debris flows:an update. *Landslides* 5, 3–17. doi: 10.1007/s10346-007-0112-1

Huang, R., and Li, W. (2009). Fault effect analysis of geo-hazard triggered by Wenchuan earthquake(In Chinese with English abstract). *J. Eng. Geol.* 17, 19–27.

Huete, A. R., Liu, H. Q., Batchily, K., and Leeuwen, W. V. A. (1997). A comparison of vegetation indices over a global set of TM images for EOS-MODIS. *Rem. Sens. Environ.* 59, 440–451. doi: 10.1016/S0034-4257(96)00112-5

Jiangxi Bureau of Geology (2017). *Geological Book of Jiangxi*. Beijing: Geology Publication. 11–42.

Jiangxi Geological Disaster Emergency Center (2014). "Reportage on geohazard," in *Jiangxi* Available online at: http://district.ce.cn/newarea/roll/201501/20/t20150120_4386022.shtml [in Chinese]

Kalantar, B., Pradhan, B., Naghibi, S. A., Motevalli, A., and Mansor, S. (2018). Assessment of the effects of training data selection on the landslide susceptibility mapping: a comparison between support vector machine (SVM), logistic regression (LR) and artificial neural networks (ANN). *Geomat. Nat. Hazards Risk* 9, 49–69. doi: 10.1080/19475705.2017.1407368

Kilburn, C. R. J., and Pasuto, A. (2003). Major risk from rapid, large - volume landslide in Europe(EU Project RUNOUT). *Geomorphology* 54, 3–9. doi: 10.1016/S0169-555X(03)00050-3

Kim, J. C., Lee, S. M., Jung, H. S., and Lee, S. (2018). Landslide susceptibility mapping using random forest and boosted tree models in pyeong-chang, Korea. *Geocarto Int.* 33, 1000–1015. doi: 10.1080/10106049.2017.1323964

Kumar, D., Thakur, M., Dubey, C. S., and Shukla, D. P. (2017). Landslide susceptibility mapping & prediction using support vector machine for mandakini river basin, garhwal himalaya,india. *Geomorphology* 295, 115–125. doi: 10.1016/j.geomorph.2017.06.013

Lan, H., Wu, F., Zhou, C., and Wang, S. (2002). Analysis on susceptibility of GIS based landslide triggering factors in Yunnan Xiaojiang watershed(In Chinese with English abstract). *Chin. J. Rock Mech. Eng.* 21, 1500–1506. doi: 10.1007/s11769-002-0042-8

Lee, S., and Min, K. (2001). Statistical analysis of landslide susceptibility at Yongin, Korea. *Environ. Geol.* 40, 1095–1113. doi: 10.1007/s002540100310

Lee, S., Ryu, J. Y., Min, K., and Won, J. (2010). Landslide susceptibility analysis using GIS and artificial neural network. *Earth Surf. Process. Landforms* 28, 1361–1376. doi: 10.1002/esp.593

Liang, Y., and Cui, X. (2010). *SPSS15.0 Statistical Analysis and Practical Application*. Beijing: China Rail- way Press, 141–148.

Li, L., Lan, H., Guo, C., Zhang, Y., Li, Q., and Wu, Y. (2017). A modified frequency ratio method for landslide susceptibility assessment. *Landslides* 14, 727–741. doi: 10.1007/s10346-016-0771-x

Li, T., Tian, Y., Wu, L., and Liu, L. (2014). Landslide susceptibility mapping using Random Forest(In Chinese with English abstract). *Geogr. Geo Inform. Sci.* 30, 25–30.

Mertens, B., and Lambin, E. F. (2000). Land cover change trajectories in Southern Cameroon, Annals of the Association of American Geographers. *Ann. Assoc. Am.* 90, 467–494. doi: 10.1111/0004-5608.00205

Meten, M., Prakashbhandary, N., and Yatabe, R. (2015). Effect of landslide factor combinations on the prediction accuracy of landslide susceptibility maps in the Blue Nile Gorge of Central Ethiopia. *Geoenviron. Disasters* 2:9.

Miao, Y., Zhu, A., Yang, L., Bai, S., Liu, J., and Deng, Y. (2016). Sensitivity of BCS for sampling landslide absence data in landslide susceptibility assessment. *Mountain Res.* 34, 432–441.

Montgomery, D. R., and Dietrich, W. E. (1994). A physically based model for the topographic control on shallow landsliding. *Water Resour. Res.* 30, 1153–1171. doi: 10.1029/93wr02979

Nadim, F., Kjekstad, O., Peduzzi, P., Herold, C., and Jaedicke, C. (2006). Global landslide and avalanche hotspots. *Landslides* 3, 159–173. doi: 10.1007/s10346-006-0036-1

Nandi, A., and Shakoor, A. (2010). A GIS-based landslide susceptibility evaluation using bivariate and multivariate statistical analyses. *Eng. Geol.* 110, 11–20. doi: 10.1016/j.enggeo.2009.10.001

Peng, L., Niu, R., Huang, B., Wu, X., Zhao, Y., and Ye, R. (2014). Landslide susceptibility mapping based on rough set theory and support vector machines: a case of the three gorges area, China. *Geomorphology* 204, 287–301. doi: 10.1016/j.geomorph.2013.08.013

Pradhan, B., and Lee, S. (2007). Utilization of optical remote sensing data and GIS tools for regional landslide hazard analysis using an artificial neural network model. *Earth Sci. Front.* 14, 143-151. doi: 10.1016/S1872-5791(08)60008-1

Ren, J., Fan, X., Zhao, C., Li, Z., and Dou, X. (2018). Evaluation of the landslide vulnerability in Duyun of Gui- zhou Province(In Chinese with English abstract). *Hyderogeol. Eng. Geol.* 45, 165–172.

Ruff, M., and Czurda, K. (2008). Landslide susceptibility analysis with a heuristic approach in the Eastern Alps (Vorarlberg, Austria). *Geomorphology* 94, 314–324. doi: 10.1016/j.geomorph.2006.10.032

Serneels, S., and Lambin, E. F. (2001). Proximate cause of land-use change in Narok District, Kenya: a spatial statistical model. Agriculture. *Ecosyst. Environ.* 85, 65–81. doi: 10.1016/s0167-8809(01)00188-8

Shan, J., Liu, X., Wei, L., and Zhu, X. (2004). Rainfall characteristics analyses on landslide in Jiangxi Province. *Meteorol. Monthly* 30, 13–15. doi: 10.1117/12.528072

Sharma, L. P., Patel, N., Ghose, M. K., and Debnath, P. (2015). Development and application of Shannon's entropy integrated information value model for landslide susceptibility assessment and zonation in Sikkim Himalayas in India. *Nat. Hazards* 75, 1555–1576. doi: 10.1007/s11069-014-1378-y

Su, Q. (2006). *Research on Loess Landslide Hazard Zonation Based on DEM(In Chinese with English abstract)*. Doctoral dissertation (in Chinese). Beijing: China University of Geosciences.

Su, X., Wei, W., Guo, W., Wang, S., Wang, G., Wu, W., et al. (2017). Analyzing the impact of relief amplitude to loess landslides based on SRTM DEM in Tianshui Prefecture(In Chinese with English abstract). *J. Nepal Geol. Soc.* 23, 99–110.

Tian, C., Liu, X., and Wang, J. (2016). Geohazard susceptibility assessment based on CF model and logistic regression models in Guangdong(In Chinese with English abstract). *Hydrogeol. Eng. Geol.* 43, 154–161.

Tian, Q., Zhang, B., Guo, J., Liu, H., Chang, Z., Li, Y., et al. (2020). Landslide susceptibility assessment based on the coupling model of information value and logistic regression(In Chinese with English abstract). *Sci. Technol. Eng.* 20, 8460–8468.

Tucker, C. J. (1979). Red and photographic infrared linear combinations for monitoring vegetation. *Rem. Sens. Environ.* 8, 127–150. doi: 10.1016/0034-4257(79)90013-0

Walsh, S. J., Crawford, T. W., Welsh, W. F., and Crews-Meyer, K. A. (2001). A multiscale analysis of LULC and NDVI variation in Nang Rong district, Northeast Thailand. *Agric. Ecosyst. Environ.* 85, 47–64. doi: 10.1016/s0167-8809(01)00202-x

Wang, H., Wang, G., Liu, G., and Xu, W. (2005). GIS-based landslide hazard assessment: an overview. *Prog. Phys. Geogr.* 29, 548–567. doi: 10.1191/0309133305pp462ra

Wang, H. (2013). Interpolation algorithm for shallow foundations settlement based on compression and load settlement curves(In Chinese with English abstract). *J. Geotechn. Eng.* 35, 663–670.

Wang, N., Guo, Y., Liu, T., and Zhu, Q. (2019). Landslide susceptibility assessment based on support vector machine model(In Chinese with English abstract). *Sci. Technol. Eng.* 19, 70–79.

Wang, X., and Wang, J. (2017). Application of comprehensive graph weight method to landslide deformat- ion prediction(In Chinese with English abstract). *J. Yangtze River Sci. Res. Inst.* 34, 82–86.

Wu, W. (2003). *Application de la Géomatique au Suivi de la Dynamique Environnementale en Zones Arides (in French)*. Ph.D dissertation. Paris: Université de Paris 1-Panthéon-Sorbonne.

Wu, W. (2014). The generalized difference vegetation index (GDVI) for dryland characterization. *Rem. Sens. Environ.* 6, 1211–1233. doi: 10.3390/rs6021211

Wu, W., and Ai, G. (1995). Risk assessment of natural disasters in the course of selection of nuclear waste disposal (in Chinese with English abstract). *J. East China Geol. Inst.* 18, 260–265.

Wu, W., Zucca, C., Karam, F., and Liu, G. (2016). Enhancing the performance of regional land cover mapping. *Int. J. Appl. Earth Observ. Geoinform.* 52, 422–432. doi: 10.1016/j.jag.2016.07.014

Wu, W., Zucca, C., Muhaimeed, A. S., Al-Shafie, W. M., Fadhil Al-Quraishi, A. M., Nangia, V., et al. (2018). Soil salinity prediction and mapping by machine learning regression in Central Mesopotamia, Iraq. *Land Degr. Dev.* 29, 4005–4014. doi: 10.1002/ldr.3148

Xia, H., Yin, K., Liang, X., and Ma, F. (2018). Landslide susceptibility assessment based on SVM-ANN models: a case study for Wushan County in the three gorges reservoir(In Chinese with English abstract). *Chin. J. Geol. Hazard Control* 29, 13–19.

Xing, Q., Zhao, C., Gao, K., and Guo, Y. (2004). Logical regression analysis on the hazard of landslide based on GIS(In Chinese with English abstract). *Geogr. Geo Inform. Sci.* 20, 49–51.

Xu, J. (2005). *Study on the Mechanism of Deformation Disintegration Failure and the Stability of Debris Landslide(In Chinese with English abstract).* Doctoral dissertation. Hangzhou: Zhejiang University.

Yang, G., Xu, P., Cao, C., Zhang, W., Lan, Z., Chen, J., et al. (2019). Assessment of regional landslide susceptibility based on combined model of certainty factor method(In Chinese with English abstract). *J. Eng. Geol.* 27, 1153–1163. doi: 10.13544/j.cnki.jeg.2019018

Yang, Q. (2003). *Natural Geography of Jiangxi Province*. Jiangxi: Fangzhi press, 1–31.

Yao, X., Tham, L., and Dai, F. (2008). Landslide susceptibility mapping based on support vector machine: a case study on natural slopes of hong kong,china. *Geomorphology* 101, 572–582. doi: 10.1016/j.geomorph.2008.02.011

Yilmaz, I. (2009). A case study from koyulhisar (sivas-turkey) for landslide susceptibility mapping by artificial neural networks. *Bull. Eng. Geol. Environ.* 68, 297–306. doi: 10.1007/s10064-009-0185-2

Yin, J., Chen, J., Xu, X., Wang, X., and Zheng, Y. (2010). The characteristics of the landslides triggered by the Wenchuan Ms 8.0 Earthquake from Anxian to Beichuan. *J. Asian Earth Sci.* 37, 452–458. doi: 10.1016/j.jseaes.2009.12.002

Yu, J. (2003). *analysis of Excavation and Support of High Rock Slope(In Chinese with English abstract).* Doctoral dissertation. Hangzhou: Zhejiang University.

Zhang, B., Tang, M., and Liu, R. (2017). Dynamic data driven multi-model coupled for analyzing the stability of landslide(In Chinese with English abstract). *Geomat. Spatial Inform. Technol.* 40, 142–147.

Zhang, L., and Jiang, S. (2004). Data driver model for regional landslide susceptibility assessment and its application(In Chinese with English abstract). *Hydrogeol. Eng. Geol.* 6, 33–35.

Zhang, Q., Ling, S., Li, X., Sun, C., Xu, J., and Huang, T. (2020). Comparison of landslide susceptibility mapping rapid assessment models in Jiuzhaigou County,Sichuan province,China(In Chinese with English abstract). *Chin. J. Rock Mech. Eng.* 39, 1595–1610.

Zhang, X. (2019). *Hazard Assessment and Zoning Research of Landslide in Shanxi Province Based on GIS(In Chinese with English abstract).* Master dissertation, Xi'an: Chang'an University.

Zhang, Y., Wu, W., Qi, Y., Lin, Z., Zhang, G., Chen, R., et al. (2020). Mapping landslide hazard risk using random forest algorithm in Guixi, Jiangxi, China. *ISPRS Int. J. Geo Inform.* 9:695. doi: 10.3390/ijgi9110695

Zhao, Y., Wang, R., Jiang, Y., Liu, H., and Wei, Z. (2019). GIS-based logistic regression for rainfall-induced landslide susceptibility mapping under different grid sizes in Yueqing, Southeastern China. *Eng. Geol.* 259:105147. doi: 10.1016/j.enggeo.2019.105147

Zhu, A., Miao, Y., Liu, J., Bai, S., and Hong, H. (2019). A similarity-based approach to sampling absence data for landslide susceptibility mapping using data-driven methods. *Catena* 183:104188. doi: 10.1016/j.catena.2019.104188

**Conflict of Interest:** The authors declare that the research was conducted in the absence of any commercial or financial relationships that could be construed as a potential conflict of interest.

frontiers in Earth Science

ORIGINAL RESEARCH
published: 24 September 2021
doi: 10.3389/feart.2021.712403

# Engineering Planning Method and Control Modes for Debris Flow Disasters in Scenic Areas

*Xing-Long Gong*[1,2,3], *Xiao-Qing Chen*[1,2,3], *Kun-Ting Chen*[4,5]*, *Wan-Yu Zhao*[1] and *Jian-Gang Chen*[1]

[1]Key Laboratory of Mountain Hazards and Earth Surface Processes, Institute of Mountain Hazards and Environment, Chinese Academy of Sciences, Chengdu, China, [2]China-Pakistan Joint Research Center on Earth Sciences, CAS-HEC, Islamabad, Pakistan, [3]University of Chinese Academy of Sciences, Beijing, China, [4]Compound Disaster Prevention Research Center, General Research Service Center, National Pingtung University of Science and Technology, Pingtung, Taiwan, [5]Department of Soil and Water Conservation, National Pingtung University of Science and Technology, Pingtung, Taiwan

Compared with debris flows in other areas, debris flows in scenic areas not only seriously threaten residents, tourists, roads, walkways, and other infrastructure, but also cause considerable damage to the landscapes and ecosystems of these areas. Extreme rainfall events in the future will increase the complexities and challenges involved in debris flow control in scenic areas. Currently, the systematic planning of the entire scenic area is not considered in the treatment of debris flows. It is not possible to realize the rapid planning of any debris flow gully control project in a scenic area and to quantify the volume of debris flow material retained by each engineering structure. Based on field investigations and data collected from debris flow control projects in gullies in Jiuzhaigou Valley, China, an engineering planning method for debris flow control projects in scenic areas is herein proposed, and the challenges confronting existing control projects in scenic areas are discussed. Moreover, based on the example of Jiuzhaigou Valley, corresponding control engineering schemes for debris flow gullies in Xiajijie Lake Gully, Zhuozhui Gully, Xuan Gully, Pingshitou Gully, and West-Zhuozhui Gully are formulated. Four control modes for debris flow disasters in scenic areas are proposed, namely, "blocking + deposit stopping," "deposit stopping," "blocking," and "drainage + deposit stopping," which provide a systematic control strategy for post-earthquake debris flow disaster management in Jiuzhaigou Valley and other similar scenic areas.

**Keywords: engineering planning method, control mode, debris flow, scenic areas, climate change**

OPEN ACCESS

***Edited by:***
*Yih-Chin Tai,*
*National Cheng Kung University, Taiwan*

***Reviewed by:***
*Kana Nakatani,*
*Kyoto University, Japan*
*Kuo-Lung Wang,*
*National Chi Nan University, Taiwan*

***Correspondence:**
*Kun-Ting Chen*
*kuntingchen@mail.npust.edu.tw*

***Specialty section:***
*This article was submitted to Geohazards and Georisks, a section of the journal Frontiers in Earth Science*

***Received:*** *20 May 2021*
***Accepted:*** *13 August 2021*
***Published:*** *24 September 2021*

***Citation:***
*Gong X-L, Chen X-Q, Chen K-T, Zhao W-Y and Chen J-G (2021) Engineering Planning Method and Control Modes for Debris Flow Disasters in Scenic Areas. Front. Earth Sci. 9:712403. doi: 10.3389/feart.2021.712403*

## INTRODUCTION

Debris flows are mixtures of sediment and water that flow down a slope under the influence of gravity. These disasters are widespread and commonplace in mountainous areas. Steep topography, abundant loose material, and concentrated rainfall are three important factors influencing debris flow formation. Numerous studies have attempted to elucidate the debris flow formation process based on rainfall thresholds and sediment supply conditions (Takahashi, 2007; Santi et al., 2008; Tang et al., 2012; Hungr et al., 2014; Zhang et al., 2014; Fan R. L. et al., 2018; Domènech et al., 2019). In particular, post-earthquake debris flows have been widely studied owing to their significant destructive power. In general, a devastating earthquake generates an adequate supply of sediment in the form of co-seismic collapses and landslides, which indirectly reduces the rainfall threshold

required to trigger a debris flow (Tang et al., 2012; Ma et al., 2017); catastrophic debris flows can be triggered even by low-intensity rainfall long after an earthquake has occurred. For example, destructive debris flows are still known to occur in the areas affected by the 1999 Chi-Chi, 2008 Wenchuan, and 2015 Gorkha earthquakes (Shieh and Tsai, 2009; Zhou et al., 2016; Dahlquist and West, 2019). Post-earthquake debris flows are characterized by their high destructive power, large scale, and the ease with which they form disaster chains (e.g., debris flows block river channels, causing river diversion and flooding of surrounding areas). Therefore, they seriously threaten human safety and endanger roads, bridges, houses, and other facilities (Cui et al., 2013; Chen et al., 2015; Chen K.-T. et al., 2018; Chen et al., 2019a; Chen et al., 2019b; Xiong et al., 2020). Wenjia Gully, in Qingping Township, Mianzhu, Sichuan Province, China, was not a debris flow gully prior to the Wenchuan earthquake. However, in the three rainy seasons immediately after the earthquake, five debris flow events were recorded here. Owing to heavy rainfall on August 13, 2010, the loose material in the channel of Wenjia Gully underwent violent erosion, resulting in a debris flow disaster. The debris flow peak discharge reached 1,530 $m^3$/s, and approximately $33.1 \times 10^6$ $m^3$ of loose material was transported to the gully mouth. Debris flow material blocked Mianyuan River, forming a dam that was 400 m long and 820 m wide. The subsequent river diversion flooded 479 newly constructed houses across and upstream of Wenjia Gully, as a result of which 7 people died, 5 were reported missing, and 39 sustained injuries (Ni et al., 2012; Tang et al., 2012; Yu et al., 2013).

Engineering measures are an effective method to mitigate debris flow disasters. Employing stabilization measures in the formation zone, blocking and drainage measures in the transport zone, and drainage and deposit stopping measures in the deposition zone of debris flow gullies are common approaches used to control debris flow disasters (Ikeya 1989; Cui and Lin, 2013; Chen et al., 2015). Stabilization measures involve stabilizing the slope, reducing erosion of the gully bed, preventing debris flow initiation, and reducing the scale of debris flows by building check dams and bed sills (Ikeya 1989; Piton et al., 2016). For example, to control debris flow disasters in Jiangjia Gully in Yunnan Province, China, a large number of check dams were built across the upstream tributaries of the watershed in 1979. These check dams effectively control erosion, stabilize the slope on both sides, promote the restoration of vegetation, and reduce the frequency of debris flows in the gully (Zeng et al., 2009). Blocking measures refer to the construction of check dams to retain debris flow material, regulate sediment transport, and reduce the destruction of downstream objects by debris flows (Ikeya 1989; Piton and Recking 2016). For example, to control debris flow disasters in the upstream region of Joganji River, Japan, check dams with a total capacity of 5 million $m^3$ were constructed to trap debris flow material (Kanbara and Imamori 2020). Drainage measures refer to the construction of drainage channels, diversion dikes, and other projects to control gully erosion and guide debris flows along the designed path so as to realize the protection of downstream objects (Ikeya 1989; Van Dine 1996). For example, a drainage channel was constructed downstream of the Xiaogangjian debris flow gully in Sichuan Province, China; it crosses the Hanqing Highway and channels part of the debris flow material into a nearby river, effectively preventing debris flows from directly damaging the road (Chen et al., 2015; Chen J. G. et al., 2018). Deposit stopping measures refer to the construction of retention basins or retaining walls to retain debris flow material and protect vulnerable structures and objects. For example, in Jiuzhaigou Valley, Sichuan Province, China, a retaining wall was built on the debris flow fan in Zechawa Gully to retain the debris flow material and protect tourists, highways, and plank roads in the scenic area (Gong et al., 2020).

Compared with debris flow gullies that threaten roads, villages, and towns, debris flows in scenic areas not only threaten human safety and facilities, but also damage landscape resources, cause the deterioration of the ecosystem and ecological environment, and adversely impact the sustainable development of scenic areas, which has attracted extensive attention from scholars around the world (Cui et al., 2003; Faccini et al., 2009; Chen et al., 2016; Wang 2016). For example, debris flows in Jiuzhaigou Valley severely damage scenic landscapes, cause lake siltation, and block scenic roads, which significantly impact normal operations in these areas (Cui et al., 2003; Chen X.-q. et al., 2018). To protect residents, tourists, the natural landscape, and the ecological environment in Jiuzhaigou Valley, engineering measures have been employed to treat 14 debris flow gullies in which serious disasters occurred since 1984. The principles, technical measures, and typical engineering structures used for debris flow control in Jiuzhaigou Valley have been previously discussed (Cui et al., 2003). In the Shuzheng debris flow gully, which poses a threat to Shuzheng Village and the Shuzheng Lakes area, debris flow disasters were effectively controlled by constructing check dams in the formation zone to prevent the formation of conditions conducive to debris flow initiation and to stabilize the slope and gully. In the Xiajijie Lake debris flow gully, which poses a threat to the lake landscape and a nearby highway, check dams were built in the upper reaches of the gully, and a drainage channel with an embankment was constructed in the middle reaches of the gully to divert the debris flow into the forest. Vegetation is used to block debris flow material and realize the organic combination of ecosystem and engineering projects to achieve synergistic disaster reduction (Cui et al., 2007). However, the aforementioned control projects are more than 30 years old. The M7.0 earthquake that struck Jiuzhaigou Valley on August 8, 2017 severely damaged the original control projects in the area, and their capacity to control debris flows was considerably reduced (Huang et al., 2020). Global climate change trends indicate that extreme rainfall events will become more common and that debris flow disasters will become more severe because of the complex terrain conditions in this region (Liu et al., 2020). To manage post-earthquake debris flow disasters in Jiuzhaigou Valley, it is necessary to analyze the characteristics of the disasters and implement appropriate and timely control measures. Based on the characteristics of debris flow disasters, some scholars proposed that the "blocking + deposit stopping" control mode should be adopted to manage these disasters comprehensively (Gong et al., 2020). Other

scholars point to the fact that the location of debris flow control projects after an earthquake in scenic areas is limited by the functional zoning of the scenic areas; control projects can only be located within the experimental zones of scenic areas, where nature conservation and the sustainable use of resources are effectively combined. The Xiajijie Lake Gully is used as a case study to illustrate that the "blocking," "deposit stopping," and "blocking + deposit stopping" control modes should be adopted to control debris flows in Jiuzhaigou Valley (Zhao et al., 2020). Based on the foregoing analysis, the Jiuzhai Valley National Park Administration Bureau has implemented debris flow control projects in 31 debris flow gullies in the scenic area, some of which were completed in May 2019. However, on June 21, 2019, and July 22, 2019, debris flow disasters occurred in several gullies in the scenic area. The disaster reduction effect of the new control projects was found to be insufficient, and vulnerable structures were not effectively protected. The following shortcomings were noted: 1) there was a lack of planning for a debris flow disaster control system for the entire scenic area; 2) the control scheme for debris flow gullies was not appropriate; and 3) the engineering design parameters of the control scheme were inappropriate.

To overcome the aforementioned challenges, this study aimed to propose an engineering planning method for debris flow control in scenic areas using field investigations and data obtained from control projects in Jiuzhaigou Valley. This planning method consisted of the following steps: 1) The region in which the experimental zone of the scenic area overlapped with the transport and deposition zones of debris flow gullies was taken as the area in which the debris flow control projects could be constructed, so as to realize the systematic planning of debris flow disaster control for the entire scenic area. 2) Based on the objects threatened by debris flows and the topographical characteristics of the debris flow gullies, the "blocking + deposit stopping," "deposit stopping," "blocking," and "drainage + deposit stopping" control modes were adopted for different debris flow gullies in the scenic area to rapidly develop engineering measures for debris flow gullies in the scenic area. 3) The debris flow control projects were planned reasonably, the amount of debris flow material that could be retained by each project structure was quantified using parameter calculation, and the project implementation plan was determined. Based on the engineering planning method for debris flow control in the scenic area, this study discussed the challenges confronting debris flow control engineering in the scenic area, and formulated corresponding engineering schemes for debris flow control in the Xiajijie Lake, Zhuozhui, Pingshitou, Xuan, and West-Zhuozhui debris flow gullies.

# DEBRIS FLOW DISASTERS AND THEIR MITIGATION MEASURES IN JIUZHAIGOU VALLEY

## Regional Setting of Jiuzhaigou Valley

Jiuzhaigou Valley is located in Zhangzha Town, Jiuzhaigou County, Sichuan Province, China, approximately 440 km away from Chengdu, Sichuan Province, China. Jiuzhaigou Valley, which has a basin area of 720 $km^2$, has a high vegetation coverage, stable surface runoff, and adequate groundwater replenishment (https://en.jiuzhai.com/). As a result of precipitation and groundwater replenishment, a large number of lakes (commonly known as Haizi) are widely distributed in the scenic area, arranged in the form of a string of beads. The largest of these is Long Lake. The terrain of Jiuzhaigou Valley is high in the south and low in the north. The main gully has developed on the northern slope of the Gaerna watershed at the southernmost end of the basin. Water flows from south to north, and most branch gullies merge into the main gully in an east-west direction (**Figure 1**). Jiuzhaigou Valley is globally renowned for its blue and green lakes, spectacular waterfalls, and narrow conic karst landforms; it was declared a UNESCO World Heritage Site in 1992.

The study area is located between the Qinghai-Tibet Plateau and the Sichuan Basin, in a zone with a high altitude and steep slopes. There are 68 mountains with peaks higher than 4,000 m above sea level (m asl) in the area. The highest point is Gaerna in the southernmost region of the watershed, and the lowest point is Yangdong in the northernmost gully of the basin. The maximum elevation difference is 2,768 m, the horizontal distance between the highest and lowest points is approximately 46 km, and the average elevation difference of the entire basin exceeds 1,600 m. These topographic conditions are conducive to the occurrence of debris flows. The study area belongs to the Songpan-Ganzi block, which lies to the east of the Bayanhar block, and the unique geological conditions in the area are the result of the intense activity along the Tazang, Minjiang, and Huya faults. This activity led to the M7.5 Diexi earthquake in 1933, the M6.7 Zhangla earthquake in 1960, the M6.5 Huanglong earthquake in 1973, the Songpan-Pingwu earthquake cluster ($M_S$ = 7.2, 6.7, and 7.2) in 1976, and the M7.0 Jiuzhaigou earthquake in 2017 (Fan X. et al., 2018; Zhao et al., 2018). Frequent seismic activity leads to the fracture and collapse of the rock mass (limestone and slate with a small amount of sandstone) and induces landslides in the study area, which provides an abundant source of loose material for debris flows. In addition, the rainfall in the study area is concentrated from May to September, usually in the form of heavy rain (Gong et al., 2020). Owing to the steep terrain and abundant loose material, debris flow disasters are frequently triggered in the study area when concentrated rainfall events and rainstorms occur.

## Debris Flow Mitigation Measures in Jiuzhaigou Valley

To protect residents, tourists, the natural landscape, and the ecological environment in Jiuzhaigou Valley, engineering control has been carried out on the debris flow gully since 1984 (Cui et al., 2007). Debris flow disasters in the scenic area have recently increased owing to the 2017 Jiuzhaigou M7.0 earthquake; these disasters have damaged infrastructure, destroyed vegetation, and polluted water bodies in the scenic area (Chen X.-q. et al., 2018; Hu et al., 2019; Gong et al., 2020). After the 2017 Jiuzhaigou earthquake, the Jiuzhai Valley National Park Administration Bureau initiated phased treatment of 31 debris flow gullies; the first phase, comprising 15 debris flow gully

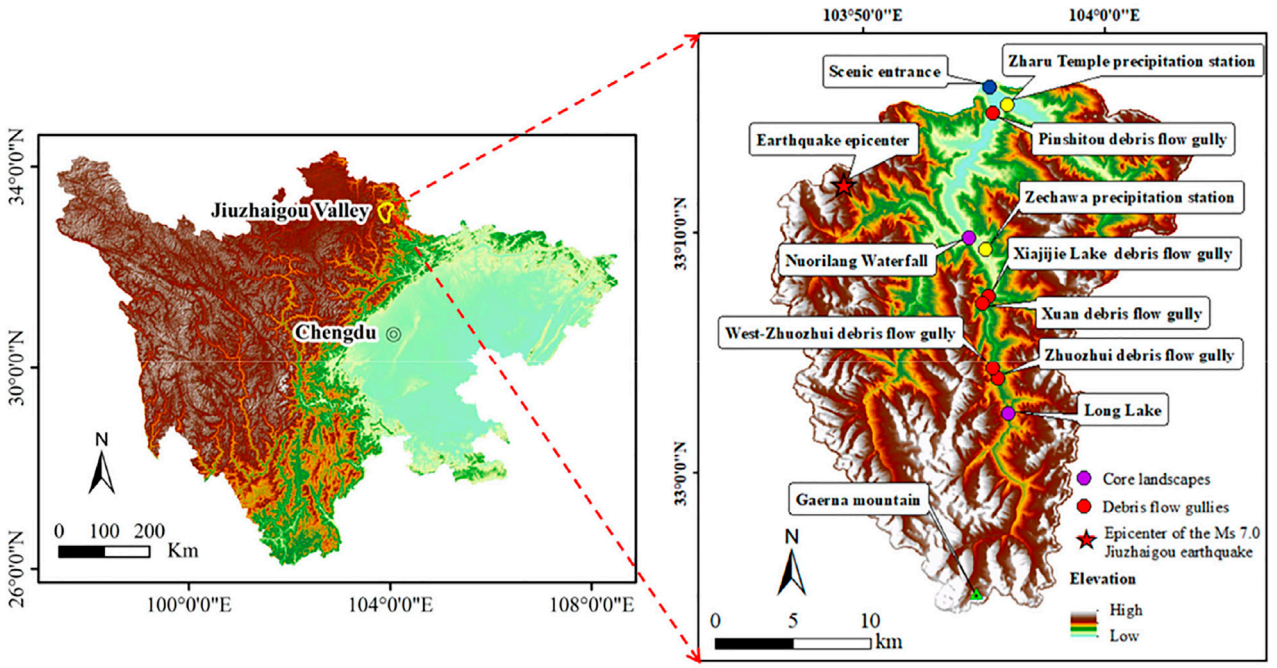


**FIGURE 1 |** Geomorphological setting of the study area and distribution of debris flow gullies in the area.

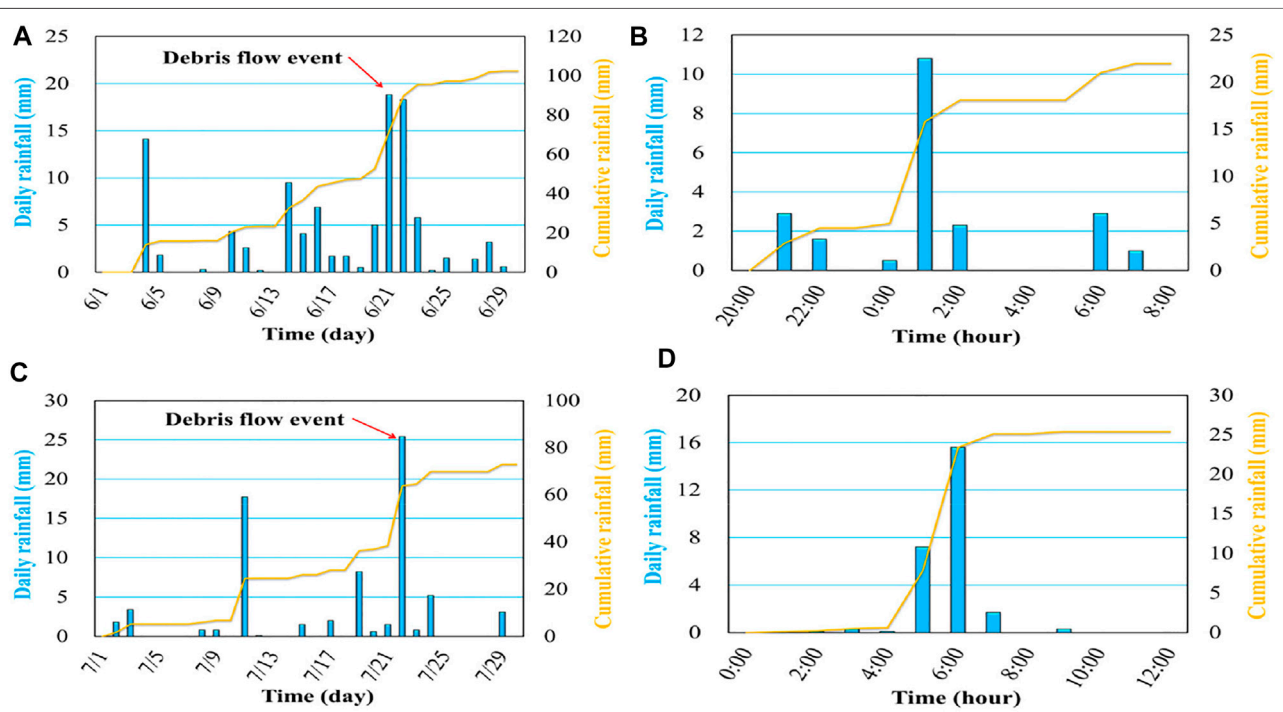


**FIGURE 2 |** Distribution of daily and hourly rainfall. **(A)** Daily rainfall in June 2019 recorded by the Zechawa precipitation station; **(B)** Hourly rainfall from 20:00 (Beijing time) on June 20 to 8:00 (Beijing time) on June 21, 2019 recorded by the Zechawa precipitation station; **(C)** Daily rainfall in July 2019 recorded by the Zharu Temple precipitation station; **(D)** Hourly rainfall from 00:00 to 12:00 (Beijing time) on July 22, 2019 recorded by the Zharu Temple precipitation station.


**FIGURE 3 |** View of Xiajijie Lake Gully. **(A)** Control engineering layout of Xiajijie Lake Gully (before the debris flow event on June 21, 2019). The blue line in the figure represents the main channel; **(B)** Debris flow material deposited on the scenic road on September 25, 2017; **(C)** Debris flow material entering Xiajijie Lake on September 25, 2017.

control projects, was completed in May 2019. From 20:00 (Beijing time) on June 20 to 08:00 (Beijing time) on June 21, 2019, heavy rainfall occurred in Jiuzhaigou Valley. Rainfall data from the Zechawa precipitation station show that the maximum 1 h rainfall was 10.8 mm, and the cumulative 6 h rainfall was 18.1 mm (**Figures 2A,B**); this rainfall intensity was almost equivalent to that of rainfall with a 2-years return period. The heavy rainfall induced simultaneous debris flows in Xiajijie Lake, Xuan, Zhuozhui, Zechawa, Zhongjijie Lake, and West-Zhuozhui in the scenic area; the gully in the West-Zhuozhui area changed from a non-debris flow gully to a debris flow gully during this heavy rainfall event. From 00:00 to 09:00 (Beijing time) on July 22, 2019, heavy rainfall occurred again in the scenic area. Rainfall data from the Zharu Temple precipitation station show that the maximum 1 h rainfall was 15.6 mm, and the cumulative 6 h rainfall was 25 mm (**Figures 2C,D**); this rainfall intensity was

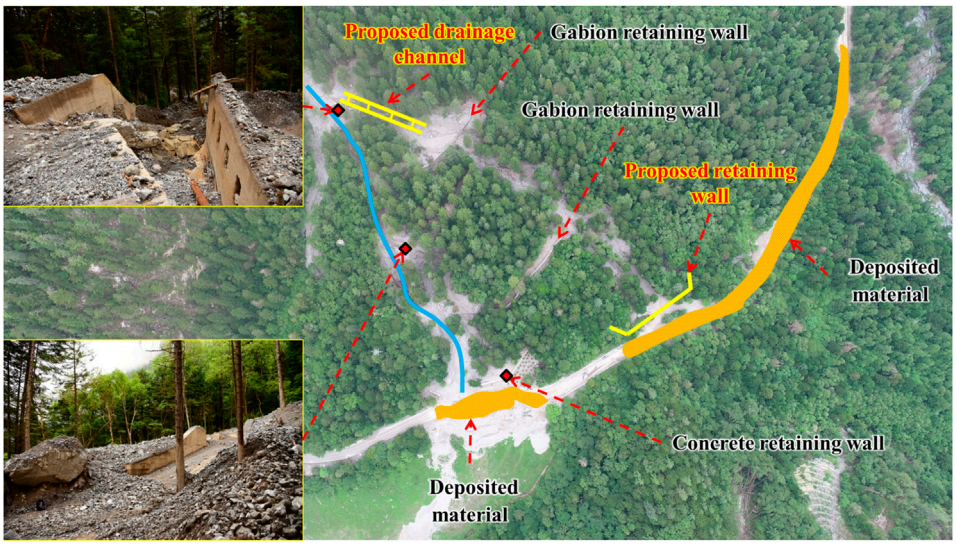


**FIGURE 4 |** Control engineering layout of Xiajijie Lake Gully (after the debris flow event on June 21, 2019). The blue line in the figure represents the main channel. The proposed drainage channel and retaining wall in the figure are the proposed engineering projects described in *Application of the Planning Method for the Xiajijie Lake, Zhuozhui, Pingshitou, Xuan, and West-Zhuozhui Debris Flow Gullies* section.

almost equivalent to that of rainfall with a return period of 2–5 years. The heavy rainfall triggered a debris flow in the scenic area of Pingshitou Gully. Field investigation revealed that the new debris flow control project could not effectively control the debris flow disasters of June 21 and July 22, 2019. The inappropriate control engineering planning scheme and parameter calculation are elucidated using the examples of the Xiajijie Lake, Pingshitou, Zhuozhui, Xuan, and West-Zhuozhui debris flows.

## Blocking and Deposit Stopping to Control Debris Flow Disasters in Xiajijie Lake Gully

Xiajijie Lake Gully is adjacent to Xiajijie Lake. The straight-line distances from this gully to Nuorilang Waterfall and the entrance of Jiuzhaigou Valley are 4.6 and 16.2 km, respectively. The only scenic highway from Nuorilang Waterfall to Long Lake passes through the accumulation fan at the gully mouth (**Figure 3A**). In general, Xiajijie Lake Gully slopes from west to east; the highest point (4,120 m asl) lies on the west side of the basin and the lowest point lies near the mouth of Xiajijie Lake Gully (2,620 m asl). The watershed area of Xiajijie Lake Gully is 1.87 $km^2$, the length of the main gully is 2.36 km, and the average longitudinal slope gradient of the gully bed is 593‰.

To mitigate debris flow disasters in Xiajijie Lake Gully, blocking measures were implemented in the debris flow gully in 1984. Three check dams and a drainage channel with an embankment were constructed in the transport zone of the debris flow gully (**Figure 3A**). This type of drainage channel can discharge part of the debris flow material to the forest on the left of the gully, and use vegetation to block debris flow, effectively realizing the combined use of ecological and engineering measures to achieve coordinated disaster mitigation. On August 8, 2017, the M7.0 Jiuzhaigou earthquake produced a large quantity of landslide material, which provided an abundant source of loose material for debris flow activity in Xiajijie Lake Gully. On September 25, 2017, a debris flow disaster occurred in Xiajijie Lake Gully. After the debris flow material filled the check dam, part of the debris flow material spilled out into the forest on the left side of the drainage channel, part of the material traveled rapidly along the main gully and flowed out, completely blocking the road in the area (**Figure 3B**), and part of the material entered Xiajijie Lake (**Figure 3C**). The debris flow material buried a 150 m section of the road in the scenic area, and the deposited material was up to 5 m thick.

In December 2017, the Jiuzhai Valley National Park Administration Bureau carried out treatment of the debris flow gully using the "blocking + deposit stopping" control mode. Three diversion dams were constructed in the transport zone to retain and divert the debris flow material. These dams ensure that a part of the debris flow material enters into the forest on the left and is blocked by retaining walls made of gabions, and another part of the debris flow material moves along the main gully and is blocked by a concrete retaining wall (**Figure 4**) (Zhao et al., 2020). Owing to heavy rainfall on June 21, 2019, a debris flow disaster occurred in Xiajijie Lake Gully. The diversion dam played an effective role during the debris flow event. A large portion of the debris flow material entered the forest on the left, and only a small portion of the material was transported along the main channel to the gully mouth, where the retaining wall effectively prevented the material from entering the Xiajijie Lake. However, owing to the tremendous destructive power of this post-earthquake debris flow, the debris flow material that was diverted to the left damaged the retaining wall made of gabions. As a result, a large amount of debris flow material was deposited on the scenic road. The length of the road section on which the debris flow material was deposited was 334 m, the width of the deposit was 12–15 m, and the thickness of the

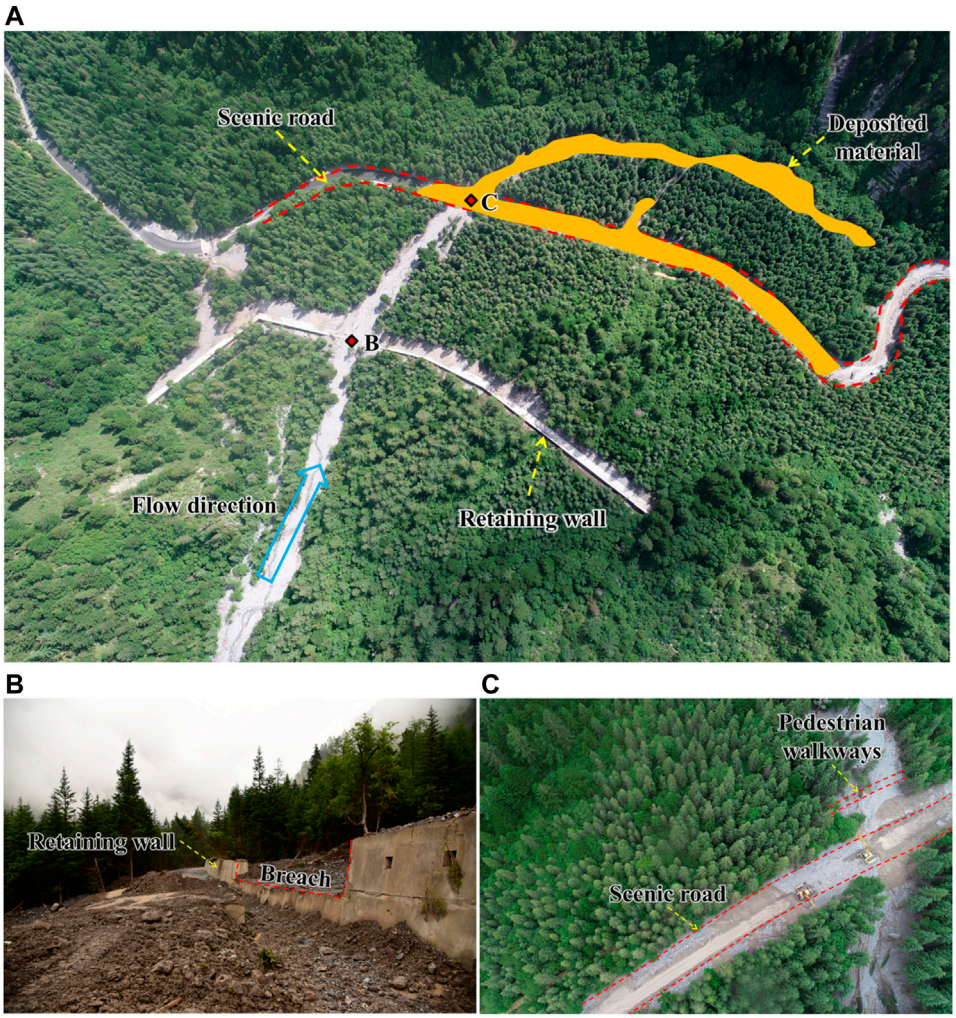


**FIGURE 5 |** Mitigation measures in Zhuozhui Gully. **(A)** Overview of the mitigation structures; **(B)** The damaged retaining wall, corresponding to point B in **(A)**. **(C)** The debris flow material deposited on the scenic road, corresponding to point C in **(A)**.

deposit was 1.5–3.0 m (**Figure 4**). By estimating the deposition area and thickness of the debris flow material at the retaining wall, in the forest, and on the road, the total amount of debris flow material was estimated to be $3.3 \times 10^4$ m$^3$.

## Deposit Stopping to Control Debris Flow Disasters in Zhuozhui Gully

Zhuozhui Gully is approximately 25 km away from the exit of the scenic area. The mouth of the gully is located along the only scenic road from Zechawa village to Long Lake. In a plan view, the watershed of the debris flow gully is leaf-like. The main gully is approximately 3.3 km in length, and the basin area is about 4.14 km$^2$. The highest point of the gully is 4,492 m asl, the elevation of the gully mouth is 2,882 m asl, the relative elevation difference between the highest point and the gully mouth is 1,610 m, and the average longitudinal slope of the gully is about 386‰. After the 2017 Jiuzhaigou earthquake, a 347 m long and 3 m high retaining wall was built in the deposition zone of the debris flow gully to mitigate post-earthquake debris flow disasters in Zhuozhui Gully; the retaining wall had a designed storage capacity of $1.2 \times 10^4$ m$^3$ (**Figure 5A**). On June 21, 2019, a debris flow disaster was triggered by rainfall in Zhuozhui Gully. The debris flow material was transported to the retaining wall along the gully. Owing to the high impact of the debris flow, the retaining wall was partially damaged along the main channel of the debris flow gully (**Figure 5B**). Thus, a large amount of debris flow material was transported downstream, resulting in the burial of a 20 m section of scenic plank road and a 313 m section of the highway. The thickness of the debris flow material deposited on the scenic road was 2–3 m, and the debris flow continued to move downward into the forest, resulting in the destruction of approximately 3,215 m$^2$ of forest (**Figure 5C**). By estimating the deposition area and thickness of debris flow material in the retaining wall, road, and forest, the total amount of debris flow material was calculated to be $2.5 \times 10^4$ m$^3$.


**FIGURE 6 |** Control engineering layout of Pingshitou Gully (after the debris flow event on July 22, 2019). The blue line in the figure represents the main channel. The drainage channel and the retaining wall in the figure are the proposed engineering projects described in *Application of the Planning Method for the Xiajijie Lake, Zhuozhui, Pingshitou, Xuan, and West-Zhuozhui Debris Flow Gullies* section.

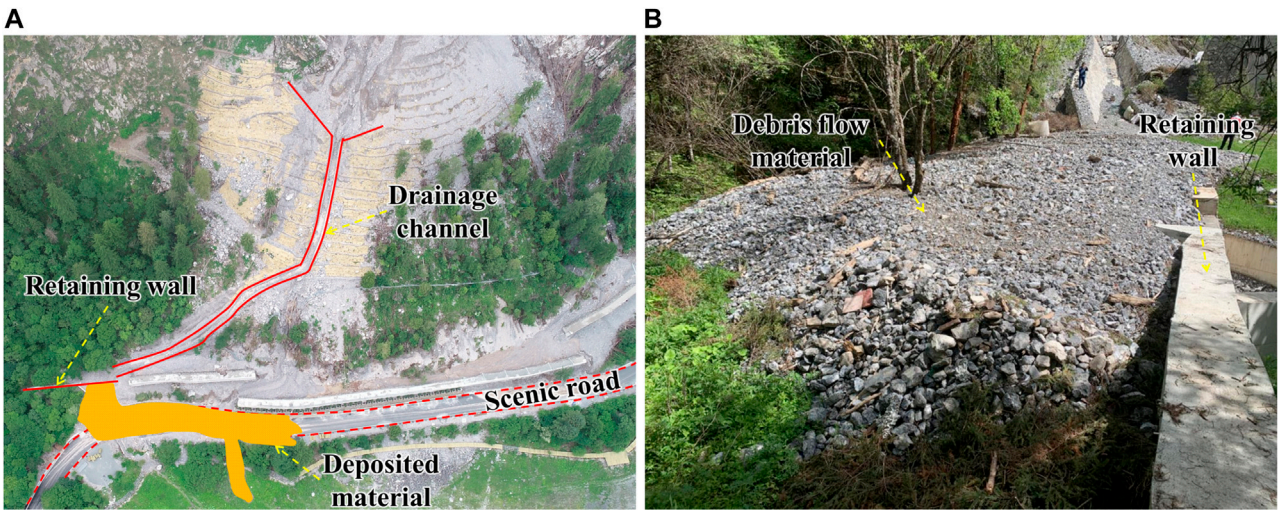


**FIGURE 7 |** Mitigation measures in Xuan Gully. **(A)** Overview of the mitigation structures. **(B)** The debris flow material transported on June 21, 2019.

## Blocking to Control Debris Flow Disasters in Pingshitou Gully

The mouth of Pingshitou Gully is about 2.6 km away from the entrance of the scenic area. The basin area of the debris flow gully is 0.10 $km^2$, and the length of the main gully is 0.90 km. The lowest point of the gully is located near the scenic road at an altitude of 2,100 m asl, and the highest point is located at an altitude of 2,970 m asl. The relative elevation difference of the terrain is 870 m, and the average longitudinal gradient of the gully bed is 775‰. To mitigate debris flow disasters, the debris flow gully was treated using the blocking control mode in 1984; five check dams were constructed in the transport zone to retain debris flow material. After the 2017 Jiuzhaigou earthquake, the original check dams were strengthened to mitigate debris flow

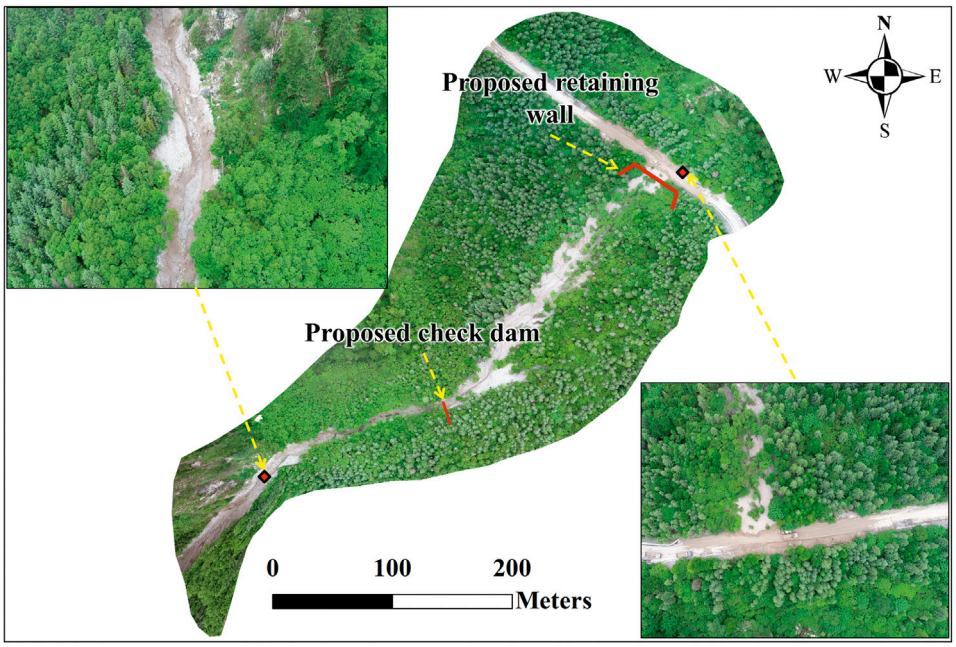


**FIGURE 8 |** UAV image of the debris flow disaster in West-Zhuozhui Gully on June 21, 2019. The check dam and retaining wall in the figure are the proposed engineering projects described in *Application of the Planning Method for the Xiajijie Lake, Zhuozhui, Pingshitou, Xuan, and West-Zhuozhui Debris Flow Gullies* section.

disasters. Moreover, the debris flow material behind the check dams was artificially cleared, and the total storage capacity of the check dams after dredging was $0.036 \times 10^4$ m$^3$. A debris flow disaster was triggered by heavy rainfall in Pingshitou Gully on July 22, 2019, and the debris flow material filled the check dams (**Figure 6**). Approximately $0.2 \times 10^4$ m$^3$ of debris flow material was transported to the scenic road of Pingshitou Gully, which resulted in road blockage.

### Drainage and Deposit Stopping to Control Debris Flow Disasters in Xuan Gully

Xuan Gully is located southwest of Xiajijie Lake. The only scenic highway from Nuorilang Waterfall to Long Lake passes through the accumulation fan at the gully mouth (**Figure 7A**). The drainage area of the debris flow gully is approximately 0.56 km$^2$, and the length of the main gully is 1.05 km. The highest point of the gully is located in the northwest corner (elevation of 3,805 m asl), and the lowest point is located near the scenic road (elevation of 2,625 m asl). The relative elevation difference of the terrain is 1,180 m, and the average longitudinal slope is 795‰. To mitigate debris flow disasters, drainage measures were implemented in 1984. A drainage channel was constructed in the transport zone of the debris flow gully to discharge debris flow material to the right side of the mouth of the debris flow gully, to manage debris flow disasters in Xuan Gully after the 2017 Jiuzhaigou earthquake, the original drainage channel was repaired and a retention basin with a storage capacity of $0.17 \times 10^4$ m$^3$ was built in the concave area to the right of the gully mouth. On June 21, 2019, a debris flow disaster occurred in Xuan Gully, and debris flow material entered the retention basin through the drainage channel. After the retention basin was full, about $0.11 \times 10^4$ m$^3$ of debris flow material reached the scenic road, blocking it and causing a traffic jam (**Figures 7A,B**). The debris flow material buried a 108 m section of the road; the width of the deposit was 9–12 m and the average thickness of the deposit was 1 m.

### Debris Flow Disaster in West-Zhuozhui Gully Without Engineering Measures

West-Zhuozhui Gully is located on the left side of the road from Long Lake to Nuorilang Waterfall. The straight-line distance from this location to the mouth of Zhuozhui Gully is 600 m. The basin area of the debris flow gully is 1.33 km$^2$, and the length of the main gully is 1.77 km. The lowest point of the gully is located near the scenic road at an altitude of 2,831 m asl, and the highest point is located at an altitude of 3,993 m asl. The relative elevation difference of the terrain is 1,162 m, and the average longitudinal gradient of the gully bed is 517‰. Prior to the 2017 Jiuzhaigou earthquake, no debris flow disaster was recorded in West-Zhuozhui Gully. On June 21, 2019, heavy rainfall triggered severe channel erosion in West-Zhuozhui Gully (**Figure 8**), and approximately $0.903 \times 10^4$ m$^3$ of loose material was transported to the accumulation fan at the gully mouth and the highway in the scenic area. The debris flow material was deposited on a 120 m section of the scenic highway; the width of the deposit was 12–16 m, the thickness of the deposit was 1.5–2.5 m, and the volume of the material deposited was $0.336 \times 10^4$ m$^3$ (**Figure 8**).

## Mitigation Effectiveness of Debris Flow Control Projects Completed in May 2019

As a consequence of the 2017 Jiuzhaigou earthquake, the scale of debris flows in Xiajijie Lake Gully, Zhuozhui Gully, Pingshitou

**TABLE 1 |** Mitigation effectiveness of the debris flow control projects completed in May 2019.

| Debris flow gullies | Design standards | Control measures | Engineering structures | Designed capacity ($m^3$) | Amount of transported debris flow material in 2019 ($m^3$) | Whether the following were endangered in 2019? | | |
|---|---|---|---|---|---|---|---|---|
| | | | | | | Tourists | Scenic road, walkways | Landscapes |
| Xiajijie Lake Gully | 50-year return period (50-year return period) | Blocking and deposit stopping measures (Drainage and deposit stopping measures) | Check dams, drainage channel, retaining walls (Drainage channel, retaining wall) | $3.0 \times 10^4$ ($3.01 \times 10^4$) | $3.3 \times 10^4$ | No | Yes | No |
| Zhuozhui Gully | 20-year return period (50-year return period) | Deposit stopping measure (Deposit stopping measure) | Retaining wall (Retaining wall) | $1.2 \times 10^4$ ($2.1 \times 10^4$) | $2.5 \times 10^4$ | No | Yes | — |
| Pingshitou Gully | 20-year return period (50-year return period) | Blocking measure (Drainage and deposit stopping measures) | Check dams (Drainage channel, retaining wall) | $0.036 \times 10^4$ ($0.32 \times 10^4$) | $0.236 \times 10^4$ | No | Yes | — |
| Xuan Gully | 20-year return period (50-year return period) | Drainage and deposit stopping measures (Drainage and deposit stopping measures) | Drainage channel, retaining wall (Drainage channel, retaining wall) | $0.17 \times 10^4$ ($0.72 \times 10^4$) | $0.28 \times 10^4$ | No | Yes | No |
| West-Zhuozhui Gully | (50-year return period) | None (Blocking and deposit stopping measures) | None (Check dam, retaining wall) | ($1.046 \times 10^4$) | $0.903 \times 10^4$ | No | Yes | — |

*Note: The data and content in parentheses show the results obtained using the engineering planning method for debris flow disasters in scenic areas proposed in Engineering Planning Method* for Debris Flow Disasters in Scenic Areas *and* Application of the Planning Method for the Xiajijie Lake, Zhuozhui, Pingshitou, Xuan, and West-Zhuozhui Debris Flow Gullies *sections*.

Gully, and Xuan Gully increased significantly. The gully in West-Zhuozhui changed from a non-debris flow gully before the earthquake to a debris flow gully. Debris flow disasters exhibit a tendency to occur in clusters. Previous studies have shown that debris flow disasters will continue to occur for at least 5–10 years after the earthquake (Chen X.-q. et al., 2018). Therefore, it is necessary to analyze the disaster characteristics of debris flows and implement appropriate and timely control engineering measures. After the 2017 Jiuzhaigou earthquake, the "blocking + deposit stopping," "deposit stopping," "blocking," and "drainage + deposit stopping" control modes were adopted to manage the debris flow disasters in Xiajijie Lake Gully, Zhuozhui Gully, Pingshitou Gully, and Xuan Gully, respectively. The construction of the new projects was completed in May 2019. However, during the debris flow events on June 21, 2019 and July 22, 2019, the new control projects did not effectively protect the vulnerable objects, and the control project schemes and parameter calculations were found to be inappropriate. The specific considerations were as follows: 1) The main gully mouth of Xiajijie Lake exhibits conditions that are not conducive to deposit stopping; thus, it is not appropriate to construct a retaining wall at the main gully mouth. The retention conditions of the transport zone in Pingshitou Gully are poor; thus, blocking is not an appropriate control mode to manage debris flow disasters. 2) The total designed storage capacity of the debris flow control engineering project in Zhuozhui Gully, Pingshitou Gully, and Xuan Gully is far lower than the amount of transported debris flow material. Therefore, to effectively overcome these challenges, this study combined field investigation and data collection, and proposed a method of debris flow control engineering planning in scenic areas taking into account the characteristics of different debris flow gullies and the engineering feasibility. The application of this method is illustrated in *Engineering Planning Method for Debris Flow Disasters in Scenic Areas* section, using the example of Jiuzhaigou Valley, and the mitigation effectiveness of debris flow control projects completed in May 2019 is analyzed in **Table 1**.

## ENGINEERING PLANNING METHOD FOR DEBRIS FLOW DISASTERS IN SCENIC AREAS

In China, owing to restrictions related to the functional zoning of nature reserves, debris flow control projects can only be constructed in experimental zones. The formation zones of debris flow gullies in scenic areas are usually located in the core and buffer zones of these areas. Typically, only the transport and deposition zones of debris flow gullies overlap with the experimental zones of scenic areas, which make it impossible to implement stabilization measures in the formation zones of debris flow gullies. Therefore, all types of control projects can only be implemented in the transport zones and deposition zones of debris flow gullies to realize the management of debris flow disasters in scenic areas. Based on field investigations and data collected from debris flow control

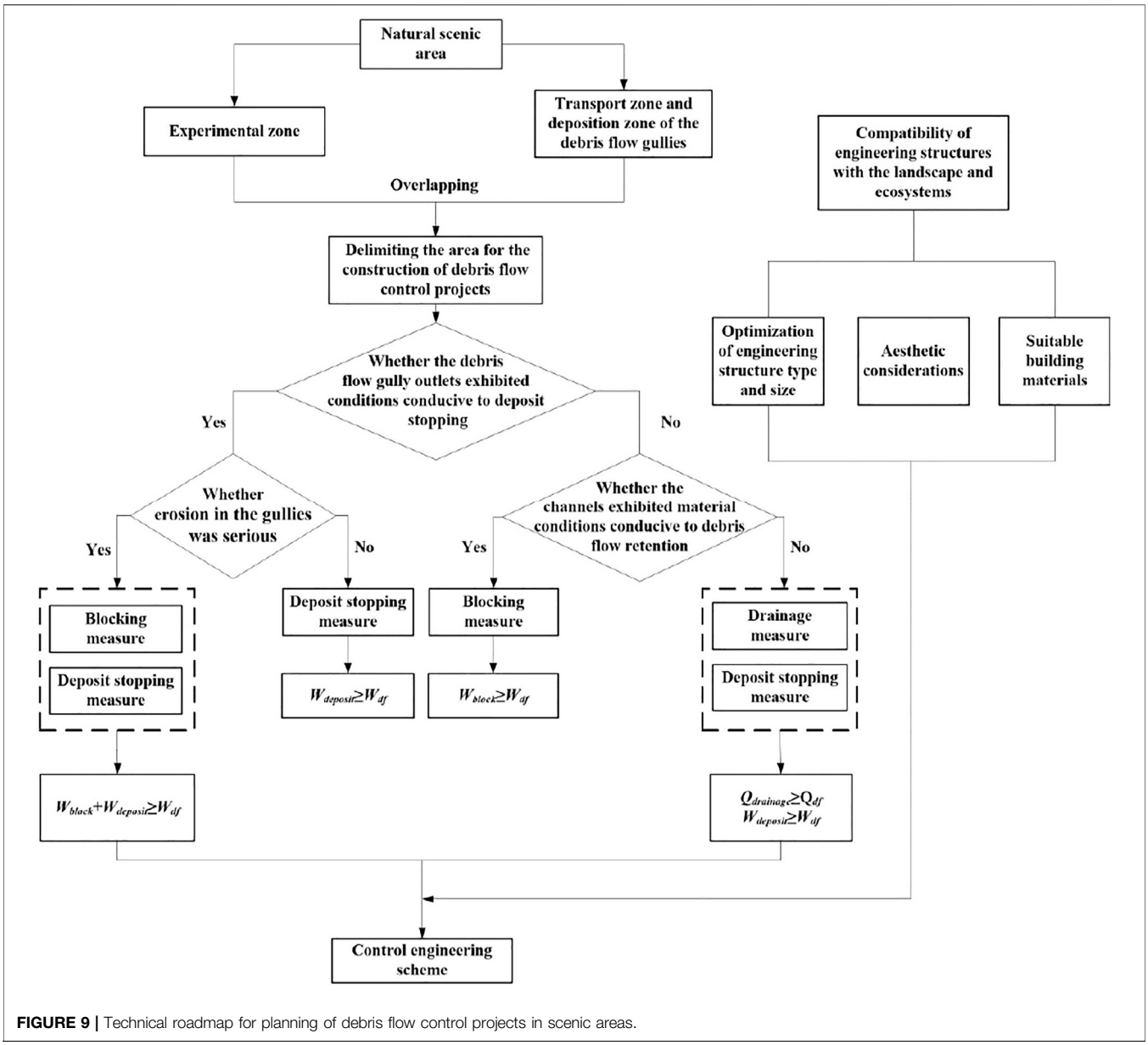


**FIGURE 9 |** Technical roadmap for planning of debris flow control projects in scenic areas.

projects in scenic areas, an engineering planning method for debris flow control projects in scenic areas is proposed. The specific steps are described in **Figure 9**:

## Delimiting the Area for the Construction of Debris Flow Control Projects

Based on data related to protected objects in scenic areas, the natural environment and natural resources, social economy, and land and water utilization, the National Standard of the People's Republic of China (Cui et al., 2018) spatially divides scenic areas into core, buffer, and experimental zones (**Figure 10**). Based on field investigations and topographic surveys, debris flow gullies are divided into formation zones, transport zones, and deposition zones. Debris flow control projects can only be constructed in areas in which the experimental zones of the natural scenic areas overlap with the transport and deposition zones of debris flow gullies.

## Obtaining Topographic Conditions and Constructing Debris Flow Control Projects

Using field investigations and topographic surveys, this study determined whether the debris flow gully mouths exhibited conditions conducive to deposit stopping, whether the channels in the transport zones exhibited material conditions conducive to debris flow retention, and whether erosion in the gullies was serious. Our study can provide the basis for the formulation of control engineering schemes.

For debris flow gullies in which conditions at the gully mouths are conducive to deposit stopping, the following

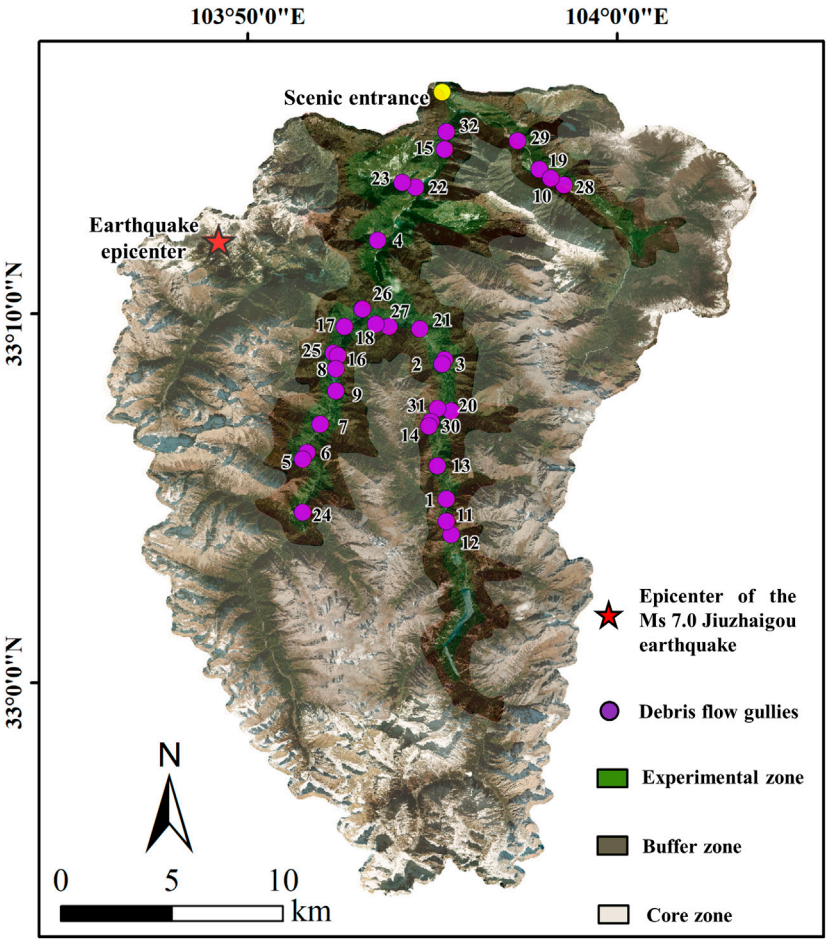


**FIGURE 10 |** Functional zoning map of Jiuzhaigou Valley.

considerations should be applied. When gully erosion is severe, blocking projects should be constructed in the transport zone and deposit stopping projects should be constructed in the deposition zone of the debris flow gully within the construction area of debris flow control projects. The blocking projects and deposit stopping projects should jointly meet the following requirement: the amount of debris flow material retained by the blocking projects ($W_{block}$) + the amount of debris flow material retained by the deposit stopping projects ($W_{deposit}$) > the total volume of debris flow material under design standards ($W_{df}$). When gully erosion is not severe, it is only necessary to construct deposit stopping projects in the deposition zone within the construction area of debris flow control projects. The deposit stopping projects should meet the following requirement: the amount of debris flow material retained by the deposit stopping projects ($W_{deposit}$) > the total volume of debris flow material projected to rush out under design standards ($W_{df}$).

For debris flow gullies in which conditions at the gully mouths are not conducive to deposit stopping, the following considerations should be taken into account. When the channel in the transport zone exhibits material conditions conducive to debris flow retention, it is only necessary to construct blocking projects in the transport zone in the construction area of debris flow control projects. The blocking projects should meet the following requirement: the amount of debris flow material retained by the blocking project ($W_{block}$) > the total volume of debris flow material projected to rush out under design standards ($W_{df}$). When the channel in the transport zone does not exhibit material conditions conducive to debris flow retention, drainage projects should be constructed in the transport zone in the construction area of debris flow control projects to discharge debris flow material into the recesses on both the sides of the gully; these should be accompanied by deposit stopping projects. The drainage projects should meet the following requirement: the peak discharge of the debris flow material discharged by the drainage projects ($Q_{drainage}$) > the peak discharge of debris flow material projected to rush out under design standards ($Q_{df}$). The amount of debris flow material retained by the deposit stopping projects ($W_{deposit}$) > the total volume of debris flow material projected to rush out under design standards ($W_{df}$). The method of calculation of all the aforementioned parameters is described in *Parameter Calculation section*.

## Parameter Calculation

### Debris Flow Peak Discharge Under Different Return Periods ($Q_{df}$)

The design standard of a control project determines the ability of the project to withstand debris flow disasters. Based on the risk level of the vulnerable objects or the disaster situation of the affected objects, the design standards of debris flow control projects in mountainous areas in China can be divided into 100, 50, and 20-year return periods (Chen et al., 2015; Liu et al., 2015; Gong et al., 2020). Considering the importance of scenic areas, a 50-year return period should be adopted as the design standard for debris flows. The rain-flood method is a widely used method to calculate the peak discharge of debris flows. The peak discharge $Q_{df}$ of debris flows under different design standards can be obtained through the following steps (Zhou et al., 1991; Liu et al., 2014; Gong et al., 2020).

Step one: based on topographic data, the basin area, $A$ ($km^2$), length of the main gully, $L$ (km), and average longitudinal gradient of the gully bed, $J$, are obtained. Then, the basin characteristic parameter of the gully, $\theta$, is calculated using **Eq. 1** and the confluence parameter, $m$, is calculated using **Eq. 2**.

$$\theta = \frac{L}{J^{1/3}A^{1/4}} \tag{1}$$

$$m = 0.221\theta^{0.204} \tag{2}$$

Step two: the characteristic rainstorm values [1/6 h average rainfall, $H_{1/6}$ (mm), 1 h average rainfall, $H_1$ (mm), and 6 h average rainfall, $H_6$ (mm)] of debris flow gullies are obtained from the rainstorm and flood calculation manual of medium-small basins in Sichuan Province. The modulus coefficients, $K_{1/6}$, $K_1$, and $K_6$, corresponding to $H_{1/6}$, $H_1$, and $H_6$, are obtained from the Pearson III frequency table. **Eq. 3** is used to calculate the rainstorm intensity, $S$ (mm), under the design standard, and **Eq. 4** is used to calculate the rainstorm attenuation index, $n$.

$$S = H_1K_1 \tag{3}$$

$$n = \begin{cases} 1 + 1.285\left(1g\dfrac{H_{1/6}K_{1/6}}{H_1K_1}\right), 1/6h < t < 1h \\ 1 + 1.285\left(1g\dfrac{H_1K_1}{H_6K_6}\right), 1h < t < 6h \end{cases}, \tag{4}$$

Step three: the confluence time, $t$ (h), and flood peak runoff coefficient, $\varphi$, are calculated using **Eqs 5–8**.

$$t = t_0\varphi^{-\frac{1}{4-n}} \tag{5}$$

$$\varphi = 1 - 1.1\frac{\mu}{S}t_0^n \tag{6}$$

$$t_0 = \left[\frac{0.383}{mS^{1/4}/\theta}\right]^{\frac{4}{4-n}} \tag{7}$$

$$\mu = K_P\eta A^{-0.19} \tag{8}$$

where $t_0$ is the basin confluence time when $\varphi = 1$, $\mu$ is the basin runoff yield parameter (mm/h), and $\eta$ is the comprehensive coefficient of runoff yield parameters. Based on the area in which the debris flow gully is located, the values of $\eta$ are 6 (Qingyi River-Lutou Mountain rainstorm area), 4.8 (basin hilly area), and 3.6 (basin margin mountainous area and southwest mountainous area), respectively. $K_p$ is the modulus ratio coefficient when the variation coefficient is 0.23, which is obtained from the Pearson III frequency table.

Step four: the peak discharge of the watershed $Q_f$ ($m^3/s$) is calculated using **Eq. 9**. Then, the peak discharge of the debris flow $Q_{df}$ ($m^3/s$) under the design standard is calculated according to **Eq. 10**.

$$Q_f = 0.278\varphi\frac{S}{t^n}A \tag{9}$$

$$Q_{df} = D_{df}\left(1 + \psi_{df}\right)Q_f \tag{10}$$

$$\psi_{df} = \left(\gamma_{df} - \gamma_w\right)/\left(\gamma_s - \gamma_{df}\right) \tag{11}$$

where $D_{df}$ is the blockage coefficient. The value of $D_{df}$ varies with the degree of blockage, namely, very serious blockage ($D_{df}$ = 3.0–2.6), serious blockage ($D_{df}$ = 2.5–2.0), normal blockage ($D_{df}$ = 1.9–1.5), and minor blockage ($D_{df}$ = 1.4–1.1). $\psi_{df}$ is the amplification coefficient of the debris flow peak discharge. $\gamma_{df}$ is the density of the debris flow ($t/m^3$), which is obtained *via* field investigations (Ministry of Land and Resources of the People's Republic of China, 2006). $\gamma_w$ is the density of water ($t/m^3$), usually taken as 1.00 $t/m^3$. $\gamma_s$ is the density of the solid material ($t/m^3$), usually taken as 2.65 $t/m^3$.

### Debris Flow Peak Discharge by Drainage Channel ($Q_{drainage}$)

Based on the morphology of the cross-section of the drainage channel, the debris flow peak discharge by the drainage channel, $Q_{drainage}$ ($m^3/s$), can be obtained using **Eq. 12**:

$$Q_{drainage} = A_{drainage}V_{df} \tag{12}$$

where $A_{drainage}$ is the area of the cross-section of the drainage channel ($m^2$), and $V_{df}$ is the average velocity of the debris flow (m/s), which can be calculated using Manning's formula (Liu et al., 2015; Gong et al., 2020):

$$V_{df} = \frac{1}{n_{drainage}}R_{df}^{2/3}I_{drainage}^{1/2} \tag{13}$$

where $n_{drainage}$ is the roughness coefficient of the drainage channel, which depends on the material properties of the drainage channel, and can be obtained from (China Association of Geological Hazard Prevention 2018). $R_{df}$ is the hydraulic radius of the debris flow (m). $I_{drainage}$ is the longitudinal slope gradient of the drainage channel bed (m/m).

### Total Volume of Debris Flow Material ($W_{df}$)

The total volume of debris flow material under the design standard, $W_{df}$, is calculated using **Equation (14)** (Zhou et al., 1991; Gong et al., 2020):

$$W_{df} = 0.264Q_{df}T_{df} \tag{14}$$

where $Q_{df}$ is the peak discharge of the debris flow under the design standard, which can be calculated using **Eq. 10**. $T_{df}$ is the duration

of the debris flow event, which can be determined by interviewing witnesses and monitoring.

### Volume of Debris Flow Material Trapped by Blocking Projects ($W_{block}$)

Since check dams are generally used in blocking projects, $W_{block}$ can be estimated using the following commonly used equation (Jiang 2018).

$$W_{block} = \frac{H_b^2}{I}\left(\frac{H_b}{2\tan\alpha} + b\right) \tag{15}$$

where $H_b$ is the effective height of the check dam (m), $I$ is the longitudinal slope of the gully at the project site, $\alpha$ is the gradient of the bank slopes of check dams (degrees), and $b$ is the average bottom width of the gully bed in the silting section of the check dam (m). $I$, $\alpha$, and $b$ are determined based on topographic data of the debris flow gully and field investigations.

### Volume of Debris Flow Material Trapped by Deposit Stopping Projects ($W_{deposit}$)

Because deposit stopping projects generally adopt retaining walls, and the retaining walls are constructed in the deposition zone with gently sloping terrain, $W_{deposit}$ can be estimated by the following commonly used equation (Jiang 2018).

$$W_{deposit} = \frac{H_d^2}{I}B_d \tag{16}$$

where $H_d$ and $B_d$ are the effective height (m) and length (m) of the retaining wall, respectively.

## Compatibility of Engineering Structures with the Landscape and Ecosystems

In general, debris flow control projects should be coordinated with the local landscape and ecosystem, especially in scenic areas (Cui et al., 2003; Wu and Feng 2006). To achieve this goal, the following aspects were considered in this study: 1) Optimization of the type and size of the engineering structure: Engineering structure with optimized type should be built to improve the disaster reduction effect of debris flow. Such as, slit dam and filtering dam should be built to effectively block wood debris and reduce water pollution respectively in scenic areas (Cui et al., 2007). Engineering structure with optimized size should be built to maximize the economic benefit and reduce the damage to the ecological environment due to construction. 2) Aesthetic considerations for the engineering structure: As far as possible, the engineering structure should be built out of sight of visitors to reduce the influence of the engineering structure on the aesthetic value of the scenic spot. Where this is not possible, local trees, shrubs, and grass should be transplanted to conceal the structure, and the structure should be spray painted using a color that blends well with that of the surrounding environment. 3) Suitable building materials: Local materials should be used to construct the engineering structures to avoid the influence of foreign materials on ecological resources, such as the pollution of local water bodies.

# RESULTS AND DISCUSSION

## Application of the Planning Method for the Xiajijie Lake, Zhuozhui, Pingshitou, Xuan, and West-Zhuozhui Debris Flow Gullies

Based on the basic information of Jiuzhaigou Valley, the experimental zone is determined using the method described in *Delimiting the Area for the Construction of Debris Flow Control Projects* section (**Figure 10**). According to the gully and distribution characteristics of loose material, the Xiajijie Lake, Zhuozhui, Pingshitou, Xuan, and West-Zhuozhui debris flow gullies can be divided into formation, transport, and deposition zones. The corresponding elevation coordinates are shown in **Table 2**. Debris flow control projects can be constructed in the area of overlap between the experimental zone of the scenic area and the transport and deposition zones of a debris flow gully. The elevations of the construction areas of the Xiajijie Lake, Zhuozhui, Pingshitou, Xuan, and West-Zhuozhui debris flow control projects are 2800–2620, 3025–2882, 2230–2100, 2830–2625, and 3040–2831 m asl, respectively (**Table 2**).

Based on field investigations and measured topographical data, the following debris flow control measures are adopted for Xiajijie Lake Gully, Zhuozhui Gully, Pingshitou Gully, Xuan Gully, and West-Zhuozhui Gully based on the considerations

**TABLE 2 |** Topographic conditions of debris flow gullies.

| Parameters | Xiajijie Lake Gully | Zhuozhui Gully | Pingshitou Gully | Xuan Gully | West-Zhuozhui Gully |
|---|---|---|---|---|---|
| Basin area ($km^2$) | 1.87 | 4.14 | 0.1 | 0.56 | 1.33 |
| Main gully length (km) | 2.36 | 3.3 | 0.9 | 1.05 | 1.77 |
| Average gully gradient (‰) | 593 | 386 | 775 | 795 | 517 |
| Highest elevation (m) | 4,120 | 4,492 | 2,970 | 3,805 | 3,993 |
| Lowest elevation (m) | 2,620 | 2,882 | 2,100 | 2,625 | 2,831 |
| Formation zone (m) | 4,120–2,960 | 4,492–3,925 | 2,970–2,600 | 3,805–2,850 | 3,993–3,317 |
| Transport zone (m) | 2,960–2,660 | 3,925–3,015 | 2,600–2,115 | 2,850–2,650 | 3,317–2,894 |
| Deposition zone (m) | 2,660–2,620 | 3,015–2,882 | 2,115–2,100 | 2,650–2,625 | 2,894–2,831 |
| Experimental zone (m) | <2,800 | <3,025 | <2,230 | <2,830 | <3,040 |
| Construction area of debris flow control projects (m) | 2,800–2,620 | 3,025–2,882 | 2,230–2,100 | 2,830–2,625 | 3,040–2,831 |
| Whether the debris flow gully mouths exhibited conditions conducive to deposit stopping | No | Yes | No | No | Yes |

described in *Obtaining Topographic Conditions and Constructing Debris Flow Control Projects* section. 1). After the September 25, 2017 and June 21, 2019 debris flows, large amounts of loose material were transported to the main gully mouth of Xiajijie Lake Gully. The main gully mouth does not exhibit conditions conducive to deposit stopping, and the transport zone of the gully within the construction area does not exhibit conditions conducive to blocking. Therefore, only the "drainage + deposit stopping" control mode can be adopted to treat the debris flow gully. 2) There is a large accumulation fan at the mouth of Zhuozhui Gully, which has the area required for a deposit stopping project. Gully erosion in the construction area of the debris flow control project is not serious, and the "deposit stopping" control mode can be implemented to manage debris flow disasters in Zhuozhui Gully. 3) The accumulation fan in Pingshitou Gully is small, and a scenic road has been constructed on the accumulation fan, which does not exhibit conditions conducive to deposit stopping. In the construction area of the debris flow control project, the channel in the transport zone is narrow and steep, and the storage capacity of check dams is limited. The dam was completely filled during the July 22, 2017 debris flow. There is a concave area to the right of the main gully mouth of Pingshitou Gully that exhibits conditions conducive to the construction of a retaining wall. Thus, the "drainage + deposit stopping" control mode can be adopted. The drainage channel should be constructed in the transport zone in the construction area of the debris flow control project to divert the debris flow material to the concave area, and the debris flow material should be intercepted using a retaining wall. 4) The accumulation fan at the mouth of Xuan Gully is small, and the scenic road threatened by debris flows passes the top of the accumulation fan; thus, there is not enough space for a deposit stopping project. Moreover, the transport zone of the gully does not exhibit conditions conducive to the construction of engineering structures such as check dams to intercept and hold debris flow material. Therefore, drainage projects can be constructed in the transport zone of the debris flow gully to drain the debris flow material to the concave gully mouth, and a deposit stopping project can be constructed to intercept the material. 5) The accumulation fan at the mouth of the debris flow gully in the West-Zhuozhui area is large and exhibits conditions suitable for deposit stopping. Furthermore, severe erosion occurs in the transport zone of the gully, so the "blocking + deposit stopping measures" control mode should be adopted to mitigate debris flow disasters.

Based on **Eqs 1–11** in *Parameter Calculation section*, the $W_{df}$ values in Xiajijie Lake Gully, Zhuozhui Gully, Pingshitou Gully, Xuan Gully, and West-Zhuozhui Gully were calculated as $2.78 \times 10^4$, $2.06 \times 10^4$, $0.228 \times 10^4$, $0.673 \times 10^4$, and $0.993 \times 10^4$ $m^3$, respectively (**Table 3**). Based on the control measures proposed above, the design parameters of debris flow control projects in Xiajijie Lake Gully, Zhuozhui Gully, Pingshitou Gully, Xuan Gully, and West-Zhuozhui Gully were calculated using **Eqs 12–16**. The specific parameters are as follows: 1) The construction of a drainage channel with a cross-sectional area of 6.0 $m^2$ is planned in the transport zone of Xiajijie Lake Gully (**Figure 4**). The designed peak discharge of debris flow in the drainage channel is 61.18 $m^3/s$, which exceeds the peak discharge of debris flow (58.55 $m^3/s$) under the design standard adopted. Thus, the drainage channel satisfies the $Q_{drainage} > Q_{df}$ criterion. The construction of a retaining wall with a length of 80 m and a height of 7 m is planned in the concave area to the left of Xiajijie Lake Gully (**Figure 4**). The designed storage capacity of the retaining wall is $3.01 \times 10^4$ $m^3$, which is greater than the total amount of debris flow material that is projected to rush out ($2.78 \times 10^4$ $m^3$) under the design standard adopted. Thus, it satisfies the $W_{deposit} > W_{df}$ criterion. 2) The height of the original retaining wall in Zhuozhui Gully is low. The construction of a retaining wall with a length of 70 m and a height of 6 m is planned (**Figure 5A**). The designed storage capacity of the retaining wall is $2.1 \times 10^4$ $m^3/s$, which is greater than the total amount of debris flow material projected to rush out ($2.06 \times 10^4$ $m^3$) under the design standard adopted. Thus, it satisfies the $W_{deposit} > W_{df}$ criterion. 3) The construction of a drainage channel with a cross-sectional area of 2.4 $m^2$ is planned in the transport zone of Pingshitou Gully (**Figure 6**). The designed peak discharge of debris flow in the drainage channel is 16.95 $m^3/s$, which exceeds the peak discharge of debris flow (3.61 $m^3/s$) under the design standard adopted. Thus, it satisfies the $Q_{drainage} > Q_{df}$ criterion. The construction of a retaining wall with a length of 30 m and a height of 4 m is planned in the concave area to the right of Pingshitou Gully (**Figure 6**). The designed storage capacity of the retaining wall is $0.32 \times 10^4$ $m^3$, which is greater than the total amount of debris flow material that is projected to rush out ($0.228 \times 10^4$ $m^3$) under the design standard adopted. Thus, it satisfies the $W_{deposit} > W_{df}$ criterion. 4) The construction of a drainage channel with a cross-sectional area of 3.0 $m^2$ is planned in Xuan Gully (**Figure 7**). The designed peak discharge of debris flow in the drainage channel is 32.01 $m^3/s$, which exceeds the peak drainage of debris flow (16.99 $m^3/s$) under the design standard adopted. Thus, it satisfies the $Q_{drainage} > Q_{df}$ criterion. The height of the existing retaining wall is low and the storage capacity is small. The construction of a retaining wall with a length of 40.0 m and a height of 3.0 m is planned. The designed storage capacity is $0.72 \times 10^4$ $m^3$, which exceeds the total amount of debris flow material that is projected to rush out ($0.673 \times 10^4$ $m^3$) under the design standard adopted. Thus, it satisfies the $W_{deposit} > W_{df}$ criterion. 5) The construction of a check dam with a height of 4 m and a length of 20 m is proposed in the transport zone of West-Zhuozhui Gully (**Figure 8**). The designed storage capacity of the check dam is $0.176 \times 10^4$ $m^3$. At the mouth of the main gully (2,850 m asl), the construction of a retaining wall with a length of 60 m and a height of 4.0 m is proposed (**Figure 8**). The storage capacity of the proposed retaining wall is $0.87 \times 10^4$ $m^3$, which satisfies the $W_{block} + W_{deposit} > W_{df}$ criterion.

As discussed in *Compatibility of Engineering Structures with the Landscape and Ecosystems* section, the proposed control engineering structure should be coordinated with the natural landscape and ecological environment. Thus, the following measures should be adopted: 1) In Xiajijie Lake Gully, the planned retaining wall is located at the mouth of the gully, where vegetation is sparse. Therefore, construction will cause minimal damage to the vegetation in the scenic spot. However, the retaining wall is only 5 m away from the scenic road, and spruce, alpine willow shrubs, and a fire grass meadow should be transplanted to conceal it. 2) The planned retaining wall in the

**TABLE 3 |** Parameter calculation results using the method in *Engineering Planning Method for Debris Flow Disasters in Scenic Areas* section.

| Calculation content | Parameters | Unit | Debris flow gullies | | | | |
|---|---|---|---|---|---|---|---|
| | | | Xiajijie Lake Gully | Zhuozhui Gully | Pingshitou Gully | Xuan Gully | West-Zhuozhui Gully |
| Flood peak discharge | $\theta$ | — | 2.40 | 3.18 | 1.74 | 1.31 | 2.05 |
| | $m$ | — | 0.26 | 0.28 | 0.25 | 0.23 | 0.26 |
| | $H_{1/6}$ | mm | 7.8 | 7.8 | 7.8 | 7.8 | 7.8 |
| | $H_1$ | mm | 15 | 15 | 15 | 15 | 15 |
| | $H_6$ | mm | 25 | 25 | 25 | 25 | 25 |
| | $K_{1/6}$ | — | 2.76 | 2.76 | 2.76 | 2.76 | 2.76 |
| | $K_1$ | — | 2.58 | 2.58 | 2.58 | 2.58 | 2.58 |
| | $K_6$ | — | 2.42 | 2.42 | 2.42 | 2.42 | 2.42 |
| | $K_P$ | — | 1.56 | 1.56 | 1.56 | 1.56 | 1.56 |
| | $n$ | — | 0.75 | 0.75 | 0.75 | 0.67 | 0.75 |
| | $\mu$ | mm/h | 4.99 | 4.29 | 8.70 | 6.27 | 5.32 |
| | $t_0$ | h | 1.51 | 1.98 | 1.10 | 0.84 | 1.29 |
| | $\varphi$ | — | 0.81 | 0.80 | 0.73 | 0.84 | 0.82 |
| | $t$ | h | 1.61 | 2.13 | 1.21 | 0.88 | 1.38 |
| | $Q_f$ | $m^3/s$ | 11.36 | 20.13 | 0.69 | 5.53 | 9.20 |
| Debris flow peak discharge | $\gamma_{df}$ | $t/m^3$ | 1.93 | 1.68 | 1.71 | 1.63 | 1.73 |
| | $D_{df}$ | — | 2.25 | 1.90 | 3.00 | 1.90 | 1.90 |
| | $Q_{df}$ | $m^3/s$ | 58.55 | 65.05 | 3.61 | 16.99 | 31.33 |
| | $T_{df}$ | s | 1800 | 1,200 | 2,400 | 1,500 | 1,200 |
| | $W_{df}$ | $m^3$ | $2.78 \times 10^4$ | $2.06 \times 10^4$ | $0.228 \times 10^4$ | $0.673 \times 10^4$ | $0.993 \times 10^4$ |
| Debris flow peak discharge by drainage channel ($Q_{drainage}$) | $A_{drainage}$ | $m^2$ | 6.0 | — | 2.4 | 3.0 | — |
| | $n_{drainage}$ | — | 0.04 | — | 0.04 | 0.04 | — |
| | $R_{df}$ | m | 0.81 | — | 0.52 | 0.60 | — |
| | $I_{drainage}$ | — | 0.22 | — | 0.19 | 0.36 | — |
| | $Q_{drainage}$ | $m^3/s$ | 61.18 | — | 16.95 | 32.01 | — |
| Volume of debris flow solid material trapped by blocking measures ($W_{block}$) | $H_b$ | m | — | — | — | — | 4 |
| | $I$ | — | — | — | — | — | 0.21 |
| | $\alpha$ | degrees | — | — | — | — | 33 |
| | $b$ | m | — | — | — | — | 20 |
| | $W_{block}$ | $m^3$ | — | — | — | — | $0.176 \times 10^4$ |
| Volume of debris flow solid material trapped by deposit stopping measures ($W_{deposit}$) | $H_d$ | mm | 7 | 6 | 4 | 3 | 4 |
| | $B_d$ | m | 80 | 70 | 30 | 40 | 60 |
| | $I$ | — | 0.13 | 0.12 | 0.15 | 0.05 | 0.11 |
| | $W_{deposit}$ | $m^3$ | $3.01 \times 10^4$ | $2.1 \times 10^4$ | $0.32 \times 10^4$ | $0.72 \times 10^4$ | $0.87 \times 10^4$ |

deposition zone of Zhuozhui Gully is approximately 100 m away from the scenic road, which is far beyond the visual range of tourists. Thus, there is no need for transplantation of vegetation to conceal the retaining wall, and the outside of the retaining wall can be painted so that it blends into the surrounding environment. 3) The proposed retaining walls at the mouths of Pingshitou Gully, Xuan Gully, and West-Zhuozhui Gully are low. Only *Salix alpina* shrubs need to be transplanted to conceal the retaining wall, and the outside of the retaining wall should be painted so that it blends into the surrounding environment.

## Control Modes of Debris Flow Disasters in Jiuzhaigou Valley

Based on the control engineering planning method proposed herein, the control modes for debris flow gullies in scenic areas can be divided into four categories (**Figure 11**). 1) For debris flow gullies that demonstrate severe erosion and conditions conducive to deposit stopping, blocking projects should be constructed in the transport zone. This control mode can realize the objective of retaining and stabilizing loose material and reduce the scale of debris flows and the damage they cause. Deposit stopping projects should then be constructed in the deposition zone within the construction area of debris flow control projects. This can stop debris flow material and reduce damage to vulnerable downstream structures (**Figure 11A**). 2) For debris flow gullies that do not demonstrate severe erosion and exhibit conditions conducive to deposit stopping, only deposit stopping projects should be constructed in the deposition zone within the construction area of debris flow control projects (**Figure 11B**). 3) In debris flow gullies that do not exhibit conditions conducive to deposit stopping but in which the channels in the transport zone exhibit material conditions conducive to debris flow retention, only blocking projects should be constructed in the transport zone within the construction area of debris flow control projects. This can realize the effective interception of debris flow material and reduce damage to

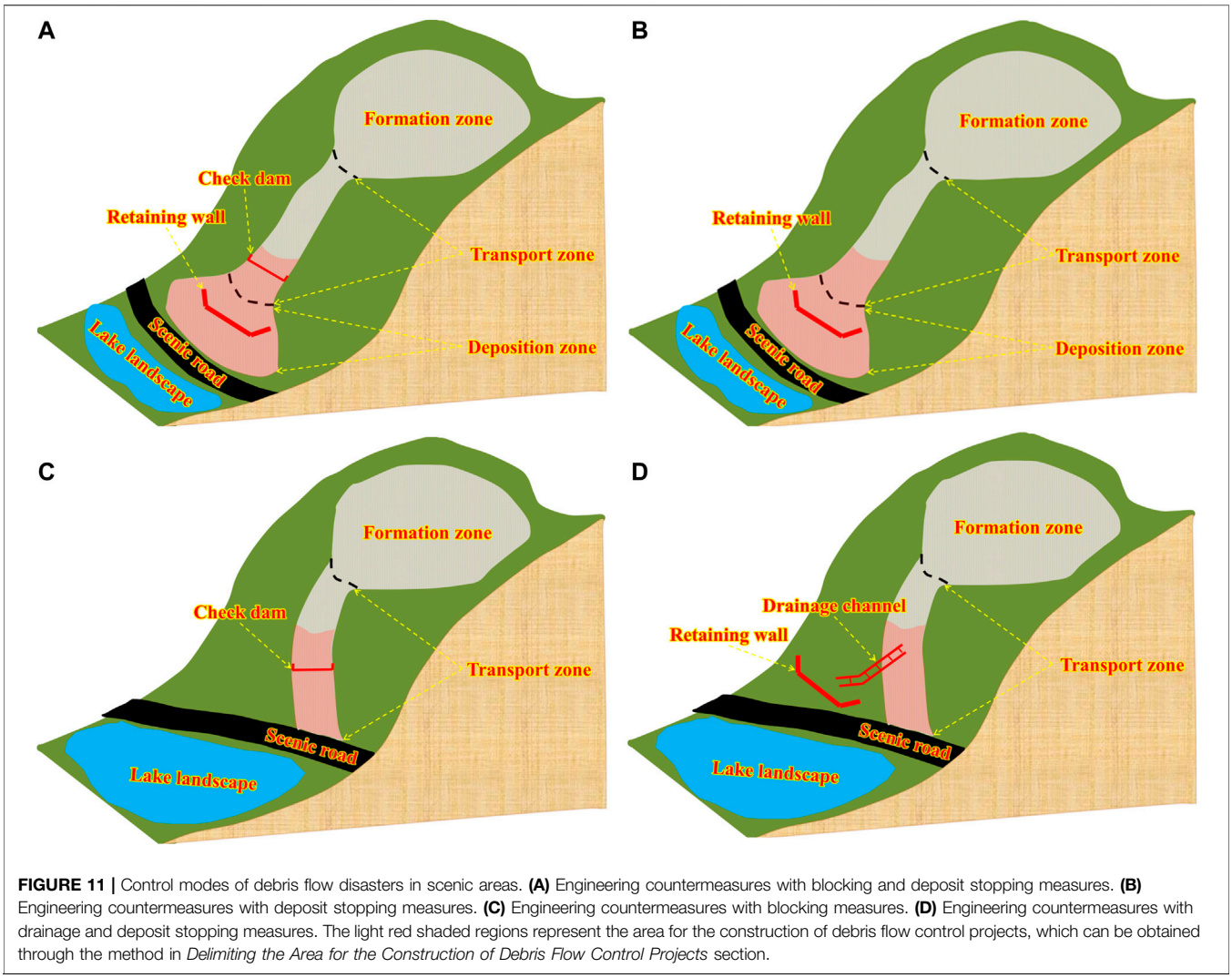


**FIGURE 11 |** Control modes of debris flow disasters in scenic areas. **(A)** Engineering countermeasures with blocking and deposit stopping measures. **(B)** Engineering countermeasures with deposit stopping measures. **(C)** Engineering countermeasures with blocking measures. **(D)** Engineering countermeasures with drainage and deposit stopping measures. The light red shaded regions represent the area for the construction of debris flow control projects, which can be obtained through the method in *Delimiting the Area for the Construction of Debris Flow Control Projects* section.

downstream objects and structures (**Figure 11C**). 4) For debris flow gullies that do not exhibit conditions conducive to deposit stopping and for which the channel in the transport zone does not exhibit material conditions conducive to debris flow retention, drainage projects should be constructed in the transport zone of the debris flow gully to divert the debris flow material into recesses on both sides of the gully, and deposit stopping projects should be constructed to retain the diverted material (**Figure 11D**).

Based on the foregoing analysis, the planning method proposed in this study is used to plan engineering countermeasures for debris flow gullies in scenic areas with severe hazards, and the control mode used in various debris flow gullies is discussed (**Table 4**). According to the analysis results, the post-earthquake control modes for the debris flow gullies in Xiajijie Lake, Zhuozhui, Pingshitou, Xuan, and West-Zhuozhui are "drainage + deposit stopping," "deposit stopping," "drainage + deposit stopping," "drainage + deposit stopping," and "blocking + deposit stopping," respectively. Field investigations indicate that the existing control modes for Xiajijie Lake Gully and Pingshitou Gully have not been effective, and the engineering structures have been partially damaged. Therefore, the results of this study can provide a reference for the improvement of subsequent management project schemes, so as to mitigate post-earthquake debris flow disasters in scenic areas under the condition of future climate change.

## Differences in the Management of Debris Flows in Scenic and Mountainous Urban Areas

The management of debris flow disasters has attracted widespread attention in mountainous urban areas. For example, by comparing approaches to debris flow control in several countries in the world (including France, Italy, Austria, Switzerland, Japan, and North America), an approach involving the construction of check dams to comprehensively manage debris flow disasters at the basin scale was proposed. These check dams perform the functions of bed stabilization, hillslope consolidation, slope gradient reduction, sediment retention, and sediment transport regulation (Piton et al., 2016). Several studies on the types, regulation

**TABLE 4 |** Debris flow control mode in Jiuzhaigou Valley.

| Number | Debris flow gullies | Topographic parameters | | | Recorded debris flow event date | Existed control engineering | Threat objects | Proposed control mode |
|---|---|---|---|---|---|---|---|---|
| | | Watershed area ($km^2$) | Main gully length (km) | Average longitudinal slope (‰) | | | | |
| 1 | Debris flow gully (10 km to Zechawa village) | 0.15 | 0.72 | 647 | 2013/5/5, 2013/5/17, 2013/6/24, 2013/7/3, 2017/6/20 | Retaining wall | Tourists and scenic road | Blocking and deposit stopping |
| 2 | Zechawa Gully | 1.96 | 2.57 | 611 | 2016/8/4, 2019/6/21 | Check dam, retaining wall | Tourists, scenic road, and walkways | |
| 3 | Zeduo Gully | 9.6 | 4.4 | 386 | 2004 | Check dam, bed sill, retaining wall | Tourists and scenic road | |
| 4 | Shuzheng Gully | 4.86 | 2.5 | 404 | 1931, 1971, 1981, 1985, 1986, 1988, 2013/8/7, 2014/5 | Check dams, retaining wall | Shuzheng village tourists, scenic road, and Shuzheng Lakes | |
| 5 | Rize No.2 Gully | 7.9 | 5.2 | 266 | 2017/7/27, 2018/7/10 | Check dams, retaining wall | Tourists and scenic road | |
| 6 | Meitan Gully | 5.2 | 4.3 | 330 | 2017/7/27 | Retaining wall | Tourists and scenic road | |
| 7 | Rize Gully | 3.73 | 3.75 | 376 | 2017/7/27 | Check dams, embankment, retaining wall | Tourists, Rize protection station, and scenic road | |
| 8 | Arrow Bamboo Lake Gully | 5.5 | 3.7 | 395 | 2008, 2017/7/27, 2017/9, 2018/6 | Check dam, retaining wall | Tourists, walkways, toilet, viewing platform, and Arrow Bamboo Lake | |
| 9 | Debris flow gully (Arrow Bamboo Lake sightseeing bus station) | 1.25 | 2.1 | 568 | 2016/8/4, 2017 | Embankment, retaining wall | Tourists, scenic road, and Arrow Bamboo Lake | |
| 10 | Debris flow gully (700 m to Guodu village) | 1.42 | 2.2 | 501 | 2018/6/25, 2018/7/10 | Check dams, retaining wall | Tourists and scenic road | |
| 11 | West-Zhuozhui Gully | 1.33 | 1.77 | 517 | 2019/6/21 | None | Tourists and scenic road | |
| 12 | Zhuozhui Gully | 4.14 | 3.3 | 386 | 2010, 2017/9, 2019/6/21, 2019/9/13 | Retaining wall | Tourists, scenic road, and walkways | Deposit stopping |
| 13 | Zhongjijie Lake Gully | 6.1 | 3.5 | 338 | 2015/6/29, 2016/8/1, 2017/9/13, 2017/10/4, 2019/6/21 | Retaining wall | Tourists and scenic road | |
| 14 | Debris flow Gully (on the right side of Xiajijie Lake) | 2.69 | 2.06 | 563 | 2009/10, 2019/6/21 | Bed sills, retaining wall | Tourists, scenic road, and Xiajijie Lake | |
| 15 | Debris flow gully (1.6 km to Heye village) | 0.58 | 1.46 | 752 | 2017/9/27, 2018/6/25, 2018/7/10 | Retaining wall | Tourists and walkways | |
| 16 | Panda Lake Gully | 0.37 | 1.1 | 800 | 2013/8/7, 2016/8/10 | Retaining wall | Tourists and Panda Lake | |
| 17 | Five-color Lake Gully | 2.6 | 3.5 | 434 | | Bed sill, retaining wall | Tourists, walkways, and Five-color Lake | |
| 18 | Debris flow Gully (Mirror Lake sightseeing bus station) | 0.23 | 0.542 | 671 | 2018 | Retaining wall | Tourists, scenic road, bus station, and Mirror Lake | |
| 19 | Guodu Gully | 1.7 | 2.3 | 554 | 2013/7/3, 2013/8/7, 2018/6/25, 2018/7/10 | Bed sill, retaining wall | Guodu village, tourists, and scenic road | |
| 20 | Keze Gully | 19.89 | 7.2 | 268 | 1992, 2011, 2018/6/25 | Check dams, embankment | Tourists, scenic road, and walkways | Blocking |
| 21 | Nuorilang Gully | 8.0 | 5.3 | 366 | 2013, 2017/6 | Check dams | Zechawa village, tourists, and restaurant | |

(Continued on following page)

**TABLE 4 |** (*Continued*) Debris flow control mode in Jiuzhaigou Valley.

| Number | Debris flow gullies | Topographic parameters | | | Recorded debris flow event date | Existed control engineering | Threat objects | Proposed control mode |
|---|---|---|---|---|---|---|---|---|
| | | Watershed area ($km^2$) | Main gully length (km) | Average longitudinal slope (‰) | | | | |
| 22 | Heye Gully | 25.5 | 8.0 | 186 | 1948, 2018/6/25, 2018/7/10 | Check dams | Heye village, tourists, scenic road, and Penjingtan attractions | |
| 23 | Debris flow gully (community group 1 of Heye village) | 3 | 3.3 | 262 | 1948, 2018/6/25, 2018/7/10 | Check dams, bed sill, embankment | Heye village | |
| 24 | Debris flow gully (opposite Swan Lake sightseeing bus station) | 0.3 | 1.5 | 597 | | Check dams | Tourists | |
| 25 | Debris flow gully (Central Panda Lake) | 3.9 | 2.9 | 501 | | Check dams | Tourists and Panda Lake | |
| 26 | Danzu Gully | 73.88 | 16.2 | 87 | 1984 | Check dams | Mirror Lake | |
| 27 | Mirror Gully | 2.55 | 2.9 | 441 | 2018 | Check dams | Tourists, scenic road, and walkways | |
| 28 | Nadi Gully | 4.68 | 3.8 | 544 | 2011/9/5, 2015/6/1, 2017/9/27 | Check dams, embankment | Burning incense attractions and scenic road | |
| 29 | Rexi Gully | 8.24 | 5.81 | 372 | 2018/6/25, 2018/7/10 | Check dams, bed sill, embankment | Rexi village and tourists | |
| 30 | Xuan Gully | 0.56 | 1.05 | 795 | 2013/7/3, 2013/7/28, 2013/8/3, 2013/8/7, 2015/6/28, 2019/6/21 | Drainage channel, retaining wall | Tourists, scenic road, and Xiajijie Lake | Drainage and deposit stopping |
| 31 | Xiajijie Lake Gully | 1.87 | 2.36 | 593 | 1976, 1983, 1984, 2012/7/21, 2013/7/3, 2013/7/28, 2017/9/9, 2017/9/14, 2017/9/24, 2017/9/25, 2019/6/21 | Check dams, drainage channel, retaining wall | Tourists, scenic road, walkways, and Xiajijie Lake | |
| 32 | Pingshitou Gully | 0.1 | 0.9 | 775 | 2011/9/5, 2012/8/13, 2019/7/22, 2020/5/6 | Check dams | Tourists and scenic road | |

*Note: The occurrence time of the recorded debris flow events is taken from the annual disaster survey report of Jiuzhaigou Valley and the investigation report for the control of debris flow disasters in Jiuzhaigou Valley. The locations of all debris flow gullies in the table have been marked in* ***Figure 10****.*

mechanisms, and disaster mitigation effects of check dams have been conducted (DeWolfe et al., 2008; Piton and Recking 2016; Cucchiaro et al., 2019a; Cucchiaro et al., 2019b; Bernard et al., 2019). In China, it is more common to implement management measures for debris flow gullies at the regional scale. The "stabilization + blocking + drainage + deposit stopping" control modes are adopted in the formation, transport, and deposition zones, respectively, with blocking measures being the most commonly implemented measures (Cui and Lin, 2013; Liu et al., 2017). This control approach is similar to that employed in Japan (Ikeya 1989; Takahashi 2007). However, after the Wenchuan earthquake, the frequency and scale of occurrence of debris flow disasters have increased significantly, and existing engineering projects have not been able to effectively mitigate these disasters. Moreover, a large number of engineering projects, particularly check dams, have been seriously damaged (Wang 2013; Chen et al., 2015). Therefore, many scholars have proposed a new approach for disaster mitigation. The proposed approach, which has proven to be effective, prioritizes the use of drainage measures, and makes full use of the transport capacity of the main river to discharge debris flow material to downstream rivers (Chen et al., 2015; Xiong et al., 2016).

The aforementioned studies have mainly focused on typical mountainous urban areas, and the proposed control methods cannot be applied to the mitigation of debris flows in the scenic area investigated herein. The reasons for this are as follows: 1) Owing to topographic conditions, no large river exists in the scenic area, and the water bodies (such as Long Lake and Nuorilang Waterfall in Jiuzhaigou Valley) distributed throughout the scenic area are important landscape resources that do not exhibit conditions conducive to the discharge of debris flow material. Thus, the control method proposed by Chen et al. (2015) is not applicable in this area. 2) Compared with the debris flow control projects in typical mountainous urban areas, debris flow control projects in scenic areas can only be implemented in the experimental zones owing to restrictions related to the functional zoning of nature reserves; it is impossible to implement large-scale engineering projects for debris flow control at the watershed scale. Therefore, the control method proposed by Piton et al. (2016) is

inappropriate for this area. The scale of debris flow disasters in scenic areas is smaller than that of disasters in typical mountainous urban areas owing to the lush vegetation and the smaller watershed area of debris flow gullies in scenic areas. Thus, the construction of small projects in the transport and deposition zones can meet the design requirements. Furthermore, these small projects are easy to integrate with the landscape and do not significantly damage the environment in scenic areas.

## Limitations of the Engineering Planning Method

This study proposed an engineering planning method for debris flow control in scenic areas, with the aim of providing guidance for relevant stakeholders to rapidly formulate control engineering plans for different debris flow gullies in scenic areas after debris flow disasters, especially mass debris flow disasters after earthquakes. However, the following limitations should be considered when this planning method is used for debris flow control engineering in scenic areas. 1) Owing to the difference of topographic conditions and threatened objects, the applicability of this planning method to debris flow control engineering planning in other scenic areas requires further verification. 2) This planning method adopts a large number of equations recommended by the code to calculate the design parameters of debris flow control engineering projects. These equations can be used to obtain the calculated values based on a small number of parameters, so they are widely used. However, the values of relevant parameters vary in different areas, so local norms should be consulted when this planning method is used to plan debris flow control projects in other scenic areas. 3) In this study, only engineering measures are considered for the control of debris flow in scenic areas. Ecological measures should also be considered for the treatment of debris flow in scenic areas. This aspect can be explored in future work.

# CONCLUSION

Based on field investigations of existing debris flow control projects in scenic areas, a planning method for debris flow control projects in scenic areas is proposed. The planning method first involves the determination of the scope of the area in which the control project can be implemented, based on the requirements related to the functional zoning of the scenic area. Then, based on the objects threatened by debris flows and the topographical features of debris flow gullies in the scenic area, the "blocking + deposit stopping," "deposit stopping," "blocking," and "drainage + deposit stopping" control modes are adopted. Finally, the amount of debris flow material that can be intercepted by the engineering structure is quantified based on parameter calculations. Based on the planning method for debris flow control engineering in the scenic area, the shortcomings of the existing control engineering projects in the scenic area are discussed. For the debris flow gullies in Xiajijie Lake, Zhuozhui, Xuan, Pingshitou, and West-Zhuozhui, the "drainage + deposit stopping," "deposit stopping," "drainage + deposit stopping," "drainage + deposit stopping," and "blocking + deposit stopping" control engineering schemes are proposed, respectively. The proposed control engineering schemes meet the requirements of coordination with the landscape and ecosystem.

On this basis, the control mode of debris flow disasters in scenic areas is discussed: 1) For debris flow gullies with severe erosion and conditions that are conducive to deposit stopping, blocking projects should be constructed in the transport zone and deposit stopping projects should be constructed in the deposition zone within the construction area of debris flow control projects. 2) For debris flow gullies without severe erosion but which exhibit conditions conducive to deposit stopping, only deposit stopping projects should be constructed in the deposition zone within the construction area of debris flow control projects. 3) For debris flow gullies that do not exhibit conditions conducive to deposit stopping but for which the channel in the transport zone exhibits material conditions conducive to debris flow retention, only blocking projects should be constructed in the transport zone within the construction area of debris flow control projects. 4) For debris flow gullies that do not exhibit conditions conducive to deposit stopping and for which the channel in the transport zone does not exhibit material conditions conducive to debris flow retention, drainage projects should be constructed in the transport zone to discharge the debris flow material into the recesses on both the sides of the gully, and deposit stopping projects should be constructed to retain the diverted material. The results of this study are expected to provide a systematic control strategy for debris flow disaster management in scenic areas.

# DATA AVAILABILITY STATEMENT

The original contributions presented in the study are included in the article/supplementary material, further inquiries can be directed to the corresponding author.

# AUTHOR CONTRIBUTIONS

X-LG and K-TC contributed to the conceptualization, methodology, analysis and manuscript writing of the study. X-QC proposed the main structure of this study and approved the final version. W-YZ and J-GC participate in field investigations and helped perform the analysis with constructive discussions.

# FUNDING

This research was supported by the National Natural Science Foundation of China (Grant No. 41925030), the Open Foundation of Key Laboratory of Mountain Hazards and Earth Surface Processes, CAS and the CAS "Light of West China" Program.

# ACKNOWLEDGMENTS

The authors wish to thank the Editor (Y-CT) and two reviewers for their constructive comments and engineer Jie Lang for providing some field photographs.

## REFERENCES


Bernard, M., Boreggio, M., Degetto, M., and Gregoretti, C. (2019). Model-based approach for design and performance evaluation of works controlling stony debris flows with an application to a case study at Rovina di Cancia (Venetian Dolomites, Northeast Italy). *Sci. Total Environ.* 688, 1373–1388. doi:10.1016/j.scitotenv.2019.05.468

Chen, J. G., Chen, X. Q., Zhao, W. Y., and You, Y. (2018). Debris Flow Drainage Channel with Energy Dissipation Structures: Experimental Study and Engineering Application. *J. Hydraulic Eng.* 144. doi:10.1061/(ASCE)HY.1943-7900.0001523

Chen, K.-T., Chen, X.-Q., Hu, G.-S., Kuo, Y.-S., Huang, Y.-R., and Shieh, C.-L. (2019a). Dimensionless Assessment Method of Landslide Dam Formation Caused by Tributary Debris Flow Events. *Geofluids* 2019, 1–14. doi:10.1155/2019/7083058

Chen, K.-T., Chen, X.-Q., Niu, Z.-P., and Guo, X.-J. (2019b). Early Identification of River Blocking Induced by Tributary Debris Flow Based on Dimensionless Volume index. *Landslides* 16, 2335–2352. doi:10.1007/s10346-019-01221-8

Chen, K.-T., Lin, C.-H., Chen, X.-Q., Hu, G.-S., Guo, X.-J., and Shieh, C.-L. (2018). An Assessment Method for Debris Flow Dam Formation in Taiwan. *Earth Sci. Res. J.* 22, 37–43. doi:10.15446/esrj.v22n1.62389

Chen, M.-l., Hu, G.-s., Chen, N.-s., Zhao, C.-y., Zhao, S.-j., and Han, D.-w. (2016). Valuation of Debris Flow Mitigation Measures in Tourist Towns: a Case Study on Hongchun Gully in Southwest China. *J. Mt. Sci.* 13, 1867–1879. doi:10.1007/s11629-015-3759-4

Chen, X.-q., Chen, J.-g., Cui, P., You, Y., Hu, K.-h., Yang, Z.-j., et al. (2018). Assessment of Prospective Hazards Resulting from the 2017 Earthquake at the World Heritage Site Jiuzhaigou Valley, Sichuan, China. *J. Mt. Sci.* 15, 779–792. doi:10.1007/s11629-017-4785-1

Chen, X., Cui, P., You, Y., Chen, J., and Li, D. (2015). Engineering Measures for Debris Flow hazard Mitigation in the Wenchuan Earthquake Area. *Eng. Geology* 194, 73–85. doi:10.1016/j.enggeo.2014.10.002

China Association of Geological Hazard Prevention (2018). *Specification of Design for Debris Flow Prevention*. T/CAGHP 021-2018. Wuhan: China University of Geosciences Press.

Cucchiaro, S., Cavalli, M., Vericat, D., Crema, S., Llena, M., Beinat, A., et al. (2019a). Geomorphic Effectiveness of Check Dams in a Debris-Flow Catchment Using Multi-Temporal Topographic Surveys. *CATENA* 174, 73–83. doi:10.1016/j.catena.2018.11.004

Cucchiaro, S., Cazorzi, F., Marchi, L., Crema, S., Beinat, A., and Cavalli, M. (2019b). Multi-temporal Analysis of the Role of Check Dams in a Debris-Flow Channel: Linking Structural and Functional Connectivity. *Geomorphology* 345, 1–13. doi:10.1016/j.geomorph.2019.106844

Cui, G. F., Li, Z., Wang, Q. C, et al. National Standard of the People's Republic of China (2018). *Technical Regulation for Nature Reserve Zoning*. Beijing: Standards Press of China. GB/T 35822-2018 (In Chinese).

Cui, P., Chen, X., Liu, S., and Tang, B. (2007). Techniques of Debris Flow Prevention in National parks. *Earth Sci. Front.* 14, 172–177. doi:10.1016/S1872-5791(08)60009-3

Cui, P., and Lin, Y. M. (2013). Debris-Flow Treatment: The Integration of Botanical and Geotechnical Methods. *J. Resour. Ecol.* 4, 97–104. doi:10.5814/j.issn.1674-764x.2013.02.001

Cui, P., Liu, S. Q., Tang, B. X., and Chen, X. Q. (2003). Debris Flow Prevention Pattern in National parks-Taking the World Natural Heritage Jiuzhaigou as an Example. *Sci. China Ser. E* 46, 1–11. doi:10.1360/03ez0004

Cui, P., Zhou, G. G. D., Zhu, X. H., and Zhang, J. Q. (2013). Scale Amplification of Natural Debris Flows Caused by Cascading Landslide Dam Failures. *Geomorphology* 182, 173–189. doi:10.1016/j.geomorph.2012.11.009

Dahlquist, M. P., and West, A. J. (2019). Initiation and Runout of Post-Seismic Debris Flows: Insights from the 2015 Gorkha Earthquake. *Geophys. Res. Lett.* 46, 9658–9668. doi:10.1029/2019GL083548

DeWolfe, V. G., Santi, P. M., Ey, J., and Gartner, J. E. (2008). Effective Mitigation of Debris Flows at Lemon Dam, La Plata County, Colorado. *Geomorphology* 96, 366–377. doi:10.1016/j.geomorph.2007.04.008

Domènech, G., Fan, X., Scaringi, G., van Asch, T. W. J., Xu, Q., Huang, R., et al. (2019). Modelling the Role of Material Depletion, Grain Coarsening and Revegetation in Debris Flow Occurrences after the 2008 Wenchuan Earthquake. *Eng. Geology* 250, 34–44. doi:10.1016/j.enggeo.2019.01.010

Faccini, Francesco, F., Piccazzo, Mauro, M., and Robbiano, Andrea, A. (2009). Valutazione della pericolosità geomorfologica da colate detritiche nel bacino idrografico di San Fruttuoso di Camogli (Parco di Portofino, Italia). *Ital. J. Geosciences* 128, 641–654. doi:10.3301/IJG.2009.128.3.641

Fan, R. L., Zhang, L. M., Wang, H. J., and Fan, X. M. (2018). Evolution of Debris Flow Activities in Gaojiagou Ravine during 2008-2016 after the Wenchuan Earthquake. *Eng. Geology* 235, 1–10. doi:10.1016/j.enggeo.2018.01.017

Fan, X., Scaringi, G., Xu, Q., Zhan, W., Dai, L., Li, Y., et al. (2018). Coseismic Landslides Triggered by the 8th August 2017 Ms 7.0 Jiuzhaigou Earthquake (Sichuan, China): Factors Controlling Their Spatial Distribution and Implications for the Seismogenic Blind Fault Identification. *Landslides* 15, 967–983. doi:10.1007/s10346-018-0960-x

Gong, X.-L., Chen, K.-T., Chen, X.-Q., You, Y., Chen, J.-G., Zhao, W.-Y., et al. (2020). Characteristics of a Debris Flow Disaster and its Mitigation Countermeasures in Zechawa Gully, Jiuzhaigou Valley, China. *Water* 12, 1256. doi:10.3390/w12051256

Hu, X., Hu, K., Tang, J., You, Y., and Wu, C. (2019). Assessment of Debris-Flow Potential Dangers in the Jiuzhaigou Valley Following the August 8, 2017, Jiuzhaigou Earthquake, Western China. *Eng. Geology* 256, 57–66. doi:10.1016/j.enggeo.2019.05.004

Huang, H., Shi, S. W., Yang, S., Tian, Y., Yang, D. X., and Liu, J. K. (2020). Study on the Damage of the August 82017 Jiuzhaigou Earthquake to Debris Flow Mitigation Engineering in the national park. *Chin. J. Rock Mech. Eng.* 39, 1773–1786. doi:10.13722/j.cnki.jrme.2020.0099

Hungr, O., Leroueil, S., and Picarelli, L. (2014). The Varnes Classification of Landslide Types, an Update. *Landslides* 11, 167–194. doi:10.1007/s10346-013-0436-y

Ikeya, H. (1989). Debris Flow and its Countermeasures in Japan. *Bull. Int. Assoc. Eng. Geology* 40, 15–33. doi:10.1007/bf02590339

Jiang, Z. X. (2018). *Practical Technology for Survey and Design of Mountain Geological Disaster Control Engineering after Earthquake*. Chengdu: Southwest Jiaotong University Press.

Junichi, K., and Naoki, I. (2020). Outline of Measures for Sediment Disaster by the Sabo Department of MLIT, Japan. *Landslides* 17, 2503–2513. doi:10.1007/s10346-020-01554-9

Liu, F. Z., Xu, Q., Dong, X. J., Yu, B., Frost, J. D., and Li, H. J. (2017). Design and Performance of a Novel Multi-Function Debris Flow Mitigation System in Wenjia Gully, Sichuan. *Landslides* 14, 2089–2104. doi:10.1007/s10346-017-0849-0

Liu, J., You, Y., Chen, X., and Chen, X. (2015). Mitigation Planning Based on the Prediction of River Blocking by a Typical Large-Scale Debris Flow in the Wenchuan Earthquake Area. *Landslides* 13, 1231–1242. doi:10.1007/s10346-015-0615-0

Liu, J., You, Y., Chen, X., Liu, J., and Chen, X. (2014). Characteristics and hazard Prediction of Large-Scale Debris Flow of Xiaojia Gully in Yingxiu Town, Sichuan Province, China. *Eng. Geology* 180, 55–67. doi:10.1016/j.enggeo.2014.03.017

Liu, S., Wei, L., and Hu, K. (2020). Topographical and Geological Variation of Effective Rainfall for Debris-Flow Occurrence from a Large-Scale Perspective. *Geomorphology* 358, 107134. doi:10.1016/j.geomorph.2020.107134

Ma, C., Wang, Y., Hu, K., Du, C., and Yang, W. (2017). Rainfall Intensity-Duration Threshold and Erosion Competence of Debris Flows in Four Areas Affected by the 2008 Wenchuan Earthquake. *Geomorphology* 282, 85–95. doi:10.1016/j.geomorph.2017.01.012

Ministry of Land and Resources of the People's Republic of China (2006). *Specification of Geological Investigation for Debris Flow stabilizationDZ/T0220-2006*. Beijing: Standards Press of China. (In Chinese).

Ni, H. Y., Zheng, W. M., Tie, Y. B., Su, P. C., Tang, Y. Q., Xu, R. G., et al. (2012). Formation and Characteristics of post-earthquake Debris Flow: a Case Study from Wenjia Gully in Mianzhu, Sichuan, SW China. *Nat. Hazards* 61, 317–335. doi:10.1007/s11069-011-9914-5

Piton, G., and Recking, A. (2016). Design of Sediment Traps with Open Check Dams. I: Hydraulic and Deposition Processes. *J. Hydraul. Eng.* 142. doi:10.1061/(ASCE)HY.1943-7900.0001048

Piton, G., Carladous, S., Recking, A., Tacnet, J. M., Liébault, F., Kuss, D., et al. (2016). Why Do We Build Check Dams in Alpine Streams? an Historical Perspective from the French Experience. *Earth Surf. Process. Landforms* 42, 91–108. doi:10.1002/esp.3967

Santi, P. M., deWolfe, V. G., Higgins, J. D., Cannon, S. H., and Gartner, J. E. (2008). Sources of Debris Flow Material in Burned Areas. *Geomorphology* 96, 310–321. doi:10.1016/j.geomorph.2007.02.022

Shieh, C. L., Chen, Y. S., Tsai, Y. J., and Wu, J. H. (2009). Variability in Rainfall Threshold for Debris Flow after the Chi-Chi Earthquake in central Taiwan, China. *Int. J. Sediment Res.* 24, 177–188. doi:10.1016/S1001-6279(09)60025-1

Takahashi, T. (2007). *Debris Flow Mechanics, Prediction and Countermeasures*. London, UK: Taylor & Francis Group.

Tang, C., van Asch, T. W. J., Chang, M., Chen, G. Q., Zhao, X. H., and Huang, X. C. (2012). Catastrophic Debris Flows on 13 August 2010 in the Qingping Area, Southwestern China: The Combined Effects of a strong Earthquake and Subsequent Rainstorms. *Geomorphology* 139-140, 559–576. doi:10.1016/j.geomorph.2011.12.021

Van Dine, D. F. (1996). *Debris Flow Control Structures for Forest Engineering*. Victoria: Res. Br., B.C. Min.

Wang, G. L. (2013). Lessons Learned from Protective Measures Associated with the 2010 Zhouqu Debris Flow Disaster in China. *Nat. Hazards* 69, 1835–1847. doi:10.1007/s11069-013-0772-1

Wang, J.-J. (2016). Large-scale Debris Flow Disasters: hazard-risk-vulnerability Analysis Approach in Taiwan. *Conservation Management Archaeological Sites* 18, 449–463. doi:10.1080/13505033.2016.1290473

Wu, H.-L., and Feng, Z.-y. (2006). Ecological Engineering Methods for Soil and Water Conservation in Taiwan. *Ecol. Eng.* 28, 333–344. doi:10.1016/j.ecoleng.2006.09.005

Xiong, J., Tang, C., Chen, M., Zhang, X., Shi, Q., and Gong, L. (2020). Activity Characteristics and Enlightenment of the Debris Flow Triggered by the Rainstorm on 20 August 2019 in Wenchuan County, China, *Bull. Eng. Geol. Environ.*, 80. 873–888. doi:10.1007/s10064-020-01981-x

Xiong, M., Meng, X., Wang, S., Guo, P., Li, Y., Chen, G., et al. (2016). Effectiveness of Debris Flow Mitigation Strategies in Mountainous Regions. *Prog. Phys. Geogr. Earth Environ.* 40, 768–793. doi:10.1177/0309133316655304

Yu, B., Ma, Y., and Wu, Y. (2013). Case Study of a Giant Debris Flow in the Wenjia Gully, Sichuan Province, China. *Nat. Hazards* 65, 835–849. doi:10.1007/s11069-012-0395-y

Zeng, Q. L., Yue, Z. Q., Yang, Z. F., and Zhang, X. J. (2009). A Case Study of Long-Term Field Performance of Check-Dams in Mitigation of Soil Erosion in Jiangjia Stream, China. *Environ. Geol.* 58, 897–911. doi:10.1007/s00254-008-1570-z

Zhang, S., Zhang, L. M., and Chen, H. X. (2014). Relationships Among Three Repeated Large-Scale Debris Flows at Pubugou Ravine in the Wenchuan Earthquake Zone. *Can. Geotech. J.* 51, 951–965. doi:10.1139/cgj-2013-0368

Zhao, D., Qu, C., Shan, X., Gong, W., Zhang, Y., and Zhang, G. (2018). InSAR and GPS Derived Coseismic Deformation and Fault Model of the 2017 Ms7.0 Jiuzhaigou Earthquake in the Northeast Bayanhar Block. *Tectonophysics* 726, 86–99. doi:10.1016/j.tecto.2018.01.026

Zhao, W., You, Y., Chen, X., Liu, J., and Chen, J. (2020). Case Study on Debris-Flow hazard Mitigation at a World Natural Heritage Site, Jiuzhaigou Valley, Western China. *Geomatics, Nat. Hazards Risk* 11, 1782–1804. doi:10.1080/19475705.2020.1810784

Zhou, B. F., Li, D. J., Luo, D. F., Lv, R. R., and Yang, Q. X. (1991). *Guide to Prevention of Debris Flow*. Beijing: Science Press. (In Chinese).

Zhou, W., Tang, C., Van Asch, T. W. J., and Chang, M. (2016). A Rapid Method to Identify the Potential of Debris Flow Development Induced by Rainfall in the Catchments of the Wenchuan Earthquake Area. *Landslides* 13, 1243–1259. doi:10.1007/s10346-015-0631-0

**Conflict of Interest:** The authors declare that the research was conducted in the absence of any commercial or financial relationships that could be construed as a potential conflict of interest.

frontiers in Earth Science

METHODS
published: 30 September 2021
doi: 10.3389/feart.2021.733413

# Landslide Scarp Assessments by Means of an Ellipse-Referenced Idealized Curved Surface

*Chi-Jyun Ko[1], Chih-Ling Wang[1], Hock-Kiet Wong[1], Wen-Chi Lai[2], Chih-Yu Kuo[3,4] and Yih-Chin Tai[1]**

[1]Department of Hydraulic and Ocean Engineering, National Cheng Kung University, Tainan, Taiwan, [2]Disaster Prevention Research Center, National Cheng Kung University, Tainan, Taiwan, [3]Center of Applied Sciences, Academia Sinica, Taipei, Taiwan, [4]Department of Civil Engineering, National Taiwan University, Taipei, Taiwan

The importance of scenario investigation in landslide-related hazard mitigation planning has long been recognized, where numerical simulation with physics-based models plays a crucial role because of its quantitative information. However, a plausible failure surface is a prerequisite in conducting the numerical simulation, but it often has a high degree of uncertainty due to the complex geological structure. The present study is devoted to proposing a methodology to mimic the plausible landslide failure surface (with some uncertainty) for investigating the consequent flow paths when failure takes place. Instead of a spherical shape, an idealized curved surface (ICS) is used, where two constant curvatures are, respectively, assigned in the down-slope and cross-slope directions. A reference ellipse is introduced for constructing the associated ICS with a specified failure depth regarding these two curvatures. Through translating, rotating, or side-tilting the reference ellipse, the most appropriate ICS is figured out with respect to the assigned constraints (failure area, volume of released mass, depth of sliding interface, etc.). The feasibility and practicability of this ellipse–ICS method are examined by application to a historical landslide event and one landslide-prone area. In application to the historical event, the fitness versus the landslide scarp area and its impacts on the consequent flow paths are investigated. For the landslide-prone area, five scenarios are arranged based on the surface features and the records of gaging wells. The most plausible failure scenario is therefore suggested as the prerequisite for mimicking the consequential flow paths.

**Keywords: landslide-prone area, slope failure surface, idealized curved surface (ICS), flow paths, HAZARD ASSESSMENT, disaster mitigation planning**

OPEN ACCESS

***Edited by:***
*Chong Xu,*
*Ministry of Emergency Management, China*

***Reviewed by:***
*Qi Yao,*
*China Earthquake Administration, China*
*Candan Gokceoglu,*
*Hacettepe University, Turkey*

****Correspondence:***
*Yih-Chin Tai*
*yctai@ncku.edu.tw*

***Specialty section:***
*This article was submitted to Geohazards and Georisks, a section of the journal Frontiers in Earth Science*

***Received:*** *30 June 2021*
***Accepted:*** *07 September 2021*
***Published:*** *30 September 2021*

***Citation:***
*Ko C-J, Wang C-L, Wong H-K, Lai W-C, Kuo C-Y and Tai Y-C (2021) Landslide Scarp Assessments by Means of an Ellipse-Referenced Idealized Curved Surface. Front. Earth Sci. 9:733413. doi: 10.3389/feart.2021.733413*

## 1 INTRODUCTION

Landslides, either with fast movement or in creeping motion, together with the sequential mass movement, pose severe threats to human lives as well as infrastructures in mountain areas (Dong et al., 2011; Lin et al., 2011; Iverson et al., 2015; Zhang et al., 2018; Sala et al., 2021; Van Tien et al., 2021). In the aspect of disaster mitigation/prevention plannings, the determination of the plausible failure surface is the core issue, which is closely related to the analysis of slope stability, the slide volume, and the influence area. However, the complex composition, spatial geological structure, and hydrological variations lead the determination of a precise failure surface on the natural slopes in mountain areas to a highly challenging task, especially when the field data are

incomplete. Hence, the determination/prediction of a landslide failure surface and estimation of the associated volume of released mass are with a high degree of uncertainty (e.g., Jaboyedoff et al., 2019; Yeh et al., 2021).

The limit equilibrium method (LEM) and the finite element method (FEM) are the two traditional and widely employed approaches for evaluating the stability of slopes (e.g., Briaud, 2013; Shen and Abbas, 2013). The LEMs evaluate the equilibrium of a slope under the influence of gravity, where the method of slides is the most popular one. The method of slices can date back to the pioneering work of Fellenius (1927), where the soil mass is sliced into vertical elements, and the forces are analyzed on a cylindrical sliding surface to determine the factor of safety of the slope. Depending on the number of the sliced vertical elements, an equation system is derived for the conservations of force and/or moment of momentum, where additional assumptions for forces between adjacent slides are introduced as closure conditions. Hence, there are several proposals for various closure conditions, such as the ones by Bishop (1955), Janbu (1954), Janbu (1973), and Morgenstern and Price (1965) for 2D analysis and by Lam and Fredlund (1993), Huang and Tsai (2000), Huang et al. (2002), and Reid et al. (2015) explicitly for 3D stability analysis. Although the layered structure or the impacts of groundwater distribution can be included in the method of slices, a predefined sliding surface should be given as input data. This approach leads to several strategies for mimicking the sliding surface, such as the most observed circular arc, piecewise linear segments, or a combination of the both, depending on the geological condition of the investigated site, e.g., the software SLOPE/W (GEO-SLOPE International Ltd, 2012). For locating the most critical failure surface (i.e., with the lowest possible factor of safety), it turns to be a procedure of iterative search (e.g., Briaud, 2013).

The FEM is based on continuum mechanics together with appropriate constitutive laws for the stress–strain relation in analyzing the stability of slopes (Griffiths and Lane, 1999). Utilizing the FEM approach, one identifies the failure surface by the weakest zones in the calculated stress field, where significant displacement/deformation takes place. Hence, the performance of FEM highly relies on the employed constitutive models. Although the FEM methods can figure out the weakest zones, the geological conditions in mountain areas are far too complex to utilize the FEM approach with simplistic constitutive laws for a precise description of the plausible failure surface. On the other hand, one can recognize, thanks to the modern techniques of remote sensing (light detection and ranging (LiDAR), interferometric synthetic-aperture radar (InSAR), uninhabited aerial vehicle SAR (UAVSAR), or temporarily coherent point interferometry SAR (TCPInSAR), etc.), the tiny geomorphological features on the surface, such as cracks or minor scarps, for identifying and delineating the potential landslide sites (Lin et al., 2013; Stumpf et al., 2013; Delbridge et al., 2016; Lai, 2019; Wang, 2020). Along this direction, assessing the associated landslide volume and the consequential influence area is essential in disaster mitigation planning in which numerical simulation can serve as a powerful tool in scenario investigation. Thus, an efficient method for mimicking the 3D failure surface and estimating the landslide volume in various scenarios is highly requested.

For approximating the 3D failure surface, Jaboyedoff et al. (2004) and Jaboyedoff et al. (2009) proposed the Sloping Local Base Level (SLBL) method to construct a curved surface, of which the second derivative along the down-slope direction remains constant. The SLBL technique has been tested against landslides triggered by Typhoon Talas in Japan, where reasonable agreements (±35%) were achieved (Jaboyedoff et al., 2019). For studying the 3D stability of stratovolcano edifice, Reid et al. (2000) and Reid et al. (2001) suggested a spherical failure surface for analyzing the slope stability by using the LEM without considering the internal/local structures. This approach has been extended for including the spatial geological structure and groundwater patterns, as available in the software Scoops3D (see, e.g., Reid et al., 2015; Tran et al., 2018; Zhang and Wang, 2019). For a specified area (convex polygon) and a predefined volume of released mass, Kuo et al. (2020) published a method for boundary-fitted, volume-constrained, smooth minimal surface (SMS). Nearly at the same time, Tai et al. (2020) proposed the concept of an idealized curved surface (ICS) to mimic the failure surface for performing numerical simulations. The ICS consists of two constant curvatures in the down-slope and cross-slope directions, respectively, so that the ICS method can be seen as a modification of the SLBL-method or the spherical approach (Scoops3D). All these approaches (SLBL, spherical approach, SMS, or ICS) aim at a low cost but efficient estimation, where the stratigraphy and geological structures can be omitted. Hence, they are not able to provide predictions with a high degree of precision. Nevertheless, higher tolerance in prediction would be allowed in the application of scenario investigations for hazard mitigation planning because the measured field data are subject to a certain degree of uncertainty.

In the present study, we adopt the concept of an idealized curved surface (ICS) to mimic the plausible failure surface as well as to define the associated scarp area. Because of the characteristic of two constant curvatures, a reference ellipse is introduced for constructing the ICS. For an assigned area (delineated area) and its associated volume of released mass, we look for the most appropriate ICS by adjusting (translating, rotating, or tilting) the reference ellipse and by trying a range of failure depth. Because the most appropriate ICS is a smooth surface, there are certainly discrepancies between the predicted scarp area and the reference one. In contrast to the smooth minimal surface (SMS) method Kuo et al. (2020), where the boundary of the predicted failure surface fits the assigned border exactly, this approach relaxes the constrain and allows modification of the area as well as released volume for matching some specified area. Because of the high degree of uncertainty, the potential site of landslide sometimes has to be modified based on updated measurement (e.g., the records of inclinometer or groundwater level). The proposed ellipse–ICS approach provides the freedom of flexible coverage for minimizing the discrepancy.

# 2 REFERENCE ELLIPSE AND IDEALIZED SURFACE FOR FAILURE SURFACE

## 2.1 Idealized Curved Surface

Based on the geomorphological concept, Tai et al. (2020) proposed an idealized curved surface (ICS) as the plausible landslide failure surface in computation for the consequent flow paths. The key

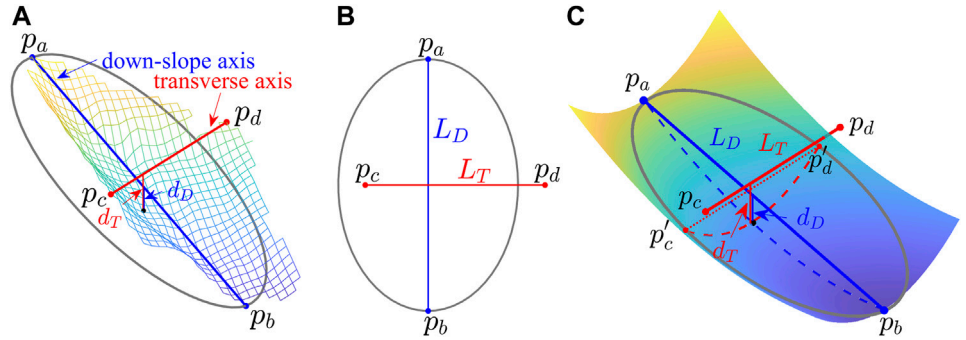


**FIGURE 1 | (A)** The main (down-slope) axis and the transverse axis of a failure surface, which are perpendicular to each other in the top view and with depths, $d_D$ and $d_T$, respectively. **(B)** The top view and the regressed ellipse. **(C)** The constructed idealized curved surface (ICS). It is noted that $p_c$ and $p_d$ lie at the scarp boundary, while $\overline{p'_c p'_d}$ denotes the minor axis of the reference ellipse.

feature of the ICS is that the surface is defined by two distinct curvatures remaining constant in the main (down-slope) and transverse (cross-slope) directions, respectively. As shown in **Figure 1A**, the ICS is fundamentally constructed by four points, $p_a$, $p_b$, $p_c$, and $p_d$, where $\overline{p_a p_b}$ is along the down-slope direction and $\overline{p_c p_d}$ lies in the transverse direction. In the work of Tai et al. (2020), $p_a$ is assigned to lie at the upper part of the scarp area and $p_b$ is at the lower points, while the vertical section of $\overline{p_c p_d}$ perpendicularly crosses the midpoint of $\overline{p_a p_b}$ (see **Figures 1A,B**). In other words, $\overline{p_a p_b}$ and $\overline{p_c p_d}$ are perpendicular to each other in the top view, but they are generally not on the sample plane (i.e., $d_D \neq d_T$). Besides, $\overline{p_c p_d}$ is not always symmetric about $\overline{p_a p_b}$ (cf. **Figure 1B**). In the present study, a reference ellipse is proposed that is determined (by the minimum root mean square of the distance) concerning the four points ($p_a$, $p_b$, $p_c$, and $p_d$) where $\overline{p_a p_b}$ defines the major axis of the ellipse and $\overline{p_c p_d}$ is parallel to the minor axis $\overline{p'_c p'_d}$; see **Figure 1C**. As illustrated in **Figure 1C**, curve $\overset{\frown}{p_a p_b}$ is defined by curvature $\kappa_D = 1/R_D$ with respect to the depth $d_D$ and curve $\overset{\frown}{p'_c p'_d}$ is by curvature $\kappa_T = 1/R_T$ and depth $d'_T = d_D$. In this aspect, the orientation of this reference ellipse plays a crucial role in determining the ICS. Hence, the next key task is the determination of the ellipse. In the work of Tai et al. (2020), 100 combinations (10 points at the top and 10 points on the lowest margin) are tried for each identified landslide source area of the historical event by determining the most appropriate ICS. There is no source area to be identified for a landslide-prone site, and it is of high uncertainty to delineate the exact boundary of a potential area. This ellipse–ICS approach may help determine the orientation of the ICS and the area size for various scenarios at the first moment. Together with the volume–area relations (e.g., Guzzetti et al., 2009; Larsen et al., 2010; Tai et al., 2020, or the ones listed therein) for the plausible volume of released mass, the utilization of an ellipse may reduce the complexity of the ICS construction, especially for disaster investigation or hazard assessment on various scenarios.

## 2.2 Reference Ellipse and Construction of the ICS

Taylor et al. (2018) have pinpointed that an ellipse is a reasonably good approximation of the landslide shape, and a substantial percentage of historical landslides supports this conclusion. Although they did not distinguish the source and runout area (due to the employed inventories), significant deviations from the ellipse are found to be caused by the inclusion of the flow paths (channel morphology and merging of debris flows) or merges of several small landslides. In the present study, we propose to construct the ICS based on the reference ellipse, which fits the source area (or landslide-prone area identified by remote-sensing technology or/and field survey). The first step is to determine the major axis of the reference ellipse, and they connect the highest and lowest points (in elevation) of the (potential) source area. The second step is to determine the minor axis, which can be obtained by setting the area of the ellipse the same as the source area $A_{sa}$ or by the width of the source area. In case only some morphological features or plausible failure locations/points are identified, the ellipse can be determined by regression with respect to these points.

An example is shown in **Figure 2**. Concerning the failure surface/area (**Figure 2A**), a reference ellipse is determined through the above elaborated two steps, where $L_1$ is the length of the major axis and $L_2$ is the length of the minor axis (**Figure 2B**). For a reference ellipse, each failure depth determines one ICS (see **Figure 2C**). The associated released mass volume can be calculated by the difference in the ICS and the pre-event topography through the digital elevation maps (DEMs). Once the released mass volume is given (e.g., by the volume–area relations), the sought ICS should yield nearly the same volume, and this can be achieved through iteration over a range of failure depths. It is obvious that the failure area determined by the ICS might deviate from the real/identified failure area; see **Figure 2D**. In the present study, it is suggested that the most appropriate ICS is the one that has minimal deviation to the failure area if the real failure area is available or the potential area is delineated. Hence, the determination of the reference ellipse plays a crucial role in constructing the ICS.

The determination of the reference ellipse depends on the shape and orientation of the source area. However, the shapes of the source area are rather complex. Excluding highly irregular and branched shapes, we can approximately group the commonly

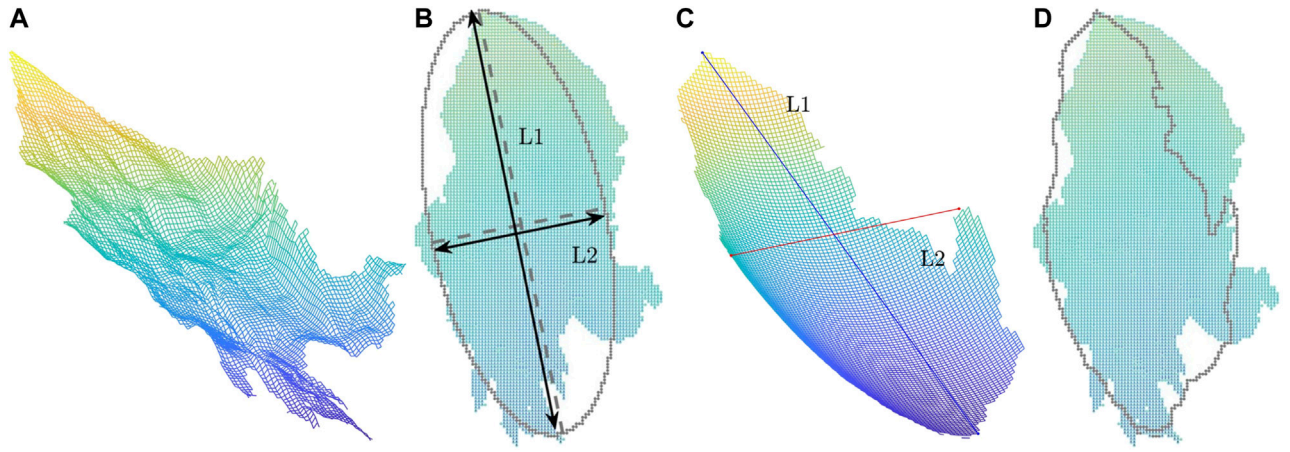


**FIGURE 2 |** Main scarp area of the 2009 Hsiaolin landslide. **(A)** The failure surface. **(B)** Top view of the failure surface and the associated reference ellipse. **(C)** The constructed ICS. **(D)** Top view of the ICS (outlined) and failure surface (shaded, used in the SMS method).

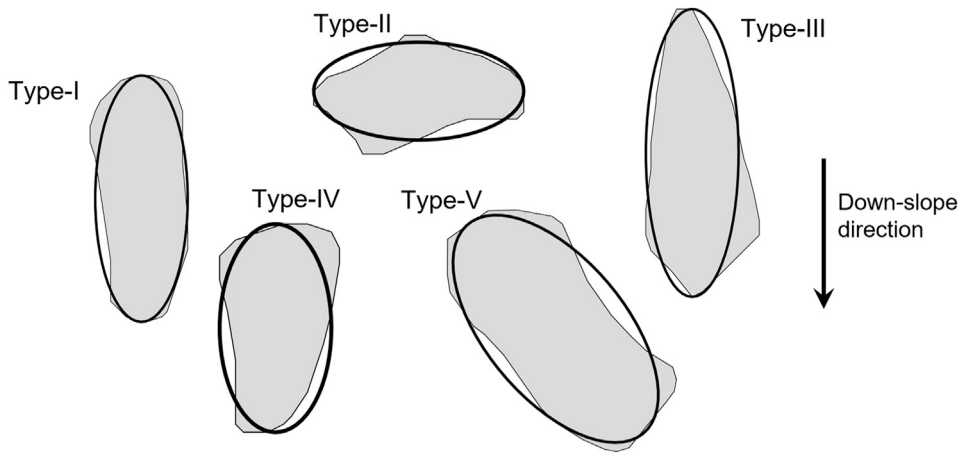


**FIGURE 3 |** The commonly observed shapes of the landslide source area.

observed shapes of landslide source area into five types (cf. **Figure 3**):

- Type I: Elliptical shape with major axis approximately in the down-slope direction.
- Type II: Elliptical shape with minor axis approximately in the down-slope direction.
- Type III: Ovate or lanceolate shape, of which the downstream part is wider.
- Type IV: Obovate or oblanceolate shape, of which the upstream part is wider.
- Type V: Concave hull, which can be seen as a distortion of the above types (Types I to IV).

Types I, III, IV, and V cover the landslide shapes of Category D (more than 82% among 20,705 landslides) defined in the work of Taylor et al. (2018), while Type II is figured out from the inventory of rainfall-triggered landslides taking place in 2009 in Taiwan (cf. Lin et al., 2013; Tai et al., 2020). As listed in **Table 1**, four methods (A to D) are considered for abstracting the landslide source area of the five shape types to the reference ellipse. For distinguishing the down-slope axis $L_D$ and transverse axis $L_T$ of the source area, the lengths of the major and minor axes of the reference ellipse are denoted by $L_1$ and $L_2$, respectively, and its area is $A_E$. With the main axis $\overline{p_a p_b}$, one tries various reference ellipses by translation and rotation, i.e., setting the top vertex at the 48 grid points around $p_a$ (i.e., ±3 grid points in the down- and cross-slope directions) and rotating with various angles (cf. **Figure 4B**). One should note that the vertices for the major/minor axis are assigned to be on the grid point of the digital elevation map (DEM), and its area is calculated with the mesh size. Hence, the length of the reference ellipse $L_1$ might not be equal to $L_D$ exactly, and its area could slightly deviate from the area of source area $A_{sa}$ in the searching process (i.e., one can only

**TABLE 1 |** Method of searching the optimal reference ellipse for constructing the most appropriate ICS.

| Method | ReferencesParameters | Description | Translation andRotation | Side-Tilting |
|---|---|---|---|---|
| Method A | $L_D$, $L_T$, $A_E$, $A_{sa}$ | $L_1 \approx L_D$, $L_2 \approx L_T$, and $A_E \approx A_{sa}$ | yes | no |
| Method B | $L_D$, $L_T$, $A_E$, $A_{sa}$ | $L_1 \approx L_D$, $L_2 \approx L_T$, and $A_E \approx A_{sa}$ | yes | yes |
| Method C | $L_D$, $A_{sa}$ | $L_1 \approx L_D$, $L_2$ and $A_E$ are variable | yes | no |
| Method D | $A_E$, $A_{sa}$ | $A_E \approx A_{sa}$ is kept fixed, both $L_1$ and $L_2$ are variable | yes | no |

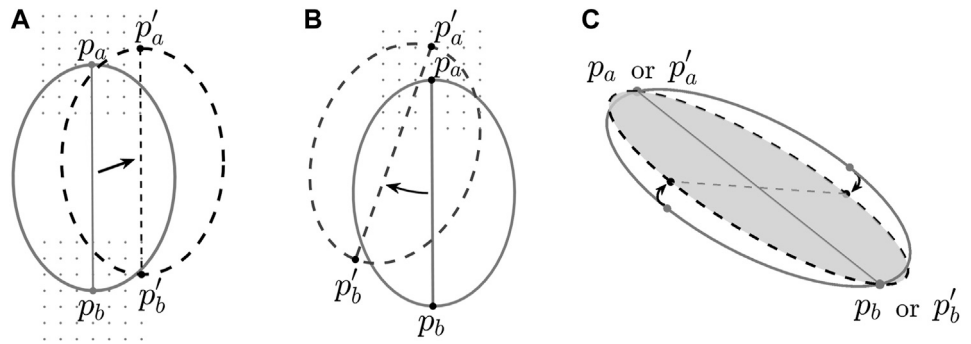


**FIGURE 4 |** The location/orientation of the reference ellipse: **(A)** translation, **(B)** translation and rotation, and **(C)** side-tilting (only in method B).

have $L_1 \approx L_D$ and $A_E \approx A_{sa}$). Once the reference ellipse is fixed, each depth ($d_D$ as shown in **Figure 1A**) determines one candidate ICS, yielding the associated released volume of mass as well as the failure area $A_{ICS}$. There are two criteria for figuring out the most appropriate ICS: 1) the released mass should be closest to the assigned one and 2) the minimum deviation of the resulted failure area $A_{ICS}$ from the source area $A_{sa}$. Here, one should notice that the ICS-yielded failure area might be divided into several blocks due to the rugged topography, especially when the ICS tends to be flat. In the present study, the separated ones will be filtered out to alleviate the complexity.

Accordingly, under the prerequisite of the assigned volume of released mass (calculated by historical event or estimated by the volume–area relations), the four methods (A to D) are briefed in **Table 1**. In methods A and B, it is set that $L_1 \approx L_D$ and $A_E \approx A_{sa}$, while the ellipse is allowed to tilt around its major axis in method B (cf. **Figure 4C**). With $L_1 \approx L_D$, various reference ellipses of different values for $L_2$ are tested for constructing the candidate ICSs in method C, while the ellipse area $A_E$ does not remain invariant (due to the different values of $L_2$). Accompanied with various values of $L_2$ but keeping $A_E \approx A_{sa}$, the magnitude of $L_1$ co-varies in method D. That is, the shape of the reference ellipse is fixed in methods A and B. In methods C and D, the shapes of the reference ellipse are variable, while the ellipse area $A_E$ remains invariant in method D. In addition, it has to be noted that the translation and rotation procedures are performed in the searching process in all of the four methods, while only in method B, the reference ellipse is allowed to tilt around its major axis (cf. **Figure 4C**).

In this ellipse–ICS approach, the major axis of the reference ellipse generally lies along the down-slope direction (for shapes of Type I, III, IV, or V). For shapes of Type II, the minor axis is assigned to follow the down-slope direction with the major axis lying in the transverse direction because its transverse extension is wider than the one in the down-slope direction. As will be detailed in the following section, the present approach (through methods A to D) is able to deliver appropriate ICSs, of which the resulted failure area may serve as a reasonable approximation to the (assigned) source area.

## 3 APPLICATION TO A HISTORICAL EVENT AND LANDSLIDE-PRONE AREAS

The proposed methods (method A to D) for constructing the most appropriate ICS are applied to a historical landslide event and one landslide-prone area. The historical event is the Hsiaolin landslide occurred in 2009 in southern Taiwan. As a representative event in Taiwan, it has received significant research interests and we would refer the readers for details to the relevant literature, such as the work of Dong et al. (2011), Kuo et al. (2011), Tai et al. (2019), and Tai et al. (2020). In application to the Hsiaolin landslide, we only consider the main scarp area, marked by HL-1 as shown in **Figure 5**, which consists of more than 94% landslide mass as given in the work of Kuo et al. (2011) and Tai et al. (2019).

For the landslide-prone areas, we consider a potential large-scale landslide area, named Taitung-Yanping-T003, which locates near Wu-Ling village in the Luliao watershed in Taitung county, south-eastern Taiwan (cf. Lai, 2019; Wang, 2020). As elaborated in the report (Wang, 2020), the plausible outline of a large-scale deep-seated landslide of potential in this area was delineated (by the high-resolution DEMs together with field survey); see the red line marked area in **Figure 6A**. Also, comprehensive LiDAR

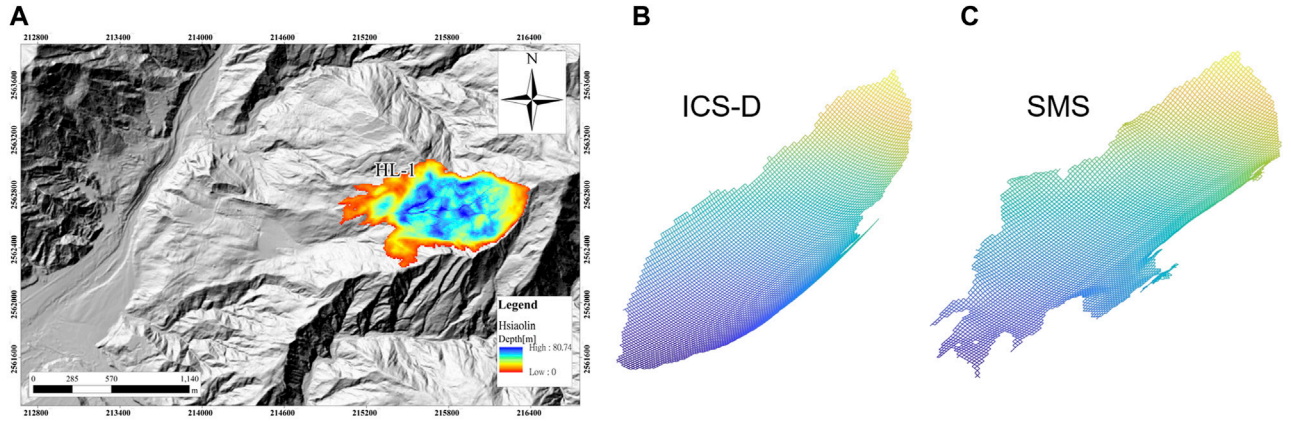


**FIGURE 5 | (A)** The main scar area (HL-1) of the Hsiaolin landslide event. **(B)** The constructed ICS for HL-1 by method D. **(C)** The surface determined by the smooth minimal surface (SMS) method proposed in Kuo et al. (2020).

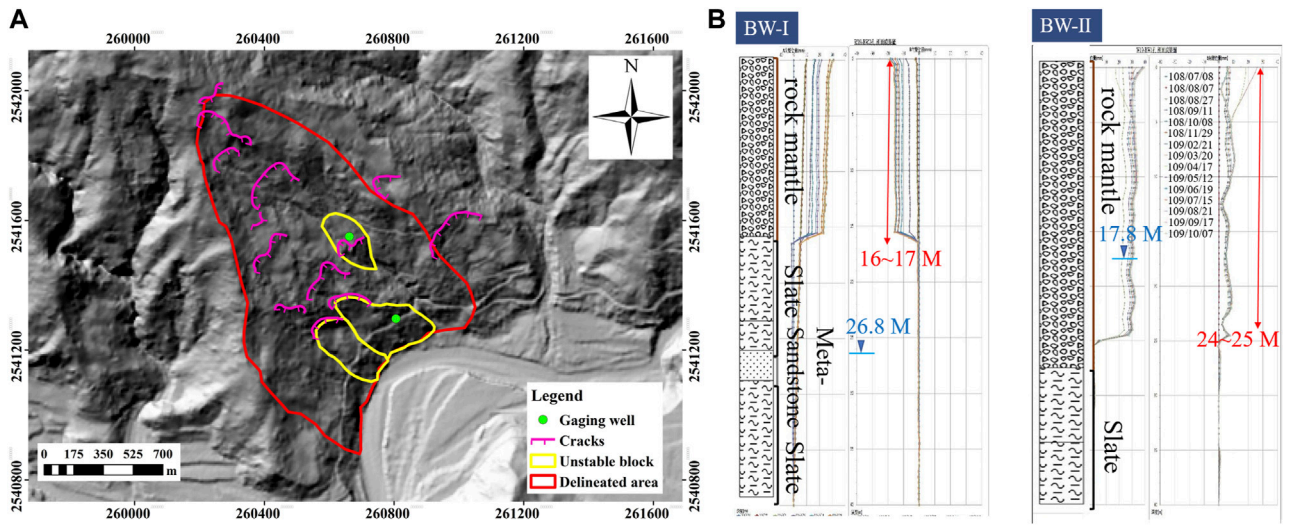


**FIGURE 6 | (A)** The hillshade map of Taitung-Yanping-T003, where the red line outlines the suspected landslide-prone area, the yellow lines indicate three blocks plausibly in movement, the cracks are depicted by red curves with bulges, and the light-yellow railing areas represent the dip slopes. **(B)** The monitoring records of gaging wells BW-I and BW-II.

image interpretation and topography analysis reveal three unstable blocks (W-1, W-2, and W-3) in plausible movement, outlined by yellow lines. Besides, many cracks are identified and depicted by red curves with bulges and the light-yellow railing areas indicate the dip slopes. For disaster monitoring and risk management, two gaging wells with inclinometers (at the middle of W-1 and W-2) are set up to monitor the groundwater level, potential failure surface, and the movement of the blocks (cf. Lai, 2019; Wang, 2020). The green circle markers (BW-I and BW-II) in **Figure 6A** indicate their locations, respectively. **Figure 6B** shows the records of these gaging wells. A definite sliding surface is detected at the depth between 16 and 17 m from the ground surface at BW-I, and the groundwater level lies at 26.8 m deep. The monitoring records of BW-II reveals that the groundwater is ca. 17.8 m deep and the sliding surface lies in the range of [24, 25] m deep. Identifying the landslide-prone area is based on geomorphological features, and the delineation of the boundary highly depends on personal experiences. These measurements provide an excellent example for re-examining the applicability of the current delineation and the associated planned mitigation countermeasure. Here, the employment of ICSs may provide plausible scenarios as useful reference information. Besides, the plausible failure surface, constructed by the volume-constrained smooth minimal surface (SMS) method (Kuo et al., 2020), is also considered and evaluated in this campaign, if applicable.

By constructing the ICS, the expected released volume $V_{ICS}$ should be given in advance. For historical events, $V_{ICS}$ is set to be

**TABLE 2 |** Indices for evaluating the performance of methods for constructing the ICS.

| Index | Definition | Description |
|---|---|---|
| $\lambda_E$ | $\frac{\lvert A_E - A_{sa}\rvert}{A_{sa}}$ | Area difference between the References ellipse $A_E$ and the source area $A_{sa}$ |
| $\Lambda_E$ | $\frac{\lvert A_E - A_{E\cap sa}\rvert + \lvert A_{sa} - A_{E\cap sa}\rvert}{A_{sa}}$ | Area difference between the coverage by $A_E$ and by $A_{sa}$ |
| $\lambda_S$ | $\frac{\lvert A_{ICS} - A_{sa}\rvert}{A_{sa}}$ | Area difference between the ICS and the source area $A_{sa}$ |
| $\Lambda_S$ | $\frac{\lvert A_{ICS} - A_{ICS\cap sa}\rvert + \lvert A_{sa} - A_{ICS\cap sa}\rvert}{A_{sa}}$ | Area difference between the coverage by ICS and by source area |

$A_{E\cap sa}$: *intersection of the reference ellipse and the source area.*
$A_{ICS\cap sa}$: *intersection of the coverage by the ICS and the source area.*

approximately equal to the exact landslide volume $V_{LS}$. For landslide-prone areas, the value of $V_{ICS}$ can be set by empirical volume–area relations. In the present study, the Guzzetti (2009)relation is employed because the considered landslides are also in sliding type, and this relation may provide sound agreement with the ones in Taiwan (see the work of Tai et al., 2020). One may choose some other appropriate empirical relations as well, if applicable. In the searching process with the four methods (methods A to D), thousands of reference ellipses and their associated ICSs are constructed. The performance of each ICS is evaluated in terms of four indices, $(\lambda_E, \Lambda_E, \lambda_S, \Lambda_S)$, as defined and listed in **Table 2**. $\lambda_E$ denotes the difference between the reference ellipse $A_E$ and the source area $A_{sa}$. It should be near zero in methods A, B, and D (cf. **Table 1**). $\Lambda_E$ stands for the deviated area of coverage. $\lambda_S$ and $\Lambda_S$ are for the resulted failure area $A_{ICS}$ and the source area $A_{sa}$, where $\Lambda_S$ represents the deviation index of area coverage. The most appropriate ICS is the one with the minimal difference between the covered area of $A_{ICS}$ and $A_{sa}$ (i.e., the one with the minimal value of the deviation index of area coverage $\Lambda_S$). In case the values of $\Lambda_S$ of two ICSs are very close, the one with the smallest value of $\lambda_S + \Lambda_S$ is chosen as the most appropriate ICS (see, e.g., Scenario I in **Table 4**).

In addition to searching the most appropriate ICS, numerical simulations are performed with the ICSs determined in various scenarios to investigate the impacts on the flow paths when the landslide takes place (e.g., hazard assessment). As a large portion of the hazardous landslides in Taiwan are triggered by heavy rainfall, the two-phase model for non-trivial topography (Tai et al., 2019) is employed here. In addition, the code has been reprogrammed and implemented for CUDA-GPU high-performance computation (MoSES_2PDF, see the work of Ko et al., 2021). For minimizing the uncertainty and for a unique reference, all the parameters are set identical to the ones used in the work of Tai et al. (2019). We refer readers to the work of Tai et al. (2019) and Ko et al. (2021) for details of the model equations and the applied GPU techniques used in the simulation tool, respectively. Besides, only the areas covered by flow depth more than 10 cm are taken into account in investigating the flow paths.

## 3.1 The 2009 Hsiaolin Landslide

Only the main source area (HL-1, in **Figure 5A**) by the 2009 Hsiaolin landslide is considered in this campaign, where the four methods (A, B, C, and D) are employed for constructing the ICSs. The area of the main scar (HL-1) is 624,900 $m^2$ with a mass volume of 21, 180, 535 $m^3$, where a 10 m resolution digital elevation map (DEM) is used. After the process of looking for the optimal reference ellipse (translation, rotations, and tilting as listed in **Table 1**) to construct the most appropriate ICS, **Table 3** shows the results of the four methods (A, B, C, and D) with respect to the four Indices $(\lambda_E, \Lambda_E, \lambda_S, \Lambda_S)$. It is found that these four methods can provide reasonable ICSs that are with a deviation of coverage less than 30% (i.e., $\Lambda_S < 0.3$). Although the ICS made by method C is with the least deviation in terms of coverage ($\Lambda_S$), the ICS area by method D is closest to the scarp area. When searching for the most appropriate ICS, one can choose the one with the smallest value of $\Lambda_S$ or the sum $\lambda_S + \Lambda_S$.

**TABLE 3 |** Performance indices with regard to the most appropriate ICS constructed by the four methods for HL-1 (2009 Hsiaolin landslide event).

| Method | $\lambda_E$ | $\Lambda_E$ | $\lambda_S$ | $\Lambda_S$ |
|---|---|---|---|---|
| Method A | 0.0 | 0.3229 | 0.0728 | 0.2930 |
| Method B | 0.0 | 0.3229 | 0.0771 | 0.2941 |
| Method C | 0.0701 | 0.3265 | 0.0887 | 0.2855[a] |
| Method D | 0.0006 | 0.3674 | 0.0414[a] | 0.2872 |

[a]*The smallest one in the column.*

To investigate the impacts of the plausible failure surface on the flow paths, we take the one constructed by method D as the most appropriate ICS (denoted by ICS-D) in the computation. Besides, the plausible failure surface determined by the smooth minimal surface (SMS) method is also considered in this campaign. The 3D illustrations of the ICS-D and SMS are given in **Figures 5B,C**, respectively, and their outlines (top view) are depicted in **Figure 2D**. In both cases, the simulation ends at $t = 181.83$ s when all the masses are nearly at the state of rest. **Figure 7** shows the flow paths computed with ICS-D and the one constructed by the SMS method (denoted by SMS), where the areas with flow thickness less than 10 cm are filtered out. The area in cyan indicates the paths in both simulations, the magenta area is covered only by the ICS-D computation, and the yellow area is only in the scenario of the SMS method. Although the deviation index of coverage $\Lambda_S$ reaches 0.2872, the differences between the flow paths are around 14.3%, i.e., ca. 85.7% of the total flow paths are overlapped. The main differences are found to be on the flanks of the source area (HL-1), and it is suspected to be mainly caused by the different outline/coverage between ICS-D and SMS. That is, deviation occurs at the first period when the mass is released and starts to slide. In the subsequent stage, most of the moving mass flows into a channelized topography so that the geometry of

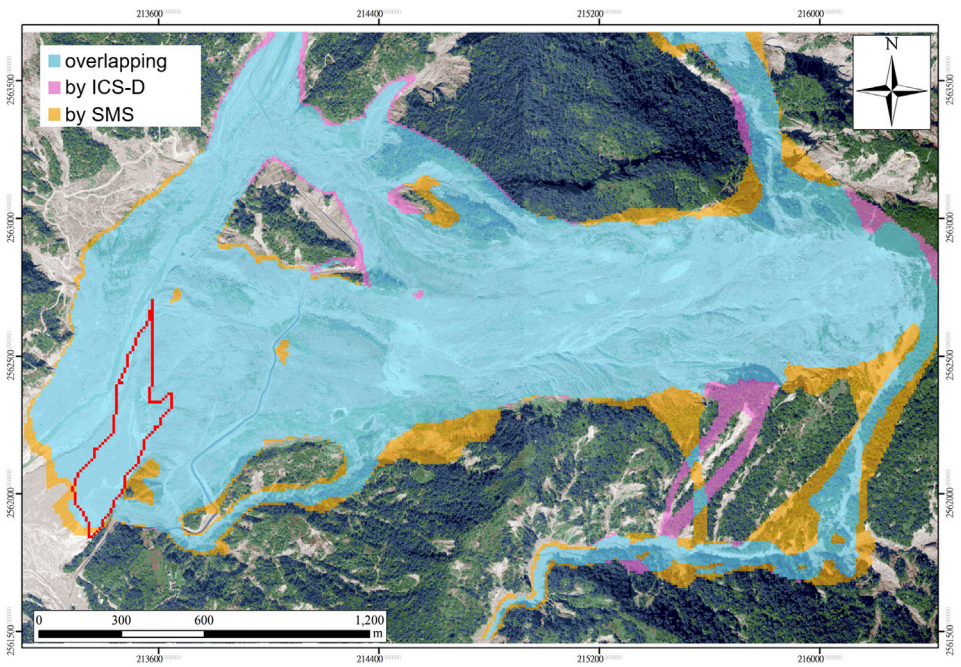


**FIGURE 7 |** Difference in the flow paths computed with the ICS-D and the smooth minimal surface method (SMS method), where the magenta area indicates the paths only by the ICS-D, the yellow area denotes the area only the SMS surface, and the cyan means the common flow paths during the simulation period (from $t = 0$ s to $t = 181.83$ s). The Hsiaolin village is depicted by the red contour. (Orthophoto: Courtesy of Aerial Survey Office, Forestry Bureau, Taiwan).

the failure surface does not have significant impacts on the following paths anymore.

## 3.2 The Landslide-Prone Area (Taitung-Yanping-T003)

The area of the landslide-prone area (Taitung-Yanping-T003) reads 515,900 $m^2$, with which the volume–area relation, suggested by Guzzetti et al. (2009), yields a plausible volume of released mass by 15, 565, 651 $m^3$. The resolution of the used digital elevation map (DEM) is 5 m. In terms of the delineated landslide-prone area and the three unstable blocks, five scenarios are assigned as listed in **Table 4**. Scenarios I and II are the individual releases of blocks W-1 and W-2, respectively. Blocks W-1 and W-3 are supposed to be released simultaneously in Scenario III. In Scenario IV, it is supposed that the landslide scarp follows the delineated outline. Scenario V is to figure out the most plausible failure scarp determined by the ellipse–ICS method, which covers all the cracks and the three unstable blocks within the delineated area, and the predicted failure depths are close to the records of the gaging well. The sketches of the scenarios are given in **Supplementary Image 1**. In all the scenarios (I to V), the associated volumes of released mass are calculated by Guzzetti's law (Guzzetti et al., 2009). Since the boundaries of the delineated areas are precisely given in Scenarios I to IV, the SMSs are also constructed for comparison.

**Table 4** lists the results of the most appropriate ICSs and SMSs with respect to the assigned areas, where the failure depths at the locations of BW-II and BW-I are the averaged values over the neighboring grids (9 grids in total) in the DEM. In Scenario I (for block W-1), both methods C and D (abbreviated by ICS-C and ICS-D, respectively) yield the ICSs with approximately the same deviation index of coverage $\Lambda_S$ and we choose ICS-C as the most appropriate ICS for its slightly better performance by $\lambda_S$. Although the value of $\Lambda_S$ by ICS-C reaches 0.4012, the associated failure depth lies at 16.59 m, exactly in the range of the inclinometer records (BW-I). On the other hand, the depth of the failure surface determined by the SMS reads 18.14 m, slightly deeper as indicated by the inclinometer (BW-I). Both predictions (by ICS-C and SMS) support the delineation of the unstable block W-1. In Scenario II (block W-2), both ICS and SMS predict the failure depths less than 5 m (3.16 and 4.68 m, respectively), which is far away from the records (in the range [24, 25]). This finding indicates that the delineation of unstable block W-2 could be questionable or more investigation seems needed. In Scenario III, predictions of ICS and SMS for the failure depth are 19.50 and 20.84 m, respectively, slightly more than the records. Since the volumes of landslide mass in scenarios I and III are estimated by the empirical volume–area relation (Guzzetti et al., 2009), the coincidence of the failure depth indicates the high possibility for these two scenarios.

The results of scenarios IV and V are shown in **Figure 8**, in which the left panels (a, b, and c) depict Scenario IV and the right panels (d, e, and f) are for Scenario V. In panels a and d, the delineated area is depicted by red contour, and the ICS-resulted failure areas are marked by jade-green shade for scenarios IV and V, respectively. The employed reference ellipses for constructing the ICSs are shown by red-outlines in panels b and e, while the

**TABLE 4 |** Scenarios for Taitung-Yanping-T003.

| Scenario | References area | Area [$m^2$] | BW-I [m] | | BW-II [m] | | $\Lambda_S$ | Method |
|---|---|---|---|---|---|---|---|---|
| | | | ICS | SMS | ICS | SMS | | |
| Scenario I | W-1 | 32, 650 | 16.59 | 18.14 | - - | - - | 0.4012 | C, D |
| Scenario II | W-2 | 16, 100 | - - | - - | 3.16 | 4.68 | 0.3478 | C |
| Scenario III | W-1 ∪ W-3 | 55, 200 | 19.50 | 20.84 | - - | - - | 0.3474 | D |
| Scenario IV | Delineated area | 515, 900 | 0.51 | 45.77 | 34.72 | 41.86 | 0.2838 | D |
| Gaging well | - - | - - | [16, 17] | | [24, 25] | | - - | - - |
| Scenario V | Cracks | $A_E$ = 367, 150 | 14.48 | - - | 27.58 | - - | 0.3672[a] | - - |

[a]*calculated with respect to the delineated area.*

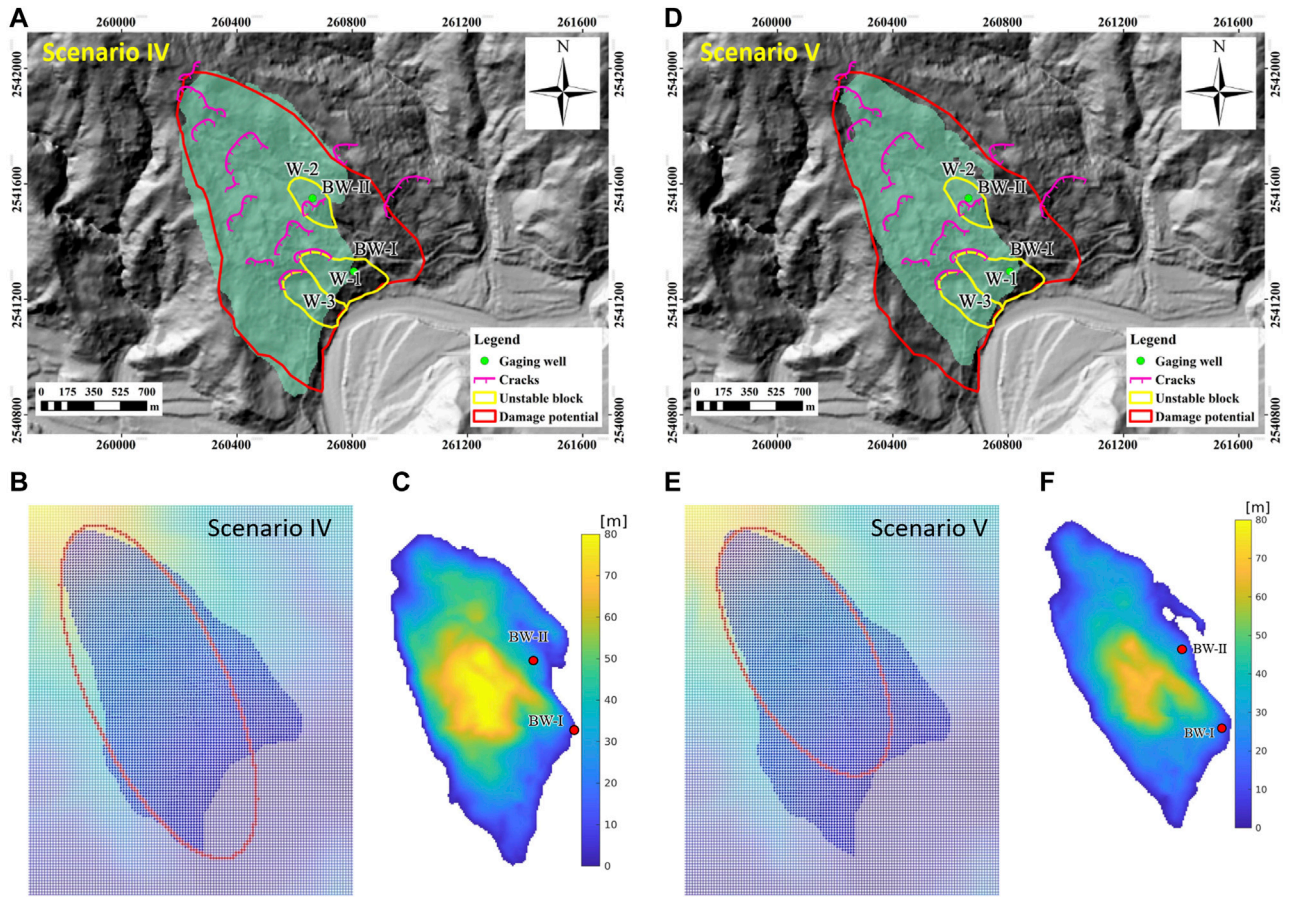


**FIGURE 8 |** Scenarios IV and V (Taitung-Yanpin-T003). **(A,D)** The covered area by the computed ICS (shaded in jade-green), the delineated landslide-prone area (red contour), and the locations of gaging wells (BW-I and BW-II). **(B,E)** The delineated landslide-prone area (blue shade) and the reference ellipse (red outlined) for constructing the most appropriate ICS. **(C,F)** Depth distribution of the released mass with respect to the ICS.

depth distributions of plausible release mass are given in panels c and f for scenarios IV and V, respectively. In Scenario IV, where the delineated area (the red-outlined area in panel a or the blue-shaded area in panel b) serves as the source area $A_{sa}$ in the searching process, the most appropriate ICS is constructed by method D (denoted by ICS-D). As listed in **Table 4**, the ICS-D predicts the failure depths of 0.51 m for BW-I and 34.72 m for BW-II, while they are 45.77 and 41.86 m, respectively, for the SMS. With respect to the inclinometer records [16, 17] m and [24, 25] m, the predicted depths are far too deep, although the ICS-D covers nearly the same area except for the south-eastern part (cf. panel a) where the deviation index of coverage $\Lambda_S$ = 0.2838. This deviation reveals that the present ellipse–ICS method seems inapplicable to Scenario IV, or the whole delineated area's failure would not take place at one time. Relating the inclinometer records with the plausible failure depths, we relax the constraint of the delineated area and suppose that all the cracks within the delineated area are induced by the same

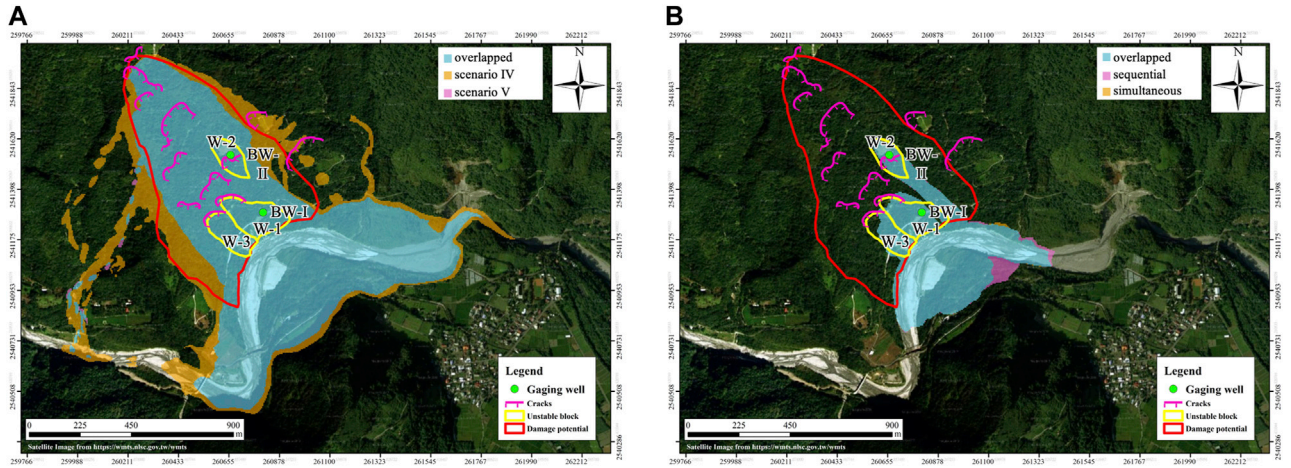


**FIGURE 9 | (A)** Flow paths in scenarios IV and V. **(B)** Flow paths by a simultaneous release of the three unstable blocks (W-1, W-2, and, W-3) or by sequential failure (Orthophoto: Courtesy of National Land Surveying and Mapping Center, Taiwan).

landslide body to be released (Scenario V). With the released volume (calculated by the Guzzetti (2009)law), the computed ICS suggests the failure depths of 14.48 m for BW-I and 27.58 m for BW-II (cf. the bottom row of **Table 4**). That is, in Scenario V, both depths predicted by ICS are close to the ones recorded by inclinometers. As shown in **Figure 8D**, the range of ICS is approximately in agreement with the delineated area in the upper part. This finding suggests a plausible failure area and its associated released volume of mass when the cracks and both records of the two gaging wells are taken into account. It indicates the practicality of the proposed ellipse–ICS approach, that it is able to deliver approximately reasonable estimation even when a precise delineation of the landslide-prone area is missing.

Based on the above scenario investigations, scenarios I, III, and V could be possible situations. Numerical simulations are therefore performed in terms of the scenarios for investigating the flow paths, where the simulation tool MoSES_2PDF (Ko et al., 2021) is employed. **Figure 9A** illustrates the flow paths of scenarios IV and V, where only the areas covered by flow thickness more than 10 cm are shown. The cyan area means the common flow paths in both scenarios, and the brown area is marked only in Scenario IV. Although the landslide mass (based on Guzzetti's (2009) empirical relation) in Scenario IV is about 1.6-fold to Scenario V, the traveling distance (along the down-slope direction) does not significantly increase compared to the one in Scenario V. The main difference lies in the lateral direction and is suspected to be induced by the discrepancies of the source area and by the different released volume. In both scenarios (IV and V), the landslide mass does not reach the Wu-Ling village located south-eastern from the landslide area. We also considered two small-scale plausible cases for the three unstable blocks (W-1, W-2, and W-3). In the first case, the three blocks are released simultaneously (simultaneous release). In the second case, the lower blocks (W-1 and W-3) are released first, followed by the release of W2 (sequential failure). **Figure 9B** presents the computed flow paths of these two cases. Similar to panel a, the cyan area indicates the common flow paths in both cases. The brown area is covered only in the first case (simultaneous release), and the fuchsia area is marked only in the second case (sequential failure). Interestingly, the sequential release yields nearly the same traveling distance but flow paths cover a larger area. Although the area expansion is around 5.2%, one has to pay attention to the impacts of a possible sequential failure by risk analysis or hazard assessment.

## 4 CONCLUDING REMARKS

This work outlines a methodology to systematically estimate the plausible landslide failure area, the associated volume of released mass, and the subsequent flow paths when the failure in an area of landslide susceptibility takes place. This method employs the concept of reference ellipse for constructing the idealized curved surface (ICS). Through translation, rotation, and side-tilting of the reference ellipse, there are thousands of ellipses (orientations) to be assessed. Together with the assigned failure depth, the constructed ICS cuts the local topography and yields the plausible failure area as well as the volume of mass to be released. Each ellipse is associated with one candidate ICS, which yields the volume of released mass as assigned (calculated by historical events or empirical volume–area relations). The most appropriate ICS is the one with the minimal deviation of the coverage between the ICS–resulted failure area and the delineated area (or the source area in historical events). As a matter of course, this approach would demand more computational resources. Nevertheless, it is an economical compromise because it does not request the expensive and time-consuming data obtained from geologic drilling, analysis of geological structure or comprehensive field survey, etc. No conflict exists. This ellipse–ICS approach can benefit from the field data (spatial geological variations, hydrological conditions, weathering effects, etc.) for its reliability. or reversely, the present

ellipse–ICS approach may provide helpful information, such as the appropriate locations of gaging stations.

We investigate the feasibility and practicability of the ellipse–ICS approach by application to the 2009 Hsiaolin landslide (historical event) and the delineated landslide-prone area (Taitung-Yanping-T003). The plausible failure surfaces determined by the SMS method (Kuo et al., 2020) are included in the campaign if a precise delineation of the source area is available. Since the SMS method requests a precise boundary of the source area, the difference in the flow paths between ICS and SMS clarifies the impacts of the geometry of the released mass on the flow paths. By simulating the 2009 Hsiaolin landslide, more than 85% of the flow paths are overlapped, although the deviation index of coverage $\Lambda_S$ between ICS and SMS reaches ca. 0.29. For the landslide-prone area (Taitung-Yanping-T003), five scenarios are arranged for mimicking plausible failure surface by ICS that agrees with the inclinometer records. This scenario investigation also highlights the characteristic that the ellipse–ICS method is applicable without a concrete delineated area. Combining the ellipse–ICS approach and the GPU-based simulation package provides an optimal tool for hazard assessment in various scenarios. The released volume of mass is estimated, and the subsequent flow paths are predicted.

It has to be noted that the present ellipse–ICS approach is based on the geomorphological concept, and it mimics the plausible failure surface by a smooth surface. It is certainly not intended to replace the conventional stability analysis. Instead, it fills the vacancy of the conventional analytical tools when only limited spatial, geological, and hydrological data are available. However, it works at the expense of computational resources that the most appropriate ICS is figured out among the thousands of reference ellipse and the associated candidate ICSs. In Scenario IV, there are 1,519 reference ellipses to be evaluated in methods A and B, while 10,633 reference ellipses in methods C and D. For each reference ellipse, one has to determine the depth to match the assigned volume of release mass utilizing iteration. A normal PC (i7-8700 CPU@3.20 GHz, 16 GB memory, Linux OS) takes about one to several hours to figure out the most appropriate ICS for one case/scenario. One possible way to enhance the computational efficiency is implementing the genetic algorithm (GA) (e.g., Whitley, 1994) together with GPU-accelerated computation for the current ellipse–ICS approach. We are working on it and will report the updates in due time.

## DATA AVAILABILITY STATEMENT

The data analyzed in this study are subject to the following licenses/restrictions: It is remarked that, following the government regulation, only the DEMs with a resolution of 20 × 20 m can be provided. The interpolated ones, not exactly identical to the ones used in the study, are available on request to the corresponding author. Requests to access these datasets should be directed to Y-CT, yctai@ncku.edu.tw.

## AUTHOR CONTRIBUTIONS

C-JK, C-LW, and H-KW: data analysis and numerical simulation. W-CL and C-YK: concept/opinion exchange and content confirmation. Y-CT: idea, design of the work, and construction of the MS. All authors contributed to the article and approved the submitted version.

## FUNDING

The financial support of the Ministry of Science and Technology, Taiwan (MOST 109-2221-E-006-022),and the Soil and Water Conservation Bureau, Council of Agriculture, Taiwan (SWCB-109-269) are acknowledged.

## SUPPLEMENTARY MATERIAL

The Supplementary Material for this article can be found online at: https://www.frontiersin.org/articles/10.3389/feart.2021.733413/full#supplementary-material

## REFERENCES

Bishop, A. W. (1955). The Use of the Slip circle in the Stability Analysis of Slopes. *Géotechnique* 5, 7–17. doi:10.1680/geot.1955.5.1.7

Briaud, J.-L. (2013). *Geotechnical Engineering: Unsaturated and Saturated Soils*. Hoboken, New Jersey: John Wiley & Sons.

Delbridge, B. G., Bürgmann, R., Fielding, E., Hensley, S., and Schulz, W. H. (2016). Three-Dimensional Surface Deformation Derived From Airborne Interferometric UAVSAR: Application to the Slumgullion Landslide. *J. Geophys. Res. Solid Earth.* 121, 3951–3977. doi:10.1002/2015jb012559

Dong, J.-J., Li, Y.-S., Kuo, C.-Y., Sung, R.-T., Li, M.-H., Lee, C.-T., et al. (2011). The Formation and Breach of a Short-Lived Landslide Dam at Hsiaolin Village, Taiwan - Part I: Post-Event Reconstruction of Dam Geometry. *Eng. Geology* 123, 40–59. doi:10.1016/j.enggeo.2011.04.001

Fellenius, W. (1927). *Swedish Slice Method Calculations With Friction and Cohesion Under the Assumption of Cylindrical Sliding Surfaces (Erdstatische Berechnungen mit Reibung und Kohäsion (Adhäsion) und Unter Annahme kreiszylindrischer Gleitflächen)*. Berlin: Verlag Ernst and Sohn Press.

GEO-SLOPE International Ltd (2012). *Stability Modeling with SLOPE/W*. Calgary, Alberta, Canada: GEO-SLOPE International Ltd.

Griffiths, D. V., and Lane, P. A. (1999). Slope Stability Analysis by Finite Elements. *Géotechnique* 49, 387–403. doi:10.1680/geot.1999.49.3.387

Guzzetti, F., Ardizzone, F., Cardinali, M., Rossi, M., and Valigi, D. (2009). Landslide Volumes and Landslide Mobilization Rates in Umbria, Central Italy. *Earth Planet. Sci. Lett.* 279, 222–229. doi:10.1016/j.epsl.2009.01.005

Huang, C.-C., Tsai, C.-C., and Chen, Y.-H. (2002). Generalized Method for Three-Dimensional Slope Stability Analysis. *J. Geotech. Geoenviron. Eng.* 128, 836–848. doi:10.1061/(asce)1090-0241(2002)128:10(836)

Huang, C.-C., and Tsai, C.-C. (2000). New Method for 3D and Asymmetrical Slope Stability Analysis. *J. Geotech. Geoenviron. Eng.* 126, 917–927. doi:10.1061/(asce)1090-0241(2000)126:10(917)

Iverson, R. M., George, D. L., Allstadt, K., Reid, M. E., Collins, B. D., Vallance, J. W., et al. (2015). Landslide Mobility and Hazards: Implications of the 2014 Oso Disaster. *Earth Planet. Sci. Lett.* 412, 197–208. doi:10.1016/j.epsl.2014.12.020

Jaboyedoff, M., Baillifard, F., Couture, R., Locat, J., Locat, P., and Rouiller, J. (2004). "New Insight of Geomorphology and Landslide Prone Area Detection Using Digital Elevation Model(s)," in *Landslides Evaluation and Stabilization*. Editors W. Lacerda, M. Ehrlich, A. Fontoura, and A. Sayo (Rotterdam: Balkema), 191–197. doi:10.1201/b16816-26

Jaboyedoff, M., Chigira, M., Arai, N., Derron, M.-H., Rudaz, B., and Tsou, C.-Y. (2019). Testing a Failure Surface Prediction and Deposit Reconstruction Method for a Landslide Cluster that Occurred During Typhoon Talas (Japan). *Earth Surf. Dynam.* 7, 439–458. doi:10.5194/esurf-7-439-2019

Jaboyedoff, M., Couture, R., and Locat, P. (2009). Structural Analysis of Turtle Mountain (Alberta) Using Digital Elevation Model: Toward a Progressive Failure. *Geomorphology* 103, 5–16. doi:10.1016/j.geomorph.2008.04.012

Janbu, N. (1973). "Slope Stability Computations," in *Embankment-dam Engineering, Casaggrande Volume* (New York: Wiley), 47–86.

Janbu, N. (1954). *Stability Analysis for Slopes with Dimensionless Parameters. Ph.D. Thesis*. Cambridge, Massachusetts: Harvard University.

Ko, C.-J., Chen, P.-C., Wong, H.-K., and Tai, Y.-C. (2021). MoSES_2PDF: A GIS-Compatible GPU-Accelerated High-Performance Simulation Tool for Grain-Fluid Shallow Flows. arXiv preprint arXiv:2104.06784 [cs.CE]

Kuo, C.-Y., Tsai, P.-W., Tai, Y.-C., Chan, Y.-H., Chen, R.-F., and Lin, C.-W. (2020). Application Assessments of Using Scarp Boundary-Fitted, Volume Constrained, Smooth Minimal Surfaces as Failure Interfaces of Deep-Seated Landslides. *Front. Earth Sci.* 8, 211. doi:10.3389/feart.2020.00211

Kuo, C., Tai, Y.-C., Chen, C., Chang, K., Siau, A., Dong, J., et al. (2011). The Landslide Stage of the Hsiaolin Catastrophe: Simulation and Validation. *J. Geophys. Res. Earth Surf.* 116, F04007. doi:10.1029/2010jf001921

Lai, W.-J. (2019). *Disaster Investigation and Countermeasure Strategy of Luliao Watershed (Taitung-Yanping-D002 Potential Large-Scale Landslide and Kanaluk Area)(in Chinese)*. Taiwan: Tech. rep., Soil and Water Conservative Bureau, Council of Agriculture. Rep.-No.: SWCB-108-127.

Lam, L., and Fredlund, D. G. (1993). A General Limit Equilibrium Model for Three-Dimensional Slope Stability Analysis. *Can. Geotech. J.* 30, 905–919. doi:10.1139/t93-089

Larsen, I. J., Montgomery, D. R., and Korup, O. (2010). Landslide Erosion Controlled by Hillslope Material. *Nat. Geosci.* 3, 247–251. doi:10.1038/ngeo776

Lin, C.-W., Chang, W.-S., Liu, S.-H., Tsai, T.-T., Lee, S.-P., Tsang, Y.-C., et al. (2011). Landslides Triggered by the 7 August 2009 Typhoon Morakot in Southern Taiwan. *Eng. Geology* 123, 3–12. doi:10.1016/j.enggeo.2011.06.007

Lin, C.-W., Tseng, C.-M., and Chen, R.-F. (2013). *Survey and Assessment of Potential Large-Scale Landslides Hazards in Mountainous Areas of Kao-Ping River Watershed*. Taiwan: Tech. rep., Soil and Water Conservative Bureau, Council of Agriculture.

Morgenstern, N. R., and Price, V. E. (1965). The Analysis of the Stability of General Slip Surfaces. *Géotechnique* 15, 79–93. doi:10.1680/geot.1965.15.1.79

Reid, M. E., Christian, S. B., and Brien, D. L. (2000). Gravitational Stability of Three-Dimensional Stratovolcano Edifices. *J. Geophys. Res.* 105, 6043–6056. doi:10.1029/1999jb900310

Reid, M. E., Christian, S. B., Brien, D. L., and Henderson, S. (2015). *Scoops3D–Software to Analyze Three-Dimensional Slope Stability Throughout a Digital Landscape*. Menlo Park, CA, USA: US Geological Survey; Volcano Science Center.

Reid, M. E., Sisson, T. W., and Brien, D. L. (2001). Volcano Collapse Promoted by Hydrothermal Alteration and Edifice Shape, Mount Rainier, Washington. *Geol.* 29, 779–782. doi:10.1130/0091-7613(2001)029<0779:vcpbha>2.0.co;2

Sala, G., Lanfranconi, C., Frattini, P., Rusconi, G., and Crosta, G. B. (2021). Cost-Sensitive Rainfall Thresholds for Shallow Landslides. *Landslides* 18, 2979–2992. doi:10.1007/s10346-021-01707-4

Shen, H., and Abbas, S. M. (2013). Rock Slope Reliability Analysis Based on Distinct Element Method and Random Set Theory. *Int. J. Rock Mech. Mining Sci.* 61, 15–22. doi:10.1016/j.ijrmms.2013.02.003

Stumpf, A., Malet, J.-P., Kerle, N., Niethammer, U., and Rothmund, S. (2013). Image-Based Mapping of Surface Fissures for the Investigation of Landslide Dynamics. *Geomorphology* 186, 12–27. doi:10.1016/j.geomorph.2012.12.010

Tai, Y.-C., Ko, C.-J., Li, K.-D., Wu, Y.-C., Kuo, C.-Y., Chen, R.-F., et al. (2020). An Idealized Landslide Failure Surface and its Impacts on the Traveling Paths. *Front. Earth Sci.* 8, 313. doi:10.3389/feart.2020.00313

Tai, Y. C., Heß, J., and Wang, Y. (2019). Modeling Two-Phase Debris Flows With Grain-Fluid Separation Over Rugged Topography: Application to the 2009 Hsiaolin Event, Taiwan. *J. Geophys. Res. Earth Surf.* 124, 305–333. doi:10.1029/2018jf004671

Taylor, F. E., Malamud, B. D., Witt, A., and Guzzetti, F. (2018). Landslide Shape, Ellipticity and Length-To-Width Ratios. *Earth Surf. Process. Landforms* 43, 3164–3189. doi:10.1002/esp.4479

Tran, T. V., Alvioli, M., and Lee, G. (2018). Three-Dimensional, Time-Dependent Modeling of Rainfall-Induced Landslides Over a Digital Landscape: a Case Study. *Landslides* 15, 1071–1084. doi:10.1007/s10346-017-0931-7

Van Tien, P., Trinh, P., Luong, L., Nhat, L., Duc, D., Hieu, T., et al. (2021). The October 13, 2020, Deadly Rapid Landslide Triggered by Heavy Rainfall in Phong Dien, Thua Thien Hue, Vietnam. *Landslides* 18, 2329–2333. doi:10.1007/s10346-021-01663-z

Wang, P.-C. (2020). *FY 109 Field Survey and Monitoring for Large-Scale Landslide in Taitung County (In Chinese)*. Taiwan: Tech. rep., Soil and Water Conservative Bureau, Council of Agriculture. Rep.-No.: SWCB-109-080.

Whitley, D. (1994). A Genetic Algorithm Tutorial. *Stat. Comput.* 4, 65–85. doi:10.1007/bf00175354

Yeh, C.-H., Dong, J.-J., Khoshnevisan, S., Juang, C. H., Huang, W.-C., and Lu, Y.-C. (2021). The Role of the Geological Uncertainty in a Geotechnical Design - A Retrospective View of Freeway No. 3 Landslide in Northern Taiwan. *Eng. Geology* 291, 106233. doi:10.1016/j.enggeo.2021.106233

Zhang, L., Li, J., Li, X., Zhang, J., and Zhu, H. (2018). *Rainfall-induced Soil Slope Failure: Stability Analysis and Probabilistic Assessment*. Boca Raton, FL: CRC Press.

Zhang, S., and Wang, F. (2019). Three-Dimensional Seismic Slope Stability Assessment With the Application of Scoops3D and GIS: a Case Study in Atsuma, Hokkaido. *Geoenviron. Disasters* 6, 9. doi:10.1186/s40677-019-0125-9

**Conflict of Interest:** The authors declare that the research was conducted in the absence of any commercial or financial relationships that could be construed as a potential conflict of interest.

**Publisher's Note:** All claims expressed in this article are solely those of the authors and do not necessarily represent those of their affiliated organizations, or those of the publisher, the editors and the reviewers. Any product that may be evaluated in this article, or claim that may be made by its manufacturer, is not guaranteed or endorsed by the publisher.

frontiers in Earth Science

ORIGINAL RESEARCH
published: 08 October 2021
doi: 10.3389/feart.2021.737271

# Electrical Resistivity Tomography (ERT) Monitoring for Landslides: Case Study in the Lantai Area, Yilan Taiping Mountain, Northeast Taiwan

*Wu-Nan Tsai[1], Chien-Chih Chen[1,2], Chih-Wen Chiang[3]*, Pei-Yuan Chen[4], Chih-Yu Kuo[5,6], Kuo-Lung Wang[7], Meei-Ling Lin[6] and Rou-Fei Chen[8]*

*[1]Department of Earth Sciences, National Central University, Taoyuan, Taiwan, [2]Earthquake-Disaster and Risk Evaluation and Management Center, National Central University, Taoyuan, Taiwan, [3]Institute of Earth Sciences, National Taiwan Ocean University, Keelung, Taiwan, [4]Graduate Institute of Hydrologic and Oceanic Sciences, National Central University, Taoyuan, Taiwan, [5]Research Center for Applied Sciences, Academia Sinica, Taipei, Taiwan, [6]Department of Civil Engineering, National Taiwan University, Taipei, Taiwan, [7]Department of Civil Engineering, National Chi Nan University, Nantou, Taiwan, [8]Department of Materials and Mineral Resources Engineering, National Taipei University of Technology, Taipei, Taiwan*

OPEN ACCESS

**Edited by:**
*Chong Xu, Ministry of Emergency Management, China*

**Reviewed by:**
*Changdong Li, China University of Geosciences Wuhan, China*
*Joern Lauterjung, German Research Centre for Geosciences, Germany*

***Correspondence:**
*Chih-Wen Chiang*
*zjiang@ntou.edu.tw*

**Specialty section:**
*This article was submitted to Geohazards and Georisks, a section of the journal Frontiers in Earth Science*

**Received:** *06 July 2021*
**Accepted:** *23 September 2021*
**Published:** *08 October 2021*

**Citation:**
*Tsai W-N, Chen C-C, Chiang C-W, Chen P-Y, Kuo C-Y, Wang K-L, Lin M-L and Chen R-F (2021) Electrical Resistivity Tomography (ERT) Monitoring for Landslides: Case Study in the Lantai Area, Yilan Taiping Mountain, Northeast Taiwan. Front. Earth Sci. 9:737271. doi: 10.3389/feart.2021.737271*

Water saturation in the bedrock or colluvium is highly related to most landslide hazards, and rainfall is likely a crucial factor. The dynamic processes of onsite rock/soil mechanics could be revealed via monitoring using the electrical resistivity tomography (ERT) technique and Archie's law. This study aims to investigate water saturation changes over time using time-lapse ERT images, providing a powerful method for monitoring landslide events. A fully automatic remote resistivity monitoring system was deployed to acquire hourly electrical resistivity data using a nontraditional hybrid array in the Lantai area of Yilan Taiping Mountain in Northeast Taiwan from 2019 to 2021. Six subzones in borehole ERT images were examined for the temporal and spatial resistivity variations, as well as possible pathways of the groundwater. Two representative cases of inverted electrical resistivity images varying with precipitation may be correlated with water saturation changes in the studied hillslope, implying the process of rainfall infiltration. Layers with decreased and increased electrical resistivity are also observed before sliding events. Accordingly, we suggest that high-frequency time-lapse ERT monitoring could play a crucial role in landslide early warning.

**Keywords: time-lapse electrical resistivity tomography, rainfall infiltration, water saturation, landslide, hazard mitigation**

## INTRODUCTION

### Motivation

Most landslide hazards occur in mountains (Dai and Lee, 2002). The initiation of a landslide requires three basic ingredients: a steep hillslope, water, and/or an earthquake (Kornei, 2019). Landslide investigations usually involve the integration of remote and ground-based sensing technologies, such as global positioning systems, differential interferometric synthetic aperture radar, electronic distance measurements, inclinometers, and piezometers. Each technique allows the study of specific triggering factors and/or particular physical features to characterize a landslide block in

comparison with nonmoving areas (Perrone et al., 2014). Remote sensing can only provide surface characteristics without subsurface information, whereas direct ground-based approaches can provide subsurface physical, mechanical, and hydraulic properties of a landslide but are limited to a specific point in the subsurface (Petley et al., 2005; Perrone et al., 2014).

*In situ* geophysical techniques can directly or indirectly measure a wide range of physical parameters associated with the lithological, hydrological, and geotechnical characteristics of terrains relevant to landslide processes (Perrone et al., 2014). The advantage of these techniques is that they are less invasive than most ground-based geotechnical sensing technologies. For example, electrical resistivity tomography (ERT) can provide information concerning a greater volume of the subsurface, therefore overcoming the point-scale feature of classic geotechnical measurements, and has increasingly been applied to landslide investigations (Jongmans and Garambois, 2007; Perrone et al., 2014). The time-lapse ERT can provide images of the subsurface electrical resistivity distribution at different times, allowing investigations of spatial and temporal variations in geological structures.

The ERT measurement is sensitive to subsurface material properties such as the nature of the electrolyte, porosity, water saturation, and salinity (Oldenborger et al., 2007; Chiang et al., 2010; Cassiani et al., 2015; Chiang et al., 2015) and has widely been used to investigate petroleum, mineral, and aquifer resources, as well as for environmental engineering studies (e.g., Daily et al., 1992; Maillol et al., 1999; Chambers et al., 2007; Tang et al., 2007; Descloitres et al., 2008; Muller et al., 2010; Yeh et al., 2015; Zhang et al., 2018). Water saturation in the bedrock or colluvium is highly related to most landslide hazards occurrences, and rainfall is likely a crucial factor (Crosta, 1998). Additionally, changes in groundwater content and consequent increases in the pore water pressure can play one of the important roles in the triggering mechanisms of landslides (Bishop, 1960; Morgenstern and Price, 1965; Perrone et al., 2014).

The ERT technique has been applied to landslide investigations being motivated by its high sensitivity to the water saturation within the bedrock and colluvium which is directly affected by rainfall, a sensitive factor causing landslides (e.g., Kuras et al., 2009; Palis et al., 2017). However, traditional campaigned ERT measures an electrical resistivity image once to survey the location of landslide events without including time-space variations and is insufficient to monitor the processes of landslides and their triggering mechanisms in detail. Besides, most landslide disasters in Taiwan happened to the slopes of mountainous roads located away from where could be easily accessible, making it difficult to frequently and repeatedly measure electrical resistivity images. Therefore, an automatic real-time remote resistivity monitoring system is required to investigate the spatiotemporal varying processes of slopes with potential landslide occurrences.

The dynamic processes of onsite rock/soil mechanics could be revealed via monitoring the subsurface properties and relevant parameters using the time-lapse ERT technique. A fully automatic multichannel remote resistivity monitoring system (R2MS) was deployed to acquire hourly electrical resistivity data using a nontraditional hybrid array (*The layout of the electrode and geotechnical monitoring arrays*) in the Lantai area of Yilan Taiping Mountain in Northeast Taiwan which has been identified as a potential landslide area (Lin M. L. et al., 2017) (**Figure 1**). Accordingly, we have presented in this study the long-term variations in electrical resistivity images to investigate the relation between rainfall and landslides in the Lantai area. High-frequency time-lapse ERT monitoring may therefore provide information concerning the collapse mechanisms of landslides and their triggers, thus playing a key role in landslide early warning systems as suggested in this paper.

## Geological Background

Taiwan formed approximately 5 million years ago in a still ongoing collision of tectonic plates (Suppe, 1981; Ho, 1986; Hall, 2002; Chiang et al., 2010) that lifts its young mountains and simultaneously generates innumerable earthquakes, is a densely populated island with 23 million inhabitants, and 70% of its area is mountainous. Its location in the tropical western Pacific Ocean means that typhoons frequently occur in summer, occasionally dropping meters of rain in just a few days. These characteristics of Taiwan make it one of the most landslide-prone countries in the world (Kornei, 2019). Landslides are complex geological phenomena with a high socio-economic impact in terms of loss of lives and damage and have indeed resulted in the loss of several lives and material belongings in Taiwan in recent years. Thus, landslide hazards require attention, including early warning systems and/or monitoring to aid in disaster preparation.

In the Lantai area, the terrain slope studied has an attitude of N29°E/30°E, and is located between the Chingshuihu Member and the Jentse Member of the Lushan formation (**Figure 2**). The geological profile is that the Jentse Member covers the Chingshuihu Member. According to field surveys and core drilling, there is a shear zone between the Jentse Member and the Chingshuihu Member. The lithology of the Lushan formation is composed of thick to massive slates with thin metamorphic sandstone or lenticular metamorphic sandstone, whereas the Chingshuihu Member contains thick black–gray shale with well-developed cleavages. Slates in the Chingshuihe Member is therefore easily eroded. Landslides thus often occur following heavy rainfalls or earthquakes in this steep terrain area (Lin M. L. et al., 2017). After completing the reinforcement works along the road in recent years, the ground deformation has slowed down. However, in the main collapse area (**Figure 1**), the GPS on the ground surface still continuously monitors the downward slope sliding situation. According to the monitoring data below 45 m, the accelerated displacements accompanied by heavy rainfalls or earthquakes had been frequently observed.

# METHODOLOGY AND DATA PROCESSING

## Electrical Resistivity Tomography Method

General ERT prospecting is widely applied to investigate electrical resistivity structures via the controlled injection of an electrical

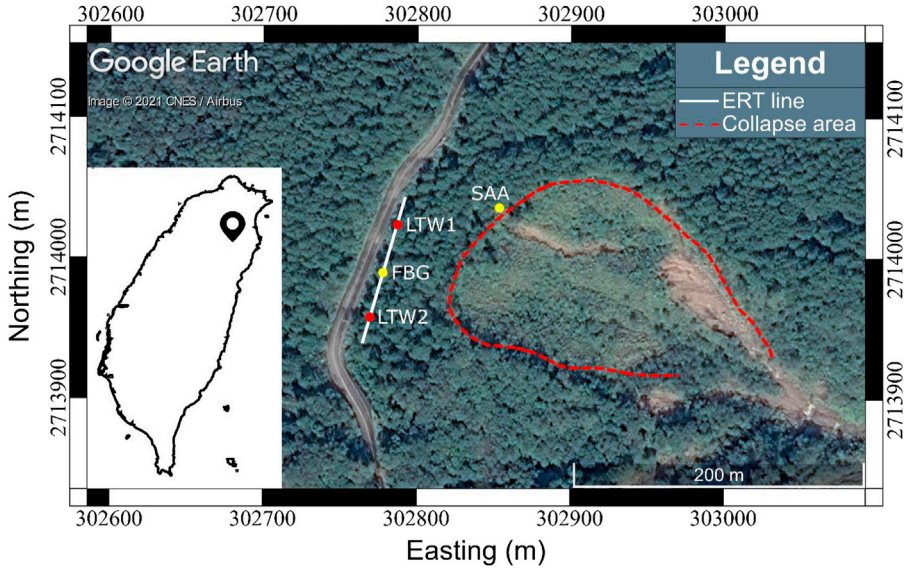


**FIGURE 1 |** Location of the landslide potential area and layout of monitoring boreholes in the study area (modified from Google Earth). LTW1 is the location of an 84-m-deep borehole with ERT electrodes and LTW2 is the location of a 98-m-deep borehole with ERT electrodes and drilling core. SAA is the location of a borehole the shape acceleration array installed at the depths between 71.5 and 81.5 m; and FBG the borehole for the optical fiber Bragg grating pore pressure sensing array installed at the depths of 40, 50, and 60 m. A surface ERT line is also indicated by the white line joining through LTW1 and LTW2.

current into the subsurface and measurements of the potential difference between pairs of electrodes at the surface (AGI, 2009; Hsu et al., 2010; Chiang et al., 2012). The ERT method is based on Ohm's law

$$\Delta V = IR \quad (1)$$

using pairs of current electrodes to inject current (I) into the ground and potential electrodes to measure the potential difference (ΔV) between two arbitrary points within a specified distance (**Figure 3**).

The electrical resistivity ρ is a measurement of the resistance R (=ΔV/I) through a cross-sectional area A with a wire of length l and can be formulated as

$$\rho = RA/l \quad (2)$$

The apparent resistivity $\rho_a$ in ERT can be derived from **Eq. 3**

$$\rho_a = K\Delta V/I \quad (3)$$

where K is a geometric factor associated with the current and potential electrodes layouts. Recent developments in ERT instruments, including the R2MS used in this study, allow automatic switching measurements throughout different pairs of current and potential electrodes in a series of equally spaced distances laid out along surveying lines predefined (AGI, 2009; Hsu et al., 2010; Chang et al., 2012; Wang et al., 2015; Chang et al., 2018; Wang et al., 2020). Versatile instrumentation and electrode configurations enable effective 2D, 3D, and time-lapse ERT measurements. For a detailed description of the well-established ERT technique, we refer the readers to literature and many relevant references we cited.

## The Layout of the Electrode and Geotechnical Monitoring Arrays

On the Lantai slope, several monitoring boreholes were drilled. They include the shape acceleration array (SAA), optical fiber Bragg grating (FBG) underground water pore pressure sensing array, two vertical linear arrays of electrodes in boreholes LTW1 and LTW2 (**Figure 1**). We will later describe the installation of the FBG pore pressure array in the following *Hydrological water tank model for underground water*

The SAA is a string of rigid segments separated by flexible joints. In each segment, it has a micro-electro-mechanical sensors system, which can measure the tilt angle relative to gravity's direction and then convert the tilt angle into horizontal displacement by utilizing the triangular formula. We utilized the SAA to monitor the subsurface deformation by installing it into the borehole, labeled as SAA in **Figure 1**, at the depths from 71.5 to 81.5 m. The total length of SAA utilized is 10 m with the length of each segment is 0.5 m. The SAA installation depth normally depends on the borehole digging conditions and, in our case, was also judged from daily drilling log photos. The drilling jammed at the depths around 79 m and then showed intact rock after that. The drilling log photos furthermore illustrate fracture zones at the depths between 78 m and 80 m.

There are 16 and 18 electrodes installed in LTW1 and LTW2, respectively, whereas all electrodes are separated by 5 m. Additionally, on the joining line through LTW1 and LTW2, a linear array of 28 electrodes separated by 4 m has been installed on the surface (**Figure 3**). The total length of the surface ERT line was 108 m, and the depths of LTW1 and LTW2 were 84 and 98 m, respectively. The mixture electrode arrays were installed on the surface and in two boreholes to enhance the resolution of the

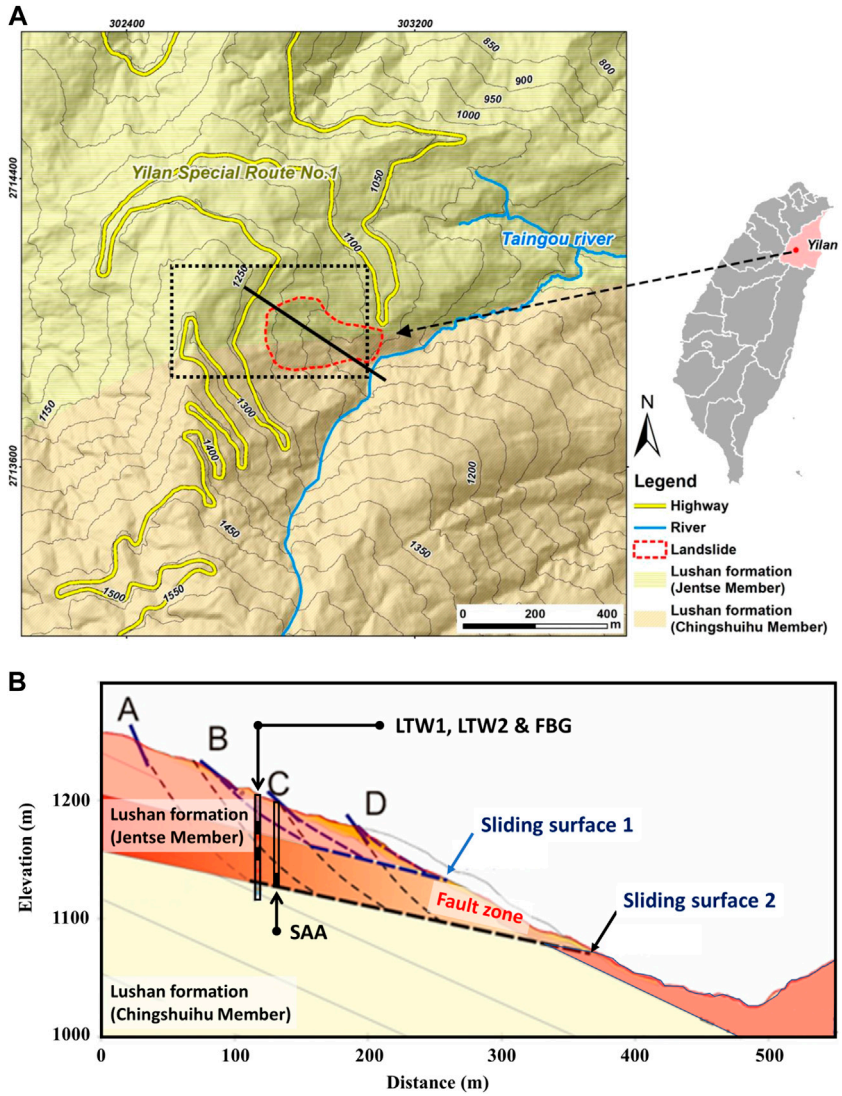


**FIGURE 2 |** Geological map **(A)**, together with a geological cross-section **(B)**, in the Lantai area, Yilan Taiping Mountain, Northeast Taiwan. A-D was identified as four landslide scarps. The black line in the geological map denotes the location of the geological cross-section and the dotted rectangle shows the area in **Figure 1**.

electrical resistivity images in deep. According to field investigation and numerical simulation of slope stability, the studied slope could have different sliding surfaces distributed at various depths. Sliding surfaces below 45 m could exist as above mentioned in *Geological background* and deeper than 100 m not that active. Also considering the budget plan, this study therefore targets at the monitoring of physical properties of the slope body shallower than 100 m.

In those surface and borehole electrode arrays, the electrodes are arranged in an alternating way with part of the electrodes used for the electric current injections and the others for the electric potential measurements. When measuring electric potentials, one of the electrodes is selected as a common reference electric potential $P_0$ such that the electric potentials can be obtained as the potential differences between $P_0$ and other potential electrodes $P_i$ (**Figure 3**). Consequently, the potential differences between every pair of potential electrodes can be estimated. With such electrode arrangement, named as the nontraditional hybrid array, conventional dipole-dipole, Wenner, Wenner-Schlumberger data, together with other four-pole data, can all be collected in a single measurement.

## Data Acquisition and Processing

The electrical resistivity measurements were performed six times per day before July 2020. Then, for reducing the cost of lightning striking damage, the measurements were shrunk to two times per day, at 04:00 and 20:00, after July 2020. **Figure 4** shows a chart of the electrical resistivity data process. The variations in the electrical resistivity data were strongly affected by rainfall; thus, for comparison in multiple ERT images, selecting a

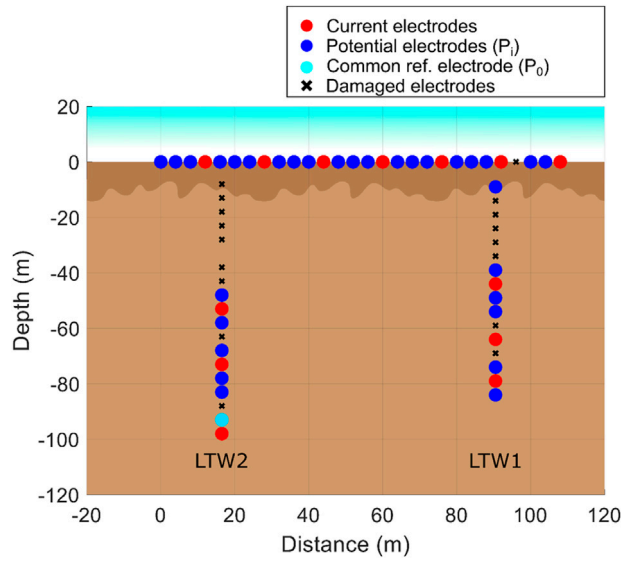


**FIGURE 3 |** Schematics of the surface and borehole ERT electrodes used in this study. Some electrodes (in cross symbols) were damaged by the lightning strikes. For the details on the electrode array, please refer to *The layout of the electrode and geotechnical monitoring arrays*.

current-potential electrodes, and median ($\vec{Obs}$) indicates the median of the N measured resistivities.

After evaluating the data quality from July 7 to 12, 2020, we selected the best 30,000 data points among ~180,000. We used the 2D inversion software EarthImager 2D developed by Advanced Geosciences Inc., United States (AGI, 2009). For dealing with the computing memory shortage, also benefiting from our extremely large amount of resistance data, we then randomly selected 20 subsets from the data population, each of which contains 6,000 data points. These 20 groups used the same parameters for the 2D inversions. The inversion procedure includes 1) fitness examination by using the root-mean-square (RMS) errors, 2) removals of the worst 5% resistance data with large RMS errors, and 3) repeated 2D inversion. The RMS error (AGI, 2009) is given by

$$x_i = \frac{\rho_i^{meas} - \rho_i^{pred}}{\rho_i^{meas}} \tag{5}$$

and

$$RMS = \sqrt{\frac{\sum_{i=1}^{N} x_i^2}{N}} * 100\% \tag{6}$$

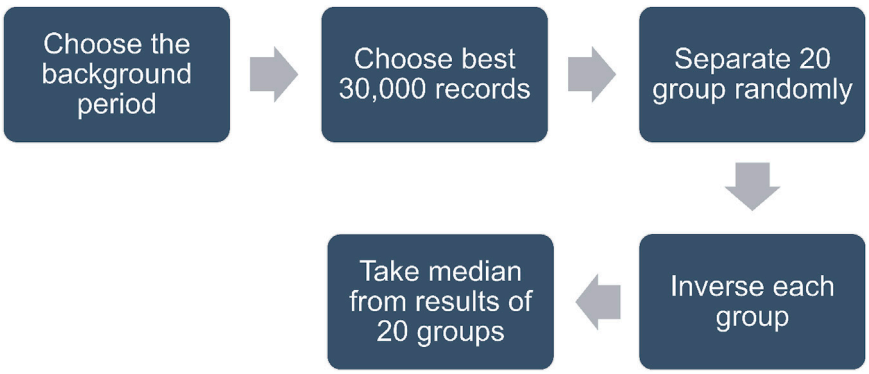


**FIGURE 4 |** Flow chart of the processing procedure of our massive ERT data. For the details on ERT data processing, please refer to *Data acquisition and processing*.

background period in the electrical resistivity data not affected by rainfall was necessary. We, therefore, select electrode pairs with high reproducibility as the stable background data. **Eq. 4** was used to evaluate the quality (reproducibility) of the resistance data collected overall electrode pairs, where low $\vec{Q}$ values indicate high-quality data:

$$\vec{Q} = \left| \sqrt{\sum_{i=1}^{N} \frac{\left(\vec{Obs}_i - \text{median}\left(\vec{Obs}\right)\right)^2}{N-1} * \frac{100}{\text{median}\left(\vec{Obs}\right)}} \right| \tag{4}$$

N is the number of measurements selected in the background period; $\vec{Obs}_i$ denotes the measured resistances for every pair of

Here, $\rho_i^{means}$ indicates the measured apparent resistivity, $\rho_i^{pred}$ indicates the inverted apparent resistivity, and N indicates the number of measurements. This procedure was repeated four times and could obtain a reasonable inverted image of the subsurface electrical structure for each subset. Having 20 inverted electrical images we took their median as the final ERT snapshot at each different time.

## Relative Water Saturation Estimation

Archie's (1942) law was applied to evaluate the water saturation:

$$\rho = a\phi^{-m} S_w^{-n} \rho_w \tag{7}$$

where ρ is the resistivity of the rock, a is the tortuosity factor, Φ is the porosity of the rock, m is the cementation coefficient, $S_w$ is the

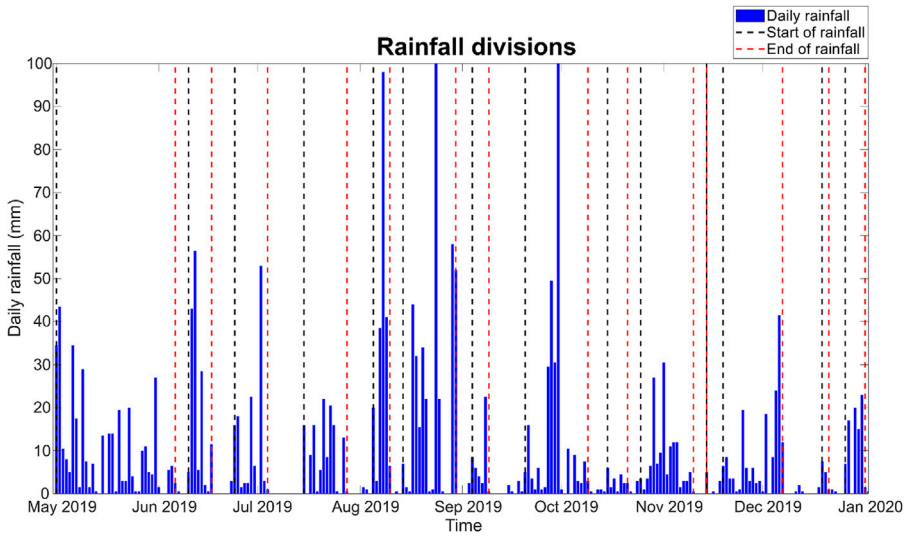


**FIGURE 5 |** Rainfall classifications following the definitions described in *Rainfall divisions defined in this study*. All rainfall events are also listed in **Table 1**.

water saturation, n is the saturation exponent, and $\rho_w$ is the water resistivity. The drilled core (Lin M. L. et al., 2017) revealed that most of the formations in the study area contain slate and that clay minerals can be ignored. Following Zhang et al. (2016), the relative water saturation (RWS) was defined as

$$RWS^{k,t2,\,t1} = \frac{\Delta S_w^{k,\,t2,t1}}{S_w^{k,\,t1}} = \frac{S_w^{k,\,t2} - S_w^{k,\,t1}}{S_w^{k,\,t1}} \tag{8}$$

where $S_w^{k,\,t1}$ is the degree of water saturation at the k-th mesh for time t1 and $S_w^{k,\,t2}$ for time t2, and $RWS^{k,\,t2,t1}$ indicates water saturation changes in percentage between the 2 days t1 and t2. **Eq. 7** can be then substituted into **Eq. 8** such that

$$RWS^{k,\,t1} = \left(\frac{\rho^{k,\,t2}}{\rho^{k,\,t1}}\right)^{-\frac{1}{n}} - 1 \tag{9}$$

where n is the saturation exponent and indicates the resistance ratio in porous water (Zhang et al., 2016). We had assumed that the tortuosity, cementation factors, rock porosity, and water resistivity do not change over short time scales in the order of tens of days and used n = 2.0 in this study to discuss the tendencies of the variations of RWS instead of its absolute values.

## Rainfall Classifications Defined in This Study

Relations between the characteristics of rainfalls and the consequential landslides are often identified in landslide studies for early-warning thresholds. Most landslide studies have used precipitation magnitude and duration as parameters in the early warning system. Guzzetti et al. (2007) integrated from previous studies 25 parameters involving the duration and amount of rainfall events to define early warning signals for different rainfall scenarios. Segoni et al. (2018) suggested that landslide triggering factors could be statistically divided into three types: 1) rainfall intensity-duration curves (48.6%), 2) antecedent rainfall (26.8%), and 3) the accumulated rainfall and its duration (15.9%). Iverson (2000) simplified the Richards equation to evaluate the effect of rain infiltration on landslides at different time scales. However, relations between rainfall parameters and their warning levels are still controversial, and dividing rainfall events has remained an important scientific issue in the successful prediction of landslide occurrences.

This study is not aimed at the discussion of rainfall events and their classifications for the prediction of landslide occurrences. The rainfall classification here serves mainly as the baseline to calculate the variations in the time-lapse ERT images, to investigate the preferential areas to different extents for groundwater transport. We defined rainfall classifications using precipitation data from the Central Weather Bureau. The precipitation station was located approximately 400 m from the study area. Referring to Chen et al. (2005) and

**TABLE 1 |** Classifications of the rainfall events. The two events in red were selected for the case study.

| Index | Start_Time | End_Time | Accum_rainfall (mm) | Duration (day) |
|---|---|---|---|---|
| a | 2019/5/1 | 2019/6/6 | 366.5 | 37 |
| b | 2019//6/10 | 2019/6/17 | 152.5 | 8 |
| c | 2019/6/24 | 2019/7/4 | 126.5 | 11 |
| d | 2019/7/25 | 2019/7/28 | 128 | 14 |
| e | 2019/8/5 | 2019/8/10 | 207 | 6 |
| f | 2019/8/14 | 2019/8/30 | 443 | 17 |
| g | 2019/9/4 | 2019/9/9 | 44 | 6 |
| h | 2019/9/20 | 2019/10/9 | 416 | 20 |
| i | 2019/10/15 | 2019/10/21 | 21 | 7 |
| j | 2019/10/25 | 2019/11/10 | 141 | 17 |
| k | 2019/11/14 | 2019/11/14 | 5 | 1 |
| l | 2019/11/19 | 2019/12/7 | 168.5 | 19 |
| m | 2019/12/19 | 2019/12/21 | 13.5 | 3 |
| n | 2019/12/26 | 2020/1/1 | 83.5 | 7 |

Melillo et al. (2015), the definitions are as follows: 1) a null rainfall is defined as 48 h of continuous rainfall of less than 4 mm, 2) a dry event is defined as over 72 h without precipitation, and 3) the starting and ending time of rainfall periods are determined according to the dry events. **Figure 5** shows a schematic diagram of the rainfall classifications following these definitions, and **Table 1** shows a schematic diagram of the rainfall classifications following these definitions, and **Table 1** shows the rainfall classification durations in 2019. Rainfall events of less than and more than 10 days are referred to as short- and long-duration precipitation events, respectively. We have selected two exemplary cases from the rainfall classifications corresponding to one long-duration and one short-duration precipitation event to examine the variations in their electrical resistivity images with time and at different spatial scales.

## Hydrological Water Tank Model for Underground Water

Installed alongside the ERT array, there is a linear array of the optical fiber Bragg grating (FBG) sensors for monitoring the underground pore water pressure. The design, instrumentation, and principles of the sensing technique are referred to by Huang et al. (2012). In the Lantai site, the array is installed in the FBG borehole shown in **Figure 1**. There are three serially connected working sensors at 40, 50, and 60 m, respectively, and their pressure sensing range is 400 kPa. The minimum gap distance was suggested to be longer than a couple of meters and 5 m was suggested in Huang, et al. (2012). For the FBG borehole, further drilling beyond 70 m became impossible because the drill head was frequently clamped by the surrounding hard fractured rocks. This condition may cause collapses of the borehole during sensor installation so that the drilling was halted. For the shallower installation, it may be above the underground water table and unsaturated so the reading of the sensor could be not trustable. Between the sensors, bentonite water sealing was realized to prevent direct water flows along the borehole and to ensure that the sensors correctly sense the pore water pressure at their depths in the aquifer. The raw data of the FBG sensing technique, after signal processing and digitalization of the FBG interrogators, are optical wavelengths, which are linearly proportional to the pore water pressure and the conversion factor is about 1 pm (wavelength) to 400 Pa, somewhat depending on the individual characteristics of the pressure sensor. The variation of the wavelength corresponds to the change of the spacing of the Bragg grating that is implemented in the optical fiber. The entire optical FBG system operates in the infrared wavelength range, about 1,450–1,600 nm. Inspecting the raw data of the three sensors, we found that the readings at 40 m had faster and occasionally daily responses, implying that this depth was probably about the underground water level and this confirms with the observation during the borehole drilling. On the other hand, the readings at 50 and 60 m are similar, indicating that they are likely in an aquifer with comparable material properties.

To compare the water content with the inverted electrical resistivity data, a semi-quantitative hydrological model is applied to map the FBG pore pressure data, taken at fixed positions, onto

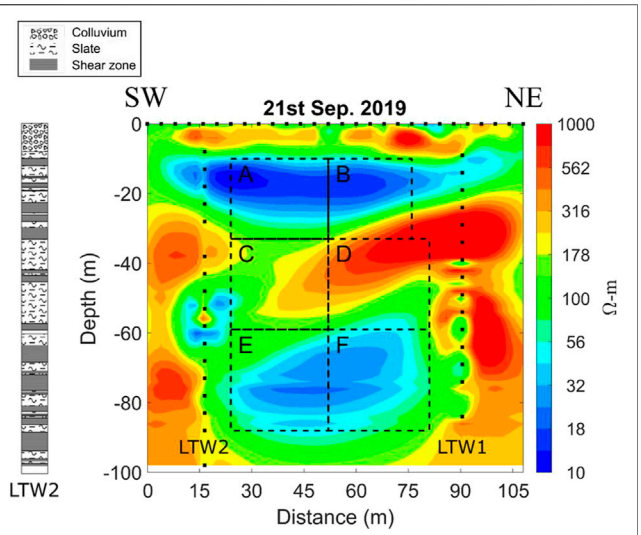


**FIGURE 6 |** Cross-section of the electrical resistivity image and its subzones. The ERT image was divided into six subzones A-F, according to the depths and the resistivity values, for discussing in the text the details of the resistivity and RWS variations caused by rainfall events. For the depths, Zones A and B are shallower than 30 m; Zones C and D from 30 to 60 m; and Zones E and F deeper than 60 m. The lower resistivity values with several tens of ohm-meters appear in Zones A, B, E, and F while Zones C and D have the higher resistivity values with several hundreds of ohm-meters. The lithology column was also carefully registered from the drill core at the borehole of LTW2 (modified from Lin M. L. et al., 2017). Comparison with the lithology column of LTW2 suggests that the resistive Zones C and D may be associated with those more intact slate formations in the depths between 30 and 60 m.

the effective underground water contents into a few representative layers. The main purpose of the hydrological model is to infer the water content in the layer above 40 m wherein it is usually not saturated and, to our knowledge, there is yet no long-term reliable technique available for direct measuring either the water content or pore water pressure.

The hydrological model used in this study is a simplified tank model. The model is used to simulate the rainfall-infiltration-runoff relations based on a series of hypothetically connected water tanks (Nash, 1957). There are many variants of the conceptual model, for example, a three serially connected tank model (Sugawara, 1961). The present tank model, on the other hand, is a simplified version with which contains two serially connected tanks (Lin S. E. et al., 2017; Kuo et al., 2021). In the model rainfall is the only input of water to the tanks. The water depth in the upper tank phenomenologically describes the water storage in the shallower layer of the unit landslide area and the lower tank is for the water storage in the deeper layer. The outflows of each tank are assumed linearly correlated with the depths of the water tanks. In total 12 parameters are to be determined in the model calibration process and the shuffled complex evolution scheme (SCE-UA, Duan et al., 1994) is applied for their calibration. In the process, the calibration target is to minimize the difference between the 60 m FBG pore pressure readings and the conceptual water depth of the second tank. This target function implies that the pressure measured at this depth is

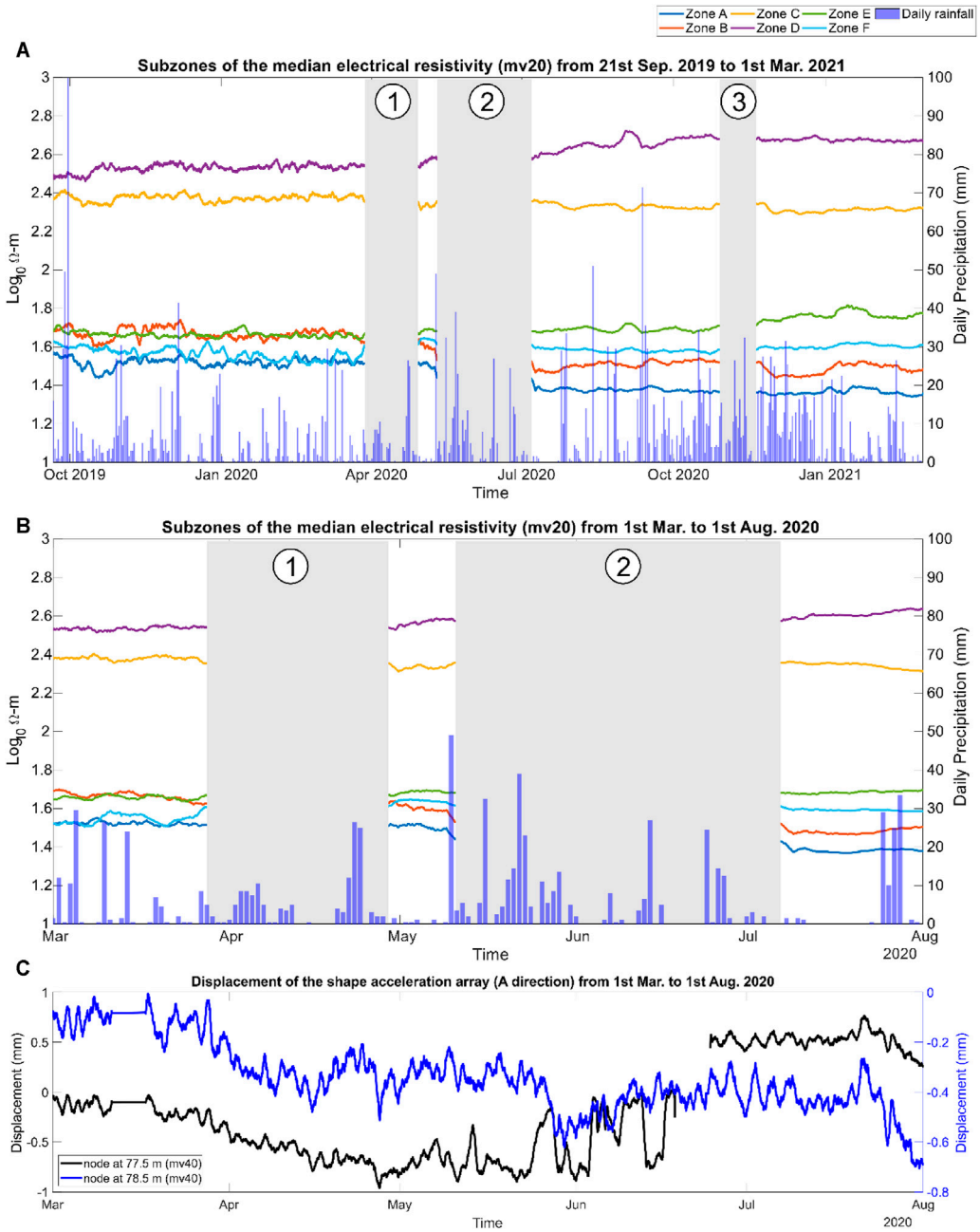


**FIGURE 7 |** Time series of the median electrical resistivity (MEER) curves overlaid with the daily rainfall data. **(A)** Moving average of 20 measurements (mv20) of the MEER curves from 21 Sept 2019 to Mar 1, 2021. The dark blue line indicates Zone A, the orange line for Zone B, the yellow line Zone C, the purple line Zone D, the green line Zone E, and the light blue line for Zone F. Three gray zones labeled with Numbers 1-3 represent three periods when ERT measurements were interrupted due to the R2MS system damages caused by lightning strikes. **(B)** A zoom-in for the MEER curves from Mar 1 to Aug 1, 2020, to compare with the SAA data. **(C)** Horizontal displacement at the depths of 77.5 and 78.5 m is estimated from the SAA data.

associated with the water storage in the deeper layer (the second tank). Without digressing into the calibration details, the explicit mathematical form of the target function, rainfall, and sensor data as well as the calibration results are relegated to the Supplementary Materials of the paper. From the former description on the pore pressure of the three depths, the referred deeper layer is likely to be below about 40 m. Nevertheless, because of the qualitative feature of the model, we cannot exactly specify the dividing depth between the deep and shallow layers but expect that it is in a vague range above 40 m. In *Discussions*, the depths of the individual tank, assumed in proportion to the water contents in the aquifer layers, are compared with the alternation of the electrical structures of the ERT images. For the full description and calibration results for

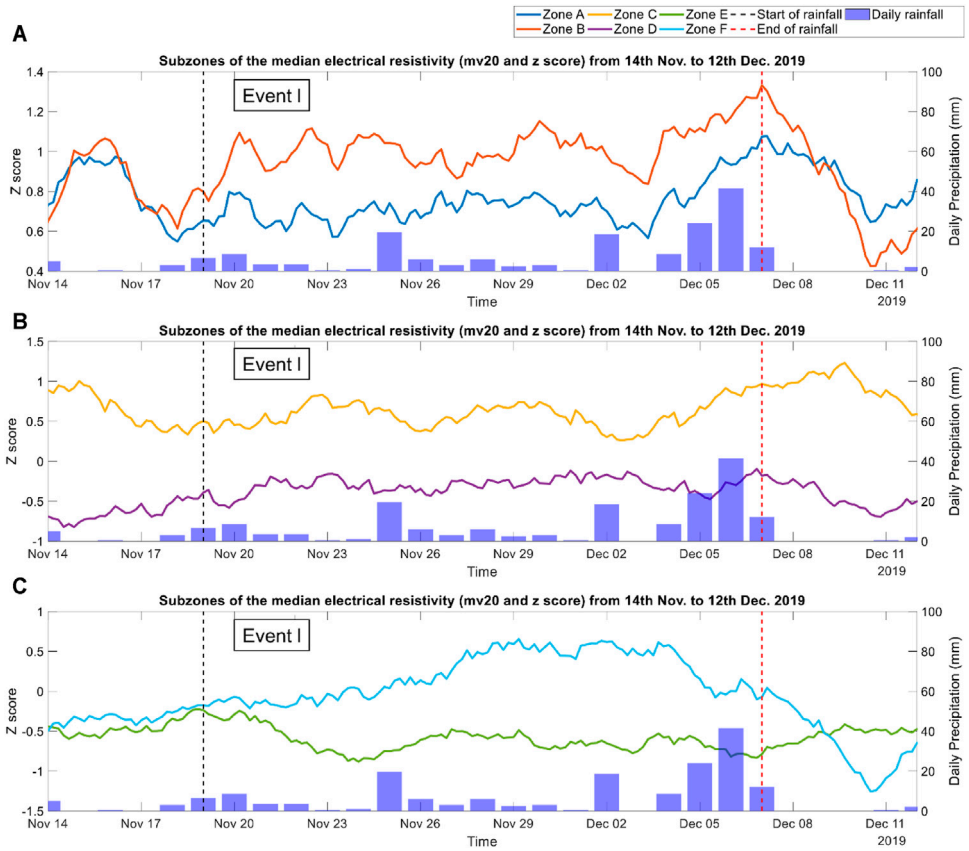


**FIGURE 8 |** Standard score, i.e., Z-score, in statistics of the median electrical resistivity (MEER) time series for the long-duration precipitation event (Event I). Moving average for 20 measurements (mv20) of the MEER curves: **(A)** Zones A and B, **(B)** Zones C and D, and **(C)** Zones E and F.

the temporal period in the present paper, please refer to the **Supplementary Materials**.

# RESULTS

## Electrical Resistivity Images and the Drill Core

**Figure 6** shows the cross-section of an electrical resistivity image obtained on 21 Sept 2019, as an example, together with the drill core extracted from the borehole of LTW2. The top soil/colluvium layer can be seen between the surface and depths of 10 m and corresponds to the red-orange-yellow colors indicating high resistivity larger than 200 Ω-m. As suggested by the drill core, the depths of 10–30 and 60–100 m are fracture zones of slate formations and correspond to the blue-light blue colors indicating low resistivity less than 50 Ω-m. The depth of 30–60 m is likely associated with a compact slate formation and corresponds to the red-orange-yellow colors with, again, high resistivity larger than 200 Ω-m. The layered structure of the electrical resistivity image looks consistent with the drill core showing more details though. The ERT image was divided into six subzones (**Figure 6**) to discuss in the following sections the details of changes caused by rainfall events. The lowest resistivity appears in zone A, and the resistivity of zone B is similar to that of zone A at the same depths shallower than 30 m. Zones C and D have higher resistivity, which may be associated with those more intact slate formations implying that the hydraulic conductivity may be lower in the depths between 30 and 60 m. Zones E and F, with depths deeper than 60 m, have low resistivity features again. With the ERT images, we can focus on the spatiotemporal variations of the slate formation below the top soil/colluvium layer in the cross-section of the electrical resistivity image.

## Subzones of the Median Electrical Resistivity

Although the R2MS was several times struck by lightning during rainy days, the long-term variations in electrical resistivity have reliably shown smooth changes over time. **Figure 7** presents the median electrical resistivity (MEER) of those subzones abovementioned, together with the daily rainfalls and the horizontal displacements measured by the SAA. We have taken the median value of electrical resistivities in model meshes within each subzone as the representative electrical resistivity to elucidate the temporal variations. Note that the MEER curves show slightly high roughness before July 2020,

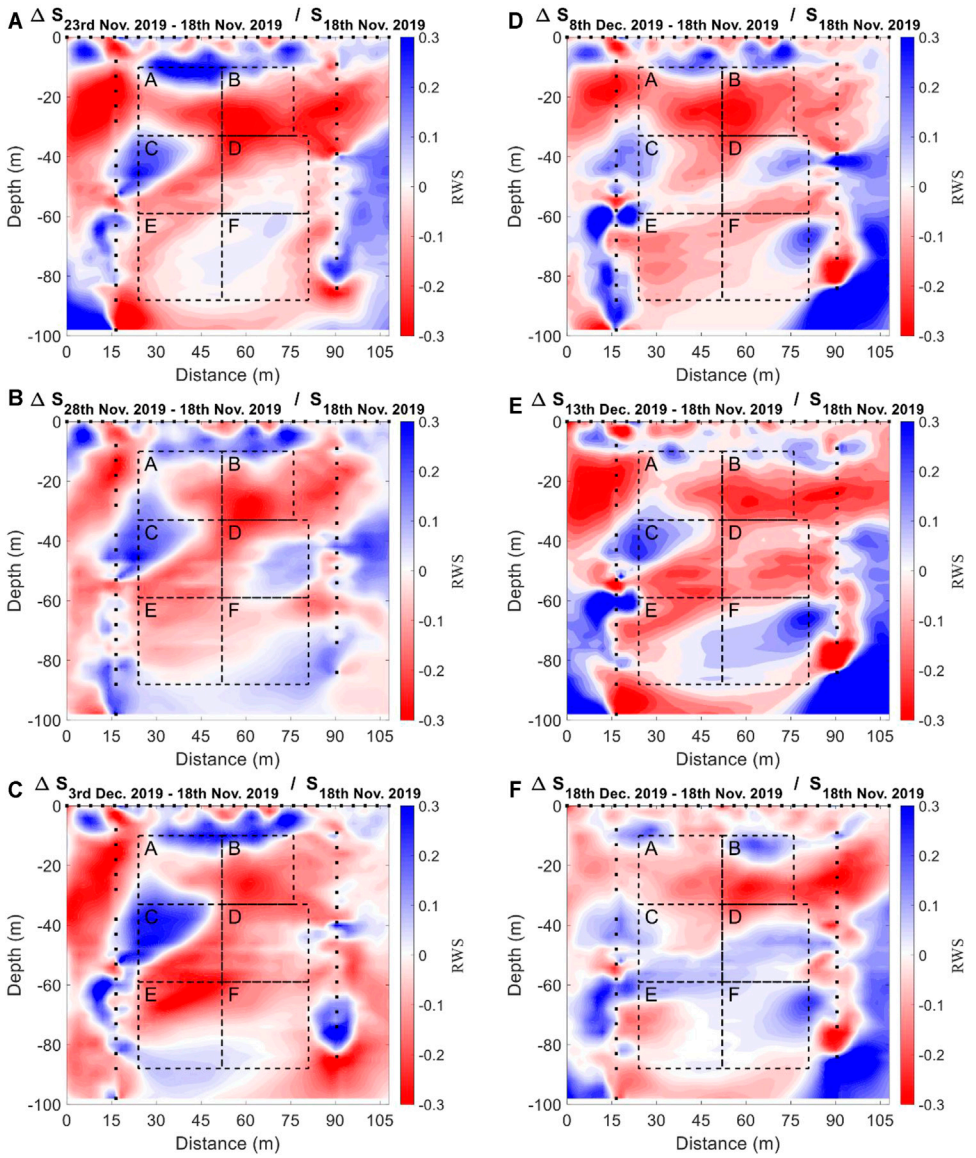


**FIGURE 9 |** Cross-section of the relative water saturation (RWS) for the long-duration precipitation event based on the map for November 18, 2019, after **(A)** 5 days, **(B)** 10 days, **(C)** 15 days, **(D)** 20 days, **(E)** 25 days, and **(F)** 30 days. Blue shows increasing RWS estimated from the decreases in the electrical resistivities, whereas red shows decreasing RWS because of the resistivity increases.

reflecting more frequent measurements taken in the early stage of this study. Overall, the MEER values show highly stable electrical resistivity measurements; it is also clear (**Figure 7A**) that, after July 2020, the MEER values decrease in zones A, B, and C, increase in zones D and E, and are steady in zone F. More detailed changes in electrical resistivity in terms of space will be discussed in *Electrical resistivity changes due to the sliding event in summer 2020*.

Based on the fact that the MEER values in zones A and B exhibited extreme decreases and that of zone D increased after July 2020, and that those MEER changes look unrecoverable, we assume a small sliding event in summer 2020. Also, according to the SAA records at two different depths (**Figure 7C**), the displacement shows a gradually decreasing/creeping tendency from March through July at the depth of 78.5 m and a discontinuous decreasing trend starting from May following by an abrupt 1-mm jump close to the end of June at the depth of 77.5 m. The SAA data suggests that two different creeping units originally located at two depths of 77.5 and 78.5 m were likely tied together after that suspected event occurred at the end of June. Therefore, the SAA displacements show identical fluctuations at those two depths after June (**Figure 7C**).

In addition, the short-term MEER variations at different depths in **Figure 7A** are likely related to rain infiltration. This is discussed in more detail using RWS in *Case study*.

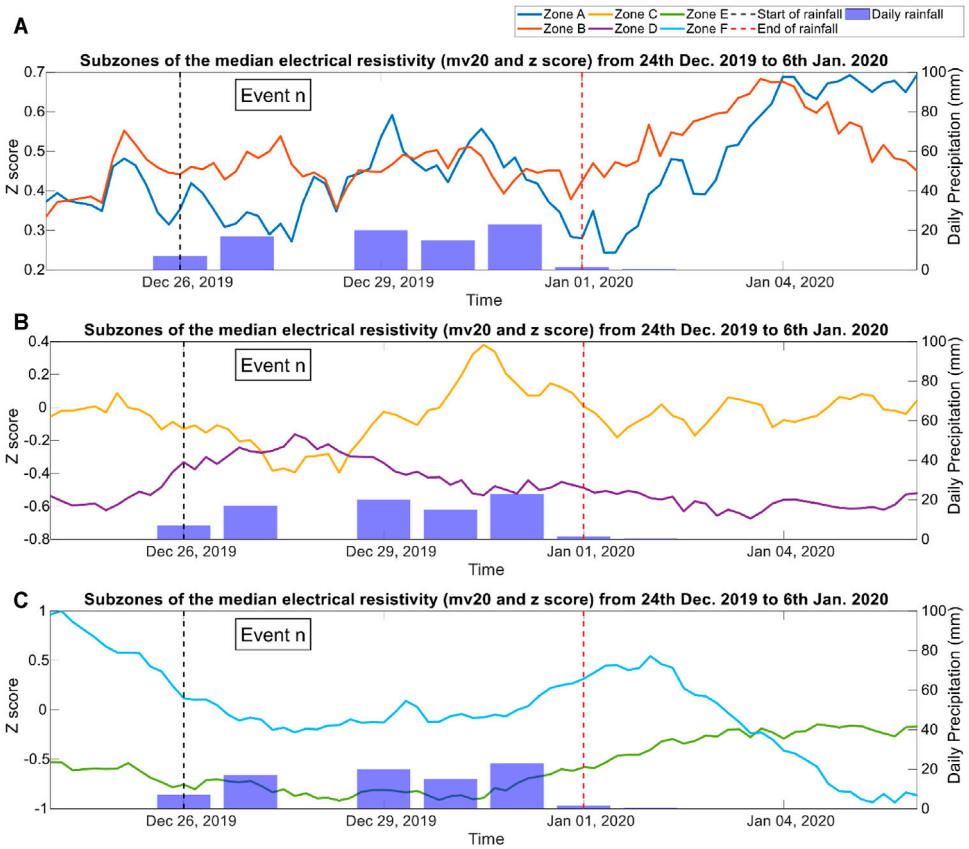


**FIGURE 10 |** Z-score of the MEER time series for the short-duration precipitation event (Event *n*). Moving average for 20 measurements of the MEER curves: **(A)** Zones A and B, **(B)** Zones C and D, and **(C)** Zones E and F.

## Case Study

In the following, we calculated the standard score, i.e., Z score, in statistics of the MEER values and the estimated RWS for two cases, one long-duration (Event l) and one short-duration (Event *n*) precipitation event in **Table 1**. The RWS calculations used reference ERT images from November 18 and December 25, 2019, for the long- and short-duration precipitation events, respectively.

### Long-Duration Precipitation (Event l)

**Figures 8A,B** show similar MEER tendencies in zones A, B, and C for the long-duration precipitation (Event l in **Table 1**), where the MEER values increase with the precipitation and decrease with the end of the rainfall event. This feature indicates that the delayed electrical resistivity variations are likely related to the rainfall. The delayed time in zone C is the longest and is associated with the compact slate formation, as demonstrated by the drill core.

**Figure 9** shows the 5-days interval of the RWS values of the cross-sectional images and illustrates more detailed spatial structures of the electrical resistivity variations linked to water saturation for the long-duration precipitation Event l. RWS increases in the top soil/colluvium layer above zones A and B at the depth around 10 m and the near-surface RWS-increased zone is distributed over a horizontally wide spatial area (**Figures 9A–D**); then, RWS decreases with the end of the rainfall event and returns to its dry status (**Figures 9E,F**). The RWS distribution in the upper left corner of zone C at a depth of 30–50 m strikingly increases with the rainfall (**Figures 9A–D**). This was identified as a fracture zone according to the drill core, implying a superior channel for fluid. On the other hand, the RWS variations in zones D, E, and F show relatively slow increases after the rainfall (**Figures 9E,F**), implying that the formations wherein caused the precipitation infiltration to be delayed or that fluids in those zones were dominated by upstream groundwater.

### Short-Duration Precipitation (Event *n*)

**Figure 10** shows the standard scored MEER values for the short-duration precipitation event (Event *n* in **Table 1**). Zones A and C (**Figures 10A,B**) show similar MEER tendencies in three stages: a delayed decrease at the start of the rainfall event from Dec 26 to Dec 28, a first increase from Dec 28 to Dec 30, and then decrease from Dec 30 to Jan 1 during the rainfall event, and an increase after the end of the rainfall event from Jan 1 to Jan 8. The differences in the MEER variations between the long- and short-duration precipitation events might indicate the existence of different types of rainfall infiltration processes in this study

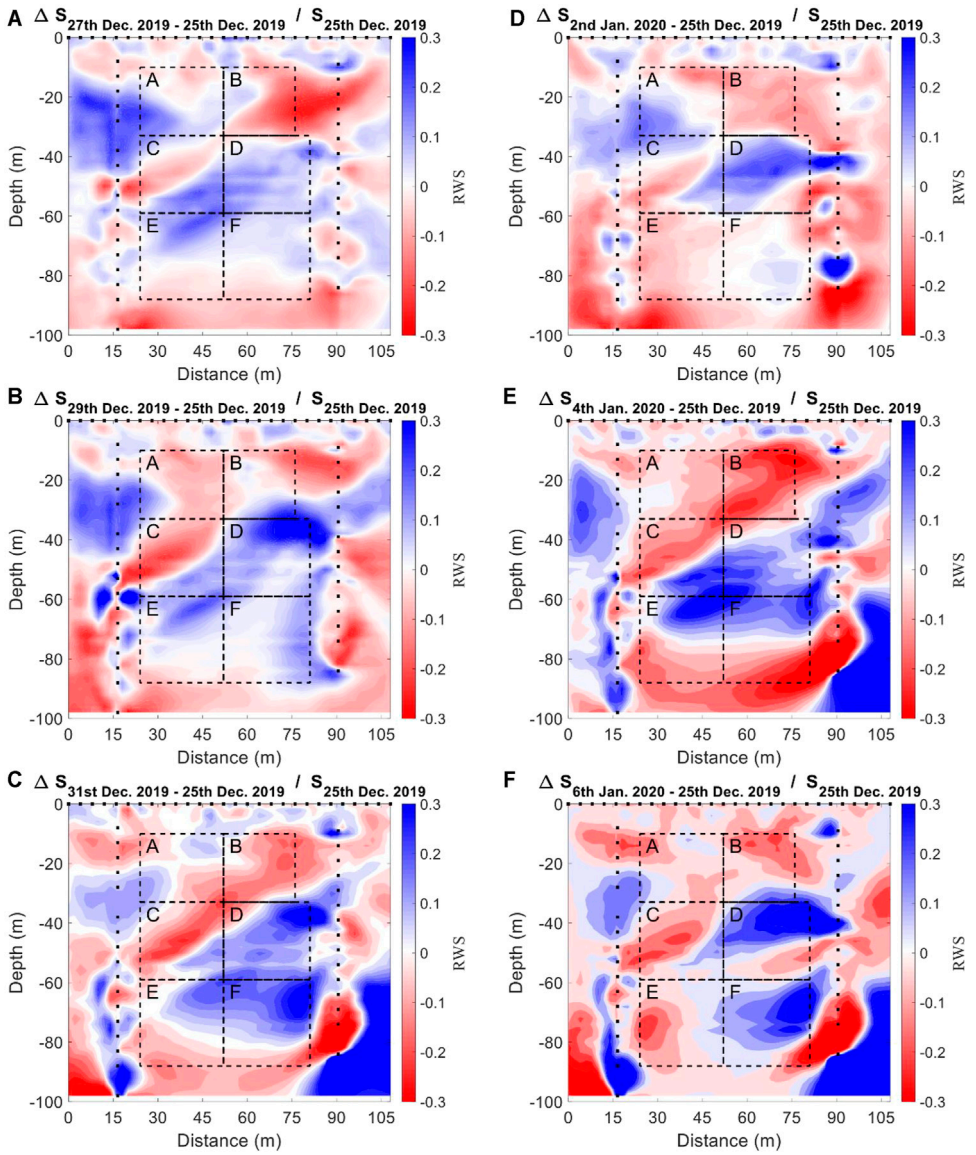


**FIGURE 11 |** Cross-section of RWS for the short-duration precipitation event (Event *n*) based on the map for 04:00 on December 25, 2019, after **(A)** 2 days, **(B)** 4 days, **(C)** 6 days, **(D)** 8 days, **(E)** 10 days, and **(F)** 12 days. Blue shows increasing RWS, whereas red shows decreasing RWS.

area. However, the mechanism causing this difference is still uncertain and requires further exploration.

**Figure 11** shows the 2-days interval of the RWS values of the cross-sectional images illustrating that the spatial electrical resistivity variations were linked to the water saturation for the short-duration precipitation Event n. RWS again increased in the top soil/colluvium layer above zones A and B and, compared with Event l, this near-surface RWS-increased zone was distributed over a relatively small spatial area (**Figures 11A–D**); RWS then slightly decreased with the end of the rainfall event (**Figures 11E,F**). The accumulated rainfall and daily rainfall in Event l were twice those in Event *n*. However, the RWS variations in zones D, E, and F were relatively larger in the short-duration event than in the long-duration event during the rainfall events and after the end of the rainfall periods, which is interesting. The deeper zones, D, E, and F, may not be able to significantly decrease their electrical resistivity with less rainfall, implying again that these deep, high RWS signals may have been affected by upstream groundwater brought in the early precipitation events.

# DISCUSSIONS

## Electrical Resistivity Changes due to Water Storages

A water tank model is a simple half-quantitative hydraulic model (Sugawara, 1961) that divides geologic materials into

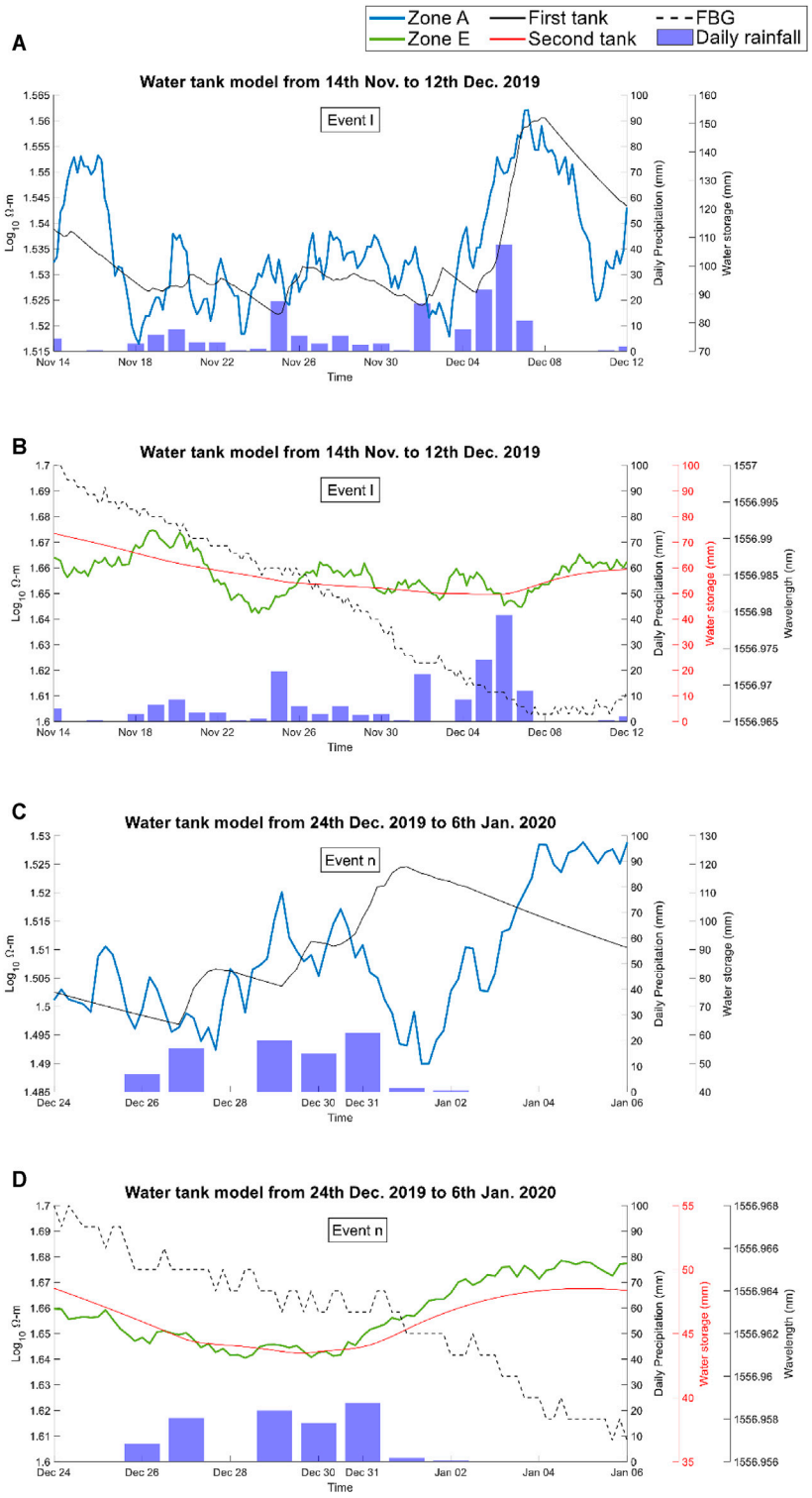


**FIGURE 12 |** Comparison of the Z-score of the MEER time series, water tank model, and fiber Bragg grating sensor array (FBG) for the long-duration (Event l) and short-duration (Event *n*) precipitation events. The moving average for 20 measurements of the MEER curves. Event l: **(A)** Zone A and first tank model; **(B)** Zone E, second tank model, and the FBG. Event *n*: **(C)** Zone A and first tank; **(D)** Zone E, second tank model, and the FBG. Note that the shallower Zone A could be correlated with the shallower, first tank whereas the deeper Zone E with the deeper, second tank. The discrepancy between the MEER and the first curves in (c) for the short-duration Event *n* may imply the complexity of geological material in response to the magnitude of rainfall infiltration.

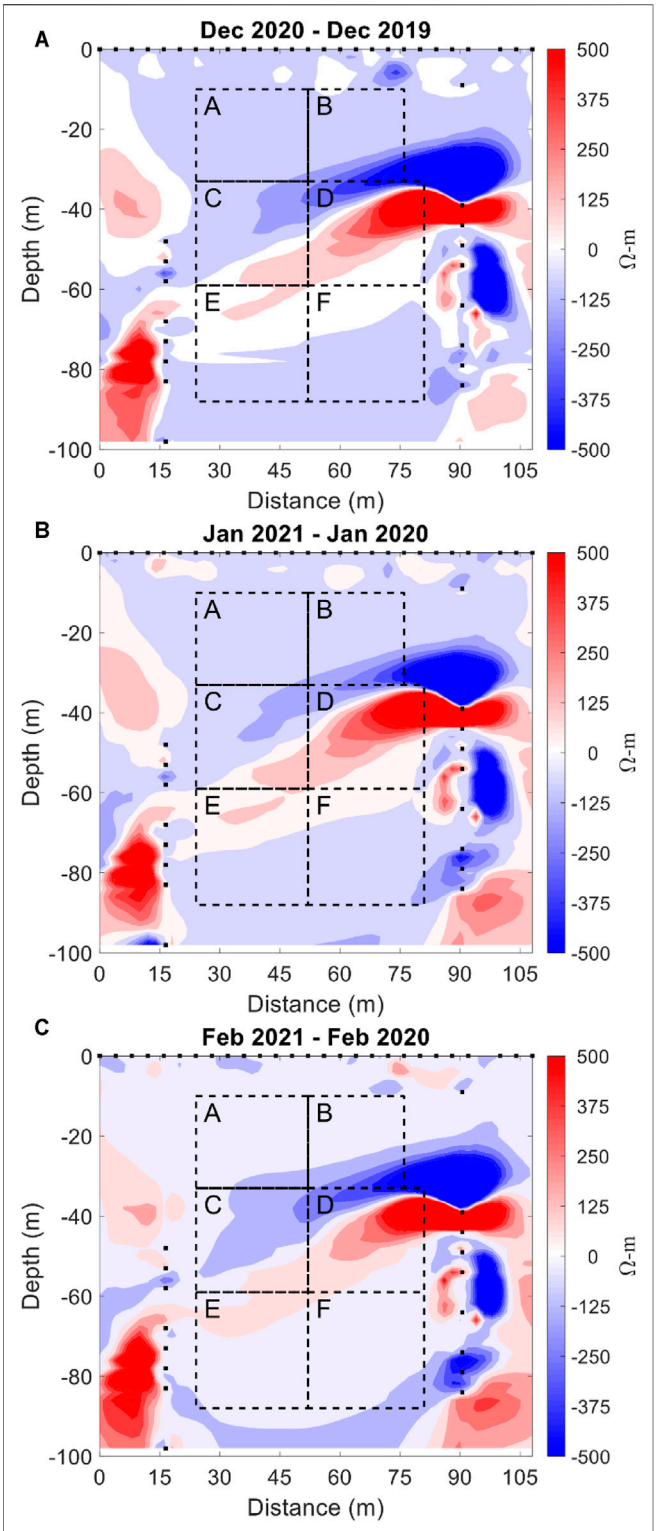


**FIGURE 13 |** Comparison of the electrical resistivity images for the months before and after a suspected creeping event. Differences in the electrical resistivity **(A)** between December 2019 and 2020, **(B)** between January 2020 and 2021, and **(C)** between February 2020 and 2021. For details please refer to the explanation in *Electrical resistivity changes due to the sliding event in summer 2020*.

multiple water tanks to model linear rainfall infiltration and runoff processes (*Hydrological water tank model for underground water*). Events l and *n* were set to have the same time windows to compare their electrical resistivity variations using a water tank model. **Figure 12** shows the modeling results for two tanks with a side stream (Duan et al., 1994; Lin S. E. et al., 2017; Rustanto et al., 2017). The black and red lines show the water depths in the first and second tanks, respectively reflecting shallower and deeper water storage layers.

We found that the shallow tank can be mostly related to zone A whereas the deep tank to zone E. Echoing the existence of different types of rainfall infiltration processes in the study area, for the short-duration precipitation Event *n*, the trend between the MEER in zone E and the water storage in the deep tank remain good correlation while the relation between zone A and shallow tank became unclear after the end of rainfall (**Figures 12C,D**). The positive correlation between the MEER and the water storage, as shown in **Figure 12**, suggests water transport on the Lantai slope. As water flows deep outward from zone A or zone E, making the MEER values increasing, also increase the underlying water storages, calibrated by the FBG pore pressure data and estimated from the precipitation data. Note that the presence of less fluid makes it difficult to pass an electrical current through the geologic material. On the other hand, the tank model is a phenomenological hydrological model and the water depths in the tanks are thought to be qualitative indicators that do not represent the actual water depths in the aquifer layers. Nevertheless, this study provides strong evidence for the consistency among rainfall, pore pressure, and electrical resistivity data.

## Electrical Resistivity Changes due to the Sliding Event in Summer 2020

A small sliding event is suspected to have occurred during the summer of 2020 according to the unrecoverable MEER changes and the SAA discontinuity as shown in **Figure 7**. **Figure 13** shows the differences in the annual electrical resistivity variations between the periods before and after the suspected (if any) sliding event in December, January, and February. The electrical resistivities appear to mostly show decreases (**Figures 13A–C**) in these 3 months, except at a depth of around 60 m in zones C and D. An electrical-resistivity-increased layer appears around 60 m that indicates the geologic property has been likely changed due to the sliding event. Since the SAA data suggests that the sliding surface could be located at ~78 m, the geological material above seems less porous after the shearing process of the sliding event. On the other hand, an electrical-resistivity-decreased zone appears to lay above at around 40 m deep, suggesting the material has possibly become more fractured. Noted that both the electrical-resistivity-decreased and increased zones abovementioned are corresponding to the original high resistivity structure located at zones C and D (**Figure 6**), implying that a new

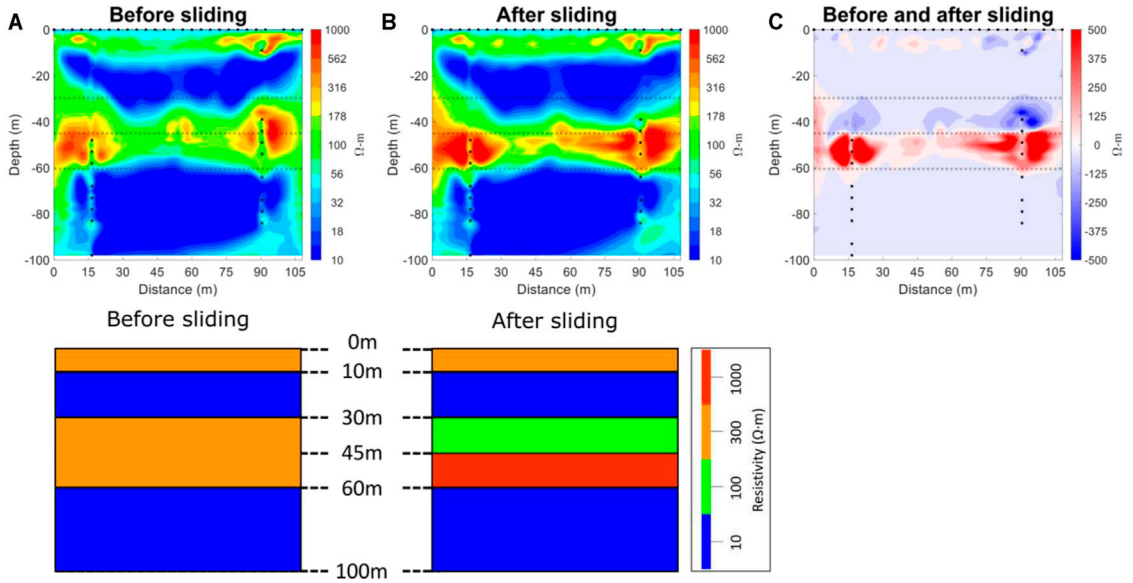


**FIGURE 14 |** Numerical modeling to test the resolving capability of the ERT electrode array used in the field. We assume that, due to a hypothetical sliding event, the shallower part of the mid-high-resistivity layer in the depths between 30 and 60 m became more conductive and the deeper part more resistive. Shown in **(A)** and **(B)** are the synthetic resistivity (lower panels) and their inverted (upper panels) models before and after, respectively, the sliding event. **(C)** Differences in time-lapse ERT images can recover the underground changes, caused by that hypothetical event, in electrical resistivities as we observed in the field experiments.

sliding surface may be growing in the area of the depths between 40 and 60 m. Observing the differences in precipitation for these 3 months, indeed, rainfall infiltration has some minor effects on zones A, B, E, and F, slightly lowering electrical resistivities. It is also important to exam the resolution to the summer 2020 event under the ERT array we used in the field. We, therefore, did the ERT forward and inversion calculations with two synthetic models before and after the sliding event (**Figures 14A,B**), wherein the shallower part of the mid-high-resistivity layer in the depths between 30 and 60 m became more conductive after the event and the deeper part more resistive. With resistance data synthesized by the same electrode array as we used in the field, the numerical experiment of time-lapse ERT can recover the changes in electrical resistivities due to the hypothetical sliding event (**Figure 14C**).

## CONCLUSION

We presented in this study the results of time-lapse ERT measurements in the Lantai slope, Yilan Taiping Mountain, Northeast Taiwan. The boundaries of the cross-sectional electrical resistivity images are mostly consistent with the drill core, suggesting that the ERT can image in a relatively macroscopic viewpoint geologic structures in potential landslide areas. The electrical resistivity profile in the study area shows a layered structure consisting of a resistive top soil/colluvium layer between the surface and 10 m depth, a conductive and fractured layer at 10–30 m depth, a resistive and compact slate formation from 30 to 60 m depth and, again, a conductive and fractured layer down to the depth of 100 m.

We also demonstrated that the spatiotemporal responses of the slope underground during rainfall events could be investigated by means of the time-lapse ERT monitoring technique. Integrating data from the ERT, the shape acceleration array, and the underground water pore pressure sensing array, we have shown different rainfall infiltration processes in the studied slope and possibly detected a small sliding/deformation event in summer 2020. The rainfall infiltration processes could be complicated in response to the duration and magnitude of precipitation. During the observation period, we have not observed a substantial landslide that could be sensed in the ground, but the suspected small slide/deformation might have caused detectable changes in the electrical resistivity data and the borehole SAA data as well. Before registering valuable multi-physical data of a notable landslide event and understanding the hydro-mechanical conditions of landslides, we believe that inspection of integrated data as shown in this study may be also helpful to improve quantitative analyses for the physical mechanism of landslide, thus to contribute the building blocks of landslide alert systems.

## DATA AVAILABILITY STATEMENT

The original contributions presented in the study are included in the article/**Supplementary Material**, further inquiries can be directed to the corresponding author.

## AUTHOR CONTRIBUTIONS

W-NT: Conceptualization, Writing-Original Draft, Validation, Investigation, Data Curation, Visualization; C-CC: Conceptualization, Methodology, Investigation, Data Curation, Supervision, Funding acquisition; C-WC: Writing-Original Draft, Investigation, Editing, Supervision; P-YC: Methodology, Resources; C-YK: Methodology, Resources; K-LW: Resources; M-LL: Resources; R-FC: Resources.

## FUNDING

This study was supported by the Ministry of Science and Technology, R.O.C., and the Soil and Water Conservation Bureau Council of Agriculture, Executive Yuan, R.O.C., under grant nos. 104-2119-M-006-008, 105-2119-M-006-010, and 106-2119-M-006-009.

## ACKNOWLEDGMENTS

We greatly thank the permission of the Taipingshan National Forest Recreation under the jurisdiction of the Luodong Forest District Office for the study.

## SUPPLEMENTARY MATERIAL

The Supplementary Material for this article can be found online at: https://www.frontiersin.org/articles/10.3389/feart.2021.737271/full#supplementary-material

## REFERENCES

AGI (2009). *Instruction manual for EarthImager 2D*. Austin, Texas, USA: Advanced Geosciences, Inc. Version 2.4. 0.

Archie, G. E. (1942). The electrical resistivity log as an aid in determining some reservoir characteristics. *Trans. AIME* 146, 54–62. doi:10.2118/942054-G

Bishop, A. W. (1960). The principle of effective stress. *Norw. Geotech. Inst. Publ.* 32, 1–5. doi:10.1021/ac60166a763

Cassiani, G., Boaga, J., Vanella, D., Perri, M. T., and Consoli, S. (2015). Monitoring and modelling of soil-plant interactions: the joint use of ERT, sap flow and eddy covariance data to characterize the volume of an orange tree root zone. *Hydrol. Earth Syst. Sci.* 19 (5), 2213–2225. doi:10.5194/hess-19-2213-2015

Chambers, J. E., Wilkinson, P. B., Weller, A. L., Meldrum, P. I., Ogilvy, R. D., and Caunt, S. (2007). Mineshaft imaging using surface and crosshole 3D electrical resistivity tomography: A case history from the East Pennine Coalfield, UK. *J. Appl. Geophys.* 62, 324–337. doi:10.1016/j.jappgeo.2007.03.004

Chang, P.-Y., Chen, C.-c., Chang, S.-K., Wang, T.-B., Wang, C.-Y., and Hsu, S.-K. (2012). An investigation into the debris flow induced by Typhoon Morakot in the Siaolin area, southern Taiwan, using the electrical resistivity imaging method. *Geophys. J. Int.* 188, 1012–1024. doi:10.1111/j.1365-246X.2011.05310.x

Chang, P.-Y., Huang, W.-J., Chen, C.-C., Hsu, H.-l., Yen, I.-C., Ho, G.-R., et al. (2018). Probing the frontal deformation zone of the Chihshang Fault with boreholes and high-resolution electrical resistivity imaging methods: A case study at the Dapo site in eastern Taiwan. *J. Appl. Geophys.* 153, 127–135. doi:10.1016/j.jappgeo.2018.04.006

Chen, W., Li, Y., and Wu, H. (2005). Study of judging debris flow occurrence by combing the physiographical factors and rainfall condition-Chen-Yu-Lan stream watershed as an example. *J. Taiwan Geogr. Info. Sci.* 2, 27–44. (in Chinese). doi:10.29790/JTGIS.200504.0003

Chiang, C.-W., Chen, C.-C., Unsworth, M., Bertrand, E., Chen, C.-S., Kieu, T. D., et al. (2010). The deep electrical structure of southern Taiwan and its tectonic implications. *Terr. Atmos. Ocean. Sci.* 21 (6), 879–895. doi:10.3319/tao.2010.02.25.01(t)

Chiang, C.-W., Goto, T.-n., Mikada, H., Chen, C.-C., and Hsu, S.-K. (2012). Sensitivity of Deep-Towed Marine Electrical Resistivity Imaging Using Two-Dimensional Inversion: A Case Study on Methane Hydrate. *Terr. Atmos. Ocean. Sci.* 23 (6), 725–732. doi:10.3319/tao.2012.06.19.01(t)

Chiang, C.-W., Hsu, H.-L., and Chen, C.-C. (2015). An Investigation of the 3D Electrical Resistivity Structure in the Chingshui Geothermal Area, NE Taiwan. *Terr. Atmos. Ocean. Sci.* 26 (3), 269–281. doi:10.3319/tao.2014.12.09.01(t)

Crosta, G. (1998). Regionalization of rainfall thresholds: an aid to landslide hazard evaluation. *Environ. Geology.* 35 (2-3), 131–145. doi:10.1007/s002540050300

Dai, F. C., and Lee, C. F. (2002). Landslide characteristics and, slope instability modeling using GIS, Lantau Island, Hong Kong. *Geomorphology* 42 (3-4), 213–228. doi:10.1016/s0169-555x(01)00087-3

Daily, W., Ramirez, A., Labrecque, D., and Nitao, J. (1992). Electrical resistivity tomography of vadose water movement. *Water Resour. Res.* 28, 1429–1442. doi:10.1029/91wr03087

Descloitres, M., Ruiz, L., Sekhar, M., Legchenko, A., Braun, J.-J., Mohan Kumar, M. S., et al. (2008). Characterization of seasonal local recharge using electrical resistivity tomography and magnetic resonance sounding. *Hydrol. Process.* 22, 384–394. doi:10.1002/hyp.6608

Duan, Q. Y., Sorooshian, S., and Gupta, V. K. (1994). Optimal use of the sce-ua global optimization method for calibrating watershed models. *J. Hydrol.* 158 (3-4), 265–284. doi:10.1016/0022-1694(94)90057-4

Guzzetti, F., Peruccacci, S., Rossi, M., and Stark, C. P. (2007). Rainfall thresholds for the initiation of landslides in central and southern Europe. *Meteorol. Atmos. Phys.* 98, 239–267. doi:10.1007/s00703-007-0262-7

Hall, R. (2002). Cenozoic geological and plate tectonic evolution of SE Asia and the SW Pacific: computer-based reconstructions, model and animations. *J. Asian Earth Sci.* 20 (4), 353–431. doi:10.1016/s1367-9120(01)00069-4

Ho, C. S. (1986). A synthesis of the geologic evolution of Taiwan. *Tectonophysics* 125, 1–16. doi:10.1016/0040-1951(86)90004-1

Hsu, H.-L., Yanites, B. J., Chen, C.-c., and Chen, Y.-G. (2010). Bedrock detection using 2D electrical resistivity imaging along the Peikang River, central Taiwan. *Geomorphology* 114, 406–414. doi:10.1016/j.geomorph.2009.08.004

Huang, A.-B., Lee, J.-T., Ho, Y.-T., Chiu, Y.-F., and Cheng, S.-Y. (2012). Stability monitoring of rainfall-induced deep landslides through pore pressure profile measurements. *Soils and Foundations* 52 (4), 737–747. doi:10.1016/j.sandf.2012.07.013

Iverson, R. M. (2000). Landslide triggering by rain infiltration. *Water Resour. Res.* 36, 1897–1910. doi:10.1029/2000WR900090

Jongmans, D., and Garambois, S. (2007). Geophysical investigation of landslides : a review. *Bull. Soc. Géol. Fr.* 178 (2), 101–112. doi:10.2113/gssgfbull.178.2.101

Kornei, K. (2019). A massive experiment in Taiwan aims to reveal landslides' surprising effect on the climate. *Science* 366, 938–940. doi:10.1126/science.aba2653

Kuo, C. Y., Lin, S. E., Chen, R. F., Hsu, Y. J., Chang, K. J., Lee, S. P., et al. (2021). Occurences of deep-seated creeping landslides in accordance with hydrological water storages in catchments. *Front. Earth Sci.* submitted.

Kuras, O., Pritchard, J. D., Meldrum, P. I., Chambers, J. E., Wilkinson, P. B., Ogilvy, R. D., et al. (2009). Monitoring hydraulic processes with automated time-lapse electrical resistivity tomography (ALERT). *Comptes Rendus Geosci.* 341 (10-11), 868–885. doi:10.1016/j.crte.2009.07.010

Lin, M. L., Chena, T. W., and Hsia, K. C. (2017a). Evolution and stability analysis of a deep-seated landslide in Lantai area, Taiwan. *Geotechnical Hazard. Mitigations: Experiment, Theor. Practice-Proceedings 5th Int. Conf. Geotechnical Eng. Disaster Mitigation Rehabil.*, 391–402. doi:10.6140/9789864371419.201710.0034

Lin, S. E., Chan, Y. H., Kuo, C. Y., Chen, R. F., Hsu, Y. J., Chang, K. J., et al. (2017b). The use of a hydrological catchment model to determine the occurrence of temporal creeping in deep-seated landslides. *J. Chin. Soil Water Conserv.* 48 (4), 153–162. doi:10.29417/JCSWC.201712_48(4).0001

Maillol, J. M., Seguin, M.-K., Gupta, O. P., Akhauri, H. M., and Sen, N. (1999). Electrical resistivity tomography survey for delineating uncharted mine galleries in West Bengal, India*. *Geophys. Prospecting* 47, 103–116. doi:10.1046/j.1365-2478.1999.00126.x

Melillo, M., Brunetti, M. T., Peruccacci, S., Gariano, S. L., and Guzzetti, F. (2015). An algorithm for the objective reconstruction of rainfall events responsible for landslides. *Landslides* 12, 311–320. doi:10.1007/s10346-014-0471-3

Morgenstern, N. R., and Price, V. E. (1965). The analysis of the stability of general slip surfaces. *Géotechnique* 15 (1), 79–93. doi:10.1680/geot.1965.15.1.79

Müller, K., Vanderborght, J., Englert, A., Kemna, A., Huisman, J. A., Rings, J., et al. (2010). Imaging and characterization of solute transport during two tracer tests in a shallow aquifer using electrical resistivity tomography and multilevel groundwater samplers. *Water Resour. Res.* 46, 23. doi:10.1029/2008wr007595

Nash, J. E. (1957). The form of the instantaneous unit hydrograph. *Int. Ass. Sci. Hydrol.* 3, 114–121.

Oldenborger, G. A., Knoll, M. D., Routh, P. S., and LaBrecque, D. J. (2007). Time-lapse ERT monitoring of an injection/withdrawal experiment in a shallow unconfined aquifer. *Geophysics* 72 (4), F177–F187. doi:10.1190/1.2734365

Palis, E., Lebourg, T., Vidal, M., Levy, C., Tric, E., and Hernandez, M. (2017). Multiyear time-lapse ERT to study short- and long-term landslide hydrological dynamics. *Landslides* 14, 1333–1343. doi:10.1007/s10346-016-0791-6

Perrone, A., Lapenna, V., and Piscitelli, S. (2014). Electrical resistivity tomography technique for landslide investigation: A review. *Earth-Science Rev.* 135, 65–82. doi:10.1016/j.earscirev.2014.04.002

Petley, D. N., Mantovani, F., Bulmer, M. H., and Zannoni, A. (2005). The use of surface monitoring data for the interpretation of landslide movement patterns. *Geomorphology* 66, 133–147. doi:10.1016/j.geomorph.2004.09.011

Rustanto, A., Booij, M. J., Wösten, H., and Hoekstra, A. Y. (2017). Application and recalibration of soil water retention pedotransfer functions in a tropical upstream catchment: case study in Bengawan Solo, Indonesia. *J. Hydrol. Hydromech.* 65 (3), 307–320. doi:10.1515/johh-2017-0020

Segoni, S., Piciullo, L., and Gariano, S. L. (2018). A review of the recent literature on rainfall thresholds for landslide occurrence. *Landslides* 15, 1483–1501. doi:10.1007/s10346-018-0966-4

Sugawara, M. (1961). On the analysis of runoff structure about several Japanese rivers, *Japanese. J. Geophys.* 2, 210–216.

Suppe, J. (1981). Mechanics of mountain-building and metamorphism in Taiwan. *Mem. Geol. Soc. China* 4, 67–89.

Tang, J.-T., Zhang, J.-F., Feng, B., Lin, J.-Y., and Liu, C.-S. (2007). Determination of borders for resistive oil and gas reservoirs by deviation rate using the hole-to-surface resistivity method. *Chin. J. Geophys.* 50, 790–795. doi:10.1002/cjg2.1094

Wang, T.-P., Chen, C.-C., Tong, L.-T., Chang, P.-Y., Chen, Y.-C., Dong, T.-H., et al. (2015). Applying FDEM, ERT and GPR at a site with soil contamination: A case study. *J. Appl. Geophys.* 121, 21–30. doi:10.1016/j.jappgeo.2015.07.005

Wang, T.-P., Chen, Y.-T., Chen, C.-C., Tung, T.-H., Cheng, S.-N., and Yu, C.-Y. (2020). Application of cross-hole electrical resistivity tomography to groundwater contaminated remediation site. *Terr. Atmos. Ocean. Sci.* 31, 507–521. doi:10.3319/TAO.2019.06.17.01

Yeh, H.-F., Lin, H.-I., Wu, C.-S., Hsu, K.-C., Lee, J.-W., and Lee, C.-H. (2015). Electrical resistivity tomography applied to groundwater aquifer at downstream of Chih-Ben Creek basin, Taiwan. *Environ. Earth Sci.* 73, 4681–4687. doi:10.1007/s12665-014-3752-1

Zhang, G., Lü, Q.-T., Zhang, G.-B., Lin, P.-R., Jia, Z.-Y., and Suo, K. (2018). Joint Interpretation of Geological, Magnetic, AMT, and ERT Data for Mineral Exploration in the Northeast of Inner Mongolia, China. *Pure Appl. Geophys.* 175, 989–1002. doi:10.1007/s00024-017-1733-5

Zhang, G., Zhang, G.-B., Chen, C.-c., Chang, P.-Y., Wang, T.-P., Yen, H.-Y., et al. (2016). Imaging Rainfall Infiltration Processes with the Time-Lapse Electrical Resistivity Imaging Method. *Pure Appl. Geophys.* 173, 2227–2239. doi:10.1007/s00024-016-1251-x

**Conflict of Interest:** The authors declare that the research was conducted in the absence of any commercial or financial relationships that could be construed as a potential conflict of interest.

**Publisher's Note:** All claims expressed in this article are solely those of the authors and do not necessarily represent those of their affiliated organizations, or those of the publisher, the editors and the reviewers. Any product that may be evaluated in this article, or claim that may be made by its manufacturer, is not guaranteed or endorsed by the publisher.

frontiers in Earth Science

ORIGINAL RESEARCH
published: 11 November 2021
doi: 10.3389/feart.2021.764393

# An Investigation of Rainfall-Induced Landslides From the Pre-Failure Stage to the Post-Failure Stage Using the Material Point Method

*Wei-Lin Lee*[1]*, *Mario Martinelli*[2]* and *Chjeng-Lun Shieh*[1]

[1]Department of Hydraulic and Ocean Engineering, National Cheng-Kung University, Tainan City, Taiwan, [2]Deltares, Delft, Netherlands

The kinematic behavior of rainfall-induced landslides from the pre-failure stage to post-failure stage contains important information for risk assessment and management. Because a complex relationship exists between rainfall conditions, pore water pressure, soil strength, and movement rates, a numerical model is the most efficient way to investigate the behavior of rainfall-induced landslides. In this study, the material point method (MPM) is used to investigate the dynamic behavior of landslides. First, the rainfall boundary conditions are extensively verified by comparing 1-D consolidation tests against other numerical solutions. Then, a numerical model is used to simulate a lab-scale rainfall-induced slope failure. A parametric study shows the influence of rainfall intensity on pore water pressure development, failure triggering time, surface displacement, and velocity. The use of the MPM provides a clear understanding in the failure mechanism and post-failure behavior of a rainfall-induced landslide.

**Keywords: landslide, rainfall boundary, infiltration, unsaturated soil, material point method**

OPEN ACCESS

***Edited by:***
*Rou-Fei Chen,*
*Chinese Culture University, Taiwan*

***Reviewed by:***
*Joern Lauterjung,*
*Helmholtz Centre Potsdam, Germany*
*Qi Yao,*
*China Earthquake Administration, China*

***Correspondence:**
*Wei-Lin Lee*
*glaciallife@gmail.com*
*Mario Martinelli*
*mario.martinelli@deltares.nl*

***Specialty section:***
*This article was submitted to Geohazards and Georisks, a section of the journal Frontiers in Earth Science*

***Received:*** *25 August 2021*
***Accepted:*** *20 October 2021*
***Published:*** *11 November 2021*

***Citation:***
*Lee W-L, Martinelli M and Shieh C-L (2021) An Investigation of Rainfall-Induced Landslides From the Pre-Failure Stage to the Post-Failure Stage Using the Material Point Method. Front. Earth Sci. 9:764393. doi: 10.3389/feart.2021.764393*

## INTRODUCTION

Rainfall-induced landslides have been a challenge for many decades. Leroueil (2001) indicated the complex relationships existing between rainfall conditions, pore water pressure, soil strength, safety factors, and movement rates. Leroueil (2001), Calvello et al. (2008), and Cascini et al. (2010) stated that rainfall-induced landslides evolve with the complexity of hydro-mechanical responses in the pre-failure, failure, and post-failure stages. Picarelli et al. (2004) depicted a schematic of slope behavior to that indicated that the characteristics of soil displacement behave differently in different stages, as shown in **Figure 1**. In the pre-failure stage, the soil moves at a constant rate, and it occurs together with local failure, such as the development of shear zones (Cascini et al., 2014). Afterwards, a continuous shear surface (slip surface) will form through the entire soil mass, which leads to the failure stage (Leroueil and Picarelli, 2012; Cascini et al., 2014). In the post-failure stage, the dynamic behavior of soil mass exhibits different types of movement, including slide, spread, and flow (Leroueil and Picarelli 2012). Many approaches have been proposed to relate these relationships in different combinations using both statistically-based models and physically-based models (Cascini et al., 2010). Cuomo (2020) reviewed a wide body of literature on the topic and concluded that a numerical model is the most efficient way to understand the complexity of rainfall-induced landslides.

The applicability of various numerical methods for landslide modeling has been compared and discussed by Bandara et al. (2016), Soga et al. (2016), Cuomo (2020), and Yuan et al. (2020).

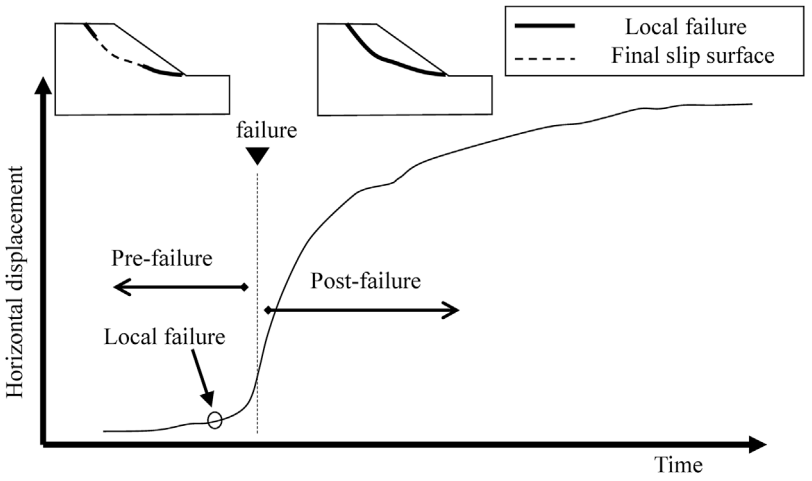


**FIGURE 1 |** Schematic of slope behavior (modified from Picarelli et al., 2004).

Yuan et al. (2020) mentioned that the finite element method (FEM) can be used to automatically detect the shape and location of slip surfaces instead of the limit equilibrium method (LEM). However, the nodal displacement can increase significantly, accompanied by the failure and post-failure stages, as shown in **Figure 1**, where severe mesh distortions result in simulation non-convergence (Bandara et al., 2016; Soga et al., 2016; Yuan et al., 2020). Thus, Bandara et al. (2016) and Soga et al. (2016) suggested that the post-failure stage be simulated independently using different numerical methods, for example, the finite difference method (FDM) with a depth-integrated model. Accordingly, the numerical parameters and results cannot be expected to have a good consistency in the pre-failure, failure, and post-failure stages. In order to overcome the aforementioned problems, Soga et al. (2016) suggested that the mesh-free technique may be a solution. The technique includes smooth particle hydrodynamics (SPH), the material point method (MPM), the particle finite-element method (PFEM), the finite-element method with Lagrangian integration points (FEMLIP), and the element-free Galerkin (EFG) method. In particular, many researchers have applied the material point method for the simulation of rainfall-induced landslides in recent decades (Yerro et al., 2015; Bandara et al., 2016; Soga et al., 2016; Wang et al., 2018; Lee et al., 2019a; Lee et al., 2019b; Ceccato et al., 2019; Cuomo et al., 2019; Lei et al., 2020; Liu et al., 2020; Martinelli et al., 2020; Liu and Wang, 2021; Nguyen et al., 2021).

The investigation of the development of rainfall-induced landslides using the material point method has been remarkably successful in the past decade. In order to model soil-water-structure interaction, Al-Kafaji (2013) and Jassim et al. (2013) proposed a coupled 2-phase 1-point MPM formulation for saturated soil, and a frictional contact algorithm was developed to simulate the interaction between a structure and soil. With the help of their contribution, the coupled 2-phase 1point MPM formulation was applied to simulate the post-failure stage of a rainfall-induced landslide assuming that a phreatic surface existed before slope failure and the effect of suction was minor as soil deformation increased (Lee et al., 2019a; Cuomo et al., 2019; Nguyen et al., 2021). Yerro et al. (2015) attempted to model infiltration in an unsaturated brittle material, where a coupled 3-phase 1-point MPM formulation associated with a suction-dependent elastoplastic Mohr-Coulomb model was proposed; the well-known van Genuchten model was applied, and the rainfall boundary conditions only considered the type of pore water pressure. Later, different pseudo-3-phase 1-point MPM formulations were proposed by Bandara et al. (2016), Wang et al. (2018), Lee et al. (2019b), Martinelli et al. (2020), and Ceccato et al. (2020). Bandara et al. (2016) derived a coupled pseudo-3-phase 1-point MPM formulation and obtained the infiltration rate of rainfall boundary based on Darcy's velocity. Other researchers derived a coupled pseudo-3-phase 1-point MPM formulation associated with true liquid velocity, and different algorithms for the infiltration rate of rainfall boundary were proposed by Martinelli et al. (2020) and Ceccato et al. (2019). The former implemented it in a linear unsaturated model and benchmarked it in a one-dimensional soil column test (Martinelli et al., 2020). The latter perform it using the van Genuchten model and benchmarked it in a two-dimensional levee test (Ceccato et al., 2020). Accordingly, a physical-based model using the material point method can be an appropriate solution to investigate the dynamic behavior of rainfall-induced landslides.

This study began the investigation with lab-scale rainfall-induced slope failure, which was implemented by Moriwaki et al. (2004) in Japan. This is a classic experiment and has been studied using different numerical models (Ghasemi et al., 2019; Nguyen et al., 2021; Yang et al., 2021). However, the deformation characteristics influenced by the rainfall conditions can only be investigated in the pre-failure stage or in the post-failure stage, separately. Yang et al. (2021) applied a numerical model based on the finite element method, so the deformation characteristics could only be investigated before the post-failure stage. Ghasemi et al. (2019) and Nguyen et al. (2021) used a different numerical model, which was developed with a 2-phase 1-point MPM formulation, but a rainfall boundary condition algorithm was not available in their model. Hence, the process of infiltration had

to be omitted in their studies, and they could only investigate the deformation characteristics in the post-failure stage. In order to improve the previous limitations, this study proposed a numerical model, which implemented a pseudo-3-phase 1-point MPM formulation, to simulate the lab-scale rainfall-induced slope failure. This study applied the rainfall boundary condition algorithm following Martinelli et al. (2020) to validate the van Genuchten model. Therefore, the deformation characteristics influenced by the rainfall conditions could be completely investigated from the pre-failure stage to the post-failure stage.

With help of the proposed model using MPM, this study was able to provide a further investigation on the effect of rainfall. Yang et al. (2021) investigated the effect of rainfall only in the pre-failure stage and did not discuss the location of rising pore water pressure against varying rainfall intensities. Ghasemi et al. (2019) and Nguyen et al. (2021) investigated post-failure behavior without considering the effect of rainfall due to the limitations inherent in their numerical model. Therefore, variations in the rainfall intensity corresponding to the pattern of rising pore water pressure and slope failure can be discussed in this study.

The paper is organized as follows: *Theory and Numerical Algorithm* presents the theory and numerical algorithm for the coupled pseudo-3-phase 1-point MPM formulation, as well as the rainfall boundary conditions. Then, the numerical simulation of the lab-scale rainfall-induced slope failure, as described in Moriwaki et al. (2004), is described in *Numerical Simulation of a Lab-Scale Rainfall-Induced Slope Failure*. Finally, the parametric study is discussed in *Parametric Study*. The proposed numerical algorithm makes it possible to investigate a rainfall-induced landslide from pre-failure stage to post-failure stage, and it offers a further understanding of the effect of rainfall intensity on dynamic soil behavior. According, the findings from this study may provide guidance for geo-environmental risk assessment.

# THEORY AND NUMERICAL ALGORITHM

## Governing Equations

A natural slope can be considered to be a media structured in the form of three phases (solid, liquid, and gas). In this study, a coupled pseudo-3-phase 1-point MPM formulation is derived assuming the gas phase is ignored in the governing equations. Thus, the mass exchange of air and water between the liquid and gas phases are also ignored, and the air pressure is set to zero. The subscripts $s$ and $l$ denote solid and liquid phases ($ph$), respectively. The subscript $m$ indicates the mixture. The summation of the volume of the solid phase ($V_s$) and the volume of the voids ($V_{void}$) is equal to the total volume ($V$). $V_{void}/V$ indicates the porosity ($n$). Since the volume of liquid is $V_l$, $V_l/V_{void}$ indicates the degree of saturation ($S_l$). $\rho_l$ and $\rho_s$ indicate the density of the liquid phase and solid phase, repectively. The density of the mixture phase ($\rho_m$) is determined by the volume fraction and the true density of each phase, i.e., $\rho_m = (1-n)\rho_s + n\rho_l$.

The following general assumptions are adopted

- Isothermal conditions
- No mass exchange between solid and liquid
- Solid grains are incompressible
- Smooth distribution of $n$ and $S_l$ in the soil
- Small spatial variations in the water mass

The momentum balance of the liquid phases is given as .

$$\rho_l \boldsymbol{a}_l = \nabla p_l + \rho_l \boldsymbol{b} + \frac{nS_l\mu_l}{k_{rel}k_l}(\boldsymbol{v}_l - \boldsymbol{v}_s), \tag{1}$$

where the vector $\boldsymbol{a}_l$ is the acceleration of the liquid; $p_l$ is the liquid pressure, and $\boldsymbol{b}$ is the body force vector. The third term in right hand side is the drag force corresponding to Darcy's law, where $\mu_l$ is the dynamic viscosity of the liquid, and $k_l$ is the intrinsic permeability of the solid skeleton. $\boldsymbol{v}_l$ and $\boldsymbol{v}_s$ indicate the velocity fields for the liquid and solid phases, respectively. The relative permeability $k_{rel}$ is given by a saturation function, which is equal to 1 for fully saturated soil and decreases with the degree of saturation. In **(1)**, $nS_l(v_l - v_s)$ is called as the seepage velocity (or Darcy's velocity) ($\boldsymbol{w}$). With help of **Eq. 1**, Martinelli et al. (2020) yielded the momentum balance of the mixture as :

$$(1-n)\rho_s \boldsymbol{a}_s = \nabla \cdot (\boldsymbol{\sigma} - nS_l p_l \boldsymbol{I}) + (\rho_m - nS_l\rho_l)\boldsymbol{b} + \frac{nS_l\mu_l}{k_{rel}k_l} nS_l(\boldsymbol{v}_l - \boldsymbol{v}_s), \tag{2}$$

where the vectors $\boldsymbol{a}_m$ and $\boldsymbol{a}_s$ are the acceleration of the mixture and solid phases, respectively. $\boldsymbol{\sigma}$ is the total stress tensor of the mixture, and $\boldsymbol{I}$ is unit stress tensor.

The expression for the mass balance of solid phase is under the third and fourth points of the general assumption, and it can be written as

$$\frac{\partial n}{\partial t} = (1-n)\nabla \cdot \boldsymbol{v}_s. \tag{3}$$

For the mass balance of the liquid phase, barotropic behavior is assumed for the fluid, and so the time derivative of the liquid density ($\partial p_l/\partial t$) is thus considered to be related to the time derivative of the pore water pressure ($\partial p_l/\partial t$) (Wang et al., 2018). When the soil is partially saturated, the air pressure ($p_a$) is assumed to be zero, where $p_a - p_l$ indicates the suction ($s$). Thus, the time derivative of the degree of saturation ($\partial S_l/\partial t$) can be the function of $\partial p_l/\partial t$ (Wang et al., 2018). Under these assumptions, the mass balance of liquid phase can be expressed as

$$\frac{\partial p_l}{\partial t} = \frac{K_l}{\left(1 - \frac{K_l}{S_l}\frac{\partial S_l}{\partial s}\right)}\left[\frac{(1-n)}{n}\nabla \cdot \boldsymbol{v}_s + \nabla \cdot \boldsymbol{v}_l\right], \tag{4}$$

where $K_l$ is the bulk modulus of the liquid. $\partial S_l/\partial s$ represents the specific moisture capacity (Zienkiewicz et al., 1990).

The relationships among $S_l$, $s$, and $k_{rel}$ are important when attempting to model the behavior of unsaturated soil. The soil-water retention curve (SWRC) for the van Genuchten model is given as follows:

$$S_l = S_{min} + (S_{max} - S_{min})\left[1 + \left(\frac{s}{p_0}\right)^{\frac{1}{1-\lambda}}\right]^{-\lambda} \quad \text{for } s \geq 0, \tag{5}$$

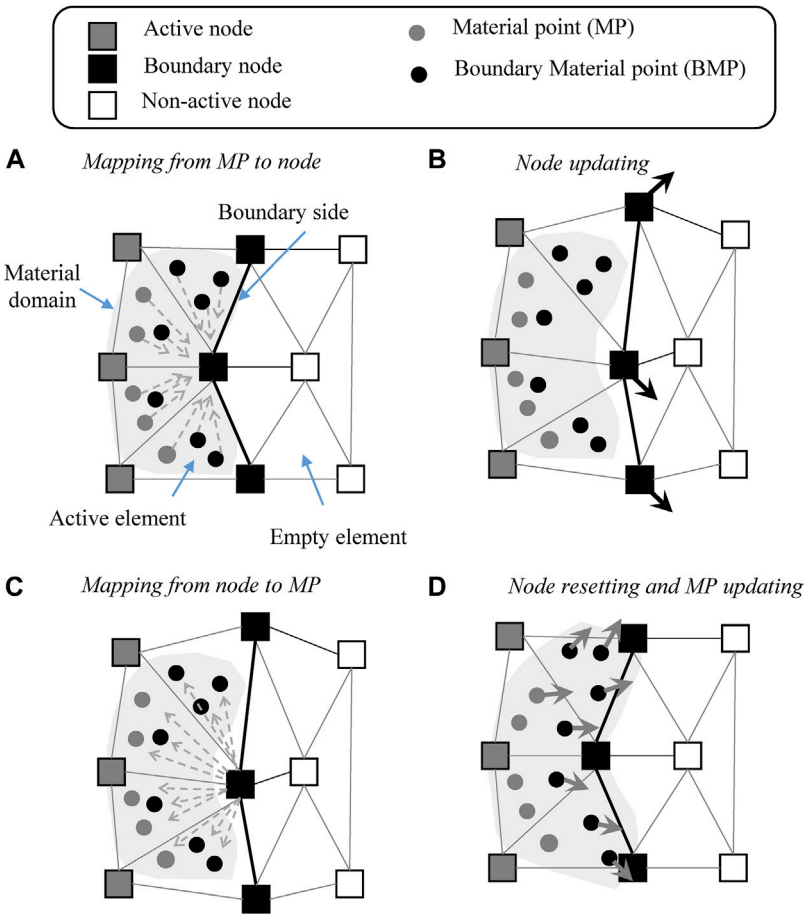


**FIGURE 2 |** Schematic of the material point method. **(A)** Mapping from MP to node. **(B)** Node updating. **(C)** Mapping from node to MP. **(D)** Node resetting and MP updating.

where $p_0$ is the air-entry pressure (unit of kPa); $\lambda$ is an empirical parameter, and $S_{max}$ and $S_{min}$ are respectively the degree of saturation at full saturation and under very dry conditions. The hydraulic conductivity curve (HCC) can be summarized as follows:

$$S_e = \frac{S_l - S_{min}}{S_{max} - S_{min}} \text{for } s \geq 0, \tag{6}$$

$$k_{rel}(S_l) = (S_e)^{0.5}\left[1 - \left(1 - S_e^{\frac{1}{\lambda}}\right)^{\lambda}\right]^2 \text{for } s \geq 0, \tag{7}$$

where $S_e$ is the effective saturation (Mualem, 1976). $\partial S_l/\partial s$ can be computed by

$$\frac{\partial S_l}{\partial s} = (S_{max} - S_{min})\left(\frac{-\lambda}{1-\lambda}\right)\left(\frac{1}{p_0}\right)\left[\frac{|s|}{p_0}^{\left(\frac{\lambda}{1-\lambda}\right)}\right]\left[1 + \left(\frac{|s|}{p_0}\right)^{\left(\frac{1}{1-\lambda}\right)}\right]^{(-\lambda-1)} \text{for } s \geq 0. \tag{8}$$

For the mechanical constitutive equation, the concept of Bishop is introduced to express the effective stress of unstated soil ($\sigma$'), which is equal to $\sigma - S_l p_l I$. The incremental effective stress ($d\sigma$') is associated with the strain increment vector ($d\varepsilon$) and can be presented as $d\sigma' = Dd\varepsilon$, where D is the tangent matrix. The stress-strain relationship is measured using the Jaumann stress rate, and the material time derivative of the Cauchy stress tensor is written as $d\sigma' = Dd\boldsymbol{\varepsilon} + \sigma' W^T - W\sigma'$, where W is the vorticity. In this paper, the elastoplastic model with the Mohr-Coulomb failure criteria is used (Bandara and Soga, 2015; Ceccato et al., 2019).

## Discretization and Material Point Method Algorithm

### Discretization of Material Point Method

Numerically implementing our proposed governing equations was accomplished using the material point method. As visualized in **Figure 2**, a set of material points (MPs) discretized the material domain and carried all information, including density, strain, stress, velocity, and other material parameters (Al-Kafaji, 2013; Zhang et al., 2016). The MPs represent the continuum body and move through an Eulerian background grid (Zhang et al., 2016; Martinelli et al., 2020). The fixed Eulerian grid structured by the node, the node was used to determine the divergence terms and spatial gradient, and no historical information was carried inside

the node (Zhang et al., 2016). In order to map the material's information from the MPs to a node or from a node to an MP, as show in **Figures 2A,C**, the linear shape function was used to assemble MPs or nodes as in the finite element method. $N^p$ and $N^n$ indicate the linear shape functions of MPs and nodes, respectively. The position of any node and material point can be denoted by

$$x^n = \sum_{i=1}^{N^p} x^i N^p, \quad x^p = \sum_{i=1}^{N^n} x^i N^n, \tag{9}$$

where $x^n$ and $x^p$ indicate the material information, $x = \mathrm{x}, v, a$ for position, velocity, and acceleration, respectively. $i$ is a series number with spatial discretization. The gradient of the linear shape function is represented as $\nabla N^p$ and $\nabla N^n$.

In the discretized equations, **Equations 1**, **2** can be presented in a weak form as follows:

$$\tilde{\boldsymbol{M}}_l^n \cdot \boldsymbol{a}_l^n = \boldsymbol{F}_l^{ext} + \boldsymbol{F}_l^{grav} - \boldsymbol{F}_l^{int} - \boldsymbol{Q}_l^n \cdot (\boldsymbol{v}_l^n - \boldsymbol{v}_s^n), \tag{10}$$

$$\boldsymbol{M}_s^n \cdot \boldsymbol{a}_s^n = \boldsymbol{F}_s^{ext} + \boldsymbol{F}_s^{grav} - \boldsymbol{F}_s^{int} + \boldsymbol{Q}_m^n \cdot (\boldsymbol{v}_l^n - \boldsymbol{v}_s^n), \tag{11}$$

where $\boldsymbol{a}_l^n$ , $\boldsymbol{a}_s^n$ , $\boldsymbol{v}_l^n$ and $\boldsymbol{v}_s^n$ are nodal acceleration and velocity vectors. $\tilde{\boldsymbol{M}}_l^n$ and $\boldsymbol{M}_s^n$ are the lumped mass matrix of liquid and solid at the nodes. $\boldsymbol{F}_l^{ext}$ , $\boldsymbol{F}_l^{grav}$ , $\boldsymbol{F}_l^{int}$ , $\boldsymbol{F}_s^{ext}$ , $\boldsymbol{F}_s^{grav}$ , and $\boldsymbol{F}_s^{int}$ are the internal nodal force, gravity nodal force, and external nodal force vectors for each phase, respectively. $\boldsymbol{Q}_l^n$ and $\boldsymbol{Q}_m^n$ are the drag force matrices for each phase at the nodes. In this paper, the nodal information in **Eqs 10**, **11** can be calculated following Al-Kafaji (2013).

An explicit Euler method is applied to integrate the model equations in time. Meanwhile, the velocities and positions of each phase could be updated respectively with the accelerations and velocities of each phase as follows:

$$\boldsymbol{v}^{k+1} = \boldsymbol{v}^k + \boldsymbol{a}^k \Delta t, \mathrm{x}^{k+1} = \mathrm{x}^k + \boldsymbol{v}^{k+1} \Delta t. \tag{12}$$

## The Material Point Method Time Marching Procedure

The MPM scheme in this study follows modified update-stress-last (MUSL) scheme (Sulsky et al., 1995). A single computational cycle of numerical algorithm is described as follows:

(I). The discrete MP information is known at time $t^k$. The initialized variables for the solid phase include $\mathrm{x}_s^{p,k}$, $v_s^{p,k}$, $\sigma'^{p,k}$, $n^{p,k}$, $V^{p,k}$, and $\rho_s$. For the liquid phase, the initialized variables include $v_l^{p,k}$, $S_l^{p,k}$, $p_l^{p,k}$, $K_l^{p,k}$, $\mu_l$, $k_l$, $k_{rel}^{p,k}$, and $\rho_l$ The linear shape function ($N^{p,k}$, $N^{n,k}$) and the gradient of the linear shape function ($\nabla N^{p,k}$, $\nabla N^{N,k}$) can be associated with the position of the solid's MP ($\mathrm{x}_s^{p,k}$) and the grid background.

(II). The liquid acceleration node ($a_l^{n,k}$) is determined using **Eq. 10**. The solid acceleration node ($a_s^{n,k}$) is determined by **Eq. 11**. Because the concept of Bishop effective stress is used, the total stress $\sigma^{p,k}$ equals to $\sigma'^{p,k} + S_l^{p,k} p_l^{p,k}$. The second step can be visualized in **Figures 2A,B**.

(III). The MP velocities for each phase at the new time $k+1$ are updated using the nodal accelerations for each phase, as shown in **Figure 2C**. With help of **Eq. 12**, the formula reads as

$$\boldsymbol{v}^{p,k+1} = \boldsymbol{v}^{p,k} + \Delta t \sum_{i=1}^{N^n} \boldsymbol{a}^{i,k} N^{p,k}. \tag{13}$$

Because the nodal momentum of each phase can be estimated using the material point masses and velocities, the nodal velocities at the new time $k+1$ are finally computed as the ratio between the nodal momentum and the nodal mass. The computation is as follows:

$$\boldsymbol{v}_l^{n,k+1} = \frac{\sum_{i=1}^{N^p} n^{i,k} S_l^{i,k} \rho_l V^{i,k} \boldsymbol{v}_l^{i,k+1} N^{n,k}}{\sum_{i=1}^{N^p} n^{i,k} S_l^{i,k} \rho_l V^{i,k} N^{n,k}},$$

$$\boldsymbol{v}_s^{n,k+1} = \frac{\sum_{i=1}^{N^p} (1 - n^{i,k}) \rho_s V^{i,k} \boldsymbol{v}_s^{i,k+1} N^{n,k}}{\sum_{i=1}^{N^p} (1 - n^{i,k}) \rho_s V^{i,k} N^{n,k}}. \tag{14}$$

(IV). The strain rates of each phases at the MPs is shown as $\dot{\varepsilon}^{p,k} = \Delta\varepsilon^{p,k}/\Delta t$. These can be determined using the nodal velocity of each phases as follows:

$$\dot{\varepsilon}^{p,k} = \frac{1}{2} \sum_{i=1}^{N^n} \left[ \left( \nabla N^{p,k} \boldsymbol{v}^{i,k+1} \right) + \left( \nabla N^{p,k} \boldsymbol{v}^{i,k+1} \right)^T \right]. \tag{15}$$

(V). The updating of the MP's effective stress at the new time ($\sigma'^{p,k+1}$) is associated with the strain increment of the solid phase ($\Delta\varepsilon_s^{p,k} = \Delta t \dot{\varepsilon}_s^{p,k}$) and the vorticity of the solid phase ($\mathrm{W}_s^{p,k}$). The stress-strain relationship is adopted using the Jaumann stress rate as follows:

$$\boldsymbol{\sigma}'^{p,k+1} = \boldsymbol{\sigma}'^{p,k} + \Delta t \left( \boldsymbol{\sigma}'^{p,k} \cdot \mathbf{W}_s^{p,k} - \mathbf{W}_s^{p,k} \cdot \boldsymbol{\sigma}'^{p,k} \right) + \mathbf{D} : \Delta\varepsilon_s^{p,k}, \tag{16}$$

$$\mathbf{W}_s^{p,k} = \sum_{i=1}^{N^n} \left[ \left( \nabla N^{p,k} \boldsymbol{v}_s^{i,k+1} \right) - \left( \nabla N^{p,k} \boldsymbol{v}_s^{i,k+1} \right)^T \right]. \tag{17}$$

The failure criteria follow the standard Mohr-Coulomb model.

(VI). The increment of the pore water pressure ($\Delta p_l^{p,k}$) at a given material point is calculated according to **(4)** and can be presented as follows:

$$\Delta p_l^{p,k} = \Delta t \frac{K_l^{p,k}}{\left( 1 - \frac{K_l^{p,k}}{S_l^{p,k}} \frac{\partial S_l^{p,k}}{\partial s_l^{p,k}} \right)} \left[ \frac{(1 - n^{p,k})}{n^{p,k}} tr\left( \dot{\varepsilon}_s^{p,k} \right) + tr\left( \dot{\varepsilon}_l^{p,k} \right) \right], \tag{18}$$

where $s_l^{p,k} = -p_l^{p,k}$. The specific moisture capacity ($\partial S_l^{p,k}/\partial s_l^{p,k}$) is obtained using **Eq. 9**. Then, the pore water pressure is updated using $p_l^{p,k+1} = p_l^{p,k} + \Delta p_l^{p,k}$.

(VII). The MP's degree of saturation ($S_l^{p,k+1}$) and relative permeability ($k_{rel}^{p,k+1}$) then update in this step. When the updating results in a pore water pressure ($p_l^{p,k+1}$) larger than zero, $S_l^{p,k+1}$ updates using **Eq. 5**. Then, $k_{rel}^{p,k+1}$ updates based on $S_l^{p,k+1}$ using **Eqs. 6**, **7**.

(VIII). The other MP information then updates at this step. The updating volume of the solid phase at MP is described as $V_s^{p,k+1} = V_s^{p,k} [1 + tr(\Delta\varepsilon_s^{p,k})]$. The MP's position at the solid phase is updated using the nodal velocity of solid phase as follows:

$$\mathrm{x}_s^{p,k+1} = \mathrm{x}_s^{p,k} + \Delta t \sum_{i=1}^{N^n} \boldsymbol{v}_s^{i,k+1} N^{p,k}. \tag{19}$$

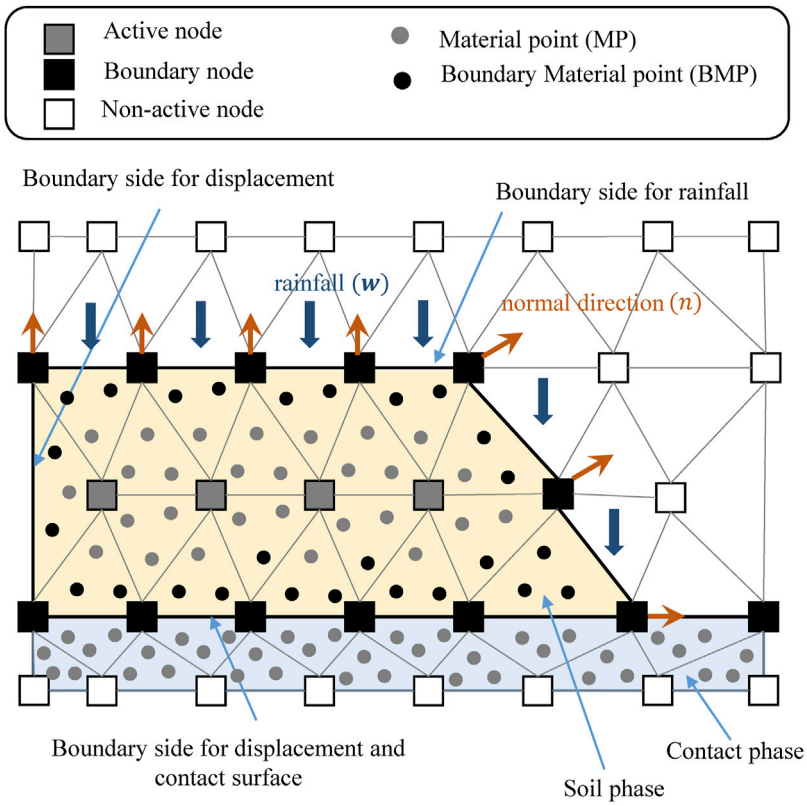


**FIGURE 3 |** Schematic of the boundary treatment.

(IX). Finally, the information for the material points at the new time $k + 1$ is carried for the next step, and the mesh nodes are initialized as shown in **Figure 2D**.

## Treatment of the Boundary and Initial Conditions

In order to deal with boundary conditions in the material point method, the boundary node, boundary side, and boundary material point have to be determined, as shown in **Figure 2**. (Bandara et al., 2016; Ceccato et al., 2020; Martinelli et al., 2020). A schematic of the boundary treatment is depicted in **Figure 3**. For the displacement and contact surface boundaries, prior to the calculation, the boundary node and the boundary side have to be assigned. For the rainfall boundaries, the boundary node and boundary side are detected using the active element and the empty element at each time step. The active element and the empty element are identified by the location of the MPs. When the material point is adjacent to the boundary side, it is defined as the boundary material point.

In a case of a fully fixed node, the nodal velocities and accelerations are set to zero (Al-Kafaji, 2013), so the specified values at the boundary node will not update in the computational cycle. Along a contact surface, the nodal velocities are adjusted to avoid interpenetration and to have tangential forces compatible with the Coulomb's friction criterion (Al-Kafaji, 2013). The solid phase nodal accelerations ($a_s^{n,k}$) along a specific contact surface are adjusted according to the given friction coefficient after the computational cycle carried out in the second step (II).

In a case under rainfall conditions, this paper follows the study of Martinelli et al. (2020). When the prescribed seepage velocity is known, i.e., rainfall intensity (mm/hr), the nodal accelerations of each phase ($a_s^{n,k}$, $a_l^{n,k}$) are adjusted in order to comply with the rainfall data after the computational cycle in the second step (II). The description about the correction of nodal acceleration is following Martinelli et al. (2020), and has been written in the first section of **Supplementary Material**. The validation of the rainfall boundary condition is mentioned in the second section of **Supplementary Material**. When the prescribed pore water pressure is specified, it is applied to the boundary material point (BMP) directly, and the pore water pressure will not update in the computational cycle in the sixth step (VI).

In the treatments that take place in the initial condition, the initial state is assumed to be satisfied with geostatic and hydrostatic conditions, and so the initial velocities of each phase can be set as zero (Bandara et al., 2016; Siemens, 2018). The initial stress distribution is set using a $K_0$ procedure (Bandara et al., 2016). The initial pore water pressure distribution is given corresponding to the phreatic surface, and the phreatic line can be defined by users. Above the phreatic surface, the suction is

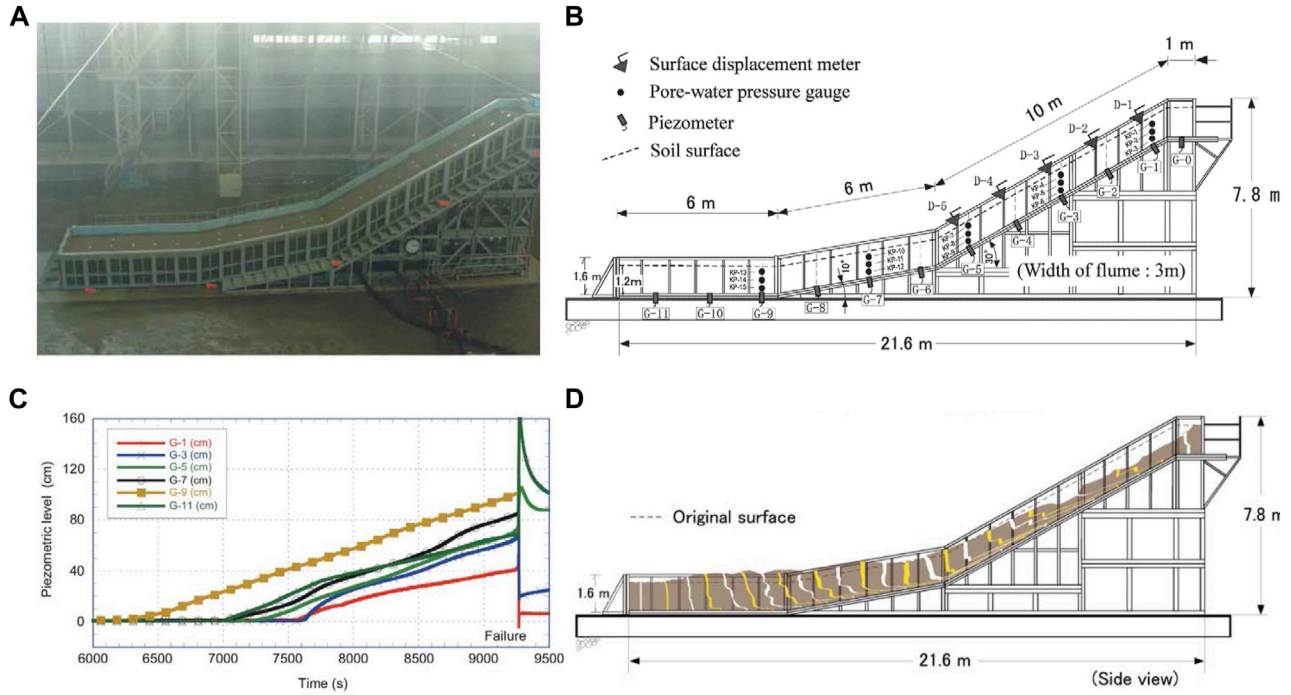


**FIGURE 4 |** The of rainfall-induced slope failure experiment (Moriwaki et al., 2004): **(A)** Model configuration during the experiment; **(B)** The setup for the steel flume and the location of the sensors; **(C)** The piezometer record before the slope failure **(D)** Material deformation after the slope failure.

generated hydrostatic until it reaches a prescribed value. Below the phreatic surface, the pore water pressure is generated according to the depth of the groundwater (Siemens, 2018).

## Numerical Simulation of a Lab-Scale Rainfall-Induced Slope Failure

The proposed model was used to simulate an experiment involving a lab-scale rainfall-induced slope failure (**Figure 4**), which was originally performed by Moriwaki et al. (2004). The steel flume was 23 m long, 7.8 m high, 3 m wide, and 1.6 m deep, as shown in **Figure 4B**. The model was composed of four segments with different lengths and inclinations. The first one, located at the toe, was horizontal and 6-m-long; the second one was 6-m-long 10° inclined segment; the third one was a 10-m-long 30° segment, and the final one was horizontal and 1 m long. The flume was filled with loose Sakuragawa River sand with a uniform depth of 1.2 m. Instruments were installed with five surface displacement meters (D-1 to D-5), fifteen pore-water pressure gauges (KP-01 to KP-15), and eleven piezometers (G-1 to G-11), as shown in **Figure 4B**. A constant intensity of rainfall at 100 mm/h ($\approx 2.78 \times 10^{-5}$ m/s) was sparked, as shown in **Figure 4A**. About 6,300 s after the start of the rainfall, the piezometers recorded rising pore-water pressure linearly, and a rapid movement of soil was triggered at 9,267 s. The evolution of the pore water pressure is shown in **Figure 4C**. The distribution of deformation after the slide stopped is depicted in **Figure 4D**.

The configuration in simulation for the experiment of rainfall-induced slope failure is depicted in **Figure 5**. The computational domain ranged from $x = 0$ m to $x = 21.6$ m and $y = -1$ m to $y = 8$ m, with a element size of 0.25 m. In total, 9,925 elements and 3,226 nodes were used. For each element, eight particles were specified. The soil phase was given according to the geometry of the soil layer, and it was located on a contact phase defined as a rigid body. A contact surface was located at the interface between the soil phase and the contact phase. For the assignment of the boundary conditions, two side and bottom boundaries for the contact phase were given as a type of fixed displacement condition, and two side boundaries for the soil phase were set as a type of roller displacement. For the rainfall boundary condition, a constant intensity of rainfall was equal to $3 \times 10^{-5}$ m/s and was indicated at soil surface phase. For the initial condition, the initial stress field was generated using a $K_0$ procedure, and the suction was generated hydrostatically from the impervious layer. Following the parametric study of Yang et al. (2021), it was assumed that the maximum suction was not over 10 kPa.

The material parameters for the soil phase are given in **Table 1**. The size of solid grain and porosity density directly followed Moriwaki et al. (2004). Yang et al. (2021) carried out a parametric study using various hydrological factors, i.e., a soil-water retention curve (SWCC) and a hydraulic conductivity curve (HCC), and their suggested parameters were used in this study. Ghasemi et al. (2019) and Nguyen et al. (2021) also did a parametric study using various geological factors, i.e., the Young's modulus, and friction angle, etc., and this study followed their suggestions for the Young's modulus, friction analge.

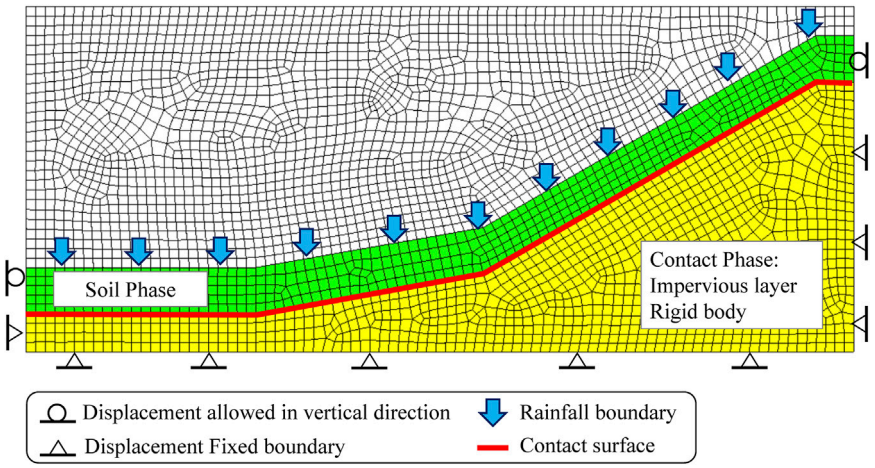


**FIGURE 5 |** Configuration in the simulation of a rainfall-induced slope failure.

**TABLE 1 |** Material parameters for the rainfall-induced slope failure.

| Parameters | Unit | Soil phase |
|---|---|---|
| Young's modulus ($E$) | kPa | 10,000[b, c, d] |
| sPoisson's ratio ($\nu$) | — | 0.3[b, c, d] |
| Density of solid grain ($\rho_s$) | kg/m$^3$ | 2,690[a] |
| Density of water ($\rho_l$) | kg/m$^3$ | 1,000[b, c, d] |
| Porosity ($n$) | — | 0.46[a] |
| Bulk modulus of water ($K_l$) | kPa | 200,000[e] |
| Dynamic viscosity of liquid ($\mu_l$) | kPa·s | $10^{-6}$[b, c, d] |
| Intrinsic permeability ($k_l$) | m$^2$ | $3 \times 10^{-11}$[b, d] |
| Air-entry pressure ($p_0$) | kPa | 4.35[b] |
| Empirical parameter ($\lambda$) | — | 0.61[b] |
| Residual degree of saturation ($S_{min}$) | — | 0.87[b] |
| Maximum degree of saturation ($S_{max}$) | — | 1[b] |
| Friction angle | ° | 34[b, c, d] |
| Friction angle at contact phase | ° | 34[e] |
| Dilatancy angle | ° | 0[b, c, d] |
| Cohesion | kPa | 0[c, d] |

[a]*Moriwaki et al. (2004);*
[b]*Yang et al. (2021);*
[c]*Nguyen et al. (2021);*
[d]*Ghasemi et al. (2019);*
[e]*Calibration parameters to match the observed result from Moriwaki et al. (2004).*

The proposed model was validated against the experimental results. The measurements and simulations of the pore water pressure were generally in acceptable agreement. The comparison is shown in **Figure 6**. Moriwaki et al. (2004) reported that the measured pore water pressure (PWP) at G-9 rose earlier than at G-5 by about 1,000 s. The measured rising speed of the PWP at G-9 and G-5 were about $3.4 \times 10^{-4}$ m/s and $3.7 \times 10^{-4}$ m/s, respectively. According to **Figure 6A**, the proposed model predicted that the time interval between the rise in the PWP between G-9 and G-5 was about 800 s. The speed at which the PWP rose at locations G-9 and G-5 were estimated to be lower by about 24 and 20%, respectively. In terms of the verification of the cumulative surface displacement, the observed and simulated evolutions of cumulative surface displacement at D-1, D-3, and D-5 are depicted in **Figure 6B**. Moriwaki et al. (2004) reported that the slope failure occurred suddenly and the elapsed time was approximately 6 s. The maximum cumulative surface displacements were measured to be between 3 and 3.7 m. In the simulation, the elapsed time for the slope movement was approximately 10 s, and the maximum cumulative surface displacements were estimated to be between 4.3 and 5 m. At D-5, the measured and simulated velocity of soil movement were consistent during the elapsed time of 0–5 s. However, the sliding velocity simulations at D-1 and D-3 were estimated to be lower than the measured results. Moriwaki et al. (2004) found that the soil filled the flume at a relative density of 3%, and the deformation was accompanied with a mix of compaction and shear. It was felt here that the proposed model using the standard Mohr-Coulomb model might not be a suitable option to simulate post-failure behavior of lab-scale rainfall-induced slope failure. In short, the proposed model using MPM exhibited better performance than that found in a previous study, in which the evolution of the pore water pressure during infiltration could be investigated and improvements in the soil deformation simulation were achieved.

## PARAMETRIC STUDY

In the parametric study, the effect of rainfall intensity on the rising pore water pressure and dynamic soil behavior characteristics were evaluated. With help of the proposed model using MPM, variations in the rainfall intensity corresponding to the pattern of rising pore water pressure and slope failure can be discussed in this section.

The ratio of $I/k_s$ was introduced by Yang et al. (2021) and applied to investigate the magnitude of the rainfall effect. Accordingly, the ratio of rainfall intensity ($I$) to hydraulic conductivity ($k_s$) is sensitive to the time required to increase the time and speed of PWP changes in the bottom soil layer ($v_{PWP}$). Hence, the $I/k_s$ ratio was applied in the parametric study.

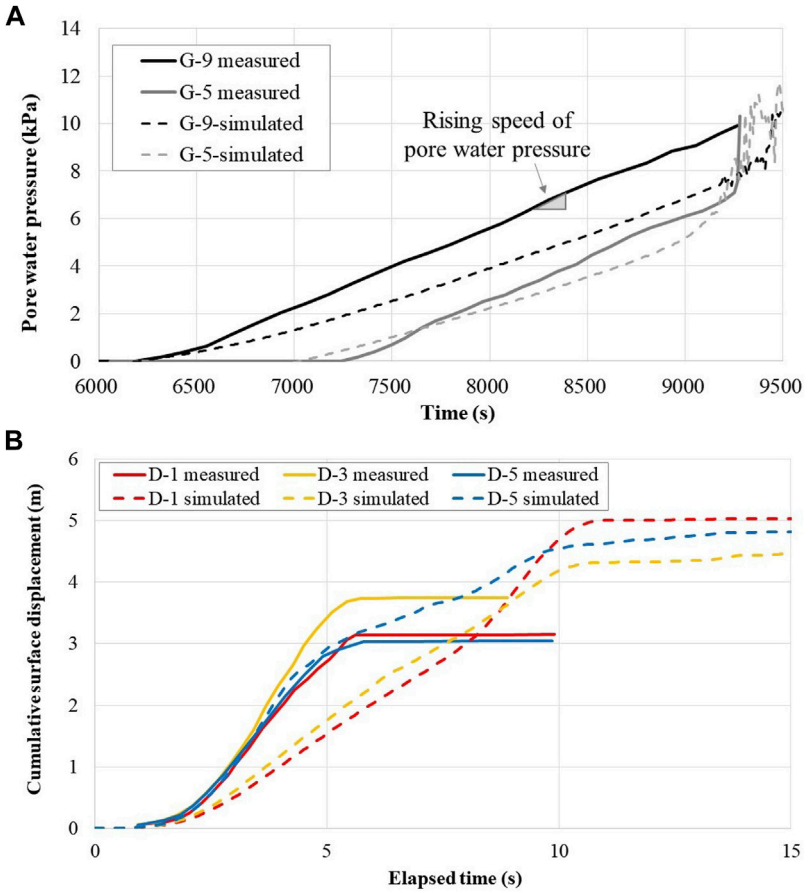


**FIGURE 6 |** Comparison of the measured and simulated results: **(A)** Evolution of pore water pressure at G-5 and G-9; **(B)** Evolution of cumulative surface displacement at D-1, D-3, and D-5.

Seven values of rainfall intensity ($I$) were used in the parametric study. According to **Table 1**, the hydraulic conductivity ($k_s$) equaled $3 \times 10^{-4}$m/s, corresponding to the intrinsic permeability ($k_I$) and dynamic viscosity of liquid ($\mu_l$) values. Because $I$ was normalized by $k_s$, the seven values could be presented as $I/k_s = 1$, $I/k_s = 0.75$, $I/k_s = 0.5$, $I/k_s = 0.25$, $I/k_s = 0.1$, $I/k_s = 0.75$, and $I/k_s = 0.67$. The lab-scale rainfall-induced slope failure was simulated with the seven different rainfall intensities, and the other parameters were kept at the given values, as shown in **Table 1**.

## Effect of Rainfall on Changes in the Pore Water Pressure

The ratio of the various rainfall intensities against the speed at which the pore water pressure rose at G-5 and G-9 is depicted in **Figure 7A**. The speed of the rise in pore water pressure ($v_{PWP}$) was divided by the hydraulic conductivity ($k_s$), and the $v_{pwp}/k_s$ ratio was introduced to present the intensity of the speed at which the pore water pressure rose. An interesting finding was that the increasing $I/k_s$ ratio caused dramatic response in the form of the growth in the $v_{pwp}/k_s$ ratio. In the case of $I/k_s = 0.1$, the $v_{pwp}/k_s$ ratios at G-9 and G-5 were 0.85 and 0.99, respectively. This means that speed at which the PWP rose was close to the hydraulic conductivity when the rainfall intensity was relatively small. In the case of $I/k_s = 0.1$, the $v_{pwp}/k_s$ ratios at G-9 and G-5 reached 18.9 and 20.7, respectively. This means that a sudden increase in pore water pressure can be caused by high intensity rainfall.

A further investigation on the effects of variations in rainfall intensity on the amount of time required for the pore water pressure rise was carried out, the results of which are plotted in **Figure 7B**. The locations where pore water pressure rose preferentially varied with the rainfall intensity. Accordingly, a schematic of the changes rainfall-induced pore water pressure is shown in **Figure 8**. When the $I/k_s < 0.5$, the simulation indicated that a unsaturated wetting front developed from the ground surface and moved forward to the bottom soil layer, as shown in **Figure 8A-i**. After the wetting front reached the bottom soil layer, as depicted in **Figure 8A-ii**, ground water was generated from the lowest location on the slope. Hence, the time required for the pore water pressure to rise at G-9 was earlier than that at G-5, as shown in **Figure 7B**. When the $I/k_s > 0.5$ in the simulation, a wetting front with high degree of saturation developed, as shown in **Figure 8B-i**. With the help of the

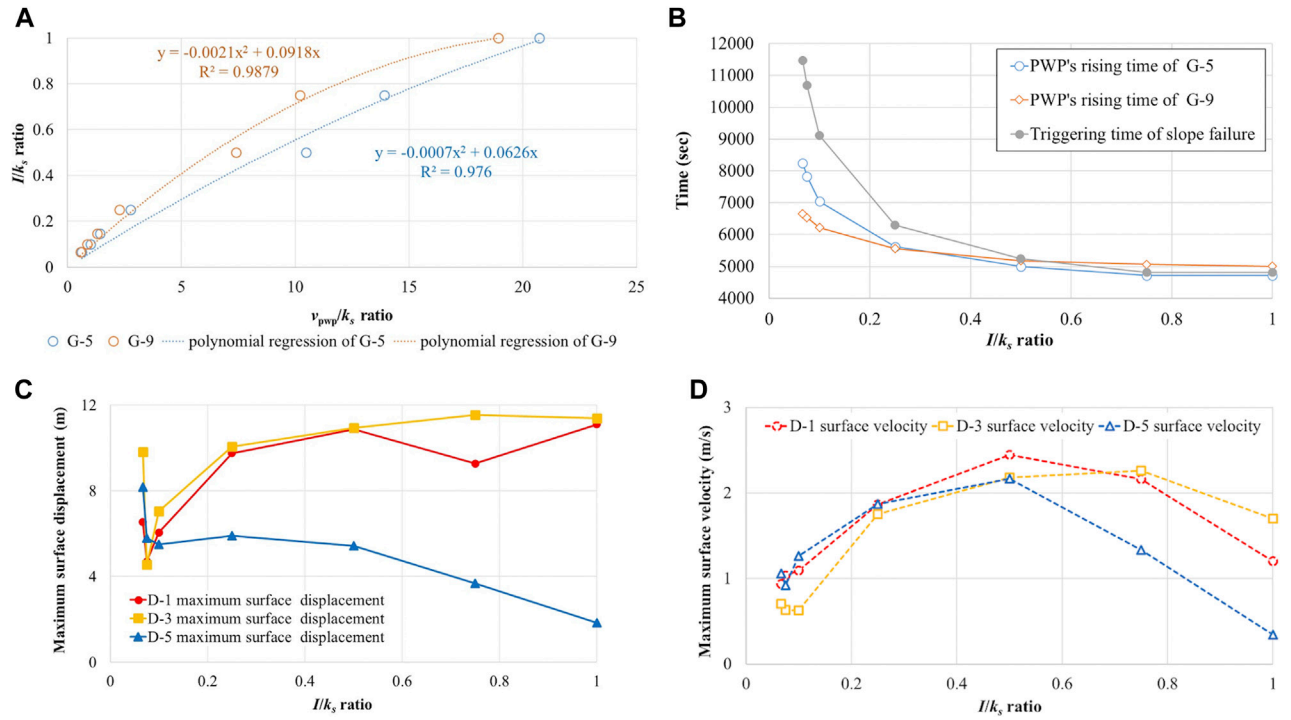


**FIGURE 7 |** Effects of rainfall intensity on a rainfall-induced landslide: **(A)** changes in the $v_{PWP}/k_s$ ratio; **(B)** changes in the time at which the PWP rose and the time at which slope failure was triggered; **(C)** changes in the maximum surface displacement; **(D)** changes in the maximum surface velocity.

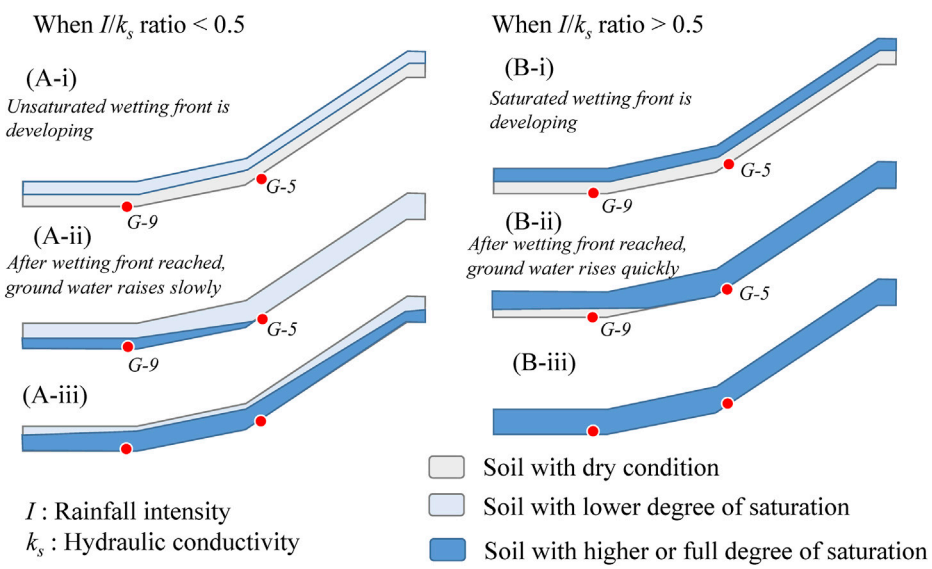


**FIGURE 8 |** Schematic of changes in rainfall-induced pore water pressure.

higher intensity rainfall, the forward speed of the wetting front was faster. As shown in **Figure 8B-ii**, the wetting front reached G-5 earlier than G-9, but the difference in the time required for the PWP to rise at G-5 and G-9 was very small. After the wetting front reached the bottom soil layer, as depicted in **Figure 8B-iii**, the soil layer was close to a fully saturated condition. The different

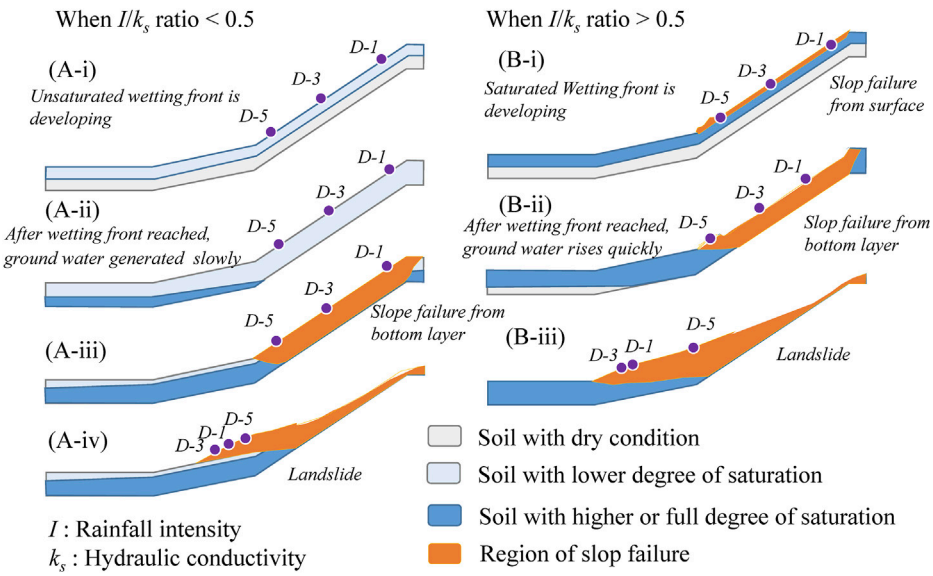


**FIGURE 9 |** Schematic of the effects of rainfall on slope failure.

characteristics of the rainfall-induced pore water pressure resulted in different types of post-failure behavior. This implied that the ratio of $I/k_s$ is a very important index to distinguish the type of slope failure.

## Effect of Rainfall on the Slope Failure

The effect of rainfall intensity in the post-failure stage was investigated according to the simulated maximum surface displacement and maximum surface velocity. As mentioned in the last paragraph, the characteristics of the dynamic soil behavior were different due to the increases in the pore water pressure. A schematic of the effects of rainfall on the slope failure patterns is depicted in **Figure 9**. When the $I/k_s < 0.5$, the unsaturated wetting front was developing and resulted in a decrease in suction. The slope remained stable due to the contribution of friction force, as shown in **Figure 9A-i**. After the wetting front reached the bottom soil layer, slope failure was triggered due to the increase in the groundwater level, and the soil body began to deform from the bottom soil layer, as depicted in **Figure 9A-ii**. The slope failure at D-5 was triggered earlier than at D-3 and D-1 due to the location of the phreatic surface, as shown in **Figure 9A-iii**. After the phreatic surface increased due to the water infiltration, slope failures at D-3 and D-1 were triggered. According to the simulation, when the rainfall intensity was less, the maximum cumulative surface displacement was shorter, and the maximum surface velocity was slower, as depicted in **Figures 7C,D**. These results implied that a slower moving and shorter run-out landslide was triggered by a lower levels of rainfall intensity.

When the $I/k_s > 0.5$, a wetting front developed with a high degree of saturation, which cause not only a decrease in the suction, but also an increase in the pore water pressure near the ground surface. Because the rainfall generated an increase in the pore water pressure from the ground surface, it resulted a shallow slope failure, as shown in **Figure 9B-i**. Hence, the surfaces of D-3 and D-1 began to move at this point. The depth of the slope failure increased corresponding to the growth of the wetting front, as shown in **Figure 9A-ii**. Until the wetting front reached the bottom soil layer, the slope with the 30° incline began to move entirely, as shown in **Figure 9B-iii**. According to the simulation shown in **Figure 7C**, the run-out distance increased with increases in the $I/k_s$ ratio. This implied that high intensity rainfall can easily induce a long run-out landslide.

Based on the parametric study, it was inferred that the rainfall intensity index plays an important role in distinguishing the slope failure pattern. In the case of the lab-scale rainfall-induced slope failure, the critical $I/k_s$ ratio was 0.5. At $I/k_s < 0.5$, the slope failure was triggered by rising ground water, and the mechanism was similar to that of the rainfall-induced deep-seated landslide. At $I/k_s > 0.5$, the slope failure was triggered by infiltration water, and the mechanism was close to that for a classic shallow landslide. This finding is important information that can be applied in the design of rainfall-induced landslide warning systems.

# CONCLUSION

In this study, a numerical model using the material point method was applied to investigate the dynamic soil behavior of a rainfall-induced landslide. The proposed numerical model was implemented based on a set of pseudo-3-phase 1-point MPM formulations and overcame the limitations related to rainfall boundary conditions encountered in previous studies, so the

effect of rainfall on the dynamic behavior of unsaturated soil could be investigated more comprehensively. A 1-D infiltration problem and a lab-scale rainfall-induced slope failure were performed to validate and benchmark the MPM code. Then, the proposed model was used to evaluate the effect of rainfall on the changes in pore water and slope failure. The following conclusions were drawn:

1) According to the effect of rainfall on changes in the pore water pressure, an important finding was that abnormally rising pore water pressure can be induced by high-intensity rainfall. The ratio of rainfall intensity and hydraulic conductivity ($I/k_s$) was introduced in this study. When the rainfall intensity was small, for example, $I/k_s = 0.1$, the speed at which the pore water pressure rose was close to the hydraulic conductivity. However, when the rainfall intensity became strong, i.e., the $I/k_s$ ratio equaled 0.5, the speed at which the pore water pressure rose became over 10 times faster than the hydraulic conductivity. Because the changes in the pore water pressure change significantly influenced the stability of the slope, understanding changes in abnormal pore water pressure was deemed to be important. In this study, the $I/k_s$ ratio was considered to be a warning index to estimate a rainfall-induced abnormal rise in pore water pressure.
2) Based on the effects of rainfall on the slope failure, another important finding was that the types of slope failure were related to the magnitude of the rainfall intensity. In the case of lab-scale rainfall-induced slope failure, the types of slope failure could be distinguished by a critical value $I/k_s = 0.5$, where when $I/k_s > 0.5$, the numerical results showed that the wetting front developed with a higher degree of saturation and did not reduce the suction but increased the pore water pressure in the nearby ground surface. Hence, the slope failure began from the surface of the soil, and the mechanism was similar to that of a classic shallow landslide. When $I/k_s \leq 0.5$, the wetting front developed with a lower degree of saturation, it only reduced the suction, and the slope remained in a stable state due to the contribution of friction force. Until the wetting front reached the bottom soil layer, pore water pressure was generated, which resulted in slope failure. The mechanism was similar to what occurs in a typical deep-seated landslide. This finding indicated that the $I/k_s$ ratio can be a warning index by which to estimate the failure types of rainfall-induced landslides.

In reality, the characteristics of landslide behavior are not only affected by the hydrological conditions but also are related to geological conditions and topography. With different constitutive models, the dynamic behavior of soil can be investigated and lead to different understandings of this phenomenon. Therefore, the proposed model should be modified with different constitutive models, so it will have more potential applications.

## DATA AVAILABILITY STATEMENT

The raw data supporting the conclusion of this article will be made available by the authors, without undue reservation.

## AUTHOR CONTRIBUTIONS

Conceptualization, W-LL and C-LS; methodology, W-LL and MM; formal analysis, W-LL and MM; W-LL wrote the manuscript, and all authors contributed to improving the paper.

## FUNDING

This work was supported by the National Cheng Kung University (project of NCKU 90 and Beyond, HUA110-3-3-090).

## SUPPLEMENTARY MATERIAL

The Supplementary Material for this article can be found online at: https://www.frontiersin.org/articles/10.3389/feart.2021.764393/full#supplementary-material

## REFERENCES

Al-Kafaji, I. K. A. (2013). *Formulation of a Dynamic Material point Method (MPM) for Geomechanical Problems. PhD Thesis*. Stuttgart, Germany: Universität Stuttgart.

Bandara, S., Ferrari, A., and Laloui, L. (2016). Modelling Landslides in Unsaturated Slopes Subjected to Rainfall Infiltration Using Material point Method. *Int. J. Numer. Anal. Meth. Geomech.* 40 (9), 1358–1380. doi:10.1002/nag.2499

Bandara, S., and Soga, K. (2015). Coupling of Soil Deformation and Pore Fluid Flow Using Material point Method. *Comput. geotechnics* 63, 199–214. doi:10.1016/j.compgeo.2014.09.009

Calvello, M., Cascini, L., and Sorbino, G. (2008). A Numerical Procedure for Predicting Rainfall-Induced Movements of Active Landslides along Pre-existing Slip Surfaces. *Int. J. Numer. Anal. Meth. Geomech.* 32 (4), 327–351. doi:10.1002/nag.624

Cascini, L., Calvello, M., and Grimaldi, G. M. (2014). Displacement Trends of Slow-Moving Landslides: Classification and Forecasting. *J. Mt. Sci.* 11 (3), 592–606. doi:10.1007/s11629-013-2961-5

Cascini, L., Calvello, M., and Grimaldi, G. M. (2010). Groundwater Modeling for the Analysis of Active Slow-Moving Landslides. *J. Geotech. Geoenviron. Eng.* 136 (9), 1220–1230. doi:10.1061/(asce)gt.1943-5606.0000323

Ceccato, F., Girardi, V., Yerro, A., and Simonini, P. (2019). *Evaluation of Dynamic Explicit MPM Formulations for Unsaturated Soils*.

Ceccato, F., Yerro, A., Girardi, V., and Simonini, P. (2020). Two-phase Dynamic MPM Formulation for Unsaturated Soil. *Comput. Geotechnics* 129, 103876.

Cuomo, S., Ghasemi, P., Martinelli, M., and Calvello, M. (2019). Simulation of Liquefaction and Retrogressive Slope Failure in Loose Coarse-Grained Material. *Int. J. Geomech.* 19 (10), 04019116. doi:10.1061/(asce)gm.1943-5622.0001500

Cuomo, S. (2020). Modelling of Flowslides and Debris Avalanches in Natural and Engineered Slopes: a Review. *Geoenviron Disasters* 7 (1), 1–25. doi:10.1186/s40677-019-0133-9

Galavi, V. (2010). *Groundwater Flow, Fully Coupled Flow Deformation and Undrained Analyses in PLAXIS 2D and 3D*. Delft, Netherlands: Plaxis Report.

Ghasemi, P., Cuomo, S., Di Perna, A., Martinelli, M., and Calvello, M. (2019). MPM-analysis of Landslide Propagation Observed in Flume Test. Proc. Of II International Conference on the Material Point Method for Modelling

Soil–Water–Structure Interaction. 8–10 January 2019. UK: University of Cambridge.

Jassim, I., Stolle, D., and Vermeer, P. (2013). Two-phase Dynamic Analysis by Material point Method. *Int. J. Numer. Anal. Meth. Geomech.* 37 (15), 2502–2522. doi:10.1002/nag.2146

Lee, W. L., Martinelli, M., and Shieh, C. L. (2019a). in Numerical Analysis of the Shiaolin Landslide Using Material Point Method. The 7th International Symposium on Geotechnical Safety and Risk (Taiwan, 638–643. https://10.3850/978-981-11-2725-0 IS7-2-cd.

Lee, W. L., Shieh, C. L., and Martinelli, M. (2019b). "Modelling Rainfall-Induced Landslides with the Material point Method: the Fei Tsui Road Case," in Proceedings of the XVII European Conference on Soil Mechanics and Geotechnical Engineering. Iceland https://10.32075/17ECSMGE-2019-0346.

Lei, X., He, S., Chen, X., Wong, H., Wu, L., and Liu, E. (2020). A Generalized Interpolation Material point Method for Modelling Coupled Seepage-Erosion-Deformation Process within Unsaturated Soils. *Adv. Water Resour.* 141, 103578. doi:10.1016/j.advwatres.2020.103578

Leroueil, S. (2001). Natural Slopes and Cuts: Movement and Failure Mechanisms. *Géotechnique* 51 (3), 197–243. doi:10.1680/geot.51.3.197.39365

Leroueil, S., and Picarelli, L. (2012). *Geotechnical Engineering State of the Art and Practice Keynote Lectures from GeoCongress 2012*, 122–156. doi:10.1061/9780784412138.0006

Liu, X., Wang, Y., and Li, D.-Q. (2020). Numerical Simulation of the 1995 Rainfall-Induced Fei Tsui Road Landslide in Hong Kong: New Insights from Hydro-Mechanically Coupled Material point Method. *Landslides* 17 (12), 2755–2775. doi:10.1007/s10346-020-01442-2Assessment of Slope Stability

Liu, X., and Wang, Y. (2021). Probabilistic Simulation of Entire Process of Rainfall-Induced Landslides Using Random Finite Element and Material point Methods with Hydro-Mechanical Coupling. *Comput. Geotechnics* 132, 103989. doi:10.1016/j.compgeo.2020.103989

Martinelli, M., Lee, W.-L., Shieh, C.-L., and Cuomo, S. (2020). "Rainfall Boundary Condition in a Multiphase Material Point Method," in Workshop on World Landslide Forum (Cham: Springer), 303–309. doi:10.1007/978-3-030-60706-7_29

Moriwaki, H., Inokuchi, T., Hattanji, T., Sassa, K., Ochiai, H., and Wang, G. (2004). Failure Processes in a Full-Scale Landslide experiment Using a Rainfall Simulator. *Landslides* 1 (4), 277–288. doi:10.1007/s10346-004-0034-0

Mualem, Y. (1976). A New Model for Predicting the Hydraulic Conductivity of Unsaturated Porous Media. *Water Resour. Res.* 12 (3), 513–522. doi:10.1029/WR012i003p00513

Nguyen, T. S., Yang, K. H., Ho, C. C., and Huang, F. C. (2021). *Postfailure Characterization of Shallow Landslides Using the Material Point Method*. London, United Kingdom: Geofluids.

Picarelli, L., Urciuoli, G., and Russo, C. (2004). Effect of Groundwater Regime on the Behaviour of Clayey Slopes. *Can. Geotech. J.* 41 (3), 467–484. doi:10.1139/t04-009

Siemens, G. A. (2018). Thirty-Ninth Canadian Geotechnical Colloquium: Unsaturated Soil Mechanics - Bridging the gap between Research and Practice. *Can. Geotech. J.* 55 (7), 909–927. doi:10.1139/cgj-2016-0709

Soga, K., Alonso, E., Yerro, A., Kumar, K., and Bandara, S. (2016). Trends in Large-Deformation Analysis of Landslide Mass Movements with Particular Emphasis on the Material point Method. *Géotechnique* 66 (3), 248–273. doi:10.1680/jgeot.15.lm.005

Sulsky, D., Zhou, S. J., and Schreyer, H. L. (1995). Application of a Particle-In-Cell Method to Solid Mechanics. *Comp. Phys. Commun.* 87 (1-2), 236–252. doi:10.1016/0010-4655(94)00170-7

Wang, B., Vardon, P. J., and Hicks, M. A. (2018). Rainfall-induced Slope Collapse with Coupled Material point Method. *Eng. Geology.* 239, 1–12. doi:10.1016/j.enggeo.2018.02.007

Yang, K.-H., Nguyen, T. S., Rahardjo, H., and Lin, D.-G. (2021). Deformation Characteristics of Unstable Shallow Slopes Triggered by Rainfall Infiltration. *Bull. Eng. Geol. Environ.* 80 (1), 317–344. doi:10.1007/s10064-020-01942-4

Yerro, A., Alonso, E. E., and Pinyol, N. M. (2015). The Material point Method for Unsaturated Soils. *Géotechnique* 65 (3), 201–217. doi:10.1680/geot.14.p.163

Yuan, W. H., Liu, K., Zhang, W., Dai, B., and Wang, Y. (2020). Dynamic Modeling of Large Deformation Slope Failure Using Smoothed Particle Finite Element Method. *Landslides*, 1–13. doi:10.1007/s10346-020-01375-w

Zhang, X., Chen, Z., and Liu, Y. (2016). *The Material point Method: A Continuum-Based Particle Method for Extreme Loading Cases*. Academic Press.

Zienkiewicz, O. C., Xie, Y. M., Schrefler, B. A., Ledesma, A., and Bičanič, N. (1990). Static and Dynamic Behaviour of Soils: a Rational Approach to Quantitative Solutions. II. Semi-saturated Problems. *Proc. R. Soc. Lond. A. Math. Phys. Sci.* 429 (1877), 311–321. doi:10.1098/rspa.1990.0062

**Conflict of Interest:** The authors declare that the research was conducted in the absence of any commercial or financial relationships that could be construed as a potential conflict of interest.

**Publisher's Note:** All claims expressed in this article are solely those of the authors and do not necessarily represent those of their affiliated organizations, or those of the publisher, the editors and the reviewers. Any product that may be evaluated in this article, or claim that may be made by its manufacturer, is not guaranteed or endorsed by the publisher.

frontiers in Earth Science

ORIGINAL RESEARCH
published: 16 November 2021
doi: 10.3389/feart.2021.743669

# Occurrences of Deep-Seated Creeping Landslides in Accordance with Hydrological Water Storage in Catchments

*Chih-Yu Kuo[1,2]*, Shen-En Lin[1], Rou-Fei Chen[3], Ya-Ju Hsu[4], Kuo-Jen Chang[5], Shin-Ping Lee[6], Rou-Ying Wu[1], Ching-Weei Lin[7] and Ya-Hsin Chan[1]*

[1]Research Center for Applied Sciences, Academia Sinica, Taipei, Taiwan, [2]Department of Civil Engineering, National Taiwan University, Taipei, Taiwan, [3]Department of Materials and Mineral Resources Engineering, National Taipei University of Technology, Taipei, Taiwan, [4]Institute of Earth Sciences, Academia Sinica, Taipei, Taiwan, [5]Department of Civil Engineering, National Taipei University of Technology, Taipei, Taiwan, [6]Disaster Prevention Research Center, National Cheng Kung University, Tainan, Taiwan, [7]Department of Earth Sciences, National Cheng Kung University, Tainan, Taiwan

OPEN ACCESS

**Edited by:**
*Chong Xu,*
*Ministry of Emergency Management, China*

**Reviewed by:**
*Siming He,*
*Institute of Mountain Hazards and Environment (CAS), China*
*Hongyue Sun,*
*Zhejiang University, China*
*Yulong Cui,*
*Anhui University of Science and Technology, China*

***Correspondence:**
*Chih-Yu Kuo*
*cykuo06@gate.sinica.edu.tw*

**Specialty section:**
*This article was submitted to Geohazards and Georisks, a section of the journal Frontiers in Earth Science*

**Received:** *19 July 2021*
**Accepted:** *15 October 2021*
**Published:** *16 November 2021*

**Citation:**
*Kuo C-Y, Lin S-E, Chen R-F, Hsu Y-J, Chang K-J, Lee S-P, Wu R-Y, Lin C-W and Chan Y-H (2021) Occurrences of Deep-Seated Creeping Landslides in Accordance with Hydrological Water Storage in Catchments. Front. Earth Sci. 9:743669. doi: 10.3389/feart.2021.743669*

Rainfall is one of the most important triggers of both shallow debris flows and deep-seated landslides. The triggering mechanism involves the process of water infiltration into the failure zone. For deep-seated landslides, the deeper and more extensive failure surfaces delay the effect of the process and thus delay landslide initiations. The delay is difficult to assess, especially if the sites only have scarce or insufficient monitoring data. Under these circumstances, we illustrate that the occurrences of landslides can be estimated by their correlations with the phenomenological water storage index (WSI) of a given catchment. In the present study, a total of five deep-seated landslides in TienChih (4) and SiangYang (1) are investigated. The displacements of the landslides were recorded by global positioning system (GPS) and the WSI was modelled using the tank model. The result demonstrates that the WSI correlates closer in time to the landslide motion than the rainfall, and the WSI thresholds for the landslides are inferred. Thus, this technique can be applied as an associated method to evaluate landslide initiation.

**Keywords: deep-seated creeping landslide, GPS-recorded displacement, tank model, water storage index, landslide initiation**

## 1 INTRODUCTION

Recently, in Taiwan, with continuous global positioning system (GPS) network data, eight deep-seated creeping landslide sites were identified and their causes were associated with hydrological loading, Hsu et al. (2014). The evidence was based on relating the creeping landslide events to the rainfall intensity (RI) or accumulated precipitation. In this paper, we further inspect the landslide events with a simple phenomenological quantitative hydrological model. The model, known as the tank model of Sugawara and Funiyuki (1956) and Sugawara (1961, 1995), can provide a simple idealized sketch for a regional water cycle: including precipitation, infiltration and runoff discharge. Using the model, we attempt to identify model thresholds for landslide occurrences and observe the sequential relationship between the landslides and regional water cycle.

Because of the wide extent area and deep failure surface of deep-seated landslides, the rainfall triggering mechanism involve delicate infiltration processes with site geological conditions. Detail investigations of the infiltrated water flows, however, can involve sophisticated techniques. For

example, Cappa et al. (2004) traced sulfate, nitrate concentration and spring waters on the slope to identify the characteristics of precipitation infiltration and concluded that landslide motions correlate to precipitation. Padilla et al. (2014) measured electrical conductivity, oxygen and hydrogen isotopic concentration of the groundwater and correlated the recharged groundwater to rainfall. The infiltration is found to be associated with high hydraulic conductivity area in the bedrock caused by the gravitational deformation in the investigated hillslope. Lv et al. (2019) applied tracer test, injection test and electrical resistivity tomography to resolve the underground water flow in their study area. The landslide is found mainly controlled by a vertical preferential flow pathway, one of the two major types of underground water flow patterns of the site. Zêzere et al. (2005) analyzed a series of long-term monitoring data since 1950s on the occurrences of rainfall induced shallow and deep landslides. The deep-seated landslides correlate to long period but less intensive rainfalls and it indicates that the infiltration causes the rise of groundwater table and the deep failures through reduction of shear strength of the slope materials. Nie et al. (2017) extended a tank model to include effects of snow accumulation, snowmelt and infiltration. These effects resulted in time lags and the model improved the groundwater level predictions in deep-seated landslides.

To adapt a simple tank model in the present study is because the landslides were in remote areas where detailed geological surveys and field observation data required to constrain sophisticated models are scarce or insufficient. In addition, because the lack of field data is common in the mountainous areas of Taiwan Island, a simple model can be a valuable tool that can be incorporated into hazard mitigation systems if its applicability is validated. For this purpose, we selected two landslide sites: the TienChih and SiangYang areas. Provided that a minimum set of hydrological data is available, the selection criteria are described as follows: the sites are in the catchments of streams of the lowest-possible order (furthest upstream); the catchments are as small as possible; and the landslide is of the translational type, according to the landslide classification in Varnes (1978). The concept of applications of the tank model was first tested feasible in a preliminary study of the TienChih area, Lin et al. (2017), and is extended in the present paper.

Both sites are on the southern transverse roadway. The roadway was built in the 1970s to connect the southwest (Kaohsiung City) and southeast (Taitung County) parts of the island. The total length of the roadway is approximately 209 km and most of the mountainous section of the roadway is in Yushan National Park. The highest elevation of the roadway is 2,722 m at approximately 147.5 km along the roadway. On the immediate west side (Kaohsiung side) of the peak point, Yakou, the terrain is in the catchment of the Laonung River and, on the east (Taitung side), the terrain is the Beinan River catchment. The Laonung River flows to the southwest, and the Beinan River flows to the southeast. The upstream-most flow-rate-monitored catchments of the studied regions are plotted in **Figure 1A**. The river flow rate observation stations for the two catchments are A-Chi-Ba Bridge and Hsin-Wu-Lu. Their monitoring catchment areas are 411 and 628 $km^2$, respectively. In the catchments, there are two and four rainfall monitoring stations, as marked in the figure. However, for simplicity, only the data recorded by the rainfall station closest to the landslide site are used to represent precipitation in each catchment in the current analysis. The adapted rainfall stations are marked in **Figure 2**.

The geological settings are shown in **Figure 1B**. The roadway cuts through two primary faults, the Singuan and Keiku Faults, in the south Central Mountain Range, adjoined with abundant secondary named or unnamed faults, according to Lee and Wang (1985); Lai et al. (1989) and Lin (2012). These faults are mainly of the thrust type and are arranged in the NNW-SSE direction. The geological layer at both sites is the Pilu Formation. The formation extends from NNE to SSW along the ridges of the Central Mountains, as marked in the light blue colour in **Figure 1B**. The formation mainly consists of Eocene rocks: slate and phyllite. Moving westward from the TienChih site, the surface layer changes to the Miocene Lushan Formation (argillite, slate, phyllite), and towards the east from the SiangYang site, it becomes Late Paleozoic and Mesozoic Tananao schists (black/green/siliceous schist). These rocks all have rich joint, cleavage and fold structures which indicates an active orogenous mechanism in the region. The common filling material in the Pilu Formation is quartz-rich calcite Lai et al. (1989), which generally has high water permeability.

The locations of the TienChih and SiangYang creeping landslide sites are marked in **Figure 1** and they are enlarged in **Figure 2**. Both sites were designed as resting and sightseeing areas on the roadway such that facilities, including a few monitoring instruments, were constructed. Therefore, creeping landslides were found by the installed instruments. The displacement measurements and field observations will be reported in the next section.

## 2 GPS NETWORK AND IDENTIFICATION OF CREEPING LANDSLIDES

GPSs have been gaining widespread use in real-time monitoring of surface displacements. With proper postprocessing procedures, continuous GPS (CGPS) data can achieve an accuracy of several millimetre. The data presented in this section were acquired from the island-wide GPS network constructed by the Institute of Earth Sciences, Academia Sinica and Central Weather Bureau since 1989, Yu et al. (1997, 2003); Chen et al. (2015). At the TienChih site, a CGPS station that is codenamed TENC, was set up, and recording started in 2002. At the SiangYang site, a similar station known as SIANY, started operating in 2009.

The postprocessing procedures of the collected GPS data were performed in the framework of GAMIT/GLOBK software, version 10.3, Herring et al. (2002). Double-difference phase observables were used and the influences of tropospheric and ionospheric effects were corrected. To obtain an accurate and consistent regional deformation pattern in Taiwan, a total data of 362 Taiwan and 17 IGS Asia-Pacific CGPS sites were used. The least squares linear fit was used to identify the tectonic linear

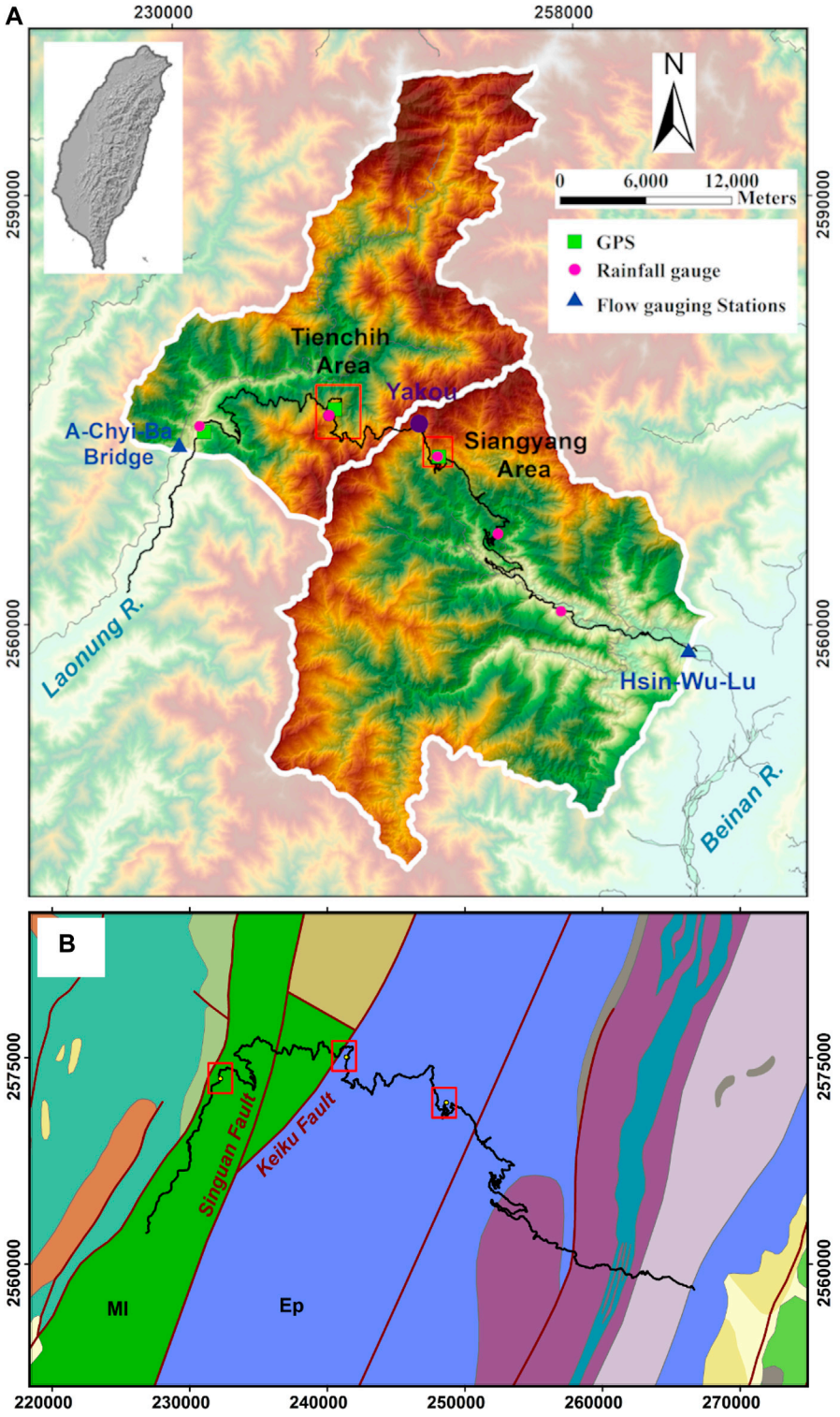


**FIGURE 1 | (A)** The upstream catchments and the section of the south transverse highway in the study area (thick solid black line). The highlighted northwest area is the 411 km$^2$ TienChih catchment and the southeast area is the 628 km$^2$ SiangYang catchment. The landslide sites, the TienChih and SiangYang areas, are marked by thick hollow red boxes. The coordinate system is TWD97. **(B)** The regional fault system and lithology. MI, Miocene argillite, slate, phyllite; Ep, Eocene slate, phyllite.

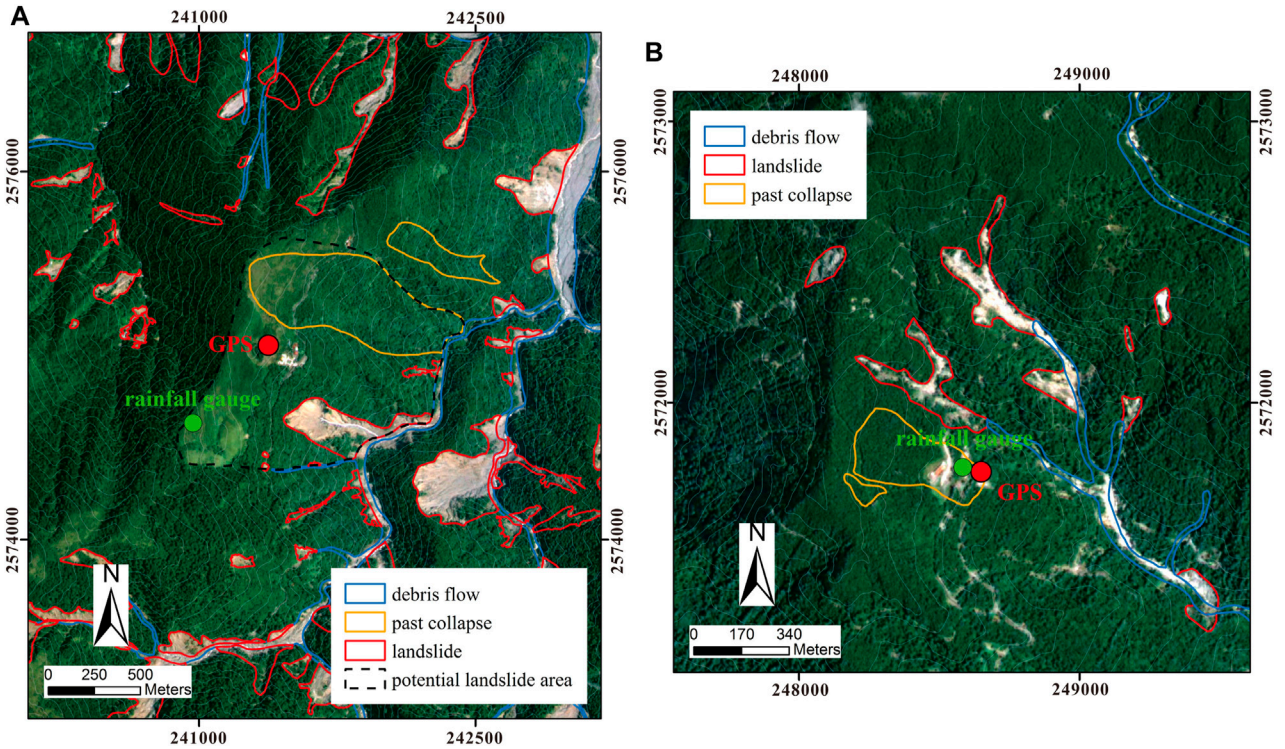


**FIGURE 2 |** Birds-eye views of the **(A)** TienChih and **(B)** SiangYang landslide areas. The aerophotos are taken in the year 2010. The rainfall and GPS stations used in the present analysis are marked, and the landslide scars and debris flow courses are outlined. The codenames of the GPS stations are TENC and SYAN for the TienChih and SiangYang areas, respectively.

station velocity, annual and semiannual periodic motions, postseismic relaxation, and offsets caused by coseismic jumps and instrument changes in the station position time series, Altamimi et al. (2007). Then, the statistical outliers, linear velocities, postseismic relaxation, and instrumental offsets were removed.

The residual GPS position time series of both stations are plotted in **Figure 3**. They exhibited several clearly identifiable intermittent displacements, of which TENC recorded four because of its longer period in operation. These intermittent displacements were correlated with extreme precipitation events: 6/29/2004 (Month/Day/Year) Mindulle typhoon, 7/18/2005 Haitang typhoon, 5/17/2006 heavy rainfall and 8/7/2009 Morakot typhoon. The successive displacements indicated that TENC moved unidirectionally towards the southeast-east (SEE) between 2002 and 2012. The extreme typhoon Morakot caused displacements with east, north and vertical components of 245, −49, −243 mm, respectively. SIANY also moved towards SEE after the Morakot typhoon. The displacement directions of the two sites are shown in **Figure 4** which correspond exactly to the descending direction of the slopes, i.e., translational landslide. Because of poor climate conditions (typhoons, heavy clouds and rainfall) when landslides are in motion, GPS stations may not obtain data, site accessibility is lost or instrumental damage occurs. The breaks in data impede hydrological analysis, except for the unique recordings taken in the Morakot event, cf. **Figure 10**.

The cumulative rainfall of Morakot typhoon was reached 2,700 mm in 5 days. The amount of precipitation was almost equal to the average annual rainfall on the island. This typhoon resulted in numerous landslides, excessive floods and severe fatalities in the southern part of Taiwan and after the strike, a series of light detection and ranging (LiDAR) surveys was performed over that area in 2010 by the Central Geological Survey. The LiDAR technique produces high-resolution digital elevation models (DEMs) and is superior in terms of high-precision and vegetation-penetrating capacities. The derived DEM of the LiDAR survey had a grid size with a 1 × 1 m resolution based on the average point cloud density of 0.5 point/$m^2$. For the two landslide sites, the DEMs are shown in **Figure 4**.

With high-resolution DEMs, surface cleavages, scarps and outcrops can be visually identified in the indoor preparation phase prior to field geological surveys. As shown in **Figure 4**, typical sackungen structures are found along ridge crests in massive competent rocks, running parallel to the slope contours and to the strikes of main rock discontinuities (foliation). Surface failure usually develops steep into the mountainside by gravitational stresses; therefore, scarps are created. For example, **Figure 5A** presents the slope profile of a shallow landslide area after the Morakot typhoon (the central scarp near the rainfall gauge marked in **Figure 2A**). A typical cleavage structure (fault gouge zone) in the area and underground water seepage are shown. **Figure 5B** illustrates the crack openings

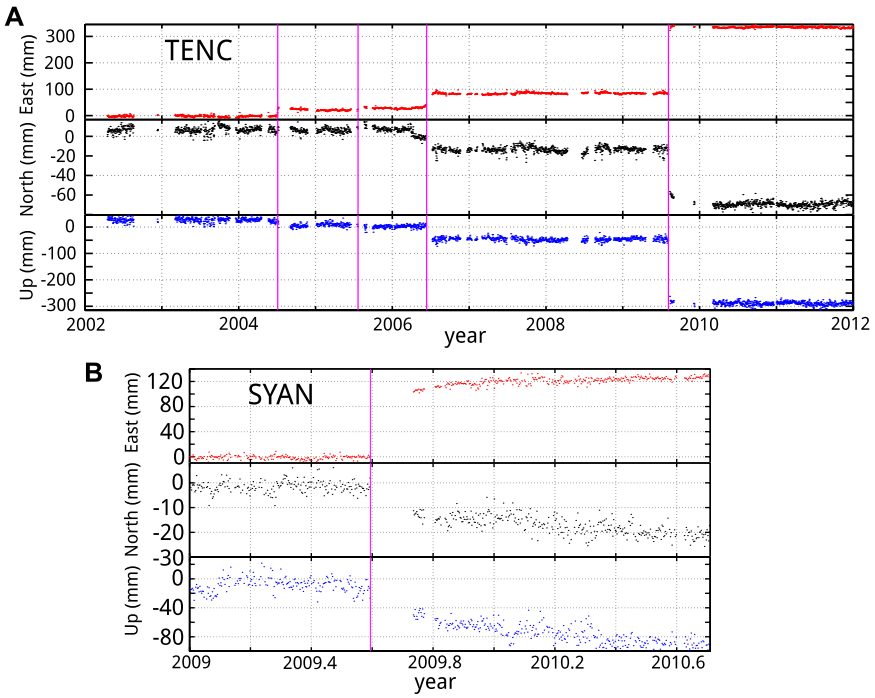


**FIGURE 3 |** Residual GPS position time series of **(A)** TienChih and **(B)** SiangYang landslide areas. The vertical magenta lines mark the landslide events: 6/29/2004 (Month/Day/Year) Mindulle typhoon, 7/18/2005 Haitang typhoon, 5/17/2006 heavy rainfall and 8/7/2009 Morakot typhoon. Note that the horizontal time axes are on different scales.

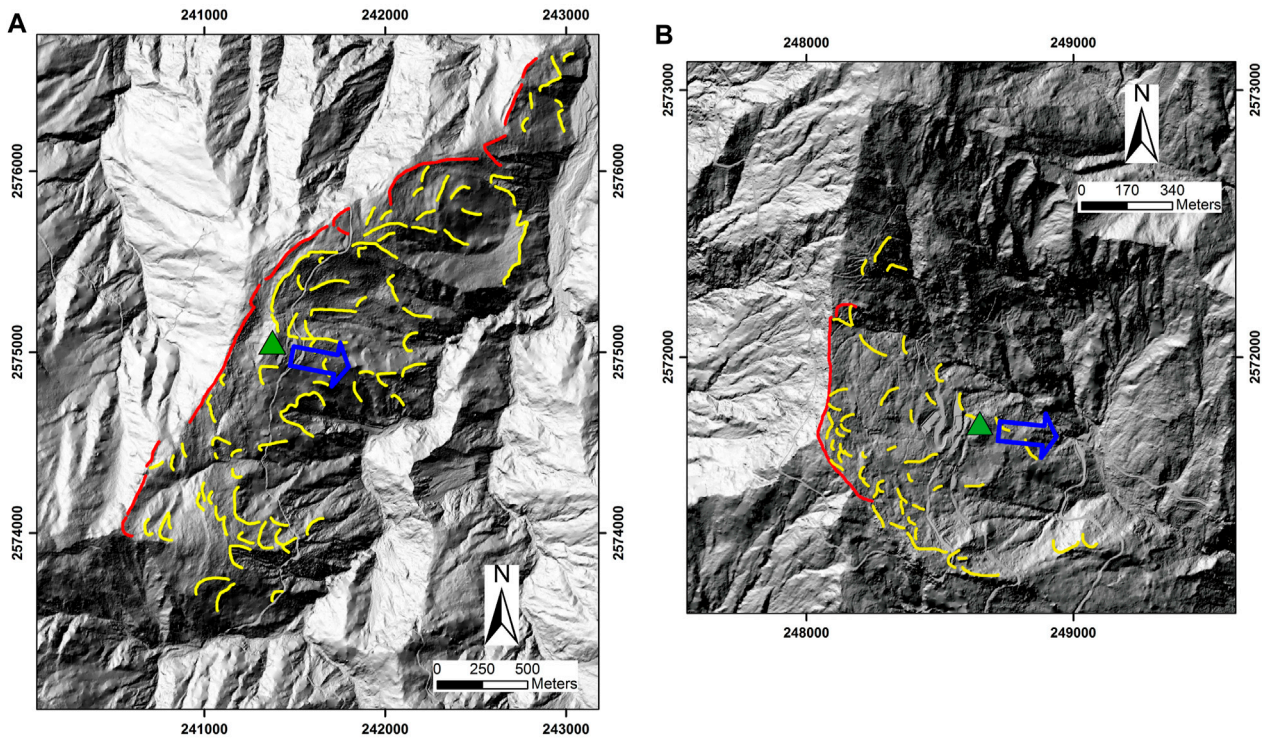


**FIGURE 4 |** LiDAR image of topographic characteristics of the **(A)** TienChih and **(B)** SiangYang sites. Red thick line: main cracks, yellow lines: minor cracks. The GPS recorded sliding direction, 8/7/2009 ~ 8/12/2009, is marked by the blue arrow.

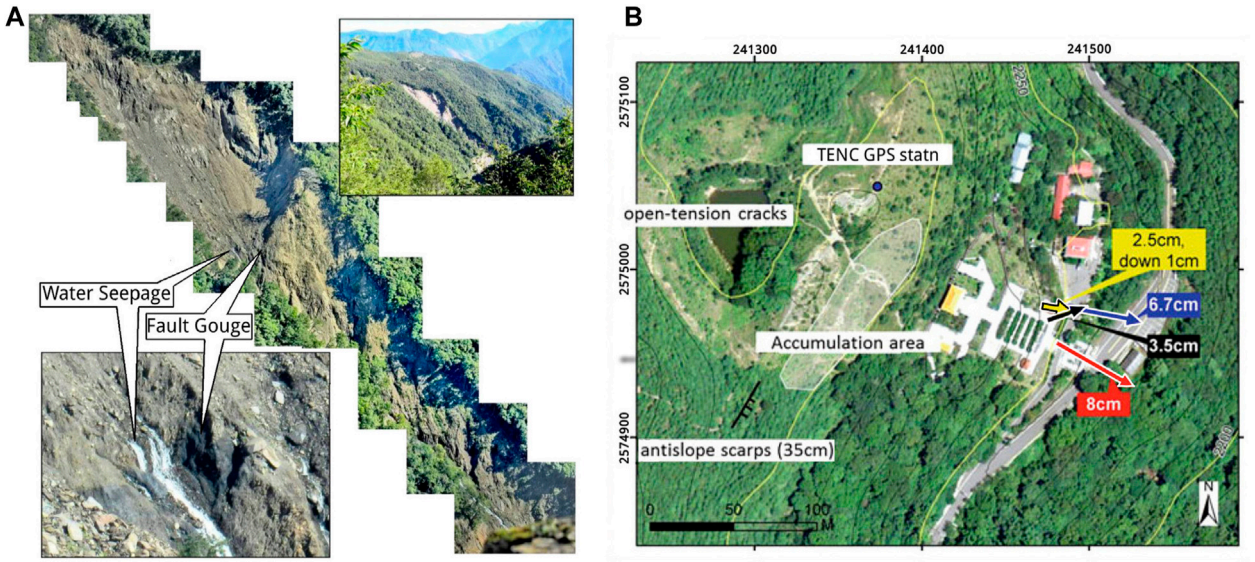


**FIGURE 5 | (A)** The slope profile of a shallow landslide in the TienChih area after the Morakot typhoon, (the central scarp near the rainfall gauge marked in **Panel 2A**). A typical cleavage structure (fault gouge zone) in the area and underground water seepage are shown. **(B)** Crack openings in the main building site of the roadway rest area.

found in the main building site of the roadway rest area. The movements, although slow (long-term gravity-driven creep), can continue for long periods in principle, producing significant cumulative displacements.

In the preliminary study? Chen et al. (2015), we visually examine the correlation between the temporal variation in GPS displacement time series and rainfall data (intensity and accumulated). The displacement takes place with a time lag compared with the rainfall hydrographs. This phenomenon suggests that the motion relates to the effect of water infiltration which alters the gravitational loads and effective stresses during typhoons and heavy precipitation. Combining the LiDAR and field observations, the two creeping landslides are concluded to be of a deep-seated cleavage and groundwater-controlled type, Chen et al. (2015). In what follows, the relationship between the displacement of the creeping landslide and the regional water cycle is investigated. The regional water cycle will be modelled using the hydrological tank model.

## 3 TANK MODEL AND PARAMETER CALIBRATION

The tank model is a simple phenomenological quantitative hydrological model that models the procedure of water flow through soil using a series of linear reservoirs, or tanks Sugawara (1961, 1995). Conceptually, each tank has several orifice exits to model discharging of water. The water in each tank represents the underground water storage and the discharges through the exits are the runoff flow to the river or the interflow to the lower cascading tanks. The computation of the resultant model is easy and fast once the model parameters are obtained. As a result, the tank model has been widely applied to flood forecasting in Asian countries, such as in Japan and Taiwan Osanai et al. (2010); Chen et al. (2013).

For example, Ishihara and Kobatake (1979) developed a synthetic flood forecasting model that combined the tank model for the rainfall-runoff conversion process of the subbasins of the studied catchments and the time-area-concentration diagram for the runoff concentration process. Lee (1993) identified that tanks provide essential continuous damping and lagging effects to model water infiltration and discharge in catchments. He also demonstrated that the tank model can be equivalently represented by a variety of linear reservoir models with different connection configurations. Yokoo et al. (2001) illustrated that to some extent the tank model parameters can be evaluated based on the geographical characteristics of the basin. Takahashi et al. (2008) used the dynamic dimensional search algorithm for parameter calibration and applied the model to forecast the groundwater table on slopes. Liu et al. (2010) applied the Kalman filter to assimilate the tank model prediction and measurements for the Singapore River catchment in Singapore. Chen et al. (2013) analysed hundreds of mudflow events and proposed a debris warning system in Taiwan, based on the soil water index (SWI), which was the total depth of the tank model.

**Figure 6** depicts the tank model used in the present study. The simplified model contains only two serially connected tanks and the water flow in the system describes the water infiltration and discharge in a unit area of the catchment. In the present paper, the model is separately applied to the TienChih and SiangYang catchments in **Sections 4**, **5**. The upper tank takes rainfall intensity, RI or $R$ in mm/hr, as the water input and its water

storage is represented by water depth $h_1(t)$ in mm in the tank. In the tank, there are three exits (top-side, bottom-side and bottom orifices) to discharge its water storage. These exits are used to model the surface runoff discharge, seepage of the surface layer and infiltration into the deep bedrock layer. The tank is assumed to be linear, i.e., the discharges of the three exits are proportional to the storage in the tank $q_1 = a_1 A\ (h_1 - H_1)\mathrm{H}\ (h_1 - H_1)$, $q_2 = a_2 A\ (h_1 - H_2)\mathrm{H}\ (h_1 - H_2)$ and $q_{12} = b_1 A h_1 \mathrm{H}\ (h_1)$, where $A$ denotes the area of the catchment to which the model is applied, and H $(\cdot)$ is the Heaviside function to ensure unidirectional water discharge and infiltration. For the upper tank, there are five constant parameters: $H_1$ and $H_2$ are the controlling threshold depths, $a_1$ and $a_2$ are the discharge coefficients of the two side exits at 1/hr, and $b_1$ is the infiltration coefficient for flow infiltrating into the second tank at 1/hr. The governing equation of the storage of the tank is $\mathrm{d}\ h_1(t)/\mathrm{d}t = R - (q_1 + q_2 + q_{12})/A$, with the initial storage $h_1\ (T_0)$ at the initial time $T_0$. The initial storage, $h_1\ (T_0)$, is denoted as $S_1$.

The lower tank in **Figure 6** models the water flow and storage in the deep bedrock layer. The water storage of the lower tank is defined as $h_2(t)$ and it has two discharge exits such that their discharges are $q_3 = a_3 A\ (h_2 - H_3)\mathrm{H}\ (h_2 - H_3)$ and $q_b = b_2 A h_2 \mathrm{H}\ (h_2)$. Similar to the upper tank counterpart, the governing equation for the lower tank is $\mathrm{d}\ h_2(t)/\mathrm{d}t = (q_{12} - q_3 - q_b)/A$, with the initial value $h_2\ (T_0) = S_2$. There are three additional constant parameters defined, $a_3$, $b_2$ and $H_3$, and their implications are the same as those of the upper counterpart. To summarize, there are two model equations to describe the water storage in each tank. The side outflows, $q_1$, $q_2$ and $q_3$, contribute to observable flow discharge and the discharge through the bottom-most exit, $q_b$, represents the discharge through an unobservable underground path. Therefore, the sum of the side exits is the volume flow rate discharged from the catchment. Rainfall in the model is the sole water input to the system.

The key triggering mechanism of landslides is the water content in slopes. During rainfall, the increase in water content increases the pore water pressure such that the effective stresses of slope materials decrease; hence, landslide motion is triggered. With the tank model, the water content in slopes is thought to be proportional to the total water storage of the two tanks, $h_1 + h_2$. Hence, we validate this assumption by inspecting the temporal correlation of the GPS surface displacement records with the water storage. This quantity, $h_1 + h_2$, is referred to as the WSI, and, we assume that it is proportional to the water content per unit area of the catchment.

To adapt the model to the present study areas, the model parameters must be calibrated. This calibration is achieved by minimizing the mean square error between the model discharge (the observable total side exit discharge) and the recorded volume flow rate. Mathematically, it reads

$$F(\mathbf{p}) = \frac{1}{T_f - T_0} \min_{\mathbf{p}} \left\{ \int_{T_0}^{T_f} (q_1 + q_2 + q_3 - q_{\mathrm{obs}})^2\, dt \right\},$$

where $T_0$, $T_f$ are the initial and terminal time of the inspected period and $\mathbf{p}$ is the parameters to be calibrated. Symbol $q_{\mathrm{obs}}$ is the monitored volume flow rate that flows out of the catchment. In our study areas, $q_{\mathrm{obs}}$ was the volume flow rate measured at A-Chy-Ba Bridge for the TienChih catchment and at Hsin-Wu-Lu for the SiangYang catchment. Precaution must be taken because even though the present tank model is simplified from a standard three-tank model, there are still ten parameters to be calibrated. These parameters, represented by $\mathbf{p}$ in the above expression, include three discharge coefficients ($a_1$, $a_2$, $a_3$), two infiltration coefficients ($b_1$, $b_2$), three controlling threshold depths ($H_1$, $H_2$, $H_3$), and two initial water storage levels ($S_1$, $S_2$). The extensive number of parameters makes the calibration a ten-dimensional optimization process and can be computationally expensive. To improve the efficiency of calibration, a global optimization method called the shuffled complex evolution method (SCE-UA) is used to search the best set of parameters, Chen et al. (2013).

The SCE-UA method was developed in the 1990s, Duan et al. (1994), and has been widely applied to many hydrological-related studies, for example, characterization of catchment properties by Nasonova et al. (2009), Funke (1999), and Rustanto et al. (2017); algorithmic and mathematical aspects of the method and similar aspects by Kuczera (1997), Singh and Bárdossy (2015) and Seong

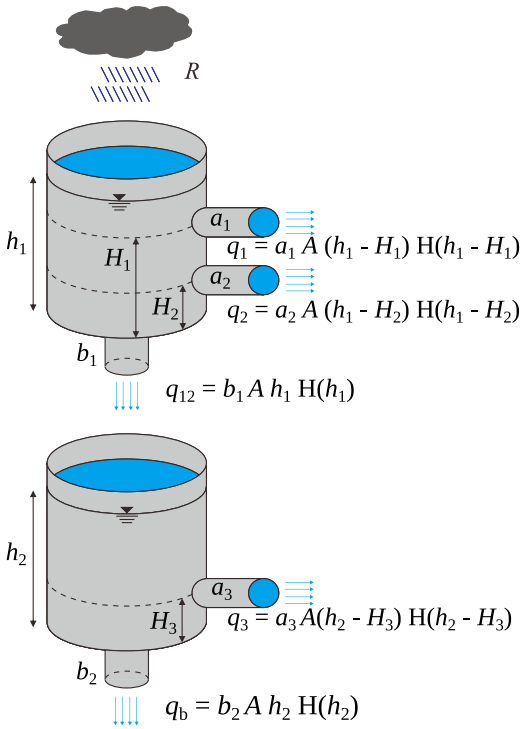


**FIGURE 6 |** Conceptual sketch of tank model. The model has two tanks with an identical area $A$. Rainfall intensity (RI), given by $R(t)$, is the water input source ($h_1$, $h_2$) are the tank water levels, ($q_1$, $q_2$, $q_3$) are discharge rates, and ($q_{12}$, $q_b$) are infiltration rates. Parameters ($a_1$, $a_2$, $a_3$) are discharge coefficients and ($b_1$, $b_2$) are infiltration coefficients. The initial values of ($h_1$, $h_2$) are denoted as ($S_1$, $S_2$) (not shown in the figure). The total water depth, $h_1 + h_2$ is referred to as the water storage index (WSI) in the present study. H $(\cdot)$ is the Heaviside function to ensure uni-directional water discharge and infiltration. In applications, $A$ is the area of the catchment.

et al. (2015); and a comprehensive review of its adaptations by Rahnamay Naeini et al. (2019). The search for the global optimum is based on the concept of competitive evolution of clusters of parameter sets, and is intrinsically a combination of probabilistic and deterministic approaches. In the present calibration scheme, we use a simple least square error estimator for a better resolution of the peak discharge rates between the model and measurement. In the following sections, the calibration and temporal correlation analysis of the TienChih landslide will first be described in detail, and then, the correlation analysis of the SiangYang landslide will be presented.

With the simple phenomenological quantitative tank model, the following two sections show that promising results can be obtained. However, we need to point out a few important precautions that should be taken when utilizing hydrological models. First, the tank model is suitable in principle for small-to medium-sized catchments. According to Okada et al. (2001), the maximum catchment size is conservatively suggested to be 10 $km^2$, although occasional applications to large catchments have been seen, e.g., ~ 600 $km^2$ in Chen et al. (2005). In this regard, the application of the model to the two areas is a somewhat exaggerated overextension. Under these circumstances, the spatial transports of surface runoff and underground water are omitted. Exaggerated applications simply arise because of the lack of field data. In the mountain ranges of the island, only a few rain gauges and flow metre are installed to monitor the catchments. Therefore, aggressive tradeoffs have been made among the model accuracy, complexity and acquisition of phenomenological information.

Second, we tested the parameter calibration using standard three-tank models but the improvements were negligibly marginal. A heteroscedastic maximum likelihood estimator [HMLE; Sorooshian (1981)], has also been tested with the calibration procedure but this scheme usually led to underestimation of the peak discharge rates. Last, WSI, as the sum of water storage in the tanks, is expected to correlate with the underground water level. Unfortunately, there is no underground water information available for the two presented sites. It remains to be answered in future studies whether underground water information can be adopted as an additional constraint for parameter calibration and what efficacy can be obtained by doing so.

## 4 ANALYSIS FOR THE TIENCHIH LANDSLIDE

For the TienChih landslide, rainfall records are taken from the Nan-Tien-Chih rainfall station, and the flow rate of the Laonung River is measured at the A-Chyi-Ba Bridge station. The locations of the two hydrological stations can be found in **Figure 2** (caption) and 1. The catchment area in the calibration process is 411 $km^2$.

A typical result of the optimized tank model is shown in **Figure 7**. The result is for the year 2009. The discharge contribution of each tank in the model to the river flow rate is plotted in **Figure 8**. The discharge from the top tank is responsible for the peak river flow rate immediately after each rainfall event while the discharge from the bottom tank contributes to the lagged recessing river discharge. This

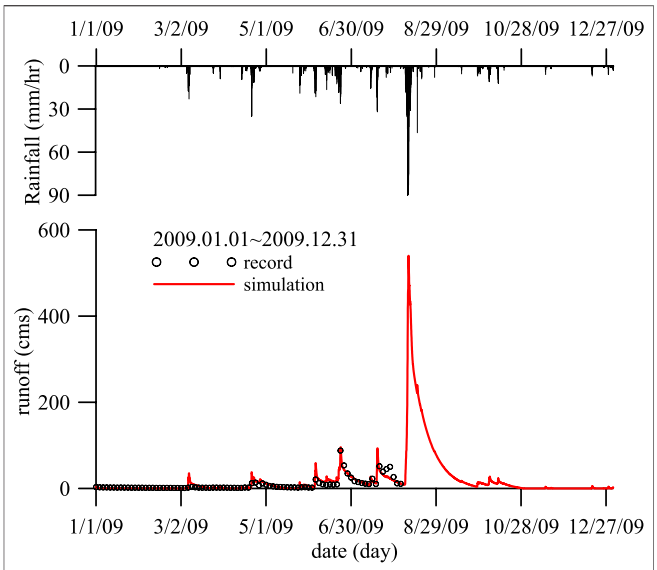


**FIGURE 7 |** Calibrated river runoff volume flow rate of the TienChih catchment for 2009. The volume flow rate data were recorded by the A-Chyi-Ba Bridge station of the Laonung River. The measurement stopped on 8/9 because the instruments were destroyed by flooding.

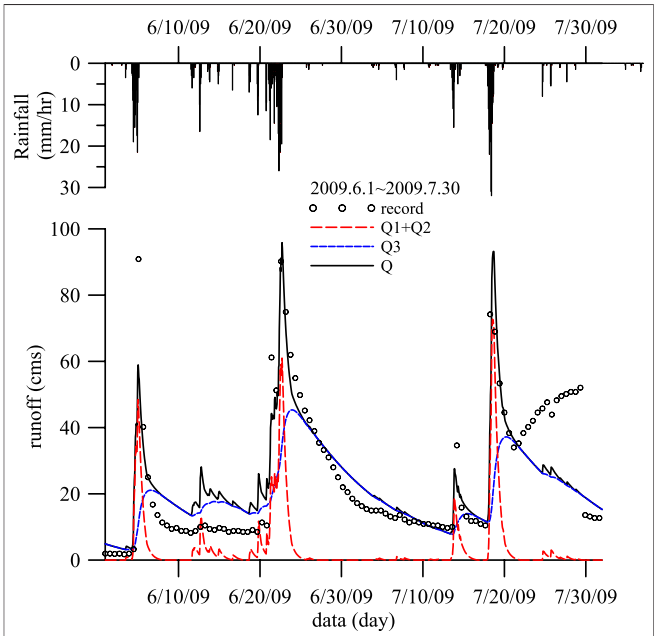


**FIGURE 8 |** Comparison of volume flow rates from each tank. The volume flow rate data were recorded by the A-Chyi-Ba Bridge station of the Laonung River. The measurement data between 7/22 and 7/29 may contain instrumental errors but have negligible effects on the present annual calibration.

**TABLE 1 |** Calibrated tank model parameters for the TienChih landslides.

| | 2004 | 2005 | 2006 | 2009 |
|---|---|---|---|---|
| $a_1$ (1/hr) | 4.49711e-3 | 6.83280e-9 | 1.37873e-3 | 2.14268e-3 |
| $a_2$ (1/hr) | 4.49784e-3 | 5.66582e-3 | 3.68092e-3 | 2.14307e-3 |
| $a_3$ (1/hr) | 3.20212e-4 | 5.10524e-2 | 4.99973e-1 | 1.17375e-3 |
| $b_1$ (1/hr) | 1.80048e-2 | 1.48904e-2 | 7.23799e-3 | 6.04037e-2 |
| $b_2$ (1/hr) | 3.18293e-4 | 3.29586e-1 | 2.75917e-1 | 2.14231e-3 |
| $H_1$ (mm) | 59.9949 | 12.8034 | 59.9985 | 21.2418 |
| $H_2$ (mm) | 00.0023 | 00.0000[a] | 00.0000[b] | 01.0282 |
| $H_3$ (mm) | 44.3768 | 43.9587 | 17.6550 | 59.9974 |
| $S_1$ (mm) | 55.5295 | 30.6332 | 00.2286 | 16.5260 |
| $S_2$ (mm) | 07.8932 | 27.0976 | 01.4574 | 14.7576 |

[a] $2.2989 \times 10^{-6}$.
[b] $2.7046 \times 10^{-5}$.

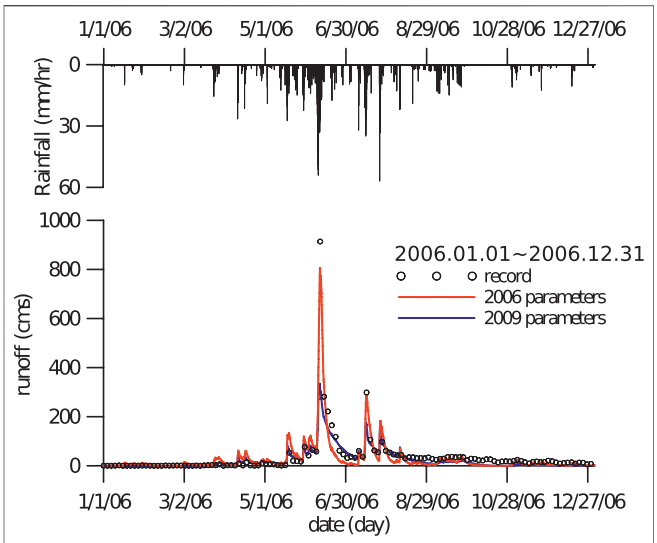


**FIGURE 9 |** Calibrated river runoff volume flow rate of the TienChih catchment for 2006. The volume flow rate data were recorded by the A-Chyi-Ba Bridge station of the Laonung River. The volume flow rate prediction using the 2009 tank model parameters is also superposed for comparison.

observation agrees with the physical interpretation of the role of the discharges in the tank model.

To streamline the analysis, we do not select any particular time series data for any individual landslide event. That is, the same procedure is applied annually to 2004, 2005, 2006 and 2009 (provided that 2009 has only 9 months of data). The optimized parameter sets for the years in which the TienChih GPS-recorded landslide motion is tabulated in **Table 1**. Because of the nonstationary regional climate system and inhomogeneous natural environment, there are variations among the four sets of model parameters. The unavoidable scarcity of data sources (one rainfall gauge and one flow station for each catchment) renders that model calibration suffers larger parameter variations among different sampling periods. Nevertheless, the results of a year-on-year comparison of the calibrated parameters are described as follows: 1) The discharge thresholds and initial water storage are on the orders of a unit magnitude, i.e., between 0 and a few tens, and 2) $H_2$ is close to zero. **Figure 9** shows a simple sensitivity test for the model using the 2009 parameters for the 2006 data. The simple sensitivity test was performed to check if the characteristics of the river flow hydrograph remain. The hydrograph characteristics are the essential information for this model to work in the limit of present data scarcity. The sensitivity results show that the timing of peak river discharges is influenced very little, but the values of peak flow rates are underestimated in the case of the 2009 parameters. By inspecting the model sensitivity with other cases, we find that the variations in the peak flow rates are limited within an order of magnitude, or more specifically, within a maximum relative error of 300%. Therefore, caution must be used in regard to the parameter effects if the model parameters are not well calibrated. To illustrate the model sensibility further, we will reveal the result of the tank model with the 2009 mismatched parameter WSI-2009 in the following discussion.

Next, we inspect the relationship between the WSI and GPS-recorded surface displacement. For the four distinct landslide events, the related time series data, RI, WSI, and displacement, are sketched in **Figure 10**. Because of the poor weather conditions during rainfall, there were three events in 2004, 2005 and 2006 with intervals where the GPS signals were lost. Comparing the GPS data of these events prior to and after rainfall, it is likely that the landslides occurred within these GPS blind intervals. For all cases, landslides take place approximately when the WSIs reach maximum values and the landslides happened around 6/29/2004 (Month/Day/Year) Mindulle typhoon, 7/18/2005 Haitang typhoon, 5/17/2006 heavy rainfall and 8/7/2009 Morakot typhoon. Note that we neglect the GPS displacement fluctuations although there are occasions that the fluctuations somewhat follow the WSI alternations. It is because the fluctuations did not cause permanent displacements after the associated WSI events.

Notably, the WSI in 2004 had a much longer water recession period which means a much lower discharge rate than the others. This difference occurs because the second tank has very low discharging rates ($a_3$ and $b_2$) after calibration for this year. Without other available auxiliary measurement data to verify this WSI estimation, we need to be cautious when interpreting its implications or adopting the model towards regional mitigation systems. For simplicity, we neglect the effects of the water recess periods but address the rising WSI on the landslide motion. A straightforward visual inspection suggests that the triggering threshold of the landslide motion is approximately WSI = 350 ~ 400 mm, as indicated by the light-blue shaded marks in **Figure 10**. The main criterion is to fit the WSI and all of the four aforementioned landslides: the higher bound of the threshold range is about the lowest possible value that the landslide occurs; and the lower bound is about the highest possible value that the landslide does not occur. The WSI-2009 curves are also superposed with their corresponding events for sensitivity comparison, and the same threshold is applicable. A similar RI threshold can be obtained, and the threshold is approximately 40 mm/h. However, based on the RI, the 6/19/2005 event is not detected, as shown in **Figure 10B**,

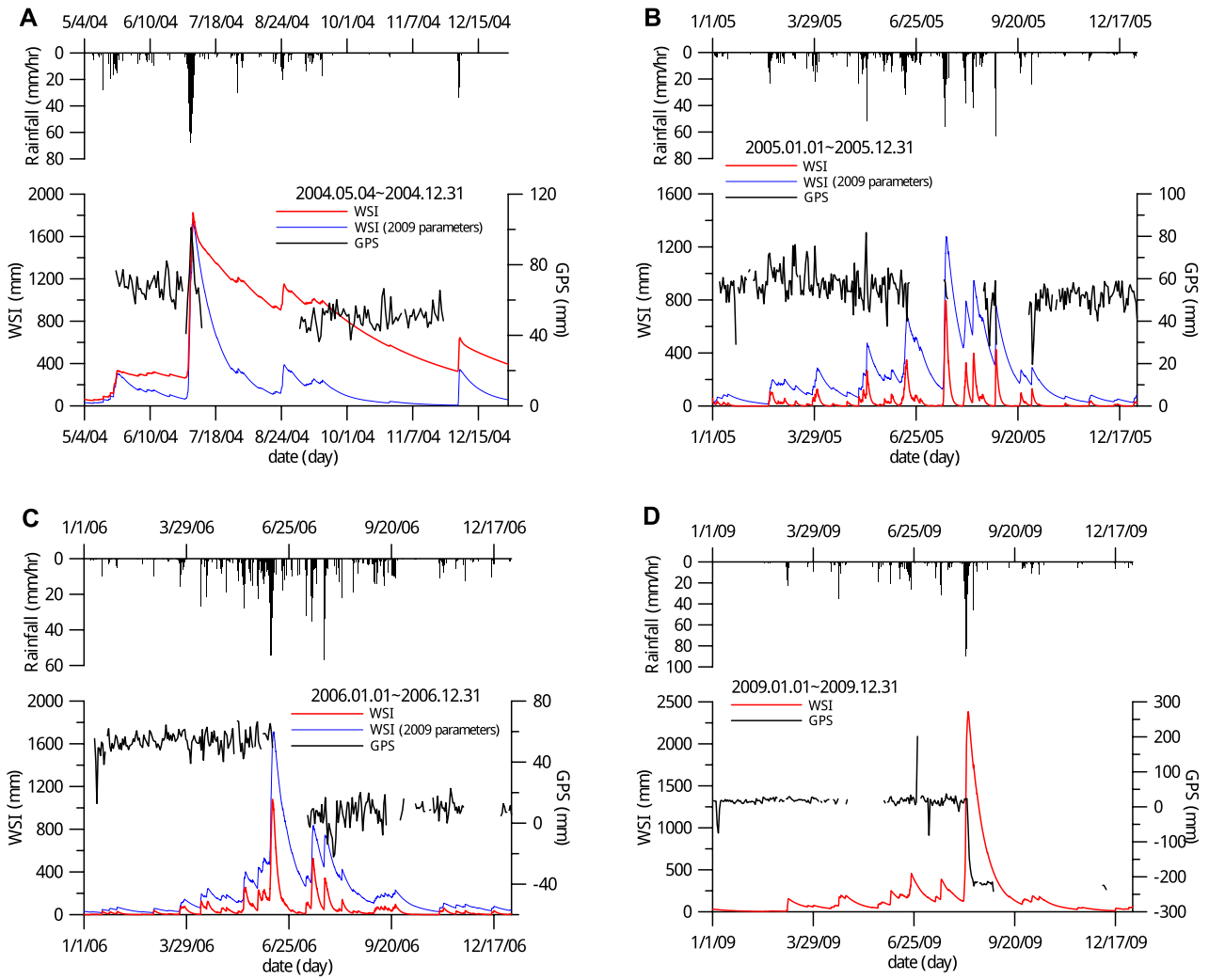


**FIGURE 10 |** RI, WSI and GPS displacement of the four landslide events. WSI-2009 curves are WSI predictions using 2009 tank model parameters and they are superimposed for a model sensitivity check. The light blue shaded lines are landslide thresholds: between 350 ~400 mm for WSI and approximately 40 mm/h for rainfall intensity. The associated landslide events from panels **(A–D)** are 6/29/2004 (Month/Day/Year) Mindulle typhoon, 7/18/2005 Haitang typhoon, 5/17/2006 heavy rainfall and 8/7/2009 Morakot typhoon.

because precipitation duration is not properly weighted in this approach.

We have to keep in mind that the WSI threshold should be treated as a suggested level and is in general site dependent. It is because the determination of the threshold is by a simple and subjective comparison between the historical landslide events and WSI hydrograph, on the assumption that the WSI in slopes is directly associated with the variations of the material strengths without time lags. The threshold may be different if the model detail or monitoring network is changed. The accuracy of the threshold is also hard to assess in the present conditions because the number of the verified landslides does not reach a level of statistical significance. In addition, we also neglected the possibility that the threshold may change after each landslide because its change may involve subtle changes in geological conditions and they are not quantifiable in the current framework. Nevertheless, we illustrated the possibility to construct a WSI threshold for a landslide site from the aspects of presented model and data.

Most of the mainstream mitigation warning systems are based on regional statistical regression analyses using rainfall data, for example the peak RI, and duration. In this type of model, the infiltration of precipitation is usually neglected. With the present tank model, infiltration can be taken into consideration. Therefore for comparison, we evaluate the predictions between the RI and WSI approaches. We use the 2009 event for this assessment because it has a continuous displacement record to cover the entire motion. We assume that the rate of displacement is proportional to the water storage, i.e., WSI in the slope because water directly reduces the strengths of the materials; thus, it is expected that the displacement rate (DR) is synchronized with the WSI. To investigate this assumption, we apply a correlation

function to calculate the phase difference, or time-lag, between the WSI and DR. The correlation function is defined as follows: as

$$\mathrm{corr}(\mathrm{DR}, \mathrm{WSI}) = \mathrm{E}(\mathrm{DR}(t) \cdot \mathrm{WSI}(t+\tau)),$$

which is the expectancy value, E (·), of the product of the DR and a time-$\tau$-shifted WSI. For comparison, the correlation functions between the DR, first tank water depth $h_1$ and RI are also calculated by replacing WSI in the above expression with $R(t)$ and $h_1(t)$. In the calculation, we use 1-month time series data starting from 7/28/2009 and the close-up time series, including RI, displacement, DR, $h_1$ and WSI are shown in **Figure 11**.

The three correlation functions are plotted in **Figure 12**. In the plot, the maximum values of the correlation functions indicate the similarities in shapes and timescales of the correlated signals and their corresponding time shifts imply time lags between the correlated signals. From the time shift, we find that the peak of the WSI correlation function occurs at approximately 13 h while those of $h_1$ and RI correlation functions are at − 22 and −34 h. The negative time shifts indicate that $h_i$ and RI events temporally occur prior to the DR. The alternation of the time shifts, from RI, $h_1$ to WSI, reveals the role of water infiltration to the landslide. The timing sequentially approaches the landslide displacement from the precursor rainfall, water accumulation in the shallow surface layer, and to the deep layer. This sequence confirms not only the assumption that the peak DR occurs closer to the predicted peak of WSI than $h_1$ and RI but also the phenomenological fact of the tank model that the deep-seated landslide involves water in the deep bed rock layer. Last, because of the water infiltration mechanism, the WSI has a much longer water recession period than rainfall, and subsequently, this recession period results in a lowering and broadening peak of the correlation function.

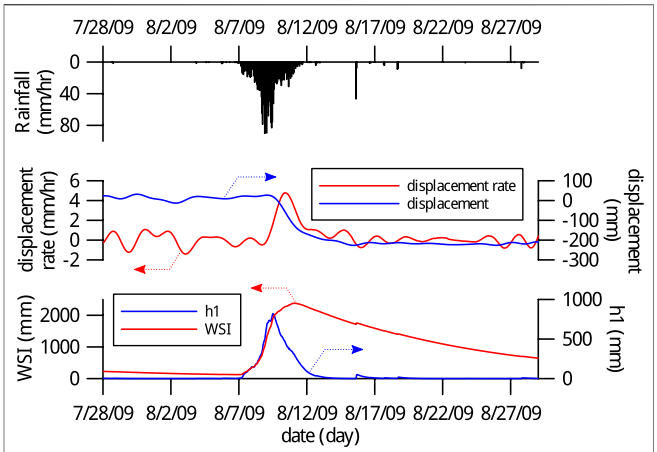


**FIGURE 11 |** Close-up time series plots of the 2009 Morakot typhoon triggered TienChih landslide. From the top panel: RI; middle: displacement, DR; bottom: $h_1$ and WSI. The DR is the negated time derivative of the GPS displacement.

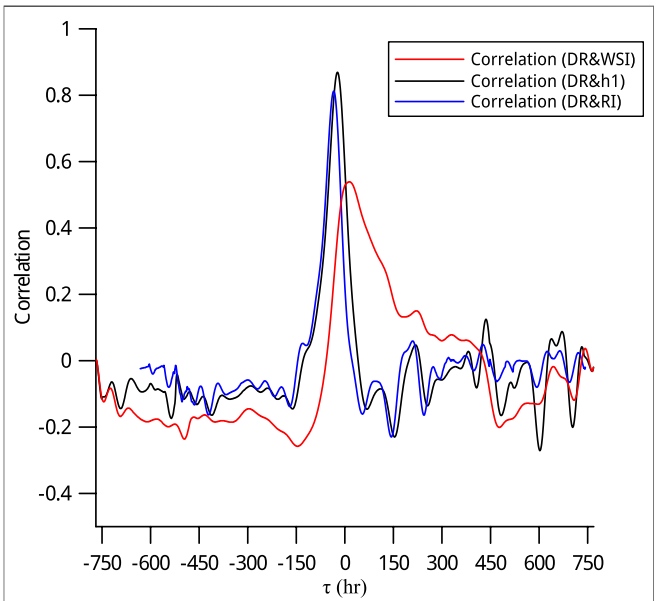


**FIGURE 12 |** Correlation functions. One month time series data from 7/28/2009 are used for calculation. The negative time shift (negative $\tau$) represents the time lead to the DR. The large horizontal time lag axis is chosen for clearer visual inspection of the correlation functions.

## 5 THE SIANGYANG LANDSLIDE CASE

The SiangYang landslide was triggered by the 2009 Morakot typhoon. By using the same technique described in **Section 3**, the tank model parameters for 2009 are computed and listed in **Table 2**. The calibrated runoff hydrograph compared with the monitoring data of the Hsin-Wu-Lu River flow station is shown in **Figure 13**. To investigate the occurrence sequence of the landslide more precisely, close-up hydrographs of the RI, displacement, DR, $h_1$ and WSI are plotted in **Figure 14**. Comparing the calibrated parameters to those of the 2009 TienChih catchment, the discharge coefficients, $a_{1,3}$, are roughly an order of magnitude larger (10×), indicating that the region has a higher water mobility, i.e., lower water retention (holding) capacity. Consequently, the discharge recession period is short and the hydrological characteristics of the catchment are dominated by those of the first tank. Verification is shown by the fact that the WSI is almost identical to $h_1$, as shown in the bottom panel of **Figure 14**. The same WSI threshold in the TienChih landslide (350 ~400 mm) is also found applicable to the SiangYang landslide. However, we cannot yet conclude if the threshold fits tightly to the landslide initiation under the present scope of data. The constraints of the threshold discussed in **Section 4** still hold to the SiangYang site. Under this circumstance, we should treat the threshold conservatively as a necessary but not a sufficient condition for triggering the SiangYang landslide motion. Nevertheless, the coincidence of the threshold in both the SiangYang and TienChih landslide sites may imply that it may be insensitive to a wide range of geological conditions. This implication is important for

**TABLE 2 |** Calibrated tank model parameters for the 2009 SiangYang landslide.

| $a_1$ (1/hr) | $a_2$ (1/hr) | $a_3$ (1/hr) | $b_1$ (1/hr) | $b_2$ (1/hr) |
|---|---|---|---|---|
| 7.93e-3 | 1.371e-2 | 7.953e-2 | 4.815e-2 | 8.279e-2 |
| $H_1$ (mm) | $H_2$ (mm) | $H_3$ (mm) | $S_1$ (mm) | $S_1$ (mm) |
| 44.4127 | 44.4032 | 0.0000[a] | 4.7947 | 1.0013 |

[a] $4.6493 \times 10^{-7}$.

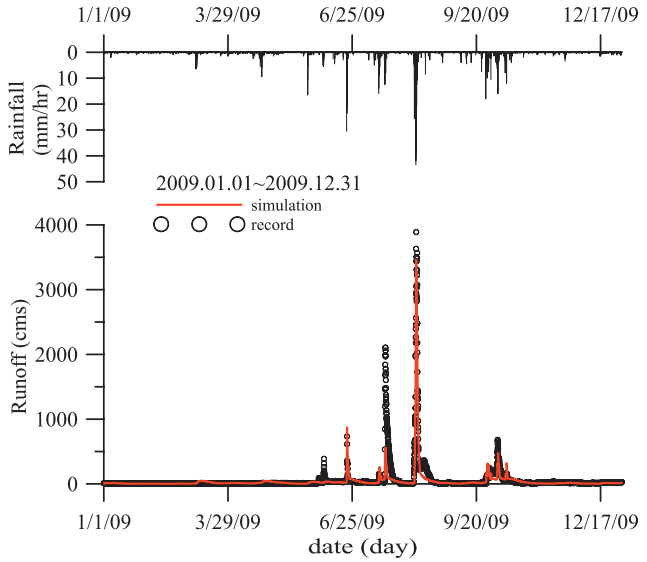


**FIGURE 13 |** Calibrated river runoff volume flow rate of the SiangYang catchment for 2009. The volume flow rate data were recorded by the Hsin-Wu-Lu river flow station of the Beinan River.

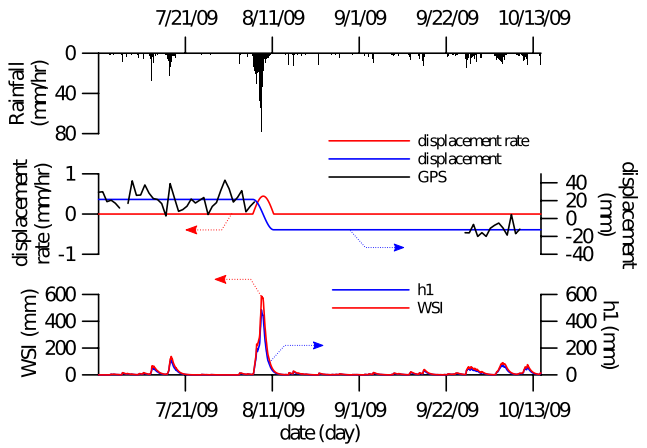


**FIGURE 14 |** Close-up time series plots of the 2009 Morakot rainfall-triggered SiangYang landslide. From the top panel: RI; middle: displacement, DR; bottom: $h_1$ and WSI. The DR is the negated time derivative of the GPS displacement. The light blue shaded line in the bottom panel indicates the WSI threshold inferred in the TienChih landslide.

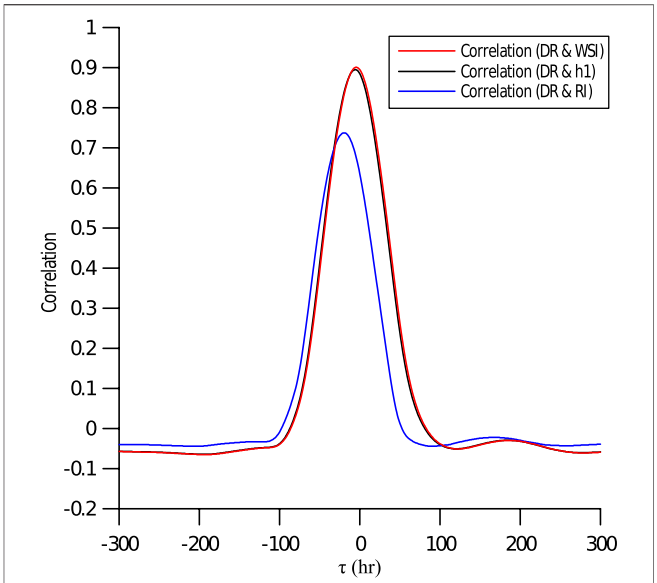


**FIGURE 15 |** Correlation functions. One-month time series data from 7/28/2009 are used for calculation. The negative time shift (negative $\tau$) represents the time lead to the DR. The large horizontal time lag axis is chosen for clearer visual inspection of the correlation functions.

applications of the technique and Whether it is true remains open for future research.

Similar to the TienChih case, the time series of the GPS displacement-related data are also missing for approximately one and a half months after the Morakot typhoon, as shown in the middle panel of **Figure 14**. To proceed with the calculation of the temporal correlation functions, we assume that the slope starts to move immediately after the time when the GPS data are missing, i.e., on September 8, 2009, and the motion lasts for approximately 5 days by referring to the TienChih landslide, cf. **Figure 11**. Over the 5-day duration, the area catches most of the precipitation from the Morakot typhoon. Under this assumption, we use two constant position values and a smooth sinusoidal function to synthesize the landslide displacement, which is a quarter wave length sinusoidal function with both ends joining the constants on its both sides, as shown by the blue line in the middle panel of **Figure 14**. The constant position values are the average position of the GPS station before and after the landslide. Based on the synthesized displacement, the DR is calculated, as shown by the red line in the same figure panel. Because the displacement of the SiangYang landslide is only approximately one-tenth of that in the TienChih case, the GPS displacement data have a low signal-to-noise ratio. To avoid employing further sophisticated signal processing techniques, we use the synthesized displacement for the temporal correlation analysis. Similar to **Section 4**, 1-month time series data starting from 7/28/2009 are used in the calculation.

The correlation functions for the SiangYang landslide are calculated and presented in **Figure 15**. Our attention is drawn to the time shifts between the hydrological variables and DR, which are −4.7, −6.3 and −19 h for the WSI, $h_1$ and RI, respectively. All negative time shift values indicate that the

hydrological hydrographs are ahead of the DR. The alternation of the time shifts follows the same order we observed in the previous section, from RI, $h_1$ to WSI, revealing the local water cycle movement. Similar to the TienChih landslide, the DR is closest to the WSI hydrograph, implying that the landslide involves water in the deep layer. Because the hydrological characteristics of the site are primarily dependent on the first tank, the WSI and $h_1$ correlation functions are also nearly identical and their time difference is only approximately 1.6 h. Finally for this case, some artefacts have been introduced into the correlation functions because of the use of the synthesized displacement. These effects include the noise-free well-defined shape of the function and the nearly perfect correlation ( $\approx 0.9$) at the function peak.

## 6 DISCUSSION

Our attention was drawn to the temporal correlation between the creeping landslide motion and water content in slopes. The TienChih and SiangYang landslides were chosen because they are rainfall-triggered, deep-seated creeping landslides, and their locations are in the upstream-most catchment areas. Because of the accessibility of the sites and the associated mountain range, field measurements for calibrating sophisticated field models are scarce. As a trade-off, we adopted a phenomenological quantitative hydrological model, the simplified tank model, to model the local water cycles.

The water storage in the solid slope was assumed to be proportional to the sum of the water depths of the two serially-connected tanks, $h_1 + h_2$, which is referred to as the WSI. In the classical literature of the model, the WSI is called the soil water index, or SWI. We deliberately avoided using the term because it is intuitively associated with shallow soil-based debris landslides. By virtue of the phenomenological tank model, no restrictions are imposed on the material types, detailed distribution configuration of the materials, or physical dimension of the slopes. These physical and geological effects are indirectly incorporated into the parameters of the model through the parameter calibration processes.

Because of the active tectonic motion Lee and Wang (1985) and Lai et al. (1989), rich networks of fracture and cleavage structures are developed in the mountain bedrock. Borehole investigations and rock core samples in the neibouring area with similar geological conditions reveal that fractured geostructures persist at least to one hundred metre from the surface Lin and Lin (1999); Chinese American Tech. Corp. et al. (1992). Therefore, it is assumed that water can infiltrate deeply into bedrock through these open disjointed networks during heavy rainfall periods. As a result, water accumulation in the slope lifts the groundwater table, leading to an increase in the pore pressure, a reduction in the effective stresses and consequently triggering landslide motion. Based on this hypothesis, the occurrence of landslide motion is expected to correlate closely with the WSI and has been verified with the two presented landslides.

In the tank model, the arrangement of the side water exits is conceptually associated with the discharges from the surface runoff, surface and deep bedrock (or subsoil) layers according to Sugawara (1995). In this arrangement, $H_1$ must be higher than $H_2$, as shown by the calibrated parameters of the two presented catchments, **Tables 1**, **2**. Having confirmed the configuration of the discharge exits of the first tank, it is noticed that the discharge coefficient of the top-most exit, $a_1$, is smaller overall than $a_2$. This result implies that the discharge of the first tank is primarily controlled by the surface layer, i.e., the discharge through the lower $a_2$ exit.

Comparing the 2009 calibration results, we find that the two sets of parameters lead to one distinct difference in the local water cycles. The TienChih catchment has a smaller $b_2$, such that it keeps water above the second tank for a longer period and causes a longer recession period of the flow rate of the Laonung River. In contrast, the SiangYang catchment has a larger infiltration capability such that water can quickly infiltrate through the second tank into the deeper bedrock layer. Despite the aforementioned distinct hydrological characteristics, the WSI threshold of 350 ~400 mm is applicable for both landslides.

## 7 CONCLUSION

In this paper, the rainfall-triggered TienChih and SiangYang deep-seated creeping landslides were compared with the regional water cycles. The landslide displacement motion was recorded by continuous GPS stations, and the regional water cycles included hydrological variables, such as precipitation, water storage in the catchment and runoff flow. The aim of this study is to illustrate that the infiltration of surface water and water storage in the catchment were associated with landslide motion. The water cycles were modelled using the phenomenological tank model, which was composed of two serially-connected tanks. The model contained a total of ten parameters to be calibrated against the rainfall and river runoff flows. The water content in the catchments, i.e., on the solid slopes, was quantified by using the water depth of the first tank ($h_1$) and the total water depth, (WSI, $h_1 + h_2$).

The association between landslide motion and water cycles was investigated by their correlations. The correlation functions, and thus the time lags, between the DR and the hydrological variables (RI, $h_1$ and WSI) were calculated. Comparing the time lags, we found that the RI lead ahead, followed by $h_1$, and finally, the WSI correlated the closest in time to landslide motion. This sequence clearly indicated the infiltration processes where the water was transported from the surface, through the shallow soil layer, and into the deep bedrock layer. When a certain depth was reached, the water weakened the slope material and triggered landslide motion. Therefore, we can expect that the WSI and landslide motion correlates the best in time but not their appearing order because the detail underground water flows and material weakening mechanism were not modelled. On the direct relationship between the WSI and landslide motion, we suggested a WSI threshold for the investigated deep-seated landslides that was between 350 and 400 mm. The same WSI threshold is applicable to both landslides lead to an important

implication that it may be insensitive to a wide range of geological conditions. This proposition needs to be carefully examined with more landslide cases in future. To summarize, the hydrological technique presented in the paper provides the interrelation among the hydrological variables, and in turn, the WSI hydrograph and its threshold can act as valuable accessorial quantities that are beneficial to accurately estimating deep-seated landslide initiation in future hazard mitigation warning system.

## DATA AVAILABILITY STATEMENT

The raw data supporting the conclusion of this article will be made available by the authors, without undue reservation.

## AUTHOR CONTRIBUTIONS

C-YK, R-FC and Y-JH contributed to conception and design of the study. C-YK, S-EL and Y-HC developed and executed the hydrological model. S-PL, R-FC and Y-JH provided GPS and hydrological data. C-WL, K-JC and R-YW provided geological investigation details. All authors contributed to manuscript revision, read, and approved the submitted version.

## FUNDING

This work is supported in parts by the Bureau of Soil Water Conservation, Taiwan, under grants SWCB-105-128 and SWCB-110-028.

## REFERENCES

Altamimi, Z., Collilieux, X., Legrand, J., Garayt, B., and Boucher, C. (2007). ITRF2005: a New Release of the International Terrestrial Reference Frame Based on Time Series of Station Positions and Earth Orientation Parameters. *J. Geophys. Res.* 112, B09401. doi:10.1029/2007jb004949

Cappa, F., Guglielmi, Y., Soukatchoff, V. M., Mudry, J., Bertrand, C., and Charmoille, A. (2004). Hydromechanical Modeling of a Large Moving Rock Slope Inferred from Slope Levelling Coupled to spring Long-Term Hydrochemical Monitoring: Example of the La Clapière Landslide (Southern Alps, France). *J. Hydrol.* 291, 67–90. doi:10.1016/j.jhydrol.2003.12.013

Chen, R.-F., Hsu, Y.-J., Yu, S.-B., Chang, K.-J., Wu, R.-Y., Hsieh, Y.-C., et al. (2015). "Real-time Monitoring of Deep-Seated Gravitational Slope Deformation in the Taiwan Mountain Belt," in *Engineering Geology for Society and Territory - Volume 2*. Editors G. Lollino, D. Giordan, G. B. Crosta, J. Corominas, R. Azzam, J. Wasowski, et al. (Berlin, Germany: Springer), 1333–1336. doi:10.1007/978-3-319-09057-3_234

Chen, R.-S., Pi, L.-C., and Hsieh, C.-C. (2005). Application of Parameter Optimization Method for Calibrating Tank Model. *J. Am. Water Resour. Assoc.* 41, 389–402. doi:10.1111/j.1752-1688.2005.tb03743.x

Chen, S. C., Tsai, C. W., Chen, C. Y., and Chen, M. C. (2013). Soil Water index Applied as a Debris Flow Warning-Reference Based on a Tank Model. *J. Chin. Soil Water Conserv.* 44, 133–143. doi:10.29417/JCSWC.201306_44(2).0004

Chinese American Tech. Corp.; China Eng. Consult. Inc.; Atci Corp. (1992). *Preliminary Planning and Feasibility Study of the National South Transverse Highway (In Chinese)*. Taiwan: Taiwan Area National Expressway Engineering Bureau, Ministry of Transportation and Communications.

Duan, Q., Sorooshian, S., and Gupta, V. K. (1994). Optimal Use of the SCE-UA Global Optimization Method for Calibrating Watershed Models. *J. Hydrol.* 158, 265–284. doi:10.1016/0022-1694(94)90057-4

Funke, R. (1999). Parameterization and Regionalization of a Runoff Generation Model for Heterogeneous Catchments. *Phys. Chem. Earth, B: Hydrol. Oceans Atmosphere* 24, 49–54. doi:10.1016/S1464-1909(98)00010-0

Herring, T. A., King, R. W., and McClusky, S. C. (2002). *Documentation for the GAMIT Analysis Software, Release 10.0 Edn*. Cambridge, MA: MIT.

Hsu, Y.-J., Chen, R.-F., Lin, C.-W., Chen, H.-Y., and Yu, S.-B. (2014). Seasonal, Long-Term, and Short-Term Deformation in the Central Range of Taiwan Induced by Landslides. *Geology* 42, 991–994. doi:10.1130/G35991.1

Ishihara, Y., and Kobatake, S. (1979). Runoff Model for Flood Forecasting. *Bull. Disaster Prev. Res. Inst. Kyoto Univ.* 29, 27–43.

Kuczera, G. (1997). Efficient Subspace Probabilistic Parameter Optimization for Catchment Models. *Water Resour. Res.* 33, 177–185. doi:10.1029/96WR02671

Lai, T. C., Aj, K. F., Chen, F. C., Fei, L. W., and Liu, H. T. (1989). Geological Survey and Study on the Potential Dangers in the Guanshan Area of Yushan National Park (In Chinese). *Tech. Rep.*, Yushan National Park Trans., No. 1017.

Lee, C. T., and Wang, Y. (1985). Stratigraphy and Structure of the Slate Terrane Near Likuan Southern Cross-Island Highway, Taiwan (In Chinese). *Ti-Chi* 8, 1–20.

Lee, K. T. (1993). Tank Model and Rainfall-Runoff Simulation. *J. Chin. Agric. Eng.* 39 (2), 20–28.

Lin, C. C., and Lin, C. C. (1999). Engineering Geological Servey and Treatment Planning Study at 191k+772 Chiabao Tunnel, South Transverse Highway (In Chinese). *Taiwan Highw. Eng.* 25, 24–38.

Lin, C. W. (2012). Geological Environment Monitoring and Facilities Safety Assessment of Yushan National Park (In Chinese). *Tech. Rep.*, Yushan National Park Trans., No. 1254.

Lin, S. E., Chan, Y. H., Kuo, C. Y., Chen, R. F., Hsu, Y. J., Chang, K. J., et al. (2017). The Use of a Hydrological Catchment Model to Determine the Occurrence of Temporal Creeping in Deep-Seated Landslides. *J. Chin. Soil Water Conserv. (in Chinese)* 48, 153–162. doi:10.29417/JCSWC.201712_48(4).0001

Liu, J. D., Doan, C. D., and Liong, S. Y. (2010). "Conceptual Rainfall-Runoff Model with Kalman Filter for Parameter and Outflow Updating," in *Advances in Geosciences, Volume 23: Hydrological Science*. Editor G. F. Lin (Singapore: World Sci. Pub.), 133–146.

Lv, H., Ling, C., Hu, B. X., Ran, J., Zheng, Y., Xu, Q., et al. (2019). Characterizing Groundwater Flow in a Translational Rock Landslide of Southwestern China. *Bull. Eng. Geol. Environ.* 78, 1989–2007. doi:10.1007/s10064-017-1212-3

Nasonova, O. N., Gusev, Y. M., and Kovalev, Y. E. (2009). Investigating the Ability of a Land Surface Model to Simulate Streamflow with the Accuracy of Hydrological Models: A Case Study Using MOPEX Materials. *J. Hydrometeorology* 10, 1128–1150. doi:10.1175/2009JHM1083.1

Nie, W., Krautblatter, M., Leith, K., Thuro, K., and Festl, J. (2017). A Modified Tank Model Including Snowmelt and Infiltration Time Lags for Deep-Seated Landslides in alpine Environments (Aggenalm, germany). *Nat. Hazards Earth Syst. Sci.* 17, 1595–1610. doi:10.5194/nhess-17-1595-2017

Okada, K., Makihara, Y., Shimpo, A., Nagata, K., Kunitsugu, M., and Saitoh, K. (2001). Soil water index (SWI) (in Japanese). *Tenki* 48, 349–356.

Osanai, N., Shimizu, T., Kuramoto, K., Kojima, S., and Noro, T. (2010). Japanese Early-Warning for Debris Flows and Slope Failures Using Rainfall Indices with Radial Basis Function Network. *Landslides* 7, 325–338. doi:10.1007/s10346-010-0229-5

Padilla, C., Onda, Y., Iida, T., Takahashi, S., and Uchida, T. (2014). Characterization of the Groundwater Response to Rainfall on a Hillslope with Fractured Bedrock by Creep Deformation and its Implication for the Generation of Deep-Seated Landslides on Mt. Wanitsuka, Kyushu Island. *Geomorphology* 204, 444–458. doi:10.1016/j.geomorph.2013.08.024

Rahnamay Naeini, M., Analui, B., Gupta, H. V., Duan, Q., and Sorooshian, S. (2019). Three Decades of the Shuffled Complex Evolution (Sce-ua) Optimization Algorithm: Review and Applications. *Scientia Iranica* 26, 2015–2031. doi:10.24200/sci.2019.21500

Rustanto, A., Booij, M. J., Wösten, H., and Hoekstra, A. Y. (2017). Application and Recalibration of Soil Water Retention Pedotransfer Functions in a Tropical Upstream Catchment: Case Study in Bengawan Solo, indonesia. *J. Hydrol. Hydromechanics* 65, 307–320. doi:10.1515/johh-2017-0020

Seong, C., Her, Y., and Benham, B. (2015). Automatic Calibration Tool for Hydrologic Simulation Program-Fortran Using a Shuffled Complex Evolution Algorithm. *Water* 7, 503–527. doi:10.3390/w7020503

Singh, S., and Bárdossy, A. (2015). Hydrological Model Calibration by Sequential Replacement of Weak Parameter Sets Using Depth Function. *Hydrology* 2, 69–92. doi:10.3390/hydrology2020069

Sorooshian, S. (1981). Parameter Estimation of Rainfall-Runoff Models with Heteroscedastic Streamflow Errors - the Noninformative Data Case. *J. Hydrol.* 52, 127–138. doi:10.1016/0022-1694(81)90099-8

Sugawara, M. (1995). "Chapter 6, Tank Model," in *Computer Models for Watershed Hydrology*. Editor V. P. Singh (Littleton, Colo: Water Res. Pub.).

Sugawara, M., and Funiyuki, M. (1956). "A Method of Revision of the River Discharge by Means of a Rainfall Model," in *Collection of Research Papers about Forecasting Hydrologic Variables* (Saitama, Japan: Geosphere Res. Institute of Saitama Univ.), 14–18.

Sugawara, M. (1961). On the Analysis of Runoff Structure about Several Japanese Rivers. *Jpn. J. Geophys.* 2 (4), 210–216.

Takahashi, K., Ohnishi, Y., Xiong, J., and Koyama, T. (2008). Tank Model and its Application to Predicting Groundwater Table in Slope. *Chin. J. Rock Mech. Eng.* 27 (12), 2501–2508.

Varnes, D. J. (1978). "Slope Movement Types and Processes," in *Special Report 176: Landslides: Analysis and Control*. Editors R. L. Schuster and R. J. Krizek (Washington D. C.: Transportation and Road Research Board, Natl. Acad. Sci.), 11–33.

Yokoo, Y., Kazama, S., Sawamoto, M., and Nishimura, H. (2001). Regionalization of Lumped Water Balance Model Parameters Based on Multiple Regression. *J. Hydrol.* 246, 209–222. doi:10.1016/s0022-1694(01)00372-9

Yu, S.-B., Chen, H.-Y., and Kuo, L.-C. (1997). Velocity Field of GPS Stations in the Taiwan Area. *Tectonophysics* 274, 41–59. doi:10.1016/s0040-1951(96)00297-1

Yu, S.-B., Hsu, Y. J., Kuo, L. C., Chen, H. Y., and Liu, C. C. (2003). GPS Measurement of Postseismic Deformation Following the 1999 Chi-Chi, Taiwan, Earthquake. *J. Geophys. Res.* 108, 2520. doi:10.1029/2003jb002396

Zêzere, J. L., Trigo, R. M., and Trigo, I. F. (2005). Shallow and Deep Landslides Induced by Rainfall in the lisbon Region (Portugal): Assessment of Relationships with the North Atlantic Oscillation. *Nat. Hazards Earth Syst. Sci.* 5, 331–344. doi:10.5194/nhess-5-331-2005

**Conflict of Interest:** The authors declare that the research was conducted in the absence of any commercial or financial relationships that could be construed as a potential conflict of interest.

**Publisher's Note:** All claims expressed in this article are solely those of the authors and do not necessarily represent those of their affiliated organizations, or those of the publisher, the editors and the reviewers. Any product that may be evaluated in this article, or claim that may be made by its manufacturer, is not guaranteed or endorsed by the publisher.

frontiers in Earth Science

ORIGINAL RESEARCH
published: 16 December 2021
doi: 10.3389/feart.2021.761455

# A Numerical Investigation of the Characteristics of Seismic Signals Induced by Rockfalls

*Zheng-Yi Feng*, Zhao-Ru Shen and Rui-Chia Zhuang*

*Department of Soil and Water Conservation, National Chung Hsing University, Taichung, Taiwan*

This study proposes a numerical coupling approach to simulate seismic signals of rockfalls and conducts a parametric analysis to explore the characteristics of the seismic signals generated by rockfalls. To validate the approach, three field rockfall tests were selected for comparison. The rockfall velocity, duration, seismic frequency, Husid plot, Arias intensity, and spectrogram of the seismic signals were compared. We found that friction between rocks and the ground affects rock falling behavior. In addition, the local damping and Rayleigh damping assignments in the numerical model have strong effects on the simulation results. The volume of the falling rock and the falling speed of the rock affect the Arias intensity. The coupling approach proposed could be extended and can potentially be used as a useful tool in rockfall hazard estimations.

**Keywords: rockfall, seismic signal, numerical simulation, time–frequency spectrum, Arias intensity**

OPEN ACCESS

***Edited by:***
*Chih-Yu Kuo,*
*Academia Sinica, Taiwan*

***Reviewed by:***
*Joern Lauterjung,*
*Helmholtz Association of German Research Centres (HZ), Germany*
*Li-Tsung Sheng,*
*National Central University, Taiwan*

****Correspondence:***
*Zheng-Yi Feng*
*tonyfeng@nchu.edu.tw*

***Specialty section:***
*This article was submitted to Geohazards and Georisks, a section of the journal Frontiers in Earth Science*

***Received:*** *19 August 2021*
***Accepted:*** *17 November 2021*
***Published:*** *16 December 2021*

***Citation:***
*Feng Z-Y, Shen Z-R and Zhuang R-C (2021) A Numerical Investigation of the Characteristics of Seismic Signals Induced by Rockfalls. Front. Earth Sci. 9:761455. doi: 10.3389/feart.2021.761455*

## INTRODUCTION

Seismic signals induced by rockfalls are transmitted over great distances and can therefore be monitored remotely by accelerometers or geophones. The movement processes of rockfall events can be well correlated to their seismic signals. Once the characteristics of the signals are analyzed, significant information about the rockfall process such as scale and velocity can be better evaluated (Provost et al., 2018; Schöpa et al., 2018). In particular, their distinct seismic frequency, duration, and spectrograms can be analyzed.

Although seismic signals are most useful for analysis if they are recorded from actual rockfalls (Vilajosana et al., 2008; Schimmel et al., 2017), it may not always be possible to successfully acquire the signals from natural rockfalls due to various constraints. Large-scale rockfall test can be conducted but are difficult to set up and control, in addition to their high cost. Small-scale rockfall tests are easier to carry out several times but still require manpower, funds, and space. Therefore, it is necessary to develop a numerical model to obtain sufficient synthetic seismic signals of rockfalls for systematic investigations and parametrical studies.

Particle flow code in 2 dimensions (PFC2D; Itasca Consulting Group, 2008) is a discrete element code and can calculate finite displacements and rotations of discrete elements and automatically recognize new contacts for rigid circular particles. Interaction between particles is treated as a dynamic process. The dynamic process is solved by an explicit finite-difference method. It is appropriate for simulating the movement of rock masses over large distances. For example, Tang et al. (2009) applied the PFC to model the Tsaoling large-scale landslide that resulted from the 1999 Chichi ML 7.3 earthquake. Yuan et al. (2014) utilized the PFC to simulate the Donghekou landslide triggered by the 2008 Wenchuan earthquake. The displacement of particles was traced to understand the landslide process. Deng et al. (2016) used the PFC to simulate the sliding processes of the Wenjiagou rock avalanche due to the 2008 Wenchuan earthquake. They classified the process into four stages: failure rupture, projectile motion, granular debris flow, and debris mass accumulation.

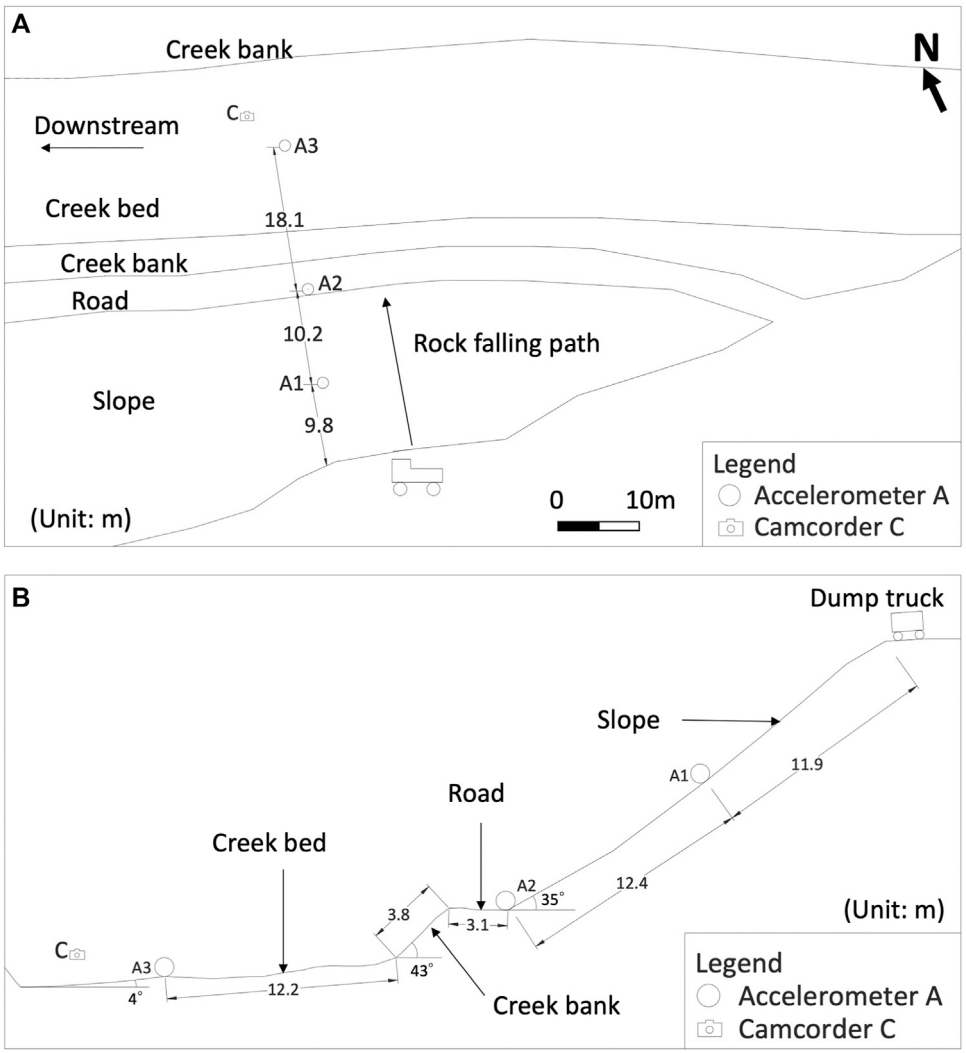


**FIGURE 1 |** Setup of the tests and layout of the sensors **(A)** top view, **(B)** side view (modified from Feng and Zhuang (2021)).

Yan et al. (2020) applied the PFC to reconstruct sliding processes and classified the landslide process into five stages: stationary, slipping, transition, entrainment–transportation, and deposition.

From the aforementioned literature, it is evident that the PFC is capable of simulating various landslide processes and their deposition very well. However, these researchers did not simulate the seismic signals induced by the landslides. To facilitate the simulation of the seismic signals induced by a landslide, Feng et al. (2017) and Feng et al. (2021) coupled the PFC and fast Lagrangian analysis of continua (FLAC, Itasca, Inc., 2011) (Itasca Consulting Group, 2011) to simulate large-scale landslides and obtained the seismic signals caused by the landslides from the numerical model. They used the PFC to reconstruct the landslide process and FLAC to compute the seismic signals induced by the landslide.

In this study, we propose and establish a numerical coupling approach using the PFC and FLAC to simulate the seismic signals of rockfalls and perform a parametric study. For assessment purposes, three rockfall field tests from Feng and Zhuang (2021) were selected for comparison with the numerical results. The reasons for the discrepancies between the numerical simulations and the field tests are discussed.

The proposed numerical coupling approach can be modified for various sizes and types of landslide movement by altering the properties and scales of the modeled moving materials in the PFC. Therefore, the coupling approach can be further extended to study the characteristics of seismic signals corresponding to various landslide processes and behaviors.

# METHODS

## The Rockfall Field Test Results for Comparison

In order to test the coupled simulations, three field test results were chosen from Feng and Zhuang (2021) for comparison. The path of the rockfall consisted of a slope, road, creek bank, and creek bed. The


**FIGURE 2 |** Serial snap pictures of the three field tests: **(A)** the single large rockfall (Test 2), **(B)** the single small rockfall (Test 5), **(C)** the rock mixture fall (Test 7). (The pictures were captured from the test films of Feng and Zhuang (2021). The test films can be viewed at https://link.springer.com/article/10.1007/s10346-021-01748-9).

dimensions of the test site and positions of 3 accelerometers are shown in **Figure 1**. Accelerometers A1–A3 (Acc. A1–A3, hereafter) were installed approximately parallel to the path of the rockfall.

The three field tests included a single large rockfall test, single small rockfall test, and rock mixture fall test. The size of the large rock was approximately 1.60 × 1.61 × 1.03 m across three of its axes and the small rock was approximately 0.91 × 0.98 × 0.72 m. The rock mixture consisted of rocks 0.3–0.8 m in diameter (approximate 4.5 $m^3$). The rock block or rock mixtures were dumped from a truck at the crest and fell, bounced, or rolled to the downslope and creek. The serial snap pictures of the three field tests are shown in **Figure 2**.

## The Numerical Coupling Approach for Rockfall Using PFC and FLAC

A numerical coupling model was established to simulate the processes of the rockfall tests using the PFC and FLAC. A numerical parametrical study was also performed to

**TABLE 1 |** Microscopic mechanical properties of the particles in the PFC models.

| Item | Single large rockfall | Single small rockfall | Rock mixture fall |
|---|---|---|---|
| Particle density (kg/m$^3$) | 2600 | 2600 | 2600 |
| Particle diameter (m) | Particles were "clumped" to be 1.25 m in diameter | Particles were "clumped" to be 0.95 m in diameter | 0.6–0.8 |
| Normal stiffness (N/m) | 1e7 | 1e7 | 1e7 |
| Shear stiffness (N/m) | 1e7 | 1e7 | 1e7 |
| Particle friction coefficient | 0.1 | 0.1 | 0.3 |
| Friction coefficient of wall | 0.3 | 0.3 | 0.2–1.6 |
| Local damping coefficient | 0.6 | 0.6 | 0.8 |
| Viscous damping ratio of normal direction | 0.36 | 0.36 | 0.32 |
| Viscous damping ratio of shear direction | 0.11 | 0.11 | 0.05 |

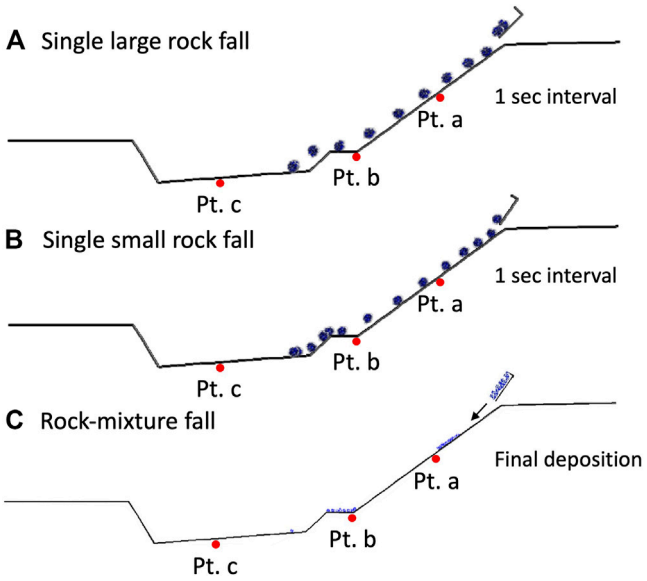


**FIGURE 3 |** Schematic of PFC models for the tests. Pt. **(a–c)** are the monitoring points in FLAC. The particle traces shown are in 1 s interval for the rock block falls and the final deposition for rock mixture fall.

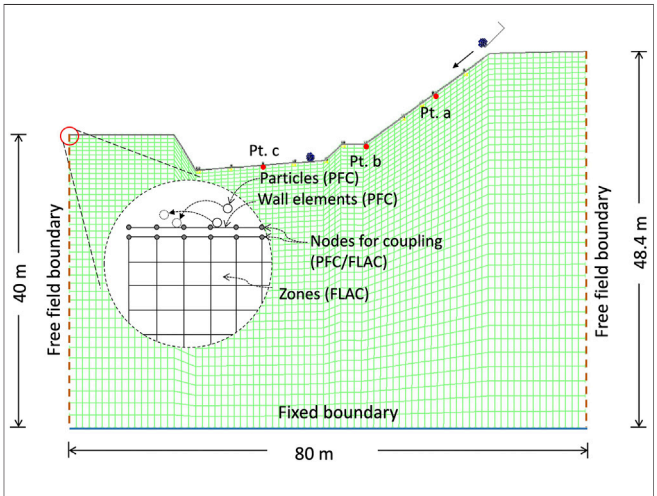


**FIGURE 4 |** Schematic plots of the PFC and FLAC coupling approach.

investigate the differences in falling velocity, energy produced, and acceleration of a rock block fall due to variation of parameters. The coupling methodology used was that of Feng et al. (2017), who used the PFC to simulate the movement of the rock particles and used FLAC to simulate the seismic signals for a large-scale landslide.

The PFC is suitable for modeling the movement and interaction of particles, while also being excellent in the simulation of rockfalls, including rock rolling/bouncing processes. PFC modeling involves particle elements and "wall" elements. The rock masses are modeled by the particles. The wall elements are the boundary that defines the particle movement; for example, the ground surface can be represented by wall elements. There are many microscopic parameters in the PFC that are required to simulate particle movement properly, including the friction between particles, friction between particles and the "wall" elements, local damping, and viscous damping (Tang et al., 2009; Lo et al., 2011). Altering the parameters will result in different particle movement behaviors and outcomes. Therefore, the parameters were first set by referring to the aforementioned literature and then adjusted with many "trial-and-error" back-analyses to fit the rockfall processes of the field tests, including falling, bouncing, rolling, and final deposition. The parameters that were considered best describing the field tests are shown in **Table 1**.

A schematic view of the PFC models for the field tests is shown in **Figure 3**. In total, 80 wall elements were used to represent the ground surface, which are the slope, road, creek bank, and creek bed. The rock block was modeled by the "clump" command of the PFC to assemble particles to form the shape of the two single test rocks. The clumped model rock is a rigid object with almost no deformation. The single large rock was modeled to be approximately 1.25 m in diameter and was modelled using 25 particles clumped together, while the single small rock was 0.95 m in diameter and composed of 15 particles. However, the two numerical model rocks were not circular in shape to mimic the shape of the two rock blocks in the tests. For the modeling of the rock mixture, 224 particles were clumped into 18 small model rocks and placed together in the model dump truck which was also modeled by wall elements. The model rocks and rock mixture were dumped from the slope crest to simulate the falling, rolling, and bouncing processes.

FLAC is a finite difference code suitable for dynamic analysis to model seismic waves traveling in geomaterial continua. To

**TABLE 2 |** Material properties for the FLAC numerical model.

| | Stratum | Road | Revetment |
|---|---|---|---|
| Density (kg/m$^3$) | 2000 | 2100 | 2300 |
| Bulk elasticity modulus (GPa) | 0.24 | 0.45 | 0.58 |
| Shear modulus (GPa) | 0.18 | 0.34 | 0.63 |
| Poisson's ratio | 0.2 | 0.2 | 0.15 |
| Shear wave velocity (m/s) | 300 | 400 | 500 |
| Rayleigh damping (%) | 1 | 1 | 1 |

achieve the simulation of seismic waves induced by the particle falling process, the PFC had to be coupled with FLAC. This strategy takes advantage of each code.

The setup of the FLAC model includes 80 * 40 = 3,200 finite difference zones. The sizes of the zones varied from 1 m * 2 m at the bottom to 1 m * 0.6 m at the top of the mesh, as shown in **Figure 4**. Three materials were modeled in FLAC: the stratum, the road, and the revetment. As the shear wave velocity was estimated from the rock block fall tests, it could then be used to estimate the shear modulus of the stratum. The soils of the road were compacted and were stiffer than the stratum. The revetment was made from rocks and was stiffer than the road. Therefore, the properties of the three materials were assigned accordingly in the FLAC model and are listed in **Table 2**.

The left- and right-side boundaries of the FLAC mesh were assigned as free-field boundaries so that the stress waves were not reflected by the boundaries. Free-field boundaries are one of the various kinds of "absorbing" boundaries in dynamic simulations. The bottom of the mesh was assigned as a fixed boundary. Rayleigh damping was assigned for material damping as it can also reduce the reflection of stress waves from the boundary.

While setting up the mesh of the FLAC model, the coordinates of the 80 zones' top surface had to be identical to the coordinates of the 80 wall elements in the PFC model to act as the coupling nodes for exchanging data between the PFC and FLAC code (**Figure 4**). Codes written in the computer language, FISH, organize the data exchange between the PFC and FLAC. During coupling calculations data are transferred between the two codes by "Socket I/O." In each timestep (cycle), FLAC passes the velocities of the coupling nodes through the Socket I/O to PFC. After calculation, the PFC then passes forces of the wall elements also through the Socket I/O to FLAC, and this then completes a coupling cycle (Itasca Consulting Group, Inc., 2011) (Itasca Consulting Group, 2011). Later, the coupling cycles were repeated until the simulation was complete. During the coupling calculation, the timestep (delta t) and stepping cycles had to be identical across the two codes. Also, to allow stable coupling calculation, the timestep was set as small as $1 \times 10^{-5}$ sec in both PFC and FLAC. The computer used was a Windows 10 desktop with an Intel® Core™ i9-9900K CPU running at processor base frequency of 3.60 GHz and with 32 GB of RAM. The computational time for each simulation was 40~60 min.

In the simulation, time series of seismic signals at selected nodes of the FLAC mesh were recorded and thus the simulation results can be compared with the field tests. Three monitoring points a, b, and c, were assigned in the FLAC model to trace the acceleration time series for analyses. However, the simulation is two-dimensional, meaning that particles rolling over the surface nodes or impacting the surface nodes, and generate much higher amplitudes of seismic signals than those of the field tests. To avoid excessively high seismic acceleration of the surface nodes due to direct impact, points a, b, and c in the model were located one node beneath the ground surface nodes. They corresponded to the locations of Acc. A1, A2, and A3, respectively, and were set up in the field tests.

## Signal Processing

### Hilbert–Huang Transform

The Hilbert–Huang transform (HHT, Huang et al., 1998) (Huang et al., 1998) is very well known and has been extensively applied in processing all kinds of signals in many research fields since its development in 1998. The HHT includes the calculation of empirical mode decomposition (EMD) and Hilbert transform (HT). EMD can decompose an original signal into many intrinsic mode functions (IMFs) and a residual signal. A time–frequency spectrum can be calculated by applying Hilbert transform to each IMF. The spectrum is very helpful when interpreting the characteristics of the signal and the relationship between spectral magnitude and instantaneous frequency over time. The average frequency of each IMF can be obtained. Also, the percentage power of each IMF can be calculated to identify the energy percentage of each IMF to the energy of the original signal. There are other methods for seismic signal analysis, such as short-time Fourier transform (STFT) and wavelet transform. However, the HHT is good for processing non-stationary and non-linear data. Therefore, the HHT was employed to process the seismic signals in this study using Visual Signal ver. 1.5 (AnCad, Inc., 2013) (AnCad, Inc., 2013).

### Arias Intensity

Arias (1970) (Arias and Hansen, 1970) proposed Arias intensity ($I_A$) to evaluate the intensity of a ground motion. $I_A$ is a reliable ground motion parameter. $I_A$ is defined as the square of the acceleration integrated over the duration of the signal, as shown in **Eq. 1**:

$$I_A = \frac{\pi}{2g} \int_0^{T_d} [a(t)]^2 dt \, (m/s), \tag{1}$$

where g is the gravity (9.81 m/sec$^2$), a(t) is the time-dependent acceleration, and Td is the duration of the acceleration signal.

A Husid plot is a time history of the normalized $I_A$ and can be obtained during integration of $I_A$. A Husid plot is sometimes used to define the duration of a strong motion. Feng et al. (2021) and Feng et al. (2020) also successfully applied Husid plots to estimate the increased energy (power) during landslides. Therefore, Husid plots were used to compare the energy development in the rockfalls discussed in this study. SeismoSignal software (Seismosoft, Ltd., 2020) (Seismosoft, Ltd, 2020) was employed to calculate $I_A$ and Husid plots in this study.

# RESULTS AND DISCUSSION

## Simulation Results and Comparison with Test Results

Three simulations (SIM-1, SIM-2, and SIM-3) were first performed for the single large rockfall, single small rockfall,

**TABLE 3 |** Simulation results from this study and the field test results from Feng and Zhuang (2021).

| Simulation/test | Movement type | Estimated falling duration (s) | Estimated rock block fall velocity (m/s) | Arias intensity of Pt. a, b, and c or A1, A2, and A3 (10-3 m/s) |
|---|---|---|---|---|
| Single large rockfall (SIM-1) | Fall | 11.3 | 4.67 | 129.3[a]<br>452.6[a]<br>70.6[a] |
| Single small rockfall (SIM-2) | Fall | 12.9 | 4.56 | 6.14[a]<br>166.6[a]<br>2.10[a] |
| Rock mixture fall (SIM-3) | Fall and roll | N/A | N/A | 1967.22[a]<br>2806.56[a]<br>24.41[a] |
| Single large rockfall (Test 2) | Fall | 9.4 | 4.86 | 1.83<br>10.03<br>0.52 |
| Single small rockfall (Test 5) | Fall | 7 | 6.08 | 0.91<br>4.04<br>0.21 |
| Rock mixture fall (Test 7) | Fall and roll | N/A | N/A | 1.27<br>2.22<br>0.10 |

[a]*Arias intensities of the numerical simulations are not comparable to the field tests due to the model rock/rocks impact very closely to the monitoring points.*

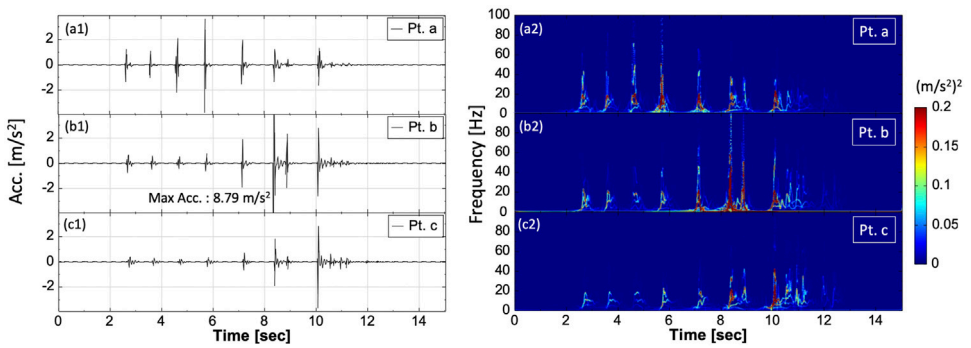


**FIGURE 5 |** Seismic signals and their corresponding time–frequency spectra with respect to the monitored points a, b, and c of the single large rockfall simulation.

and rock mixture fall. Correspondingly, three test results (Test 2, Test 5, and Test 7) from Feng and Zhuang (2021) were chosen for comparison.

The 3 simulation results and the 3 test results are summarized in **Table 3**. For each simulation and test, the estimated falling duration and averaged falling velocity of the rock block falls were estimated as well as the Arias intensities of the signals acquired at the numerical monitoring points a, b, and c and recorded by Acc. A1–A3 during the tests were listed respectively for reference.

**Figure 5** shows the SIM-1 simulated signals alongside the time-–frequency spectra of the single large rockfall. **Figure 6** depicts the seismic signals alongside time–frequency spectra of the single large rockfall test (Test 2) for comparison with **Figure 5**. The T1–T5 marked in **Figure 6** are the timings of when the rock arrives at certain locations on the slope, bank, and creek bed and are explained in the figure caption. The timings also correspond to the snap pictures in **Figure 3**.

Similarly, **Figures 7**, **8** present the resulting signals and spectra for the single small rockfall simulation SIM-2 and Test 5; **Figures 9**, **10** present the results of the rock mixture fall simulation SIM-3 and Test 7.

After many trial-and-error simulations of coupling PFC and FLAC, it was found that the rock size, shape, friction, and local damping of a rock block fall have the most influence on the simulation results. According to Itasca Consulting Group, Inc. (2008) (Itasca Consulting Group, 2008), the local damping used in the PFC is achieved by adding a damping force term to the equations of motion. The damping force is controlled by a damping constant. This form of damping has the advantage that only the accelerating motion is damped; the damping constant is non-dimensional, and the damping is frequency-independent.

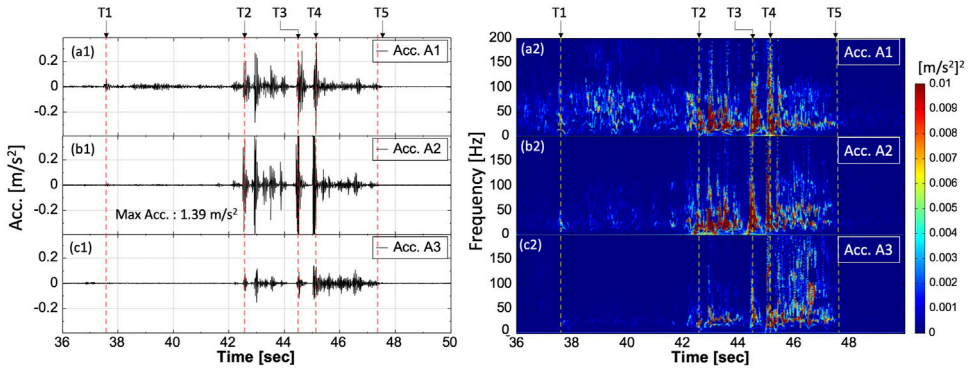


**FIGURE 6 |** Seismic signals and their corresponding time–frequency spectra of the single large rockfall test (Test 2). T1: 37.6 s, the rock first impacting on the slope; T2: 42.6 s, the rock arriving the slope toe; T3: 44.6 s, the rock impacting on the bank; T4: 45.1 s, the rock impacting on the creek bed; and T5: 47.6 s, the rock stop.

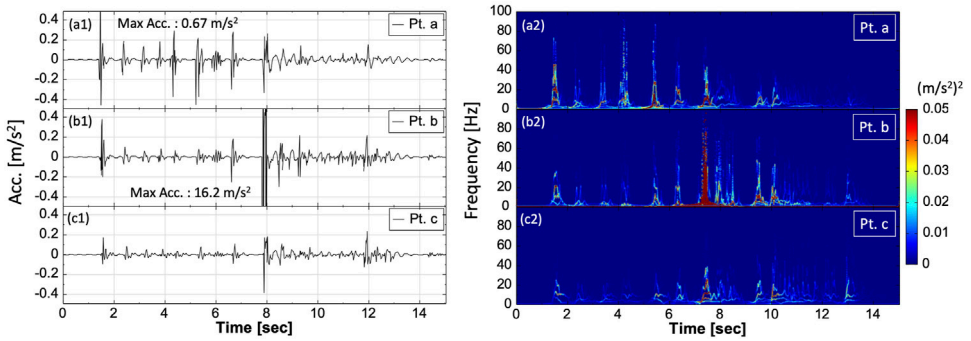


**FIGURE 7 |** Seismic signals and their corresponding time–frequency spectra with respect to the monitored points a, b, and c of the single small rockfall simulation.

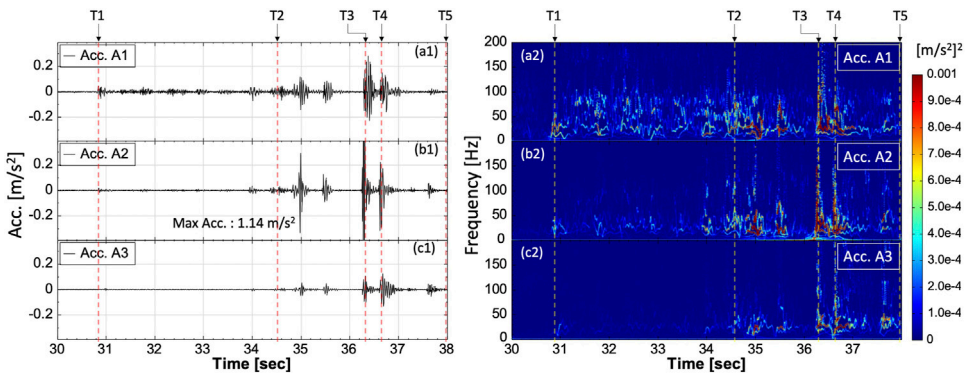


**FIGURE 8 |** Seismic signals and their corresponding time-–frequency spectra of the single small rockfall test (Test 5). T1: 30.9 s, the rock first impacting on the slope; T2: 34.6 s, the rock arriving at the slope toe; T3: 36.3 s, the rock impacting on the bank; T4: 36.6 s, the rock impacting on the creek bed; and T5: 38.0 s, the rock stop.

From our preliminary simulations, it was found that the larger the rock block, the greater the momentum, and the longer the resulting rolling distance. The rounder the shape of the rock, the less bouncing occurred, resulting in more rolling movement. The more irregular the shape of the rock (with an angular shape), the greater will be the occurrence of bouncing. The presence of a flat face on the model rock could also cause it to suddenly stop when the flat surface of the rock made contact with the ground. Therefore, when simulating a rock block fall, the shape of the model rock should reflect that of the rock block used in the tests as closely as possible.

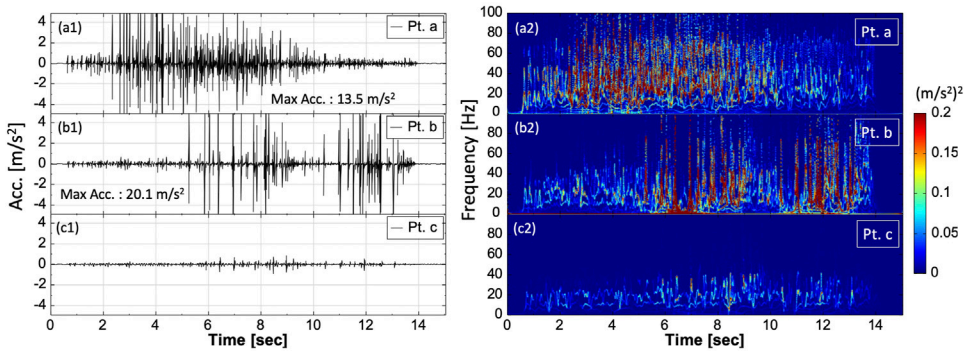


**FIGURE 9 |** Seismic signals and their corresponding time–frequency spectra with respect to the monitored points a, b, and c of the rock mixture fall simulation.

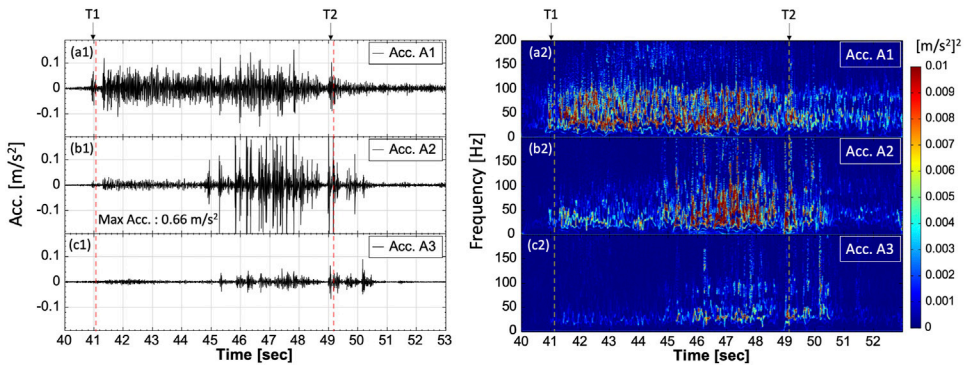


**FIGURE 10 |** Seismic signals and their corresponding time–frequency spectra of the rock mixture fall test (Test 7). T1: 41.0 s, rock mixtures impacting on the slope; T2: 49.1 s, the rocks impacting on the creek bed.

The friction parameter of the wall elements in the PFC will affect the rolling distance and behavior of rockfall. If friction is set too low, the rock will slide and not roll, while if friction is set too high, the rock will come to a stop on the slope and cease to move. In the PFC, the local damping setting will affect the distance of rock movement and bounce height. The smaller the local damping value assigned, the greater the distance of movement will be and the more obvious the incidences of bouncing will be. Therefore, a set of parameters should be assigned in the PFC to allow the model rocks to fall/roll/bounce from top of the slope to the creek bed in a similar way to the field tests. The three simulations (SIM-1–3) were considered successful without too many occurrences of bouncing during the falling processes and were closely reflected the field tests.

In this study, local damping was adjusted to make the bouncing of the rocks fit the field tests; however, this resulted in a decrease in the falling speed of the simulated rocks. Therefore, the falling speeds of a rock block fall in SIM-1 and SIM-2 was slower than Test 2 and Test 5, respectively (**Table 3**).

The surface wave velocity of the numerical mesh was estimated to be 242 m/s by using the differences in arrival time and distance between points a and c for SIM-1. The surface wave velocity calculated from SIM-2 was 263.6 m/s. These two velocities are fairly close to the field test estimated average surface wave velocity of 291.4 m/s (Feng and Zhuang, 2021). This also supports that the estimation of the shear modulus of the stratum is quite realistic.

Most of the simulated signals of SIM-1 and SIM-2 have obvious "aperiodical impulse signals" (**Figures 5**, **7**), which is the result of the rock bouncing on the ground surface. In Tests 2 and 5, such "aperiodical impulse signals" were also observed when the rock bounced on the road, bank, and creek bed (**Figures 6**, **8**).

The signals and time–frequency spectra of SIM-3 Pt. a and Test 7 Acc. A1 in **Figure 9**a and **Figure 10**a are continuous due to percussion, rolling, and falling of the rock mixture. However, in field Test 7 when the rock mixture rolled down, debris on the slope surface moved downward too, resulting in a longer signal duration at Test 7 Acc. A1. The numerical simulation SIM-3 only contains rock mixture itself (i.e., the debris particles were not simulated) causing the duration of the SIM-3 signal to be shorter than that of Test 7 Acc. A1.

Average frequencies were also obtained from points a, b, and c for SIM-1 to SIM-3 (**Table 4**). In **Table 4**, only the major signal components (i.e., major IMFs) were selected from the field tests

**TABLE 4 |** Average frequency in Hz of the seismic signals from the simulations and tests.

| Simulation/test | Pt. a/Acc. A1 | Pt. b/Acc. A2 | Pt. c Acc./A3 |
|---|---|---|---|
| Single large rockfall (SIM-1) | 17.8 | 23.6 | 17.7 |
| Single small rockfall (SIM-2) | 10.4 | 117[a] | 13.2 |
| Rock mixture fall (SIM-3) | 52.7 | 56 | 22.1 |
| Single large rockfall (Test 2) | 29.5 (IMF 3 + 4+5, 84.5%) | 35.8 (IMF 3 + 4, 82.3%) | 28.8 (IMF 3 + 4+5, 81.4%) |
| Single small rockfall (Test 5) | 28.4 (IMF 3 + 4+5, 92.5%) | 36.0 (IMF 3 + 4, 94.0%) | 25.4 (IMF 4, 86.2%) |
| Rock mixture fall (Test 7) | 50.3 (IMF 2 + 3+4, 94.5%) | 55.1 (IMF 2 + 3+4, 90.1%) | 41.7 (IMF 2 + 3+4, 83.5%) |

[a]*Due to the rock directly impacting Pt. b and causing the very high average frequency.*

**TABLE 5 |** Parameters settings and results of the parametrical study for single large rockfall. The friction coefficient of walls, bulk modulus, and Rayleigh damping were varied.

| Parameter | SIM-1 baseline | SIM-4 | SIM-5 | SIM-6 | SIM-7 | SIM-8 | SIM-9 | SIM-10 | SIM-11 |
|---|---|---|---|---|---|---|---|---|---|
| Friction coefficient of wall | 0.3 | 0.1 | 0.5 | 0.7 | 0.3 | 0.3 | 0.3 | 0.3 | 0.3 |
| Bulk modulus of the strata, road, and bank (GPa) | 0.24 | 0.24 | 0.24 | 0.24 | 0.20 | 0.39 | 0.54 | 0.24 | 0.24 |
| | 0.45 | 0.45 | 0.45 | 0.45 | 0.37 | 0.73 | 0.10 | 0.45 | 0.45 |
| | 0.58 | 0.58 | 0.58 | 0.58 | 0.53 | 0.77 | 0.96 | 0.58 | 0.58 |
| Rayleigh damping (%) | 1 | 1 | 1 | 1 | 1 | 1 | 1 | 3 | 5 |
| Estimated falling velocity (m/s) | 4.98 | 5.72 | 4.64 | 4.34 | 4.98 | 4.98 | 4.89 | 4.58 | 4.50 |
| Significant duration ($D_{0595}$) of points a, b, and c (s) | 7.46 | 5.52 | 6.50 | 5.50 | 5.64 | 7.45 | 5.95 | 4.70 | 4.19 |
| | 2.93 | 4.73 | 5.32 | 1.02 | 0.65 | 3.36 | 0.97 | 0.66 | 2.32 |
| | 4.76 | 10.31 | 10.15 | 9.50 | 5.86 | 7.80 | 5.98 | 5.74 | 4.33 |
| Arias intensity of points a, b, and c (m/s) | 129.3 | 102.73 | 139.63 | 213.99 | 101.09 | 79.75 | 70.87 | 73.70 | 50.81 |
| | 452.64 | 207.62 | 222.52 | 886.82[a] | 993.53[a] | 142.05 | 318.90 | 265.43 | 64.98 |
| | 70.61 | 49.40 | 26.31 | 33.77 | 34.23 | 37.98 | 19.76 | 9.86 | 11.33 |
| Max Acc. of Pt. a, m/s$^2$ | 3.63 | 4.15 | 4.35 | 4.82 | 2.45 | 2.72 | 2.66 | 3.14 | 3.08 |
| Min Acc. of Pt. a, m/s$^2$ | −3.83 | −2.66 | −4.31 | −5.88 | −2.93 | −2.75 | −2.70 | −2.92 | −2.66 |
| Max Acc. of Pt. a for the first impact, m/s$^2$ | 1.23 | 1.15 | 1.53 | 1.76 | 1.27 | 1.11 | 1.05 | 0.66 | 0.50 |
| Min Acc. of Pt. a for the first impact, m/s$^2$ | −1.29 | −1.21 | −1.36 | −1.36 | −1.39 | −1.10 | −1.02 | −0.76 | −0.58 |

[a]*Arias intensities of Pt. b are very high due to that Pt. b being very close to the impact points of the rock block.*

for frequency calculation based on higher energy content in the IMFs and screening of the noise signals from the environment. The average frequencies of the numerical simulations of rock block falls (SIM-1 and -2) were much lower than those of field tests 2 and 5. The reason for this is that the rock in the rock block fall tests mainly rolled on the slope and continued to generate high-frequency seismic waves from the slope. However, the average frequency of the signals of point a and b of SIM-3 are very close to those of Test 7 which indicates that the simulation of the rock mixture fall process is reflective of field Test 7.

Discrepancies were observed between the results of the numerical simulations and the field tests. The main source of the differences is that the numerical simulation is two-dimensional, resulting in the model rock/rocks contacting the monitoring points directly, causing large seismic signals. In addition, the model rock rolls on only one axis, but the rolling axis of the rock in the field tests could change randomly and did not necessarily adhere to a straight path. Moreover, the surface soils of the slope in the field tests were taken along by the falling rock, which was not accounted for in the simulations. All of these reasons result in differences between the numerical simulations and the field tests. Feng et al. (2017) indicated that the simulated seismic signals were obviously larger than those from station records because of the direct impacts of the particles on the mesh nodes.

## Numerical Parametric Analysis of the Single Large Rockfall

The SIM-1 single large rockfall simulation was chosen as the baseline case in terms of parameters to discuss the influence of the friction coefficient of wall, bulk modulus, and Rayleigh damping on the numerical simulations. The results and parameters used are summarized in **Table 5**. The friction coefficient of wall elements in SIM-4, -5, and -6 were varied in the PFC, that is, by varying the friction of the modeled ground surface. It was observed that the greater the friction, the slower the rockfall velocity is, that is, friction slows the falling of the rock. However, due to increasing wall friction, the rock impacts on the slope (which is close to Pt. a) more often, increasing the Arias intensity of Pt. a. The acceleration amplitudes of Pt. a during the first impact also increased with increasing wall friction.

The bulk modulus of the strata, road, and bank in FLAC was varied in SIM-7, -8 and -9. The results show that the bulk modulus had little effect on the rockfall velocity, that is, the rockfall velocities of SIM-1, -7, and -8 greatly altered. It was found that the larger the bulk modulus, the smaller the acceleration amplitude of the first impact of the rock. As bulk modulus increases, dynamic deformation of the geomaterials decreases, resulting in less acceleration.

Rayleigh damping in FLAC was varied in SIM-10 and -11. The comparison results show that the larger the Rayleigh

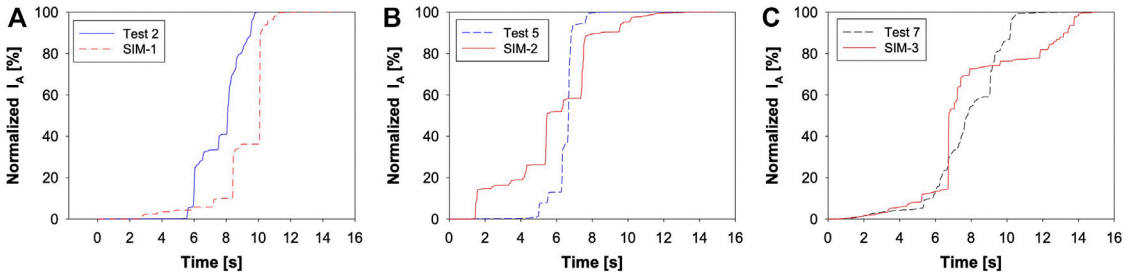


**FIGURE 11 |** Husid plots of seismic signals form Pt. c and Acc. 3: **(A)** single large rockfall, **(B)** single small rockfall, and **(C)** rock mixture fall.

damping, the smaller the amplitude of the seismic signal and the smaller the Arias intensity, which indicates that Rayleigh damping models the dissipation of energy. There are limitations of modeling with Rayleigh damping in FLAC. Rayleigh damping is frequency dependent and requires the selection of a central frequency as an input parameter. The central frequency is neither the natural frequency of the stratum nor the major frequency of the external exciting forces but a combination of both (Mánica et al., 2014). We used a central frequency of 1 Hz for the Rayleigh damping setting in FLAC, but we were not able to calibrate it due to a lack of data. Also, while Rayleigh is assigned in FLAC, its use results in increase calculation times as it requires a smaller timestep (delta t) for a stable solution.

## Husid Plot and Accumulation of Arias Intensity Versus Time

**Figure 11** shows the Husid plots of seismic signals from Pt. c and Acc. 3, located in the creek bed, of simulations and field tests. The time zero for the Husid plot is the time when the rock first touched the ground surface.

The Husid plots for single large rockfalls of SIM-1 and Test 2 are shown in **Figure 11A**. The significant durations of SIM-1 and Test 2 are 4.76 and 3.95 s, respectively. The significant duration ($D_{0595}$) of a signal is defined as the time interval between 5 and 95% accumulated Arias intensity. It can be observed that when the rock rolled on the slope, the accumulated Arias intensity increased very slowly. However, when the rock impacted the road, bank, or the creek bed, the accumulated Arias intensity increased rapidly. Since Pt. c and Acc. A3 are located in the creek bed, a large kink will appear in the Husid plots when the falling rock impacts the creek bed. It was found that when the rock was still rolling on the slope in SIM-1, the Arias intensity increment was larger than the field Test 2 as in **Figure 11A**. The reasons could be: 1) the energy of the rock rolling on the slope in the field tests was dissipated by the soft surface soils. 2) increased bouncing movement on the slope of SIM-1 resulting in greater seismic energy.

It can be seen from **Table 3** that the Arias intensities of the simulations were much higher than those of the field tests. This was caused by the fact that the monitoring points of the numerical simulations were very close to the impact points of the model rock. The accelerometers of the field tests were at a distance >10 m from the rolling path of the rock. Moreover, the monitoring points of simulations and the rolling path of the model rock are in-line, that is, the model rock was able to roll over or impact the monitoring points directly.

**Figure 11B** shows the Husid plots for the single small rockfall SIM-2 and Test 5. The significant duration of Test 5 is 2.60 s. The significant duration of SIM-2 is comparatively long (11.01 s) and can be observed from **Figure 11B**. From the simulation film, it can be understood that the rock rolled slowly on the slope in SIM-2, impacted the road, and continued to slowly roll on the bank, resulting in an elongated significant duration. Compared with SIM-1 from its simulation film, the rock did not roll on the bank; it instead bounced from the road, impacted the creek bed, and came to a stop, resulting in a shorter significant duration. Similarly, when the rock was still rolling on the slope in SIM-2, the Arias intensity increment was larger than in field Test 5 as shown in **Figure 11B**.

**Figure 11C** shows the Husid plots for rock mixture fall SIM-3 and Test 7. The significant duration of Test 7 was 5.21 s, while the significant duration of SIM-3 was also rather long at 10.3 s. That is because the rocks slowly and sporadically rolled down the slope, and this can be observed from the simulation film of SIM-3. Also, the Husid plot of SIM-3 shows that the Arias intensity was still increasing between 12and 15 s. Generally, the rate of increase in the Arias intensity of the rock mixture fall tests is slower than that of the rock block fall tests and with less kinks in the Husid plots.

## CONCLUSION

This study proposed a numerical coupling approach to simulate seismic signals of rockfalls to discuss the characteristics of seismic signals generated by rockfalls. The PFC was used to construct the rockfall mass and simulate the falling processes. The FLAC code was coupled with the PFC to calculate seismic signals induced by the rockfalls. Three field rockfall test results were used for comparison with the simulated results and to validate the numerical results of the approach. Hilbert–Huang transform (HHT) was employed to analyze the seismic signals to obtain the frequency, intrinsic mode functions, and time–frequency spectra of the seismic signals. We discussed the rockfall velocity, duration, seismic frequency, Husid plot, Arias intensity, and the characteristics of the time–frequency spectra of the seismic signals in detail. Finally, a numerical parametric study was performed to explore the parameters that were most sensitive with regard to their influence on the numerical simulations.

The results showed that the waveform patterns of the seismic signals of the simulations were similar to those of the field tests in general. The velocities of the surface waves of the stratum in the numerical models were estimated and compared well with the velocity obtained by the single large rock fall test. The friction of the ground surface affects the rolling distance and behavior of rockfalls. When we selected the friction parameter, we shall refer to the conditions of the surface soil and vegetation and with a trial-and-error approach. Due to better falling process simulation, the time-frequency spectra of the rock-mixture fall simulation was closer to that of the field tests than in the single rock fall simulation. Therefore, the closer to the real-life process of the rock fall the simulation was, the closer the characteristics of seismic signals were to the field results in general. Damping parameters in the numerical simulations influenced the kinematic behavior of the rock fall significantly. The local damping setting in PFC affects the distance of rock movement and bounce height. The Rayleigh damping in FLAC has a strong effect on energy dissipation. The Arias intensity and Husid plot reflect the seismic energy received by an accelerometer. They are affected by rock fall volume and falling speed.

The numerical coupling approach can be further extended to general landslide movements such as translational slides, rock flows, and various sizes of rock mass falls to study the seismic characteristics and movement processes. This will assist in interpretation of the seismic records of various landslide events acquired from seismic stations such that the evaluation of landslide movement types and magnitudes based on seismic signals can maturate.

## DATA AVAILABILITY STATEMENT

The raw data supporting the conclusions of this article will be made available by the authors, without undue reservation.

## AUTHOR CONTRIBUTIONS

Z-YF contributed to methodology, formal analysis, investigation, supervision, and writing original draft. Z-RS helped with data curation, formal analysis, visualization, and writing original draft. R-CZ assisted with data curation, formal analysis, visualization, and writing original draft.

## FUNDING

The authors acknowledge the Ministry of Science and Technology, Taiwan, R.O.C, for providing research funding (Grant Number: 108-2625-M-005-006).

## ACKNOWLEDGMENTS

The authors thank Hallam Atherton for reviewing the manuscript style.

## SUPPLEMENTARY MATERIAL

The Supplementary Material for this article can be found online at: https://www.frontiersin.org/articles/10.3389/feart.2021.761455/full#supplementary-material

**Supplementary Film SIM-1 |** Numerical simulation for the single large rockfall SIM-1.

**Supplementary Film SIM-2 |** Numerical simulation for the single small rockfall SIM-2.

**Supplementary Film SIM-3 |** Numerical simulation for the rock mixture fall SIM-3.

## REFERENCES

AnCad Inc (2013). Visual Signal Reference Guide Version 1.5. Available at: http://www.ancad.com.tw/VisualSignal/doc/1.5/RefGuide.html (Accessed June 28, 2021).

Arias, A. (1970). "A Measure of Earthquake Intensity," in *Seismic Design for Nuclear Power Plants*. Editor RJ Hansen (Cambridge: MIT Press), 438–483.

Deng, Q., Gong, L., Zhang, L., Yuan, R., Xue, Y., Geng, X., et al. (2016). Simulating Dynamic Processes and Hypermobility Mechanisms of the Wenjiagou Rock Avalanche Triggered by the 2008 Wenchuan Earthquake Using Discrete Element Modelling. *Bull. Eng. Geol. Environ.* 76 (3), 923–936. doi:10.1007/s10064-016-0914-2

Feng, Z.-Y., Huang, H.-Y., and Chen, S.-C. (2020). Analysis of the Characteristics of Seismic and Acoustic Signals Produced by a Dam Failure and Slope Erosion Test. *Landslides* 17 (7), 1605–1618. doi:10.1007/s10346-020-01390-x

Feng, Z.-Y., Lo, C.-M., and Lin, Q.-F. (2017). The Characteristics of the Seismic Signals Induced by Landslides Using a Coupling of Discrete Element and Finite Difference Methods. *Landslides* 14 (2), 661–674. doi:10.1007/s10346-016-0714-6

Feng, Z.-Y., Lu, Y.-R., and Shen, Z.-R. (2021). A Numerical Simulation of Seismic Signals of Coseismic Landslides. *Eng. Geology* 289, 106191. doi:10.1016/j.enggeo.2021.106191

Feng, Z.-Y., and Zhuang, R.-C. (2021). Characteristics of Seismic and Acoustic Signals of rock falls: an Experimental Study. *Landslides* 18, 3695–3706. doi:10.1007/s10346-021-01748-9

Huang, N. E., Shen, Z., Long, S. R., Wu, M. C., Shih, H. H., Zheng, Q., et al. (1998). The Empirical Mode Decomposition and the Hilbert Spectrum for Nonlinear and Non-stationary Time Series Analysis. *Proc. R. Soc. Lond. A.* 454, 903–995. doi:10.1098/rspa.1998.0193

Itasca Consulting Group, Inc (2011). *Fast Lagrangian Analysis of ContinuaVer. 7.0 User Manuals*. Minneapolis, USA: Itasca.

Itasca Consulting Group, Inc (2008). *Particle Flow Code in 2 dimensionsVer. 4.0 User Manuals*. Minneapolis, USA: Itasca.

Lo, C.-M., Lin, M.-L., Tang, C.-L., and Hu, J.-C. (2011). A Kinematic Model of the Hsiaolin Landslide Calibrated to the Morphology of the Landslide deposit. *Eng. Geology* 123 (1-2), 22–39. doi:10.1016/j.enggeo.2011.07.002

Mánica, M., Ovando, E., and Botero, E. (2014). Assessment of Damping Models in FLAC. *Comput. Geotechnics* 59, 12–20. doi:10.1016/j.compgeo.2014.02.007

Provost, F., Malet, J.-P., Hibert, C., Helmstetter, A., Radiguet, M., Amitrano, D., et al. (2018). Towards a Standard Typology of Endogenous Landslide Seismic Sources. *Earth Surf. Dynam.* 6, 1059–1088. doi:10.5194/esurf-6-1059-2018

Schimmel, A., Hübl, J., Koschuch, R., and Reiweger, I. (2017). Automatic Detection of Avalanches: Evaluation of Three Different Approaches. *Nat. Hazards* 87, 83–102. doi:10.1007/s11069-017-2754-1

Schöpa, A., Chao, W.-A., Lipovsky, B. P., Hovius, N., White, R. S., Green, R. G., et al. (2018). Dynamics of the Askja Caldera July 2014 Landslide, Iceland, from Seismic Signal Analysis: Precursor, Motion and Aftermath. *Earth Surf. Dynam.* 6 (2), 467–485. doi:10.5194/esurf-6-467-2018

Seismosoft, Ltd (2020). SeismoSignal Software, Ver. 2020. Available at: https://seismosoft.com/products/seismosignal/ (Accessed on April 14, 2020).

Tang, C.-L., Hu, J.-C., Lin, M.-L., Angelier, J., Lu, C.-Y., Chan, Y.-C., et al. (2009). The Tsaoling Landslide Triggered by the Chi-Chi Earthquake, Taiwan: Insights from a Discrete Element Simulation. *Eng. Geology* 106 (1-2), 1–19. doi:10.1016/j.enggeo.2009.02.011

Vilajosana, I., Suriñach, E., Abellán, A., Khazaradze, G., Garcia, D., and Llosa, J. (2008). Rockfall Induced Seismic Signals: Case Study in Montserrat, Catalonia. *Nat. Hazards Earth Syst. Sci.* 8 (4), 805–812. doi:10.5194/nhess-8-805-2008

Yan, Y., Cui, Y., Guo, J., Hu, S., Wang, Z., and Yin, S. (2020). Landslide Reconstruction Using Seismic Signal Characteristics and Numerical Simulations: Case Study of the 2017 "6.24" Xinmo Landslide. *Eng. Geology* 270, 105582. doi:10.1016/j.enggeo.2020.105582

Yuan, R.-M., Tang, C.-L., Hu, J.-C., and Xu, X.-W. (2014). Mechanism of the Donghekou Landslide Triggered by the 2008 Wenchuan Earthquake Revealed by Discrete Element Modeling. *Nat. Hazards Earth Syst. Sci.* 14 (5), 1195–1205. doi:10.5194/nhess-14-1195-2014

**Conflict of Interest:** The authors declare that the research was conducted in the absence of any commercial or financial relationships that could be construed as a potential conflict of interest.

frontiers in Earth Science

ORIGINAL RESEARCH
published: 31 January 2022
doi: 10.3389/feart.2021.788029

# Damage Types and Deterioration Characteristics of Check Dams Built on Mountain Streams in Southeast Korea

*Ki-Hwan Lee*[1,2], *Ewane Basil Ewane*[3,2]*, *Taro Uchida*[4] *and Choong-Shik Woo*[1]

[1]Department of Forest Environment and Conservation, National Institute of Forest Science, Seoul, South Korea, [2]Department of Forest Resources, College of Natural Resources, Yeungnam University, Gyeongsan-si, South Korea, [3]Department of Geography, Faculty of Social and Management Sciences, University of Buea, Buea, Cameroon, [4]Faculty of Life and Environmental Sciences, University of Tsukuba, Tsukuba, Japan

Check dams are one of representative structural measures to reduce sediment disaster at a forest watershed. Therefore, it is essential to assess the structural vulnerability and functionality of check dams in the management of sediment disaster risk at watersheds. This study examined the main types of damages and deterioration characteristics in concrete and stone check dams, which comprise more than 80.0% of Korea's check dam stock. This was based on the 4-step condition assessment, which is the modified version of condition assessment methodology for embankment dams to meet the characteristics of check dams. As a result, the damages and deterioration of concrete check dams were classified into ten representative types. And representative damage types of stone check dams were classified into nine types. The condition assessment results demonstrated that the spillway part frequently contacted with water and debris flows was deteriorated approximately 1.2 times faster than the wing parts for both concrete and stone check dams, and the maintenance demands of both types of check dams increased 15–20 years after construction. Thus, these deterioration characteristics of concrete and stone check dams should be considered in decision-making to determine maintenance priorities among the check dams stock. Furturemore, we analyzed the relationship between condition index and service time in the examined concrete and stone check dams. The degree of deterioration in concrete and stone check dams increased significantly as the service time increased. Based on the relationship between condition index and service time, we classified deterioration characteristics of check dams into two groups: 1) those that follow the average deterioration trends of their facility group (Group II) and 2) those that undergo an unexpected end-of-service life because of exceptional incidents or severe defects (Group I). We hope that our work will form a useful resource for engineers and decision-makers involved in planning, designing, constructing, and maintaining check dams.

**Keywords: condition assessment, non-permeable check dams, stream management, check dam deterioration, visual inspection**

OPEN ACCESS

***Edited by:***
*Norifumi Hotta,*
*The University of Tokyo, Japan*

***Reviewed by:***
*Shusuke Miyata,*
*Kyoto University, Japan*
*Nour Chahrour,*
*Université Grenoble Alpes, France*

***Correspondence:**
*Ewane Basil Ewane*
*ewane.basil@ubuea.cm*

***Specialty section:***
*This article was submitted to Geohazards and Georisks, a section of the journal Frontiers in Earth Science*

***Received:*** *01 October 2021*
***Accepted:*** *16 December 2021*
***Published:*** *31 January 2022*

***Citation:***
*Lee K-H, Ewane EB, Uchida T and Woo C-S (2022) Damage Types and Deterioration Characteristics of Check Dams Built on Mountain Streams in Southeast Korea. Front. Earth Sci. 9:788029. doi: 10.3389/feart.2021.788029*

## INTRODUCTION

Mountain streams and rivers (hereinafter "Mountain Stream") are main passages of sediments generated from slopes and floodplains. This sediment transport process from a forest watershed sometimes causes debris flows and large-scale fluvial transport, resulting in great damage to developed areas on a downstream alluvial fans and flood plains (Rickenmann and Koschi, 2010). In particular, in countries of mountainous terrain with small land surface areas like South Korea, residential areas and agricultural land are developed up to upstream mountainous areas that are vulnerable to flooding and sediment disasters. As a result, there is a tendency that damages at relevant spheres of life continues to occur due to flood water and sediment yield caused by typhoons and an intensive rainfall. Therefore, river managers have constructed protective structures of various types on mountain streams over the past decades in order to protect vulnerable areas downstreams by controlling flood water, channel erosion, and reducing the magnitude of sediment yield (Hueble and Fiebiger, 2005; Mizuyama, 2010; Piton et al., 2016).

A check dam is a transverse structure constructed across a mountain stream to stabilize the riverbed and control sediment yield and is one of representative structural measures to reduce sediment disaster at a forest watershed (Mizuyama et al., 1988; Armanini et al., 1991; Matsumura, 2000; Suda et al., 2009; Piton et al., 2016). Check dams, however, continues to get damaged during its life cycle due to the purpose of its design. Its superannuation due to the deterioration of structure and the reduction of debris storage capacity sometimes causes the phenomenon of large sediment yield that results in great damage to downstream areas (Hueble and Fiebiger, 2005; Suda et al., 2009; Dell'Agnese et al., 2013; Mazzorana et al., 2014). Therefore, it is important in the management of sediment disaster risk at forest watersheds to assess the durability, performance, and sustainability of check dams constructed on mountain streams to inform management and maintenance decision-making and policy. In particular, the assessment of check dam deterioration involves assessing the degree of change in the condition inside and outside the check dam by investigating and analyzing structural deterioration caused by localized environment factors and the properties of construction materials, or damages to the structure caused by debris flow and flooding events that exceeds the structure's permissible limits, as applied to studies on maintenance practices (Dell'Agnese et al., 2013; Cortes Arevalo et al., 2016; Lee et al., 2018; Mazzorana et al., 2018).

In South Korea, it is estimated that approximately 12,000 check dams were constructed from 1986 to 2020 (Korea Forest Service; https://kfss.forest.go.kr/stat/ptl/fyb/frstyYrBookList.do?curMenu=9854). In particular, with increase in the frequency, intensity, and magnitude of typhoon events in the early 2000s and affecting watersheds drainage systems in the South Korea, check dam construction projects increased greatly; about 3,400 check dams were constructed from 2001–2010, and about 7,300 from 2011–2020. In other words, about 90.0% of South Korea's check dam inventory was constructed intensively in 20 years, that is, from 2001 to 2020. The Korea Forest Service (KFS) classifies 20-year old check dams as deteriorated facilities and manages them with more conservative standards than recently-built check dams (Korea Forest Service, 2018; Korea Forest Service, 2020). Therefore, it is expected that the cumulative number of deteriorated check dams will increase rapidly in the future, and accordingly, the burden of maintaining them will be aggravated. However, studies on standard systems and advanced methodological guidelines for investigating and assessing the causes of check dam damage and deterioration and decision-making on their maintenance and sustainability are still insufficient. Check dams in South Korea can be broadly divided into non-permeable and permeable structures (Hueble and Fiebiger, 2005). The former prevents water and sediment from passing, and they are most often built on Korea's mountain streams. The latter structures allow untargeted water and fine particles (but not, for example, debris flows or driftwood) to flow downstream through a part of the check dam body. We studied non-permeable concrete and stone check dams (hereinafter "Concrete and Stone Check Dams), which comprise more than 80% of the check dam inventory in South Korea, thus, priority must be given to managing this type of check dams because of the maintenance demand (Lee et al., 2018). Only few studies have conducted a comprehensive and detailed condition assessment of check dams in South Korea or develop new condition assessment indicators that modify the existing guidelines to achieve more robust results and generate more reliable generalizations (Lee, 2017; Lee et al., 2018; Lee et al., 2021).

Therefore, the main objective of this study is to examine the different types of damage and deterioration characteristics of the check dams in relation to service times, structural features, and construction environments. We specifically evaluated the degree of deterioration of existing check dams in relation to their service time and localized environmental condition factors. Lastly, we developed new indicators and modified the existing guidelines to fit the observed detailed and specific damage and deterioration characteristics of check dams. This was based on the condition assessment methodology, which is commonly applied to quantify the structural conditions of facilities.

## BACKGROUND: CHECK DAM CONDITION ASSESSMENT

Current river managers design check-dam maintenance plans (e.g., investments in repairs and new dams) by considering two potential factors: functional effect and cost-efficient (Piton et al., 2016). This needs to take reliable inspection data on the current conditions of single or multiple cases of check dams. In previous studies, the structural vulnerability and functionality of check dams have been evaluated using methods that examine physical condition *via* visual inspections and non-destructive testing (Mizuyama, 1979; Dell'Agnese et al., 2013; Lee et al., 2021; Cortes Arevalo et al., 2016; Lee et al., 2018; Mazzorana et al., 2018), as well as methods that examine the structure's effectiveness, including bed stabilization, slope reduction, and

sediment retention (Makita et al., 1987; Lenzi et al., 2003; Comiti et al., 2010; Chahrour et al., 2021). However, the damages and deterioration of existing check dams are generally evaluated by qualitative methods (condition rating) in maintenance practice. The condition rating system provides a direct, descriptive indicator of the check dam condition rather than using a numeric scale. Thus, the method is helpful to identify objects to need repair, but its application is limited in the analysis that requires differentiation within the individual structures (e.g., service life analysis and prioritizing maintenance work orders).

This study evaluated check dams for the degree of their deterioration, using a condition assessment system that is widely used by the facility management system to determine priorities among objects of repair or re-construction. The condition assessment evaluates the deterioration of facilities with standardized methods and provides information that is essential for making decisions on maintenance (Andersen and Torrey, 1995; Jeong et al., 2018). In particular, it can quantify the structural and functional condition of an object by computational approach (condition index), and thus it is used to determine priorities among various facilities such as dams, roads and bridges (Japanese Ministry of Land, Infrastructure, Transportation, and Tourism, 2014; Federal Highway Administration [FHWA], 2016; Korean Ministry of Land, Infrastructure, and Transport [MOLIT], 2020). Methods for calculating the condition index in the condition assessment vary according to users (the state or responsible agencies) and the objects of maintenance; basically, however, it is determined on the basis of information on the deteriorated condition of the lowest component of a facility (type, size, severity) (Andersen and Torrey, 1995; Miyamoto et al., 2000; Gattulli and Chiaramonte, 2005). Particularly, in the case of calculating the condition index by computational approach, "weighted average approaches, hereinafter WAA", in which members of universally high importance are weighted to determine the condition index of the entire facility, and "worst-conditioned component approaches, hereinafter WCA" in which the deteriorated condition of an assessment object is estimated by using the condition information of its worst-damaged member (FHWA, 2016).

Furthermore, this study conducted the condition assessment of check dams by applying mutatis mutandis the Korea Infrastructure Safety and Technology Corporation's "Standards and Methods for Assessing the Condition of Dam Facilities". The condition assessment of dam facilities determines the condition index for an object of maintenance by conducting stepwise evaluation with WAA and WCA on the basis of information on the condition of various dam members such as the upstream face, the downstream face, floodgates, and electric facilities (Korea Infrastructure Safety and Technology Corporation [KISTEC], 2019a). In the condition assessment of check dams, the deterioration condition of components classified according to functional characteristics was evaluated by the standards and methods of KISTEC, and the results thereof were synthesized to determine the condition index of an object of research. Here, the assessment system and detailed review items (deterioration and damage evaluation items) were applied to the object of research after being adjusted so that the characteristics of check dam may be reflected in the results of assessment.

In South Korea, the safety inspection of existing check dams can be defined by three types of enforcement: routine inspection (every year), emergency, and in-depth inspection. Based on the information of structural conditions from these activities, a maintenance manager determines whether it is necessary to adopt repair or a more detailed examination for the inspected check dam (i.e., precise safety diagnosis). The precise safety diagnosis of existing check dams is prescribed to be performed by an agency specializing in safety examinations of facilities (Korea Forest Service, 2018). However, in maintenance practice, since there are no independent methods for diagnosing the damage and deterioration of check dams, engineers commonly use safety inspection guidelines for the embankment dam developed for flood control, water storage, and hydropower (Korean Ministry of Land, Infrastructure, and Transport [MOLIT], 2020). This limitation is also the case in the condition assessment of check dams, which is the basis of safety diagnosis. We used the condition assessment procedure to evaluate the structural statuses of check dams within a specific mountainous region. In addition, we classified the described the damage and deterioration characteristics of check dams to indicate their physical condition.

# MATERIALS AND METHODS

## Study Area

The field study was performed in the Gyeongsangbuk-do region, which features the largest number of non-permeable check dams in South Korea (**Figure 1A**). The studied check dams were located in small/medium streams flowing through a mountainous area with an elevation of 25.2–575.6 m above sea level (**Figure 1B**). The catchment area upstream of the check dam varied from 3.9 to 2,464.1 ha. In the study area, the streambed width varied from 3.5 to 22.0 m, and the slope gradient varied from 4.8 to 24.9%. The annual average temperatures of the study sites varied from 10.8 to 14.4°C, and the average temperature during winter (December to February) was 1.3°C (**Figure 1C**). The average annual rainfall of the study sites ranged from 1,017.7 to 1,445.2 mm (**Figure 1D**), and approximately 70% of the accumulated rainfall was concentrated in the summer rainy season (June to September) [as calculated by collecting observation data for the years 1997–2016 from the Korea Meteorological Administration (automated) weather observation stations located closest to the study sites]. The check dams at the study site were built in mountainous areas featuring highly variable weather conditions and high amounts of rainfall. During the period of the check dam construction from 1986 to 2014, the streams at the construction sites underwent freezing and thawing in the winter, respectively. Check dams found in mountain environmental conditions are more vulnerable to damages and deterioration than hydraulic structures on low-altitude rivers (Adamo et al., 2020).

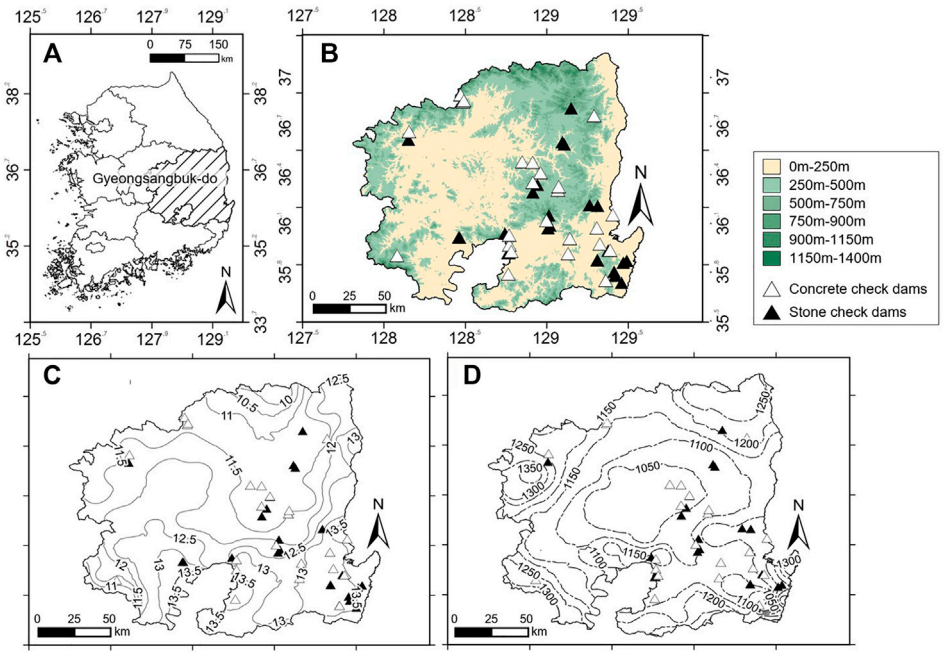


**FIGURE 1 | (A)** Map of the study area and check dam locations. The figure shows the study sites' **(B)** elevation above sea level (m), **(C)** average annual temperature (°C), and **(D)** average annual rainfall distribution (mm).


**FIGURE 2 |** Front views of **(A)** concrete, **(B)** stone check dams, and **(C)** The debris and driftwood laden check dam. The check dams in figures (2a) and (2c) effectively captured the rivers' debris and driftwood.

## Characteristics of Inspected Check Dams

The examination targets included 30 concrete check dams built between 1986 and 2013, as well as 23 stone check dams built between 1988 and 2014 (see **Supplementary Material A1**). The average service times were found to be 18.8 and 16.9 years for the concrete and stone check dams, respectively, as calculated in 2016, when the field study was completed (Lee 2017). The concrete check dams' lengths range from 10.1 to 33.3 m, and their heights range from 2.2 to 7.5 m, while the stone check dams' lengths range from as 12.0–31.7 m, and their heights range from

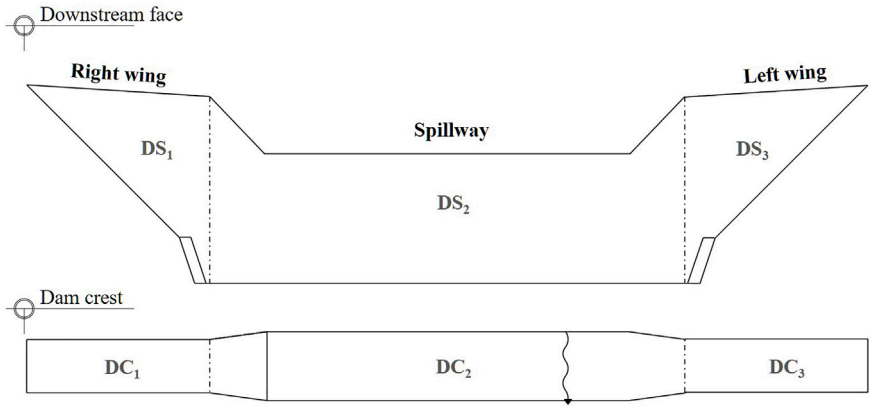


**FIGURE 3 |** Subdivision of the check dam to inspect damages and deterioration. The two major zones include the dam crest (*DC*) and downstream face (*DS*). The six specific elements are classified between those located on the spillway and those on the wings. The spillway consists of $DC_2$ and $DS_2$. The right wing consists of $DC_1$ and $DS_1$, and the left wing consists of $DC_3$ and $DS_3$. Inspections of the upstream faces were omitted because of the retention deposits and water.

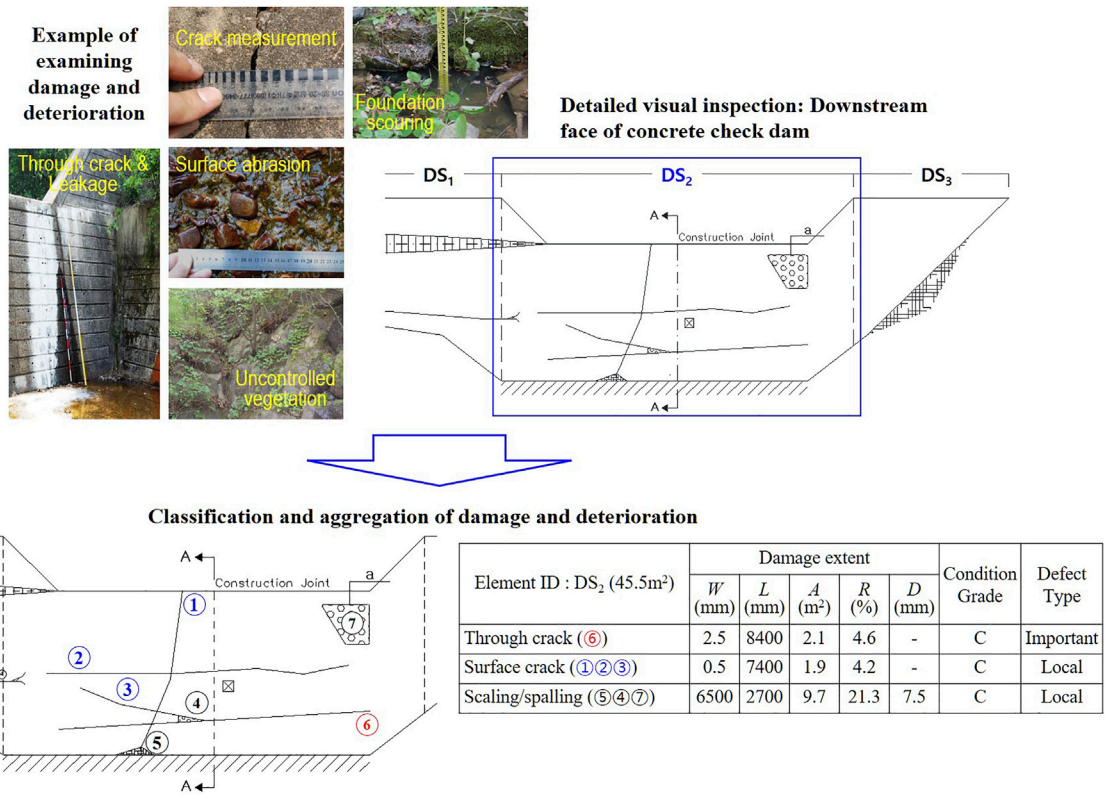


| Element ID : $DS_2$ (45.5m²) | Damage extent | | | | | Condition Grade | Defect Type |
|---|---|---|---|---|---|---|---|
| | *W* (mm) | *L* (mm) | *A* (m²) | *R* (%) | *D* (mm) | | |
| Through crack (⑥) | 2.5 | 8400 | 2.1 | 4.6 | - | C | Important |
| Surface crack (①②③) | 0.5 | 7400 | 1.9 | 4.2 | - | C | Local |
| Scaling/spalling (⑤④⑦) | 6500 | 2700 | 9.7 | 21.3 | 7.5 | C | Local |

**FIGURE 4 |** An example of a detailed visual inspection of a concrete check dam, including examples of measuring damage and deterioration and diagrammed visual inspection results. The inspection results are aggregated to representative damage types: *W*, width (mm); *L*, length (mm); *A*, damaged area (m²); *R*, damaged area ratio (%); *D*, depth (mm).

3.1 to 6.4 m. These values were determined by measuring the lengths and heights of the structures protruding from the ground surface. All examination targets were designed as gravity structures that maintain stability using their own weight; however, stone check dams feature composite bodies composed of stone and concrete, making them structurally distinct from concrete check dams, which consist of a single concrete element (**Figure 2A** and **Figure 2B**).

## Detailed Visual Inspection

To inspect the damage and deterioration of the check dams, we first divided the check dam structure into three components: dam crest (*DC*), downstream face (*DS*), and upstream face (**Figure 3**). Inspections of the upstream faces were omitted because of the retention deposits and water (**Figure 2C**). We then divided each component into spillway and wing elements ($DC_1$, $DC_2$, $DC_3$, $DS_1$, $DS_2$, and $DS_3$) based on the functional features. Finally, visual inspections were performed on the six individual elements.

For each element, we recorded the location, sizes, and shapes of damage using a crack ruler (measurement range: 0.05–7.0 mm), crack scope (× 10magnification), measurement poles (2.0 and 5.0 m), tape measures (20.0 and 50.0 m), a ladder (5.07 m), and a digital camera, as appropriate (**Figure 4**). For instance, cracks were classified into surface-level cracks, featuring a depth limited to the surface layer of the structure, and through cracks that extended from the upstream face to the downstream face. We measured the width, length, and direction of damaged areas in the visual inspection of both types of cracks. Abrasion/erosion is generally manifested as erosion of the concrete surface; this exposes the aggregate or deeply dents the damaged surface (Portland Cement Association, 2002; Adamo et al., 2020). An inspection of abrasion/erosion was examined the depth of the damaged structure surfaces. The uncontrolled vegetation was one of the most frequently observed damage types in stone check dams. This could be because the surfaces of stone check dams, which feature many weak joints and irregularities, provide favourable conditions for seeds to infiltrate and take root. Where stream vegetation covered the dam's, the types of invasive species (grasses, shrubs, and trees) and the areas of coverage were recorded.

The field examination results were analyzed using AutoCAD 2010 and the diagrammed visual inspection results and aggregated results on damage and deterioration in a specific element ($DS_2$) are presented in **Figure 4**. Then, the damage in individual elements of each specific element was classified by type, and its attributes (e.g., width, depth, length, and area) were combined and used as assessment elements for the damage and deterioration analysis in the next section. Each check dam was visually inspected only ones, and the field inspection period lasted from March to May 2016.

## Condition Assessment

In general, a system for assessing the structural condition of embankment dams carries out (1) a detailed inspection of a structure for its deterioration damage, thereby analyzing the condition of **(2)** individual elements, which are the lowest components; and by using results of the analysis, it evaluates successively the condition of **(3)** composite members (upstream face n, downstream face n, approach channel n, etc., n = 1,. . ., i), which are upper components, (4) individual facilities (non-overflow part j, overflow part j, machinery and electric facilities, etc., j = 1,. . . ., k), (5) composite facilities (dam body, spillway, and other facilities), and (6) integrated facilities (dam facilities) (Korea Infrastructure Safety and Technology Corporation [KISTEC], 2019a). In terms of structure, check dams of mountain streams show the characteristics of small facilities, compared with river dam facilities consisting of various structures and ancillary facilities like above (Lee et al., 2021). In particular, because this study conducted the condition assessment of check dam body, with omitting the assessment of ancillary facilities such as side wall and apron, it was needed to adjust the assessment procedure. Thus, in this study, the above condition assessment system for embankment dam was applied to objects of research after being adjusted into four steps of **(1)** the condition assessment of damages and deterioration, (2) the condition assessment of individual elements ($DC_{1\sim3}$ and

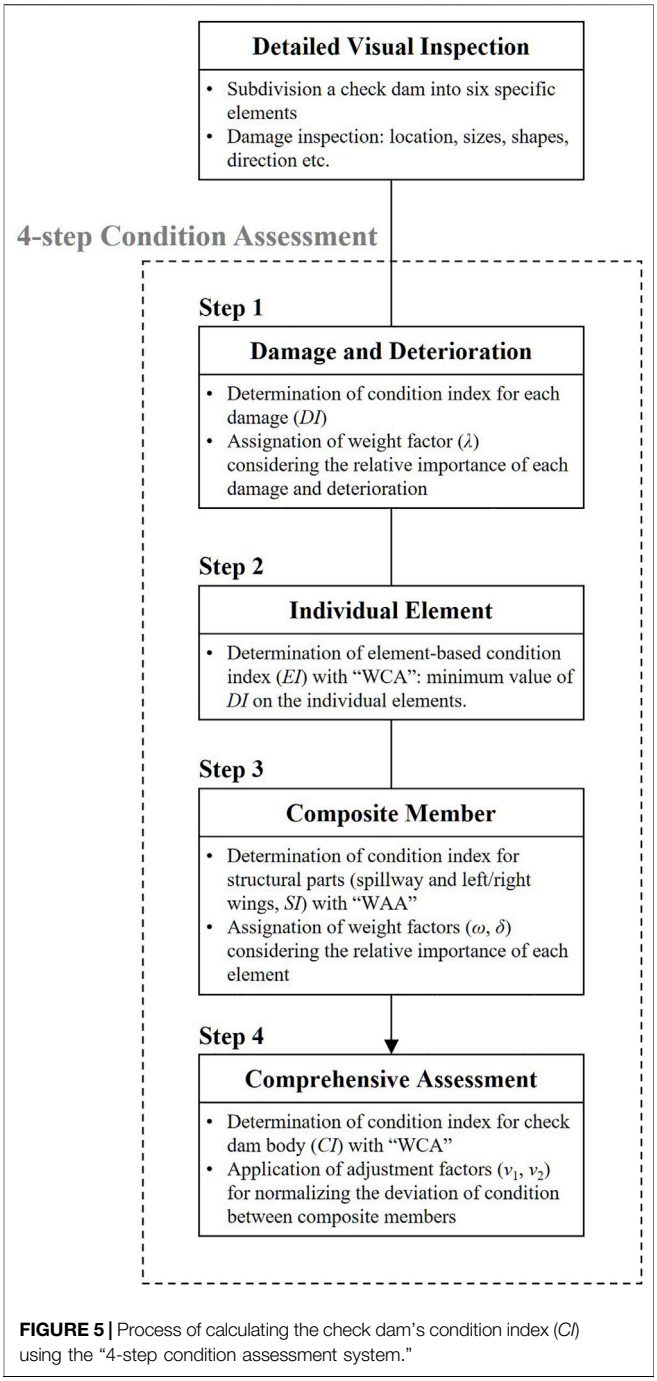


**FIGURE 5 |** Process of calculating the check dam's condition index (*CI*) using the "4-step condition assessment system."

**TABLE 1 |** Overview of damage and deterioration inspection and assessment criteria.

| Inspection items and content | | Condition Grade | Assessment criteria[a] | Applied target[b] |
|---|---|---|---|---|
| Cracking | Direction, Length, Width, Location, Through Cracking | A | Crack width less than 0.1 mm | *C* |
| | | B | Area ratio under 20.0%, crack width less than 0.5 mm | |
| | | C | | |
| | | D | Area ratio above 5.0%, crack width 0.5 mm or more Area ratio above | |
| | | E | 20.0%, crack width 0.3 mm or more | |
| Scaling/Spalling | Depth, area | A | Minor condition | *C* |
| | | B | Area ratio under 10.0%, scaling depth less than 1.0 mm, spalling less | |
| | | C | than 20.0 mm Area ratio above 10.0%, scaling depth less than 0.5 mm, spalling less than 15.0 mm | |
| | | D | Area ratio under 10.0%, scaling depth 1.0 mm or more, spalling | |
| | | E | 20.0 mm or more Area ratio above 10.0%, scaling depth 0.5 mm or more, spalling 15.0 mm or more | |
| Abrasion/Erosion | Location, Depth | A | Minor condition | *C, S* |
| | | B | Aggregate exposed, spillway cross section reduced by abrasion/ | |
| | | C | erosion | |
| | | D | Abrasion/erosion depth of ~1.0 m in vertical direction | |
| | | E | | |
| Foundation Erosion | Depth, Length | A | Minor condition | *C, S* |
| | | B | Vertical depth of erosion less than 1/2 point of foundation | |
| | | C | | |
| | | D | Vertical depth of erosion at 1/2 point of foundation or more | |
| | | E | | |
| Joint Deterioration | Cracking, Width, Length, Leakage | A | Minor condition | *C* |
| | | B | Crack width less than 2.0 mm, minor leakage | |
| | | C | | |
| | | D | Crack width 2.0 mm or more, conspicuous leakage | |
| | | E | | |
| Leakage | Location, Degree of Leakage, Area | A | Minor condition | *C, S* |
| | | B | Minor leakage partially progressing on the dam body surface | |
| | | C | | |
| | | D | Conspicuous, widely progressing leakage on dam body surface, | |
| | | E | foundation, and embedded component | |
| Efflorescence | Area | A | Minor condition | *C* |
| | | B | Area ratio less than 10.0% | |
| | | C | | |
| | | D | Area ratio of 10.0% or more | |
| | | E | | |
| Breakage | Depth, Area | A | Minor condition | *C, S* |
| | | B | Area ratio less than 10.0%, breakage depth less than 50.0 mm | |
| | | C | Area ratio of 10.0% or more, breakage depth of less than 50.0 mm | |
| | | D | Area ratio of less than 10.0%, breakage depth of 50.0 mm or more | |
| | | E | Area ratio of 10.0% or more, breakage depth of less than 50.0 mm | |
| Uncontrolled Vegetation | Type of Vegetation, Area | A | Minor condition | *C, S* |
| | | B | Grasses (perennial) or shrubs taking root on part of dam body surface | |
| | | C | | |
| | | D | Shrubs taking root on entire dam body, trees invading part of dam | |
| | | E | body | |
| Displacement | Displacement (Subsidence, Stepping, Swelling) | A | Minor condition | *C, S* |
| | | B | Vertical/horizontal displacement of less than 50.0 mm | |
| | | C | | |
| | | D | Vertical/horizontal displacement of 50.0 mm or more | |
| | | E | | |
| Falling Out | Quantity, Displacement | A | Minor condition | *S* |
| | | B | Less than three instances of occurrence, no displacement in | |
| | | C | damaged area | |
| | | D | Three instances of occurrence or more, displacement in damaged | |
| | | E | area | |
| Cavity | Quantity, Displacement, Leakage | A | Minor condition | *S* |
| | | B | Less than three instances, no displacement or leakage in damaged | |
| | | C | area | |
| | | D | Three or more instances, displacement or leakage in damaged area | |
| | | E | | |

(Continued on following page)

**TABLE 1 |** (*Continued*) Overview of damage and deterioration inspection and assessment criteria.

| Inspection items and content | | Condition Grade | Assessment criteria[a] | Applied target[b] |
|---|---|---|---|---|
| Joint Mortar Deterioration | Area | A | Minor condition | S |
| | | B | Damaged area ratio under 20.0% | |
| | | C | Damaged area ratio in the range of 20.0–50.0% | |
| | | D | Damaged area ratio above 50.0% | |
| | | E | Damaged area ratio above 50.0% with cavitation | |

[a]*Refer to the "Standards and Methods for Assessing the Condition of Dam Facilities" by Korea Infrastructure Safety and Technology Corporation [KISTEC]. (2019a) for cracking, scaling/spalling, joint deterioration, and efflorescence. Refer to "Standards and Methods for Assessing the Condition of Retaining Wall" by Korea Infrastructure Safety and Technology Corporation [KISTEC]. (2019b), "Inspection Procedure Manual for Sabo Facilities" by MLIT (2014b), and "Guidelines on the Maintenance of Erosion Control Facilities." by Korea Forest Service, 2018 for abrasion/erosion, foundation Erosion, leakage, breakage, uncontrolled vegetation, falling out, and cavity.*
[b]*C and S refer to concrete and stone check dams, respectively.*

**TABLE 2 |** Description of condition grades for damages and deterioration.

| Condition grade | Description |
|---|---|
| Good (A) | Only minor damages and deterioration are evident |
| Pair (B) | Some damages and deterioration are evident, but it is not significantly affected |
| Marginal (C) | Moderate deterioration |
| Poor (D) | Serious defects in at least some portions of the structure |
| Very poor (E) | Critical defects |

$DS_{1\sim3}$), (3) the condition assessment of composite members (spillway and left/right wings), and (4) comprehensive assessment (dam body) (**Figure 5**).

On the other hand, in the detailed visual inspection, various damages and deterioration observed in objects of research was classified in terms of morphological characteristics, and then the representative damage types of concrete and stone check dams were selected. As a result, the deterioration of concrete check dam was classified into ten damage types including surface crack, through crack, joint deterioration, and abrasion/erosion. And representative damage types of stone check dam were classified into nine types including uncontrolled vegetation, joint mortar deterioration, and falling out (see 4.1 and 4.2). The representative deterioration types of concrete and stone check dams were used as items for assessing deterioration damage, which serves as basic data for condition assessment. Further, among the representative deterioration types of concrete and stone check dams, structural defects such as foundation erosion, vertical/horizontal displacement, and breakage, which have direct effects on the stability conditions of gravity-type check dam (overturning, sliding, failure, bearing capacity), were re-classified as "critical defects"; and differential assessment weights were applied to the "critical defects" so that decrease in the stability of research objects caused by the occurrence of "critical defects" might be reflected in the assessment results (see 5.1).

## Damage and Deterioration Assessment

The assessment of damage and deterioration was carried out by applying (Korea Infrastructure Safety and Technology Corporation [KISTEC]. (2019a); Korea Infrastructure Safety and Technology Corporation [KISTEC]. (2019b)Standards and Methods for Assessing the Condition of Facilities (Dam & Retaining Wall)", Japanese Ministry of Land, Infrastructure, Transportation, and Tourism, 2014b) "Inspection Procedure Manual for Sabo Facilities", and "Assessment Criteria by Condition Assessment Item" based on Korea Forest Service (2018) "Guidelines on the Maintenance of Erosion Control Facilities" (**Table 1**). The condition assessment items comprised the representative damage types of concrete and stone check dams, and results of assessment were expressed as condition grades (A-E) based on assessment criteria that reflected the type, size, and location of damage (**Table 2**). The condition index was calculated by converting a condition grade into a simple score (1.0–5.0), which was then multiplied by the weight of relevant deterioration, as follows:

$$DI_i = s_i \times \lambda_i. \quad (1)$$

where $DI_i$, $S_i$, and $\lambda_i$ are the condition index, a score based on a condition grade, and a weight based on relative importance for each $i$th damage, respectively. $\lambda$ was classified into three types, i.e., "critical defect", "local defect", and "ordinary damage" (**Table 3**). In particular, the weights of "local defect" and "ordinary damage", which have relatively small effects on structure compared with "critical defect", were adjusted upward so that their effects on the entire structure might be devaluated (Korea Infrastructure Safety and Technology Corporation [KISTEC]. 2019a). For example, in **Figure 4**, the *DI* value for the surface and through cracks was calculated by assigning the $\lambda$ values corresponding to "local defect" and "important defect", respectively. Therefore, the *DI* value for C-grade through crack ($s$ = 3.0) is 3.0 because the weight for "critical defect ($\lambda$ = 1.0)" is applied to it.

## Individual Element and Structural Component

The condition index of an individual member was calculated with the results of evaluating the damage and deterioration of the lowest condition index among its i damages, as follows:

$$EI_j = \min(DI_i). \quad (2)$$

where $EI_j$ is the condition index of $j$th individual element determined by the minimum value of $D_i$.

For the assessment of composite members, the check dam was divided into spillway part ($DC_2$ and $DS_2$), which controls the

**TABLE 3 |** Use of the damage score (*s*) and the importance factor (*λ*), according to the KISC-based (2019a) damage assessment system.

| Importance | Inspected content | Condition grade | Condition score (*s*) | Importance factor (*λ*) | Maintenance measures[a] |
|---|---|---|---|---|---|
| Critical Defect | Defects that directly affect the entire facility's structural stability: clear displacement of the dam body, through cracking, severe structural breakage, erosion and leakage in the foundation and embedded components | A | 5 | 1.0 | Requires immediate repair and reinforcement |
| | | B | 4 | 1.0 | |
| | | C | 3 | 1.0 | |
| | | D | 2 | 1.0 | |
| | | E | 1 | 1.0 | |
| Local Defect | Defects that are not currently a severe problem but may affect the structural safety of the facility if the damage develops: concrete cracking, scaling/spalling, abrasion/erosion, stone cavities and falling out, leakage, infiltration and growth of trees | A | 5 | 1.0 | Requires continued observation and consideration of repair or reinforcement for damaged area |
| | | B | 4 | 1.1 | |
| | | C | 3 | 1.2 | |
| | | D | 2 | 1.4 | |
| | | E | 1 | 2.0 | |
| Ordinary Damage | Normal damage that does not greatly affect the safety of the facility: concrete material segregation and aggregate exposure, annual grasses infiltrating and taking root, joint deterioration, efflorescence phenomena | A | 5 | 1.0 | Requires continued observation, repair if needed |
| | | B | 4 | 1.1 | |
| | | C | 3 | 1.3 | |
| | | D | 2 | 1.7 | |
| | | E | 1 | 3.0 | |

[a]*Applied to Grades C, D, and E grade defects as a result of the assessment.*

**TABLE 4 |** Use of the adjustment factor (*ω*), according to the KISC-based (2019a) element condition index (*EI*).

| Condition grade | A | B | C | D | E |
|---|---|---|---|---|---|
| *EI* | 4.5–5.0 | 3.5–4.5 | 2.5–3.5 | 1.5–2.5 | 1.0–1.5 |
| *ω* | 1.0 | 2.0 | 3.0 | 6.0 | 6.0 |

thalweg and regulated peak flood (or debris flow), and dam wing part ($DC_1$, $DC_3$, $DS_1$, and $DS_3$), which prevents damage to the body caused by overflow (Hueble and Fiebiger, 2005). The condition index of composite member was calculated with condition indices of individual members comprising each structural part, as follows:

$$SI_k = \frac{\sum_{j=1}^{n} EI_j \times \omega_j \times \delta_j}{\sum_{j=1}^{n} \omega_j \times \delta_j}. \quad (3)$$

where $SI_k$ is the condition index of *k*th composite member (the spillway part and wing parts), and $\omega_j$ and $\delta_j$ are the weight factors determined by considering the condition index of *j*th individual element and its importance-based weight, respectively (**Table 4**). *ω* was defined by referencing the "adjustment factor based on Korea Infrastructure Safety and Technology Corporation [KISTEC]. (2019a) condition index of individual element." *δ* is a weight reflecting the size of an individual element, and may be applied differentially to the extent that the sum does not exceed 1.0, according to an engineer's judgment (Korea Infrastructure Safety and Technology Corporation [KISTEC]. 2019a). In this study, the *δ* values of 0.4 and 0.6 were applied to the spillway and the wing parts, respectively, by referring to the results of condition assessment in Lee, (2017), Lee et al. (2018), and Lee et al. (2021).

### Comprehensive Assessment

As for the condition index (*CI*) of check dam in the comprehensive assessment, the condition index of a structural part whose deterioration was worst among composite members was calculated in priority, as follows:

$$CI = \min(SI_k) + (\nu_1 \times \nu_2). \quad (4)$$

where $\nu_1$ and $\nu_2$ are adjustment factors for the normalization of assessment results, and were calculated as follows:

$$\nu_1 = 0.3 \times \{\max(SI_k) - \min(SI_k)\} \quad (5)$$

$$\nu_2 = \frac{\sum_{k=1}^{n} SI_k \times A_k}{5.0 \times \sum_{k=1}^{n} A_k} \quad (6)$$

Where $\nu_1$ is a factor to adjust the deviation of condition between composite members, and a value equivalent to 30.0% of the $SI_k$ range (if $\nu_1 \neq 0.0$) was applied to it; and $\nu_2$ is the rate of condition deterioration for an assessment object compared with its best condition ($SI_k = 5.0$), and was determined by reflecting the size of composite member ($A_k$) in the condition index (Korea Infrastructure Safety and Technology Corporation [KISTEC]. 2019a).

Finally, the condition of the check dam was expressed as a condition index within the range of 1.0–5.0, and consequent conditions were classified into five grades of Excellent (A), Good (B), Average (C), Poor (D), and Very Poor (E) (**Table 5**).

## RESULTS

### Calssification of Dmagage and Deterioration Characteristics of Concrete Check Dams

A total of 235 instances of deterioration (dam crest: 79 instances; downstream face: 156 instances) were observed on the 30 reviewed concrete check dams (**Figure 6** and **Figure 7**). These were classified into ten representative types (according to their morphological features): through crack (*TC*), surface crack (*SC*), joint deterioration (*JD*), abrasion/erosion (*AE*), leakage (*L*),

**TABLE 5 |** Use of the check-dam condition grade and the maintenance measures, which are based on KISC's (2019a) condition index (*CI*).

| *CI* | Condition grade | Description | Recommended actions |
|---|---|---|---|
| 4.5–5.0 | Excellent (A) | Optimal condition with no problems | - |
| 3.5–4.5 | Good (B) | Minor damage and deterioration have occurred but no safety problems | Continued observation |
| 2.5–3.5 | Average € | Widespread damage and deterioration have occurred but no safety problems | Continued observation, repair or reinforcement of damaged areas if necessary |
| 1.5–2.5 | Poor (D) | Service limitation must be considered owing to significant damage and deterioration | Immediate repair and reinforcement of damaged areas, consideration of service limitation |
| 1.0–1.5 | Very Poor€) | Service must be ended immediately owing to severe damage and deterioration | Consideration of suspending service and rebuilding |

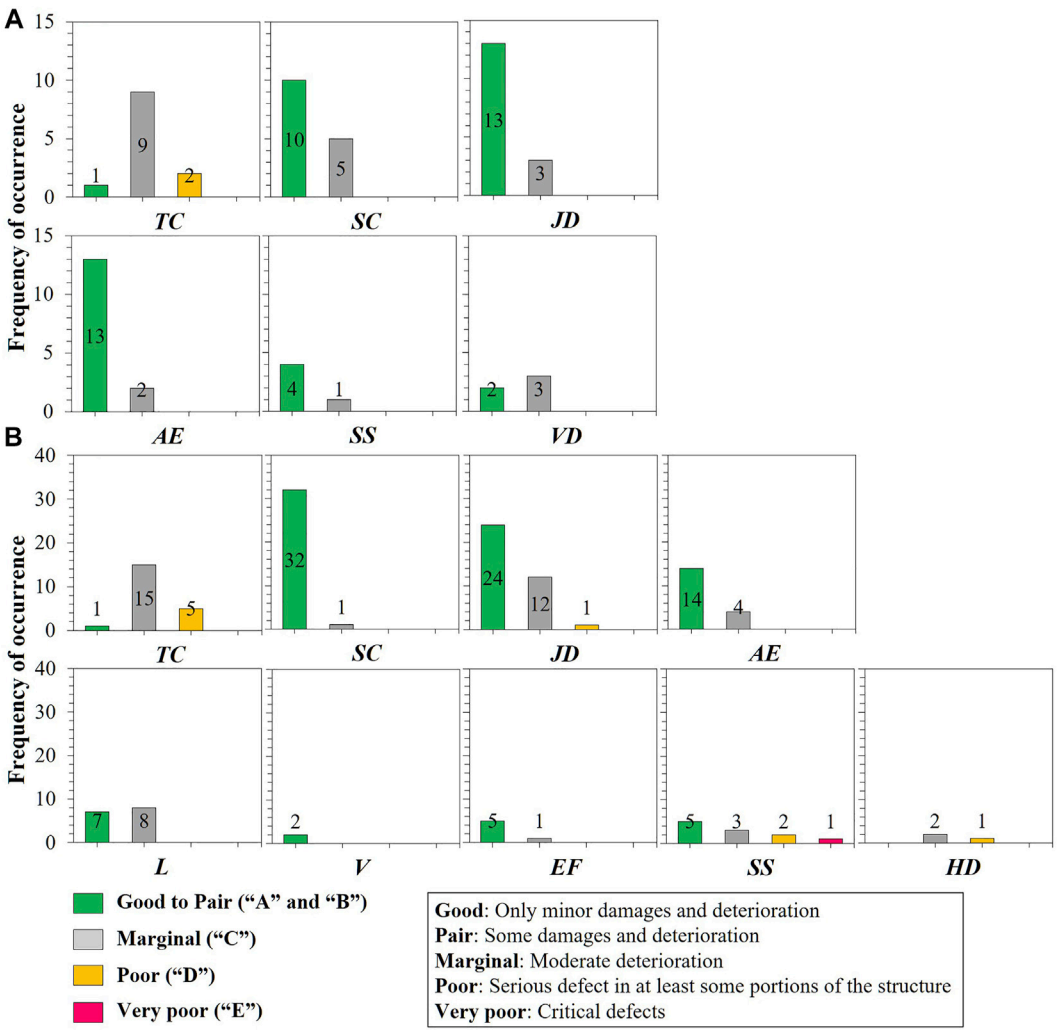


**FIGURE 6 |** Typical damage and deterioration of the **(A)** dam crest and **(B)** downstream face of a concrete check dam: *TC*, through crack; *SC*, surface crack; *JD*, joint deterioration; *AE*, abrasion and erosion; *L*, leakage; *V*, uncontrolled vegetation; *EF*, efflorescence; *SS*, scaling and spalling; *VD*, vertical displacement; *HD*, horizontal displacement.

uncontrolled vegetation (*V*), efflorescence (*EF*), scaling/spalling (*SS*), horizontal displacement (*HD*), and vertical displacement (*VD*).

In the case of *TC* cracks with a width of 0.4–15.0 mm and an area ratio of 0.7–15.0%, which were found on 16 check dams, 31 of the 33 found instances (dam crest: 12 instances; downstream

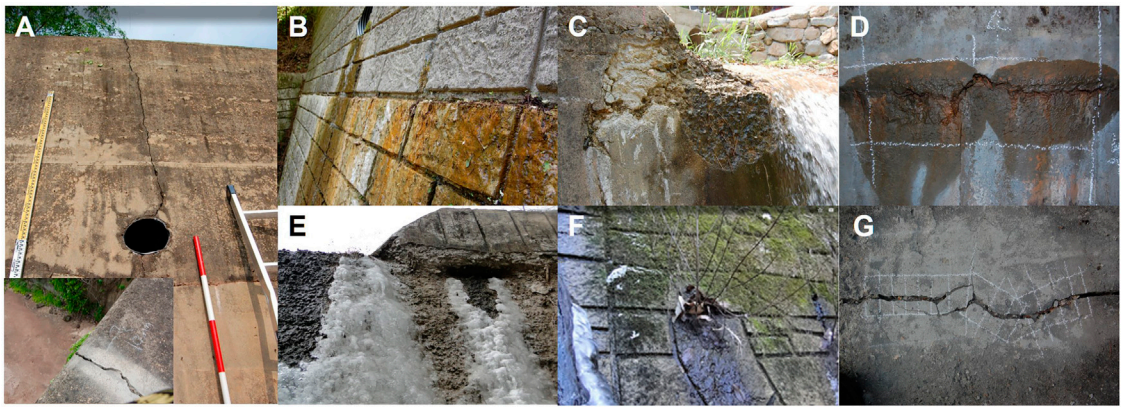


**FIGURE 7 |** Various deterioration types observed on concrete check dams. **(A)** vertical through crack and displacement caused by drying shrinkage cracking; **(B)** water leakage from a gap in a horizontal construction joint; **(C)** exposed aggregate and spalling, respectively, due to erosion at the spillway; **(D)** leakage and efflorescence at a horizontal construction joint; scaling and spalling of the downstream face due to freezing and thawing; **(E) (F)** uncontrolled vegetation around a drainage channel; **(G)** through crack and dam crest stepping.

face: 21 instances) were Grades C and D damages; that is, repair/reinforcement was considered and recommended (**Figure 7A**). In contrast, 48 instances of *SC* (dam crest: 15 instances; downstream face: 33 instances) with widths of 0.2–9.9 mm and area ratios of 0.1–23.7% were found on 23 check dams, but no more than six of these were Grade C defect. Cracking was the most frequent damage type on all the dam crests and downstream faces but not necessarily a problem that directly leads to severe defects in concrete check dams (Korea Concrete Institute, 2014).

*JD* refers to damage (e.g., cracks and leakages) that occurs at shrinkage and construction joints (**Figure 7B**) and was observed on 19 concrete check dams. Sixteen instances were found on dam crests, and three of these were Grade C damage (with a width of 3.5–7 mm), which occurred at the shrinkage joints and extended to the downstream face. Of the 37 instances of damage on the downstream face, 12 were determined to be of Grades C and one of D damage. In addition, in two of these instances, water continued to leak at the crack surface of the construction joint during the field inspection.

*AE* was found in 20 inspection targets, including 15 instances at the dam crest and 18 instances at the downstream face (**Figure 7C**). The depths of the damaged surfaces at the dam crests and downstream faces were below 10 mm. Foundation erosion scoured the riverbed directly below the spillway to depths of 0.04–0.7 m. Specifically, there is a tendency that *AE* is concentrated in the spillway (which is directly affected by water flow and debris flow) and its underground foundation (Mizuyama, 1979; Comiti et al., 2010; Piton and Recking, 2014; Ogasawara and Kambara, 2015).

*L*, *V*, *EF*, and *HD* are deterioration phenomena that specifically occur on the downstream face. Fifteen instances of *L* were found on ten concrete check dams, and six of these were accompanied by *EF* (**Figure 7D**). Of the eight leakages of Grade C, two instances occurred at the cracks, and two and four instances were found at the construction joints and foundations, respectively. The freezing and thawing of leaking areas in winter and summer, respectively, leads to secondary damages, including cracks and scaling/spalling. In the case of concrete check dams (which are unreinforced concrete structures), the damage was concentrated around the leakage areas that were damaged by frost, as well as in the drainage channel (**Figure 7E**). Of the 16 instances of *SS* found in eight inspection targets, two instances were determined to be of Grade D and one of Grade E. These were observed throughout the entire inspection area at depths of 7.2–11.2 cm. Single instances of *V* were identified in the gap between the shrinkage and drainage channels (**Figure 7F**). *HD* was observed along with *VD* of the dam crest in three inspection targets. Of the three instances of *HD*, two instances were Grade C and one of Grade D. This is believed to be caused by structural deformation produced by growth of the drying shrinkage cracks; as a result, steps with depths of 3.0–7.0 mm were created on the dam crest surface (**Figure 7A** and **Figure 7G**).

## Classification of Damage and Deterioration Characteristics of Stone Check Dams

In the case of stone check dams, 87 instances (dam crest: 29 instances; downstream face: 58 instances) of damage were found in 17 inspection targets (**Figure 8** and **Figure 9**). The damage was classified into nine representative types: *V*, mortar joint deterioration (*MJD*), falling out (*F*), erosion (*ER*), internal erosion and cavities (*IC*), *L*, *HD*, *VD*, and breakage (*B*).

The patterns of *V* were classified into instances where grasses infiltrated and took root by themselves, where grasses and shrubs were found mixed together, and where trees infiltrated and grew by themselves (**Figure 9A**). Twenty-seven instances (dam crest: 11 instances; downstream face: 16 instances) of *V* occurred in 13 stone check dams. Of these observed instances, one was that of a tree and the remainder were that of combined grasses and shrubs growing together.

Twenty-one instances of *MJD* (dam crest: 11 instances; downstream face: 10 instances) were found in 11 inspection targets, and they were classified as typical stone check dam deterioration (**Figure 9B**). The *MJD* damage area accounted for 3.6–67.7% of the inspection area, but the majority of it was

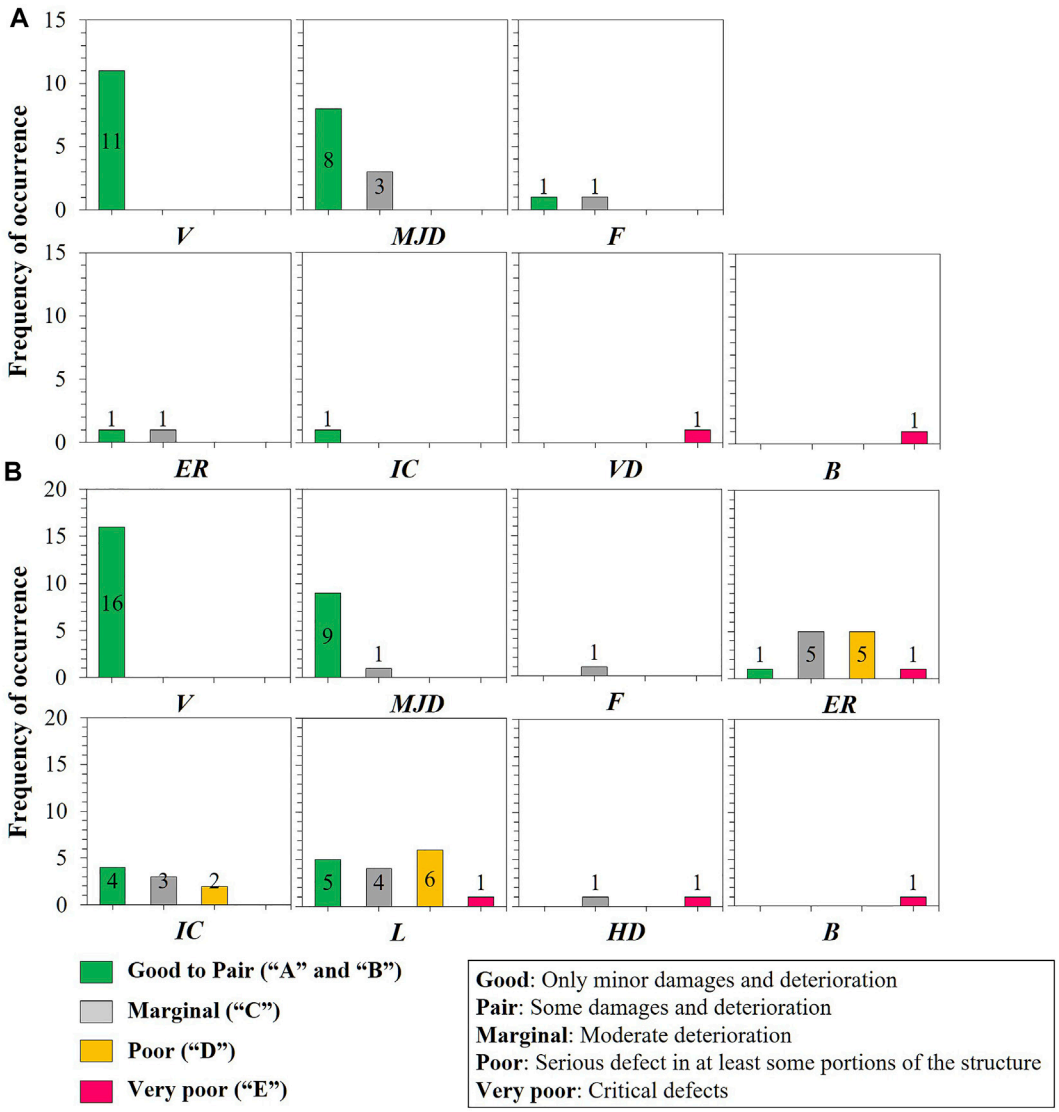


**FIGURE 8 |** Typical damage and deterioration on the **(A)** dam crest and **(B)** downstream face of stone check dams: *V*, uncontrolled vegetation; *MJD*, mortar joints deterioration; *F*, falling out; *ER*, erosion; *IC*: internal erosion and cavity; *L*, leakage; *VD*, vertical displacement; *HD*, horizontal displacement; *B*, Breakage.

Grade A or B defects. *MJD* is considered to be a condition change that requires further observation because it not only allows vegetation to infiltrate the damaged area but can also lead to various kinds of deterioration through the exposure of internal material to environmental conditions.

Three instances of *F* were observed on two stone check dams. Two instances were attributed to impacts from debris flows at the spillway of the dam crest (**Figure 9C**), which produced cavities with depths of approximately 0.45 m in the damaged area. One instance displayed continuous concrete leakage in a cracked area, attributable to earth pressure, where vertical subsidence proceeded in the damaged area and developed into a Grade E horizontal displacement defect.

The stone check dam inspection results showed a progression of *ER*, *IC*, and *L*. *ER* is the greatest repair priority among the stone check dam damage types. *ER* was identified in 11 stone check dams, with two instances occurring at the dam crest and 12 instances occurring at the downstream face (**Figures 9D,E**). In the *ER* instances identified in the downstream face, the foundation was scoured to a depth of 0.15–0.65 m in 11 instances of Grades C, D, and E defects. *IC* indicates an empty cavity that occurs when the flow in leaking areas continually carries away the internal material and discharges it downstream. *IC* is a significant defect that reduces the durability and stability of a check dam body, by increasing the dam's internal porosity (Kasahara et al., 2010) (**Figure 9F**). *IC* inspection was performed on ten stone check dams (dam crest: 1 instance; downstream face: 9 instances). In the three instances of C and the two instances of D damages, multiple (2–4) defects with depths of 0.19–0.45 m were observed in a single inspection target.

*L* denotes the continuous flow of water through gaps inside the check dam (**Figure 9G**). Stone check dams are composed of

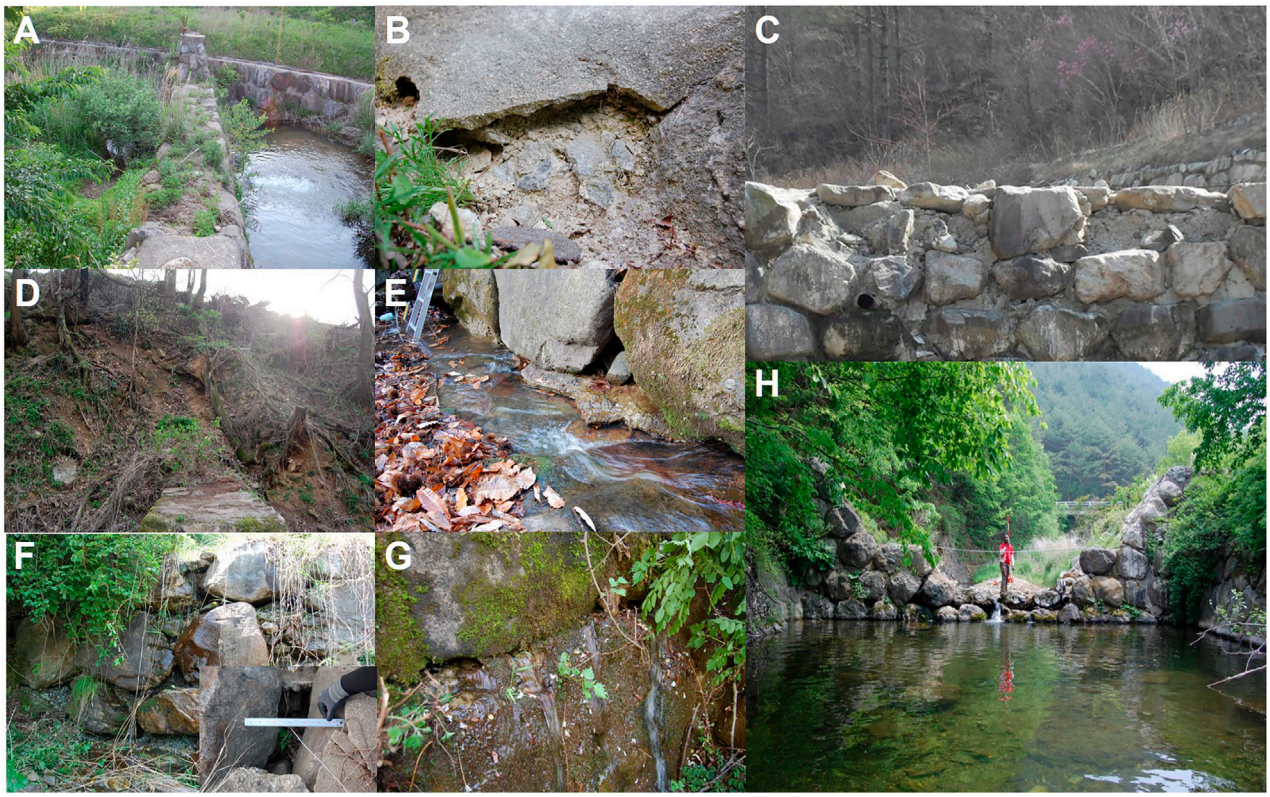


**FIGURE 9 |** Various deterioration types observed on stone check dams: **(A)** grasses and shrubs infiltrating the dam crest, (B) exposure of internal concrete due to joint spalling, **(C)** falling out caused by impact of bedload transport, **(D)** and **(E)** erosion of abutment slope and foundation; **(F)** vertical subsidence due to internal concrete outflow; **(G)** clear leakage and horizontal displacement of downstream face; **(H)** damage to the dam body due to the hydraulic force of flooding.

heterogeneous materials, and they are structurally less watertight than their concrete counterparts. Sixteen instances of *L* were found in the 12 stone check dams, and of these, 12 instances of leakages were observed together with foundation erosion, and a section of the damaged area had been washed downstream. In the seven instances of *L* that were Grade C or above, the filling concrete had flowed out and the internal porosity had increased, compromising the structural stability of the dam. Three instances of *VD* and *HD* were found in two inspection targets, and they were accompanied by *L* and *IC*, regardless of direction. One instance of *B* damage was confirmed, where the dam could not withstand the hydraulic force of flooding, and more than 70% of the structure had been washed away (**Figure 9H**).

## Concrete and Stone Check Dams Condition Assessment

The concrete check dam condition index values ($CI_{concrete}$) ranged from 1.5 to 4.9 (n = 30). The data mean ($\overline{CI}_{concrete}$) was 3.37, and its variance ($\sigma^2$) was 0.55. Seventeen inspection targets required repair/reinforcement ($CI$ < 3.5), and usage restrictions were considered for four of these targets ($CI$ < 2.5). The stone check dam condition Index values ($CI_{stone}$) varied as 1.3–5.0 (n = 23). $\overline{CI}_{stone}$ was 3.84, and $\sigma^2$ was 1.30, eight stone check dam targets required repair/reinforcement, while service limitations were considered for three of these targets (**Figure 10** and see **Supplementary Material A2** and **Supplementary Material A3**).

Since 2009, Korea Association of Soil and Water Conservation (KASWC) has been regularly conducting visual inspections on the existing check dams through an expert group composed of engineers with abundant practical experience. The maintenance judgments derived from the condition assessments were consistent with the KASWC visual inspection results in 43 cases (repair/reinforcement: 16 cases; follow-up observation: 27 cases). Even though an existing process was adopted, the assessment employed produced consistent results with inspections conducted by the expert group of the KASWC (Korea Association of Soil and Water Conservation, 2014; Korea Association of Soil and Water Conservation, 2015; Korea Association of Soil and Water Conservation, 2016). However, condition assessment results are somewhat more conservative in the field, where interpretation may vary according to the inspector. For example, the condition indices for stone check dams exhibited a wider distribution than those of concrete ones (Mazzorana et al., 2018). In practice, the construction of stone check dams depends heavily upon the engineers' skill level. As such, there are more variations in quality between specimens in stone check dams than concrete check dams (Lee et al., 2018), and the variations in *CI* for stone check dams are attributable to field factors.

The conditions of the inspection targets were found to be relatively poor for check dams of 20 years and older. The condition indices for

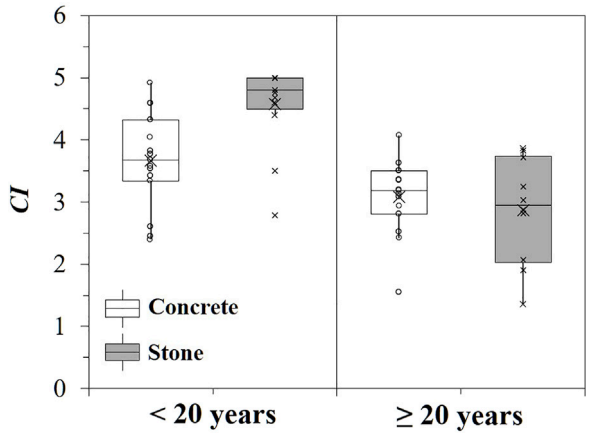


**FIGURE 10 |** Comparison of condition index (*CI*) for check dams less than 20 years and 20 + years after construction.

concrete check dams of 20 + years of age ($CI_{\geq 20,\ concrete}$) ranged from 1.5 to 4.1 ($\overline{CI}_{\geq 20,\ concrete}$ = 3.1), 1.2 times lower (on average) than the condition indices of concrete check dams less than 20 years old ($CI_{<20,\ concrete}$), which ranged from 2.4 to 4.9 ($\overline{CI}_{<20,\ concrete}$ = 3.7). In addition, repair/reinforcement ($CI < 3.5$) was required in 12 concrete check dams of 20 + years of age, 2.4 times more than in those of less than 20 years of age (five inspection targets). Similarly, the $CI_{\geq 20}$, stone ranged from 1.4 to 3.9 ($\overline{CI}_{\geq 20,\ stone}$ = 2.9), 1.6 times lower than the range of 2.8–5.0 found for $CI_{<20}$, stone ($\overline{CI}_{stone}$ = 4.6). Seven stone check dams of 20 + years of age required repair/reinforcement, which is 3.5 times higher than that observed in the check dams of less than 20 years (two inspection targets). These results are consistent with Lee (2015), who investigated the stability of 35 concrete check dams in northern South Korea by using a rebound hammer test. In their examinations, the number of concrete check dams that were insufficient to satisfy the designed strength was six of 14 instances in test objects more than 20 years, indicating that its degree of deterioration was higher than that of test objects less than 20 years (two of 21 instances). Similarly, Lee et al. (2021) reported that the maintenance demand of concrete check dams (i.e., $CI < 3.5$) significantly increased 15 years after construction, based on the results of condition assessment for 426 concrete check dams in South Korea's northern mountain region.

Similar findings have been made in the other mountain streams. Dell'Agnese et al. (2013) reported that the damage factors of check dams of 20 + years of age tended to be greater than those of more recently constructed ones, following an evaluation of the physical vulnerabilities of 362 check dams constructed on Mountain Rivers in northern Italy before and after large-scale events. Field inspections by Fujita et al. (2020) showed that the occurrence of abrasion/erosion in check dams increased 20–30 years after construction. Considering that previous studies were based on visual inspections, the deterioration characteristics of check dams could be apparent in the check dams of 20 + years of age, although its conditions varied depending on such factors as climate, geology, and construction materials.

## Condition Assessment of Spillway and Wings of Check Dams

The condition indices for the spillways of concrete check dams ($SI_{spillway}$) ranged from 1.5 to 4.9, and the condition indices for the wings ($SI_{wings}$) ranged from 2.3 to 5.0 (**Figure 11A**). The average condition index for the spillways ($\overline{SI}_{spillway}$) was 3.2, 1.3 times lower than that for the wings ($\overline{SI}_{wings}$), which was 4.2. For stone check dams, the condition indices of the spillways ranged from 1.0 to 5.0, and the condition indices for the wings ranged from 1.5 to 5.0 (**Figure 11B**). The value of $\overline{SI}_{spillway}$ was 3.7, 1.2 times lower than the value (4.7) of $\overline{SI}_{wings}$.

We compared the condition factors of the spillways and wings of check dams less than 20 years after construction and check dams of 20 + years of age. For concrete check dams of 20 + years of age, the values of $\overline{SI}_{spillway}$ and $\overline{SI}_{wings}$ were 2.9 and 3.9, respectively, approximately 1.2 times lower than the corresponding values calculated for inspection targets of less than 20 years of age ($\overline{SI}_{spillway}$ = 3.5; $\overline{SI}_{wings}$ = 4.5). In the case of stone check dams, the $\overline{SI}_{spillway}$ and $\overline{SI}_{wings}$ values for inspection targets of 20 + years of age were 2.5 and 4.3, respectively. Compared to the average condition indices calculated for stone check dams of less than 20 years of age, the value for the spillways ($\overline{SI}_{spillway}$ = 4.5) and wings ($\overline{SI}_{wings}$ = 5.0) were 1.8 and 1.2 times lower, respectively. Notably, the $\overline{SI}_{spillway}$ value for check dams of 20 + years of age was less than 3.0, the value at which repair/reinforcement was considered.

In concrete and stone check dams, the conditions of the spillways were poorer than those of the wings. Consistent with this result, Lee et al. (2018) and Mazzorana et al. (2018) reported spillway damage factors that were approximately 1.2–4.0 times higher than those of the wings. The spillways of the check dams tended to deteriorate faster than the wings. We conclude that the design standards for spillways must be strengthened with regard to preventative maintenance, through measures such as the implementation of high-strength concrete or reinforcement structures.

# DISCUSSION

## Critical Defect Classification of Concrete and Stone Check Dams

Stability conditions for a check dam in a mountain stream are greatly affected by factors of its surrounding environment (external factors) and damages and defects occurring in its structure (internal factors) (Suda et al., 2009). In most cases, serious defects or deformations of check dams occurs due to the complex and combined actions of internal and external factors. The stability conditions of gravity-type check dam are examined in terms of four items: overturning, sliding, dam body failure, and the bearing capacity of foundation ground (Suda et al., 2009). In this regard, streambed erosion at the downstream of a check dam is judged to be a critical factor that causes the body failure of a check dam by decreasing the capacity of dam body to resist fluid force (water pressure and earth pressure) or impulsive force (debris flow) (Mizuyama, 1979; Hueble and Fiebiger, 2005; Suda and Huebl, 2007; Rudolf-Miklau and Suda, 2011). It is caused by restricted upstream sediment supply or the hydraulic behavior of fluid falling from the channel part (Lenzi et al., 2003; Comiti et al., 2010; Recking, 2012;

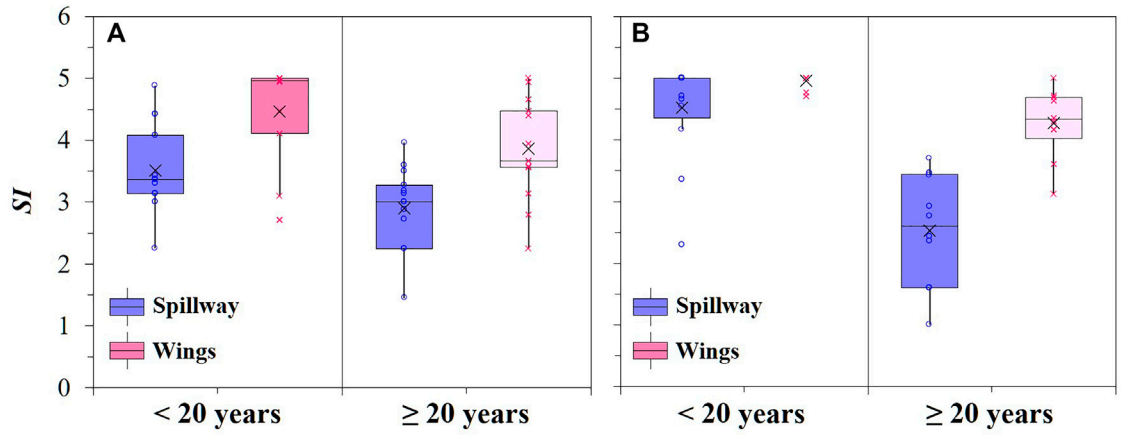


**FIGURE 11 |** Comparison of condition indices for the spillways ($SI_{spillway}$) and wings ($SI_{wings}$) of check dams of less than 20 years old and 20 + years old: **(A)** concrete check dam and **(B)** stone check dams.

Chahrour et al., 2021), and it appeared in this study as local scour around the foundation of a check dam and the exposure of foundation. In addition, leakage was one of important factors that hinder the durability and structural stability of the check dams. In particular, leakage occurring at the root part of a check dam (e.g., abutment and foundation) and its base is a critical defect that lowers the resistance force (frictional force) of the body to horizontal external force. In the case of a stone check dam, leakage increased the internal porosity and caused subsidence of the dam, which is a critical defect (Lee et al., 2018).

In the case of concrete check dams, through crack that occurs and grows in the dam body is an important factor in lowering the load-carrying capacity of the structure and is the cause of leakage. Although through crack in concrete check dams mostly occurs due to internal factors such as drying shrinkage and joint deterioration, it may also be triggered by the action of silt pressure that exceeds the carrying capacity. Therefore, through crack is one of the critical defects that should be examined carefully in the condition assessment of concrete check dam.

In this study, "foundation erosion", "vertical/horizontal displacement", "leakage from foundation and root part", and "serious breakage" were classified as the "critical defects" of concrete and stone check dams, and were classified as damage types that should be repaired urgently to secure the stability of structure. These "critical defects" as damage types were distinguished in the assessment from other deterioration damage types, such as surface crack, wear, scaling/spalling and falling out that have effects on the durability and functions of check dams. In addition, defects that are probable to develop into critical defects, such as leakage, crack, and cavity, were classified as "local defects," and the rest were classified as "ordinary damage" in the quantification of the degree of damage and deterioration types.

## Comparison of Deterioration Characteristics in Concrete and Stone Check Dams

The condition index assumes its initial value when the inspection target is constructed, and it decreases over time as the target's condition deteriorates due to structural characteristics (e.g., material properties, section dimensions, and loads) and external effects (environmental conditions and extreme events). Therefore, the check dam's degree of deterioration can be expressed as a ratio of the current condition (*CI*current) to the initial construction condition (*CI*initial). We term this ratio as degree of deterioration (*DE*), that is deterioration rate and we used *CI* to express it as:

$$DE = 1 - \frac{CI_{\,current}}{CI_{\,initial}}. \tag{8}$$

The *DE* value in concrete check dams (*DE*concrete) increased from 0.02 to 0.5 at a *T* of 4–31 years (r2 = 0.209, $p < 0.05$) (**Figure 12A**). The degree of deterioration in stone check dams (*DE*stone) increased from 0.00 to 0.62 at a *T* of 3–28 years (r2 = 0.670, $p < 0.001$) (**Figure 12B**). This result clearly shows that the inspection targets' conditions worsen as their service time increases, consistent with the results of other studies (Dell'Agnese et al., 2013; Ogasawara and Kambara, 2015; Lee et al., 2018; Mazzorana et al., 2018).

In concrete check dams of 16–30 years of age, the average $DE_{concrete}$ for *T* (i.e., the estimated value of the regression equation) increased by a factor of approximately 1.5. The data for this period's concrete check dams appear to exceed *DE* = 0.30 (*CI* < 3.5), at which point repair/reinforcement is needed once *T* exceeds 20 years. In the case of stone check dams, the estimated value of $DE_{stone}$ at a *T* of 16–30 years is increased by a factor of approximately 2.6. Apart from three instances, the data for this period's stone check dams indicate that repair/reinforcement is needed once *T* exceeds 15 years. The deterioration of concrete and stone check dams was expected to proceed at different rates. In particular, the average trend in the *DE* values of stone check dams was higher than that of concrete stone check dams when *T* exceeded 23 years Lee et al. (2018) proposed a relationship between a check dam's condition index and service times. In this relationship, the deterioration of stone check dams proceeds more rapidly than that of concrete check dams 20 years after construction. This is consistent with studies by Dell'Agnese et al.

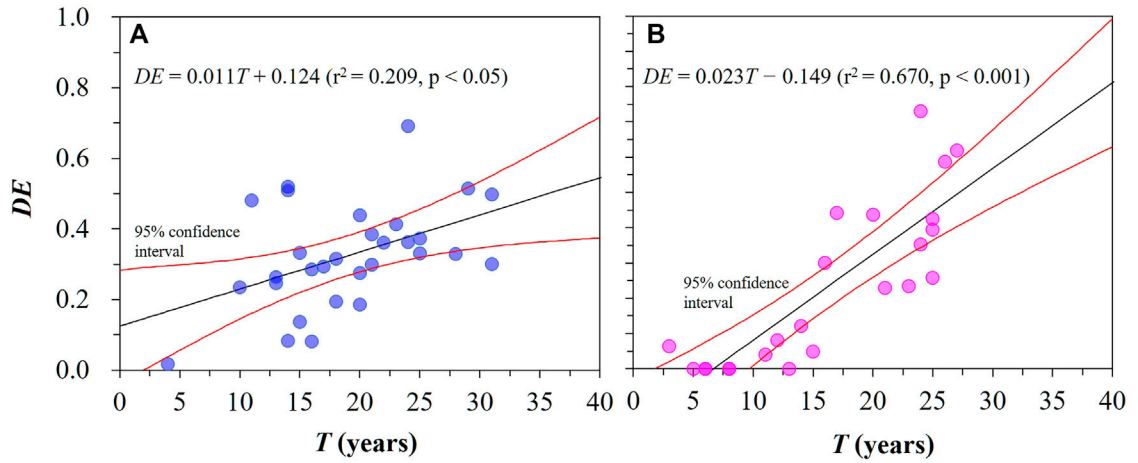


**FIGURE 12 |** Temporal changes in the check dams' degree of deterioration (*DE*) with respect to the increase in service time (*T*) for **(A)** concrete and **(B)** stone check dams.

(2013) and Mazzorana et al. (2014; 2018), which showed that the condition of stone check dams was poorer than that of concrete ones in visual inspections of both types. Although information regarding the construction environment of the analysis targets was insufficient, it is concluded that deterioration progresses relatively quickly in stone than concrete check dams.

Using the 95% confidence interval of the estimated regression line, the distribution of *DE* in concrete might be and stone check dams can be classified into the following three groups:

1) Group I: The data were distributed in the area above the 95% confidence interval. Deterioration occurred more quickly than other check dams constructed during a similar period.
2) Group II: Data were distributed within the 95% confidence interval. The data can be estimated to follow the average deterioration trends of the examined check dams.
3) Group III: Data were distributed in the area below the 95% confidence interval. Deterioration occurred more slowly than in other check dams constructed during a similar period.

Five instances of concrete check dams appeared in Group I. In the Group I data, *DE* varied from 0.44 to 0.69, showing a degree of deterioration 1.6–3.3 times higher (on average) than that of Groups II and III. The examined check dams' average service time was 16.6 years in Group I, 23.5 years in Group II, and 26.5 years in Group III, showing a 7 years difference. Expressed otherwise, the degree of deterioration in the dam bodies was highest in Group I, which contained relatively recently constructed check dams. Although there is a paucity of field information to demonstrate it, this difference in Group I and Groups II and II would seem to be relevant to the environmental factors (e.g., climate, catchment area, bed slope, sediment retention, etc.) and construction qualities (e.g., construction materials, concrete hardening time, concrete forming work, etc.).

In the case of stone check dams, the *DE* values of the seven instances in Group I varied from 0.06 to 0.73, showing a degree of deterioration three times higher (on average) than that of Groups II and III. The average service time for Group I was 13.6 years, which did not significantly differ from the age of 11.2 and 12.7 years observed for Groups II and III, respectively. The visual inspection method is highly reliant on human perception. Therefore, the irregular shapes of the stone check dams are not conducive to evaluating changes on the structure exterior (Hughes, 2007). The data in **Figure 12B** show that the degree of deterioration in stone check dams significantly increased at T exceeding 15 years. Considering the difficulties of visual inspections in stone check dams, this allows us to infer that the severity of damages and deterioration in stone check dams may become apparent 15 years after construction. Therefore, the stone check dams in Group I, which are older than those of Groups II and III, may have been favorable for evaluating the changes on the structure exterior; in the Group I data, the erosion depth varied as 0.10–0.65 m, 1.5 times higher (on average) than Groups II and III (0.01–0.57 m). Thus, further information on the inspection practice and methodology seems to be required to demonstrate the deterioration characteristics of stone check dams.

The effects of catchment and structure features on the check dam deterioration were investigated to find the causes of the high deterioration rate in Group I data (**Figure 13**). In both concrete and stone check dams, the variables for the elevation level (*EL*) and channel bed width (*CW*) in Group I were on average higher than those of Groups II and III (**Figure 13A** and **Figure 13B**). There was also a notable difference in catchment areas (*A*) between the three groups, except for two highest values of the stone check dams (>2,000ha) (**Figure 13C**). However, low variabilities in the channel bed slopes (*S*) were observed in both types of check dams in comparing the variables for each data group (**Figure 13D**). For the variables related to the structure features, the structure length and height (*DW* and *DH*) measured in concrete check dams revealed higher levels in Group I than in Groups II and III on average (**Figure 13E** and **Figure 13F**). However, there were no significant differences in the structural features between the three groups for the stone check dams.

Weather conditions such as precipitation, temperature, and humidity are closely related to extreme events and material

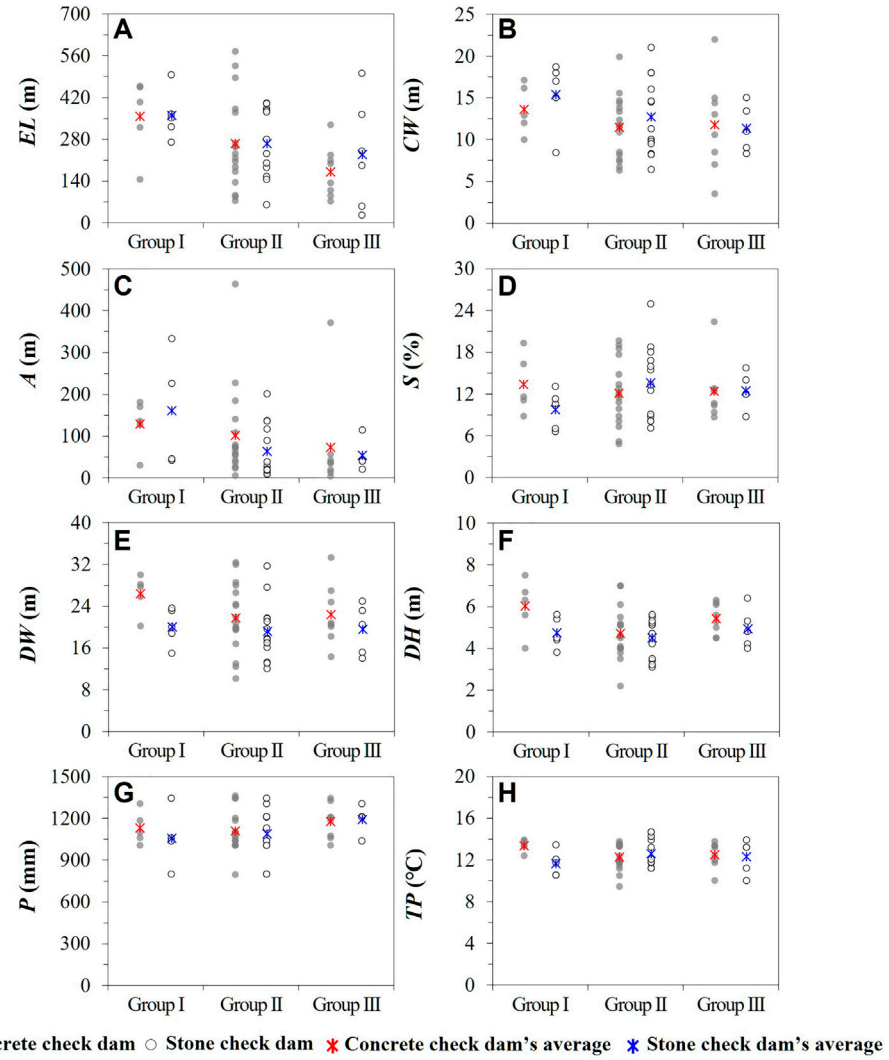


**FIGURE 13 |** Effects of catchment and structure features on the check dam's degree of deterioration: **(A)** *A*, catchment area ($m^2$); **(B)** *EL*, elevation level (m); **(C)** *CW*, channel bed width (m); **(D)** *S*, channel bed slope (%); **(E)** *DW* and **(F)** *DH*, structure width and height (m); **(G)** *P*, average annual precipitation (mm); **(H)** *TP*, average annual temperature (°C).

deterioration of structures. However, there was no significant difference in the average annual precipitation (*P*) and annual temperature (*TP*) variables between Groups I, II, and III (**Figure 13G** and **Figure 13H**). Our meteorological data were acquired from a weather observation station located at 1.5–13.5 km from each study site. This would not have provided sufficient data resolution to analyze the weather conditions of the stream where the check dam was built, considering the climate characteristics of mountainous areas with high temporal and spatial variability. Therefore, it is considered that more localized data is required to evaluate the contribution of climatic factors on the check dam damages and deterioration. Although it is insufficient evidence to fully explain the effect of catchment and structure features on the check dam conditions, we can discover a difference in the deterioration rate of the check dams under conditions such as high elevation levels, broad catchment areas, and geometric properties (Dell'Agnese et al., 2013). Therefore, these variables are desirable to be considered for establishing maintenance strategies.

## CONCLUSION

Check dams are one of representative structural measures to reduce sediment disaster at a forest watershed. Therefore, it is essential to assess the structural vulnerability and functionality of check dams in the management of sediment disaster risk at watersheds. This study examined the main types of damages and deterioration characteristics in concrete and stone check dams, which comprise more than 80.0% of Korea's check dam stock. This was based on the 4-step condition assessment, which is the modified version of condition assessment methodology for embankment dams to meet the characteristics of check dams.

As a result, the damages and deterioration of concrete check dams were classified into ten representative types including cracking, joint deterioration, and abrasion/erosion. And representative damage types of stone check dams were classified into nine types including uncontrolled vegetation, joint mortar deterioration, and falling out. The representative damage types of concrete and stone check dams were used as basis data for condition assessment.

The 4-step condition assessment consisted of the condition assessment of damages and deterioration, the condition assessment of individual elements, the condition assessment of composite members, and the comprehensive assessment. We evaluated the structural conditions of concrete and stone check dams, which was expressed as a numerical index. The assessment results demonstrated that the spillway part frequently contacted with water and debris flows was deteriorated approximately 1.2 times faster than the wing parts for both concrete and stone check dams, and the maintenance demands of both types of check dams increased 20 years after construction. Thus, these deterioration characteristics of concrete and stone check dams should be considered in decision-making to determine maintenance priorities among the check dams stock.

We analyzed the relationship between condition index and service time in the examined concrete and stone check dams. The degree of deterioration in concrete and stone check dams increased significantly as the service time increased. In particular, the average trend in stone check dams' deterioration was higher than that of concrete check dams when the service time increased as 23–30 years. This suggested that the maintenance priority for the deteriorated check dams (i.e., 20 years after construction) should be given to the stone check dams rather than concrete check dams.

Based on the relationship between condition index and service time, we classified deterioration characteristics of check dams into two groups: 1) those that follow the average deterioration trends of their facility group (Group II) and 2) those that undergo an unexpected end-of-service life because of exceptional incidents or severe defects (Group I). For both groups, the service environment and construction quality are determinant factors; however, the maintenance of Group II is considered to be an issue that engineers can, to some extent, predict and respond to, by using established case data. However, Group I is associated with unpredictable events and hidden problems, thus, it is not a suitable target for a generalized maintenance plan. Considering maintenance conditions and disaster-prediction difficulties produced by the Earth's increasingly changing climate, we believe that fundamental measures (e.g., strengthening design standards and quality control) will need to be implemented with reference to the cases in Group I.

This work will form a useful resource for engineers and decision-makers involved in planning, designing, constructing, and maintaining check dams. However, this study is limited by the lack of information on the quantitative methodology for evaluating the deterioration of different types of check dams. In addition, the sample size was insufficient to allow for a generalizable conclusion in the other mountain streams, which have diverse environmental conditions. Therefore, further studies need to be carried out in order to develop scientific standards for condition assessment by utilizing the field information obtained from the routine inspections.

## DATA AVAILABILITY STATEMENT

The original contributions presented in the study are included in the article/**Supplementary files**, further inquiries can be directed to the corresponding author.

## AUTHOR CONTRIBUTIONS

KHL, EBE, and TU. contributed to conception and design of the study. KHL, EBE, and CSW organized the database and KHL and EBE. performed the statistical analysis. KHL, EBE, and TU wrote sections of the manuscript. KHL wrote and complied the first draft of the manuscript. All authors contributed to the manuscript revision, and read and approved the submitted version.

## FUNDING

This study was financially supported by Gyeongsanbuk-do Forest Environment Research Institute Grant No. 20150401.

## SUPPLEMENTARY MATERIAL

The Supplementary Material for this article can be found online at: https://www.frontiersin.org/articles/10.3389/feart.2021.788029/full#supplementary-material

## REFERENCES

Adamo, N., Al-Ansari, N., Sissakian, V., Laue, J., and Knutsson, S. (2020). Dams Safety: Inspections, Safety Reviews, and Legislations. *J. Earth Sci. Geotech. Eng.*, 109–143. doi:10.47260/jesge/1114

Andersen, G. R., and Torrey III, V. H., III (1995). Function-based Condition Indexing for Embankment Dams. *J. Geotechnical Eng.* 121, 579–588. doi:10.1061/(asce)0733-9410(1995)121:8(579)

Armanini, A., Dellagiacoma, F., and Ferrari, L. (1991). From the Check Dam to the Development of Functional Check Dams. *Fluv. Hydraul. Mt. Reg.* 37, 331–344. doi:10.1007/bfb0011200

Chahrour, N., Nasr, M., Tacnet, J.-M., and Bérenguer, C. (2021). Deterioration Modeling and Maintenance Assessment Using Physics-Informed Stochastic Petri Nets: Application to Torrent protection Structures. *Reliability Eng. Syst. Saf.* 210, 107524. doi:10.1016/j.ress.2021.107524

Comiti, F., Lenzi, M. A., and Mao, L. (2010). "Local Scouring at Check-Dams in Mountain Rivers," in *Check Dams, Morphological Adjustments and Erosion Control in Torrential Streams*. Editors M. Conesa-Garcia and M. A. Lenzi ((NY, USA: Nova Science Publ), 263–282.

Cortes Arevalo, V. J., Sterlacchini, S., Bogaard, T. A., Junier, S., and van de Giesen, N. (2016). Decision Support Method to Systematically Evaluate First-Level Inspections of the Functional Status of Check Dams. *Struct. Infrastructure Eng.* 12, 1–18. doi:10.1080/15732479.2016.1144619

Dell'Agnese, A., Mazzorana, B., Comiti, F., Von Maravic, P., and D'agostino, V. (2013). Assessing the Physical Vulnerability of Check Dams through an Empirical Damage index. *J. Agricult Engineer* 43, 2–16. doi:10.4081/jae.2013.e2

Federal Highway Administration (2016). *Synthesis of National and International Methodologies Used for Bridge Health Indices*. Washington, D.C: Synthesis of National and International Methodologies Used for Bridge Health Indices.

Fujita, M., Mizuyama, T., Honda, N., Ikeda, A., Nagayama, T., Mike, C., et al. (2020). Effect of Chatchment Characteristics on Sabo Dam Deterioration. in" Proceedings of the 68th Annual Meeting of the Japan Society of Erosion Control Engineering. Iwate, Japan, 109–110.

Gattulli, V., and Chiaramonte, L. (2005). Condition Assessment by Visual Inspection for a Bridge Management System. *Comp-aided Civil Eng.* 20, 95–107. doi:10.1111/j.1467-8667.2005.00379.x

Hueble, J., and Fiebiger, G. (2005). "Debris-flow Mitigation Measures," in *Debris Flow Hazards and Related Phenomena*. Editors M. Jakob and O. Hunger (Berlin: Springer), 445–448.

Hughes, A. (2007). *Training Aids for Dam Safety Module: Inspection of concrete and Masonry Dams*. Washington, D.C.: Bureau of Reclamation.

Japanese Ministiry of Land, Infrastructure, Transportation, and Tourism (2014b). *Inspection Procedure Manual for Sabo Facilities*. Tokyo: Japanese Ministry of Land, Infrastructure, Transport and Tourism.

Japanese Ministiry of Land, Infrastructure, Transportation, and Tourism (2014a). *Manual for Road and Bridge Periodic Inspection*. Tokyo: Japanese Ministiry of Land, Infrastructure, Transportation, and Tourism.

Jeong, Y., Kim, W., Lee, I., and Lee, J. (2018). Bridge Inspection Practices and Bridge Management Programs in China, Japan, Korea, and U.S. *J. Struct. Integrity Maintenance* 3, 126–135. doi:10.1080/24705314.2018.1461548

Kasahara, Y., Otsubo, S., Ogawauchi, Y., Nihei, A., Yamakage, S., and Yamanaka, R. (2010). A Study on the Soundness Evaluation Method of the Existing Sabo Dams. in" Proceedings of the 59th Annual Meeting of the Japan Society of Erosion Control Engineering. Nagano, Japan, May 26–28, 2010, 392–393.

Korea Association of Soil and Water Conservation (2014). *Annual Check Dam Inspection Report: Gyeongsangbuk-Do*. Gyeongsangbuk-do, 2015.

Korea Association of Soil and Water Conservation (2015). *Annual Check Dam Inspection Report: Gyeongsangbuk-Do*. Gyeongsangbuk-do.

Korea Association of Soil and Water Conservation (2016). *Annual Check Dam Inspection Report: Gyeongsangbuk-Do*. Gyeongsangbuk-do.

Korea Concrete Institute (2014). *Guidelines for Inspection and Maintenance of Underwater Structures*. Gujarun: K. C. Institute Seoul.

Korea Forest Service (2020). *Development of a Safety Assurance Guidance for Sediment-Related Disaster Prevention Measures and a Watershed Management Framework for Risk Reduction in forest Watersheds*. Sejong: Japanese Ministry of Land, Infrastructure, Transport and Tourism.

Korea Forest Service (2018). *Guidelines for Maintenance of Erosion Control Facilities*. Sejong: Japanese Ministry of Land, Infrastructure, Transport and Tourism.

Korea Infrastructures Safety and Technology Coporation (2019a). *Giudeline and Commentary of Safety Inspection and In-Depth Safety Inspection for Structures-Dam*. Sejong: Korean Ministry of Land, Infrastructure, and Transport.

Korea Infrastructures Safety and Technology Coporation (2019b). *Giudeline and Commentary of Safety Inspection and In-Depth Safety Inspection for Structures-Retaning Wall*. Sejong: Korean Ministry of Land, Infrastructure, and Transport.

Korean Ministry of Land Infrastructure and Transport (2020). *Guideline of Safety Inspection and In-Depth Safety Inspection for Facilities*. Sejong: Korean Ministry of Land Infrastructure and Transport.

Lee, J. H. (2015). *Analysis of Condition Assessment and Damage Patterns of concrete Check Dam*. Ph. D. dissertation. South Korea: Kangwon National University.

Lee, J. H., Kim, S. W., Lee, K. Y., Bae, H. S., and Chun, K. W. (2021). Analysis of Factors Affecting Damage of the concrete Check Dams Based on the Exterior Condition Assessment. *Crisisonomy* 17, 59–72.

Lee, K. H. (2017). *A Study on the Determination of Maintenance Priority Order Among Debris Barriers on the Basis of Exterior Condition Evaluation*. Ph. D. dissertation. South Korea: Yeungnam University.

Lee, K. H., Lee, H. H., Ewane, B. E., Uchida, T., and Sakurai, W. (2018). Analysis of Damage Characteristics and Aging Trend of Debris Barriers Using Exterior Condition Assessment. in" Proceedings of the International Symposium Interpraevent. Toyama, Japan, October 1–4, 2018.

Lenzi, M. A., Marion, A., and Comiti, F. (2003). Local Scouring at Grade-Control Structures in Alluvial Mountain Rivers. *Water Resour. Res.* 39, 1176. doi:10.1029/2002WR001815

Makita, K., Ohkubo, S., Mizuyama, T., and Ido, K. (1987). Analysis of an Example of Disaster Prevention with a Sabo Dam. *J. Jpn. Soc. Eros. Control. Eng.* 40, 3–10.

Matsumura, K. (2000). Recent Developement in Sabo Plan and Sabo Facilities Functions. *J. Jpn. Soc. Eros. Control. Eng.* 52, 76–80.

Mazzorana, B., Trenkwalder-Platzer, H., Heiser, M., and Hübl, J. (2018). Quantifying the Damage Susceptibility to Extreme Events of Mountain Stream Check Dams Using Rough Set Analysis. *J. Flood Risk Manage.* 11, e12333. doi:10.1111/jfr3.12333

Mazzorana, B., Trenkwalder-Platzer, H. J., Fuchs, S., and Hübl, J. (2014). The Susceptibility of Consolidation Check Dams as a Key Factor for Maintenance Planning. *Österr Wasser- und Abfallw* 66, 214–216. doi:10.1007/s00506-014-0160-4

Miyamoto, A., Kawamura, K., and Nakamura, H. (2000). Bridge Management System and Maintenance Optimization for Existing Bridges. *Comp-aided Civil Eng.* 15, 45–55. doi:10.1111/0885-9507.00170

Mizuyama, T., Habara, S., and Furukawa, M. (1988). Sabo Dam Converting Debris Flow to Bedload. *J. Jpn. Soc. Eros. Control. Eng.* 40, 20–23. doi:10.11475/sabo1973.40.6_20

Mizuyama, T. (2010). Recent Developments in Sabo Technology in Japan. *Ijece* 3, 1–3. doi:10.13101/ijece.3.1

Mizuyama, T. (1979). Survey of Disaster of Check Dam. *J. Jpn. Soc. Eros. Control. Eng.* 4, 26–30. doi:10.11475/sabo1973.31.4_26

Ogasawara, K., and Kambara, J. (2015). Efforts in Maintenance of Sabo Facilities in Nagano Prefecture. *J. Jpn. Soc. Eros. Control. Eng.* 68, 47–51. doi:10.11475/sabo.68.4_47

Piton, G., Carladous, S., Recking, A., Tacnet, J. M., Liébault, F., Kuss, D., et al. (2016). Why Do We Build Check Dams in Alpine Streams? an Historical Perspective from the French Experience. *Earth Surf. Process. Landforms* 42, 91–108. doi:10.1002/esp.3967

Piton, G., and Recking, A. (2014). "River Flow 2014," Proceedings of the International Conference on Fluvial Hydraulics, Lausanne, Switzerland, September 3–5, 2014, 1437–1445. doi:10.1201/b17133-192

Portland Cement Association (2002). Types and Causes of concrete Deterioration. Available at: https://www.cement.org/docs/default-source/fc_concrete_technology/durability/is536-types-and-causes-of-concrete-deterioration.pdf?sfvrsn=4&sfvrsn=4.

Recking, A. (2012). Influence of Sediment Supply on Mountain Streams Bedload Transport. *Geomorphology* 175, 139–150.

Rickenmann, D., and Koschni, A. (2010). Sediment Loads Due to Fluvial Transport and Debris Flows during the 2005 Flood Events in Switzerland. *Hydrol. Process.* 24, 993–1007. doi:10.1002/hyp.7536

Rudolf-Miklau, F., and Suda, J. (2011).Technical Standards for Debris Flow Barriers and Breakers. in" Proceedings of the 5th International Conference on Debris-Flow Hazards Mitigation: Mechanics. Padua, Italy, June 14–17, 2011: Prediction and Assessment, 1083–1091. doi:10.4408/IJEGE.2011-03.B-117

Suda, J., and Huebl, J. (2007). Schäden und schadmechanismen an schutzbauwerken der wildbachverbauung. *Wildbach-und Lawinenverbau* 155, 56–83.

Suda, J., Strauss, A., Rudolf-Miklau, F., and Hübl, J. (2009). Safety Assessment of Barrier Structures. *Struct. Infrastructure Eng.* 5, 311–324. doi:10.1080/15732470701189498

**Conflict of Interest:** The authors declare that the research was conducted in the absence of any commercial or financial relationships that could be construed as a potential conflict of interest.

**Publisher's Note:** All claims expressed in this article are solely those of the authors and do not necessarily represent those of their affiliated organizations, or those of the publisher, the editors and the reviewers. Any product that may be evaluated in this article, or claim that may be made by its manufacturer, is not guaranteed or endorsed by the publisher.

frontiers in Earth Science

ORIGINAL RESEARCH
published: 11 February 2022
doi: 10.3389/feart.2022.759556

# Application of Stream Conductivity to Activity of Potential Large-Scale Landslide

*Yuan Jung Tsai*[1]*, *Yi Jing Chen*[1], *Chieh Hsuan Weng*[1], *Fang Tsz Syu*[1], *Kun-An Hsu*[1] and *Wei Lin Lee*[2]

[1]Disaster Prevention Research Center, National Cheng-Kung University, Tainan, Taiwan, [2]National Science and Technology Center for Disaster Reduction, New Taipei City, Taiwan

Underclimate changes, extreme rainfall events can cause catastrophic sediment-related disasters such as large-scale landslides. To work on disaster prevention, the government has investigated the location of potential large-scale landslides by a geological and geomorphological approach. However, the activity of potential large-scale landslides has to rely on expensive on-site monitoring system, for example, observed drill hole of groundwater and underground displacement. Recently, the variation of stream electronic conductivity has been proposed to investigate the activity of large-scale landslide in Japan. Therefore, this study applied this concept in Taiwan. First, the temporal and spatial variations of stream electronic conductivity near the potential large-scale landslide have been surveyed. Accordingly, an interesting finding is that the spring water from the potential large-scale landslide can increase the concentration of chemical ion, and thus, the value of stream electronic conductivity increases. Second, the comparison of rainfall data, stream electronic conductivity, and ground surface displacement has been analyzed. There is a sound agreement between stream electronic conductivity and ground surface displacement. This result implied that stream electronic conductivity could be a possible index to monitoring the activity of potential large-scale landslides indirectly.

**Keywords: large-scale landslide, electrical conductivity, surface displacement, rainfall, landslide mechanism**

OPEN ACCESS

***Edited by:***
*Chong Xu,*
*Ministry of Emergency Management, China*

***Reviewed by:***
*Siyuan Ma,*
*China Earthquake Administration, China*
*Changdong Li,*
*China University of Geosciences Wuhan, China*

***Correspondence:**
*Yuan Jung Tsai*
*rongtsai@dprc.ncku.edu.tw*

***Specialty section:***
*This article was submitted to Geohazards and Georisks, a section of the journal Frontiers in Earth Science*

***Received:*** *16 August 2021*
***Accepted:*** *05 January 2022*
***Published:*** *11 February 2022*

***Citation:***
*Tsai YJ, Chen YJ, Weng CH, Syu FT, Hsu K-A and Lee WL (2022) Application of Stream Conductivity to Activity of Potential Large-Scale Landslide. Front. Earth Sci. 10:759556. doi: 10.3389/feart.2022.759556*

## 1 INTRODUCTION

Extreme climatic effects have accelerated rainfall-induced large-scale landslides (LSLs) (Stanley and Kirschbaum, 2017; Kirschbaum and Stanley, 2018); therefore, occurrence assessment has emerged as the critical issue in slope management. After the Hsiaolin Village disaster caused by Typhoon Morakot in Taiwan in 2009, it has become imperative for the government to prevent and mitigate rainfall-induced LSLs. Numerous potential large-scale landslide (PLSL) areas (with an area exceeding 10 ha, depth in excess of 10 m, or volume greater than 100,000 $m^3$) have been identified using high-resolution topographic images (Lin et al., 2012). Marui (2017) pointed out that the investigation of LSLs can be detected by specific topographic features, such as "double ridge," "head scarp," and "gully." Chigira (2014) called it a geological and geomorphological approach and has wildly applied it for the detection of LSLs. However, the images could only elucidate areas of deformation that the time of occurrence of the deformation remains unknown. Also, there is currently a lack of precision of quantitative methods to accurately predict when the PLSL will collapse.

Extant research indicates that LSL incidence is closely correlated with rainfall, infiltration processes, and groundwater alteration (Celia and Binning, 1992; Van Asch et al., 1999;

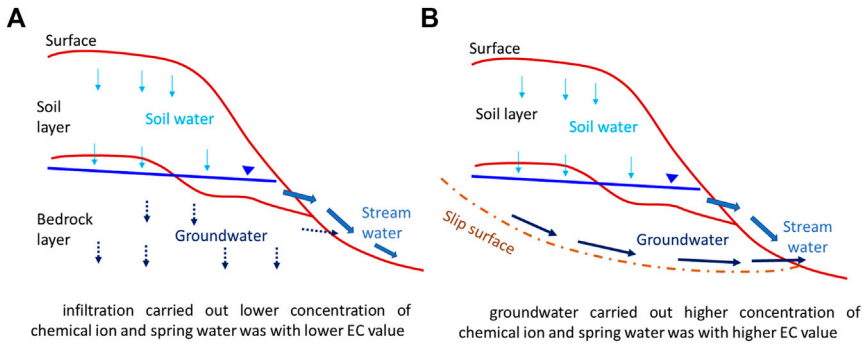


**FIGURE 1 |** Concept of stream EC variation corresponding to infiltration and groundwater. **(A)** Infiltration carried out lower concentration of chemical ion and spring water was with lower EC value. **(B)** Groundwater carried out higher concentration of chemical ion and spring water was with higher EC value.

Mantovani et al., 2000; Trigo et al., 2005; Ray and Jacobs, 2007; Miyamoto and Imaizumi, 2012). As rainfall infiltrates the slope, the inherent slope mass increases, thereby increasing driving force. At the same time, infiltration causes pore water pressure to rise and makes effective stress decrease, following reduced resistance force. This process finally decreases overall safety factors. This indicates that precipitous elevation in pore water pressure and sudden drop in effective stress lead to slope instability (Terzaghi, 1943; Lee et al., 2019). The research indicated that the monitoring of infiltration and groundwater plays an important role in the rainfall-induced LSLs.

In the case of PLSL, the phreatic surface could exist at a very deep location (Wei et al. 2019; Wei et al. 2020). Thus, the installation of deep groundwater wells for real-time monitoring is high cost and difficult to maintain as the PLSL with high activity. The observation of infiltration and groundwater volume poses significant challenges; some scholars have deployed stream electrical conductivity (EC) as an alternative to groundwater observation. Jitousono et al. (2006) investigated stream EC in catchment areas finding significant groundwater volume flowed out in the area where landslides occurred, causing the EC of the water body to be significantly higher than the areas where no collapse occurred and can be used to estimate the location of such groundwater springs. Jitousono (2014) proposed a relationship between LSLs and EC values, mentioning that with landslide occurrence, the measured conductivity value will be significantly higher than the value upstream of the landslide. Jitousono (2014) pointed out that the time consumed for the groundwater draining outside the slope is longer than the infiltration, so that groundwater can carry out a higher concentration of chemical ions and the spring water is with a higher EC value; the concept is shown in **Figure 1**. Weng et al. (2018) also discussed landslide rates and EC in Taiwan. Using survey results for 24 catchment areas, they found that catchment areas with high landslide rates also have higher EC values measured at the outlet. These research studies implied that the observation of stream EC could be an alternative option to the monitoring of PLSL.

The purpose of this study is to focus on the application of stream EC on the PLSL. A catchment where PLSL existed was chosen to be the study area. The recorded data of stream EC, rainfall, and ground surface displacement in the catchment were collected to understand the relationship between stream EC and PLSL. This study was conducted in two stages. First, the temporal and spatial changes in EC across the PLSL in the catchment area were used to elicit the understanding of the spatial relationship between the PLSL and the EC variation. Second, the relationship between EC variation and landslide activity was probed by conducting correlation analysis between parameters, such as accumulated rainfall, surface deformation, and EC. Finally, the potential application of stream EC on the PLSL was suggested in this study.

In the present study, the study area, the collection data, and the data processing were introduced in **Section 2**. In **Section 3**, the relationship between stream EC and PLSL was discussed, which includes the spatial characteristics of stream EC response to the location of PLSL, and the activity of PLSL related to the evolution of stream EC. In **Section 4**, the finding about the relationship between the stream EC and the PLSL and its potential application were concluded.

# 2 STUDY AREA AND METHODOLOGY

## 2.1 Study Area

### 2.1.1 Location and Its Geological Condition

The selected study area was ZulinPLSL, located in the Kaoping River basin of southern Taiwan (**Figure 2E**). The study area has a catchment area of 133 ha, a river length of 945 m, and an average elevation distribution ranging from 1,300 m to 6,650 m, with a slope of 32° (**Figure 2A**). The catchment area stratum mainly belongs to the Changshan Formation Low-Grade Pelites (**Figure 2B**). This area was severely damaged by Typhoon Morakot in 2009, as shown in **Figure 2C** and **Figure 2D**. The landslides induced by typhoon was about 30 ha, with houses and roads in the area pervasively destroyed.

### 2.1.2 Potential Large-Scale Landslide Area

Because of the passing of the Changshan Formation and the fragility of geology in the upper member, at the upper edge of

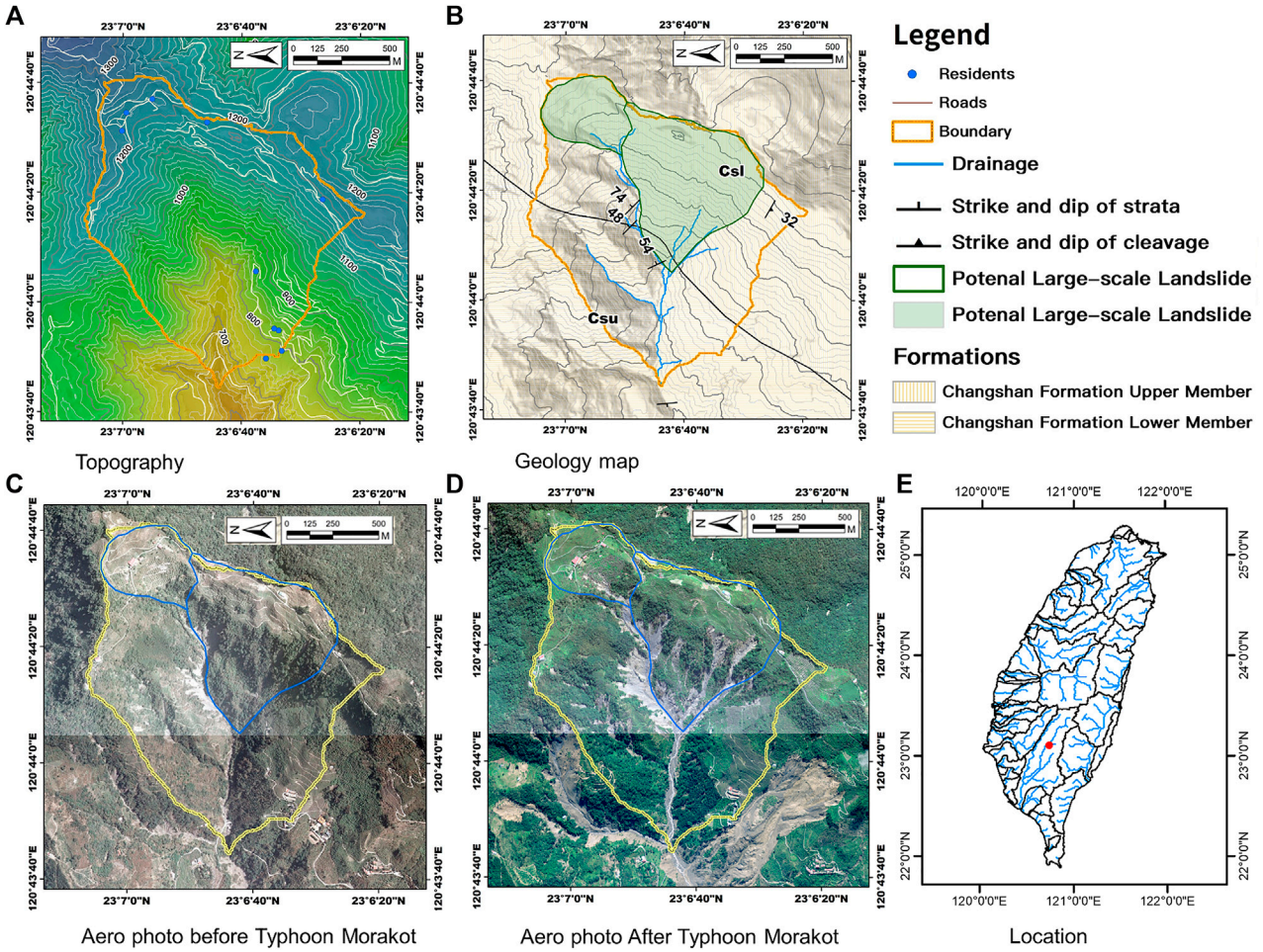


**FIGURE 2 |** Location, topography, and historical image of research area. **(A)** Topography, **(B)** geology map, **(C)** aero photo before Typhoon Morakot, **(D)** aero photo after Typhoon Morakot, **(E)** location.

the slope near the ridge, there is obviously a double ridge feature, which may develop during early large-scale slope sliding, as shown in **Figure 3A**. After field investigation, it can be divided into upper and lower members according to lithology. The upper member has a low degree of metamorphism. Lithology is dominated by hard shale (argillite) and prevalent pencil structures developed by weathering (**Figure 3B**). It implied that penetration could be faster and the fluctuation of groundwater could be more sensitive in this region. The lower member has a higher degree of metamorphism, and the lithology is dominated by slate rock. Due to the low degree of metamorphism, slaty cleavage is less developed (**Figure 3C**). Near the gully on the slope, the resultant from low lithology resistance to weathering, there is susceptibility to river and creek erosion, leading to side bank collapses. The upper slope was affected and started to deform, which could be observed from the damaged on-site artificial structures. Taiwan's Central Geological Survey has set up a continuous GPS monitoring station to observe the slope activity status. These observations help quantify area activity. Hence, there are two PLSLs in this catchment. The green area in **Figure 3A** is one PLSL area that has been recognized by the Central Geological Survey 1). The other one in **Figure 3A** is another PLSL area 2), which defined by this study.

## 2.2 Data Collection and Its Processing

### 2.2.1 Stream Electrical Conductivity

To elucidate spatial changes of EC, this study was performed using direct on-site observation. Water samples of streams in the study area were collected from downstream to upstream for EC measurement. Sampling locations (**Figure 4A**) were selected as outlets 1), downstream sections of the river 2), middle reaches of the river 3), the boundary of the PLSL 4), and location in the PLSL area 5). The sampling method was to

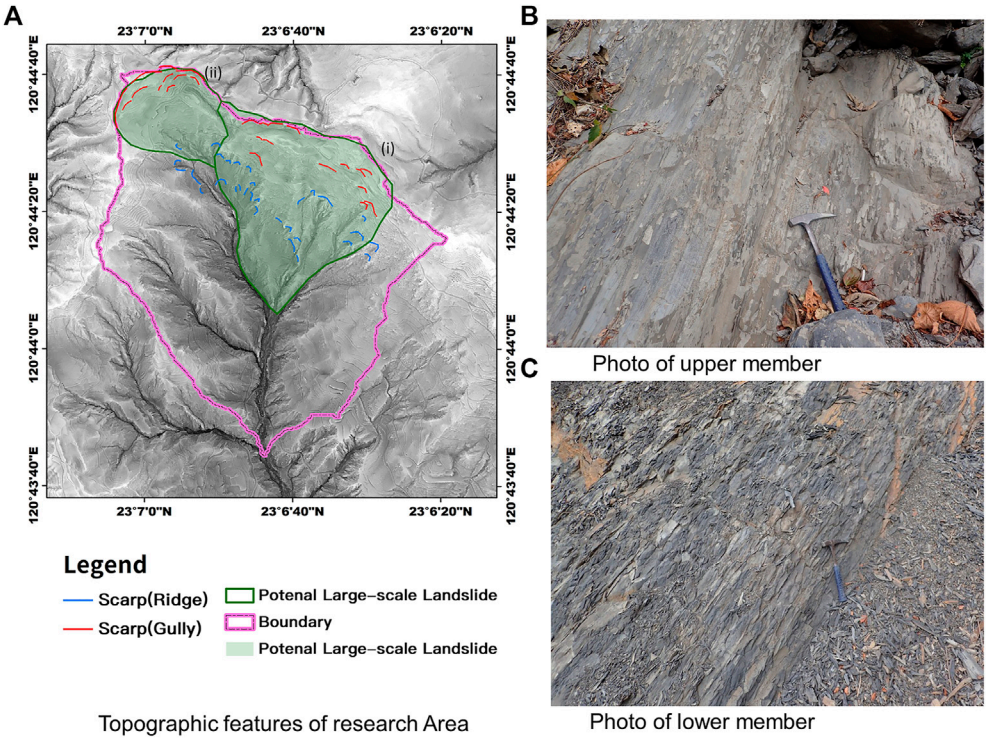


**FIGURE 3 |** Geology information of research area. **(A)** Geology map, **(B)** photo of upper member, **(C)** photo of lower member.

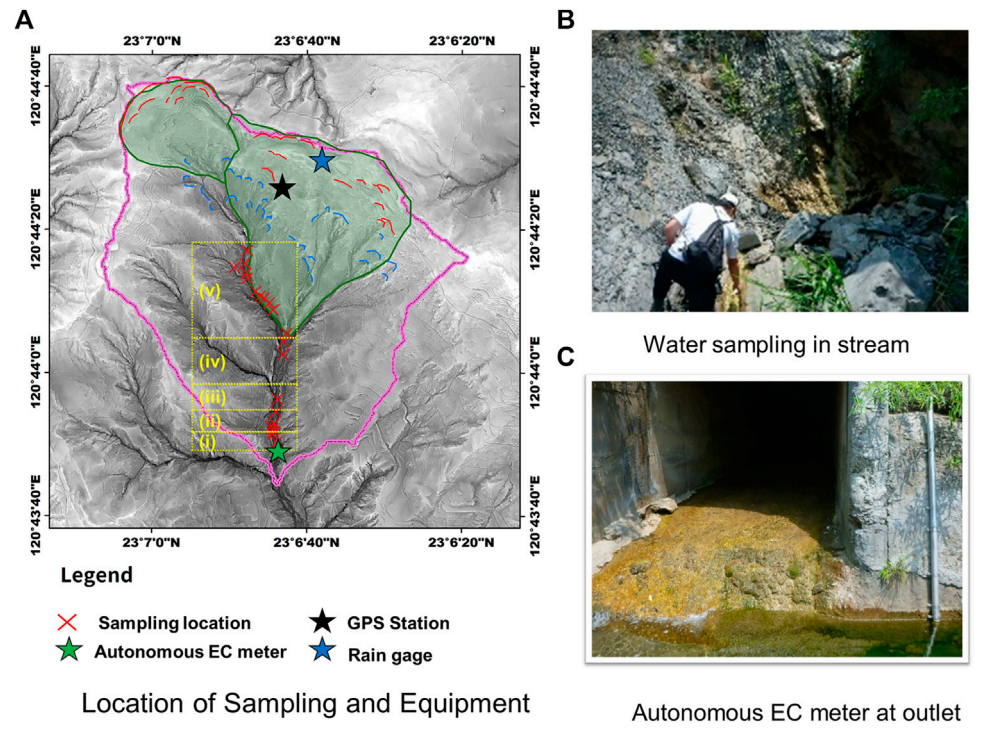


**FIGURE 4 |** Stream conductivity survey method. **(A)** Location of sampling and equipment, **(B)** on-site sampling, **(C)** automatic observation at the outlet point.

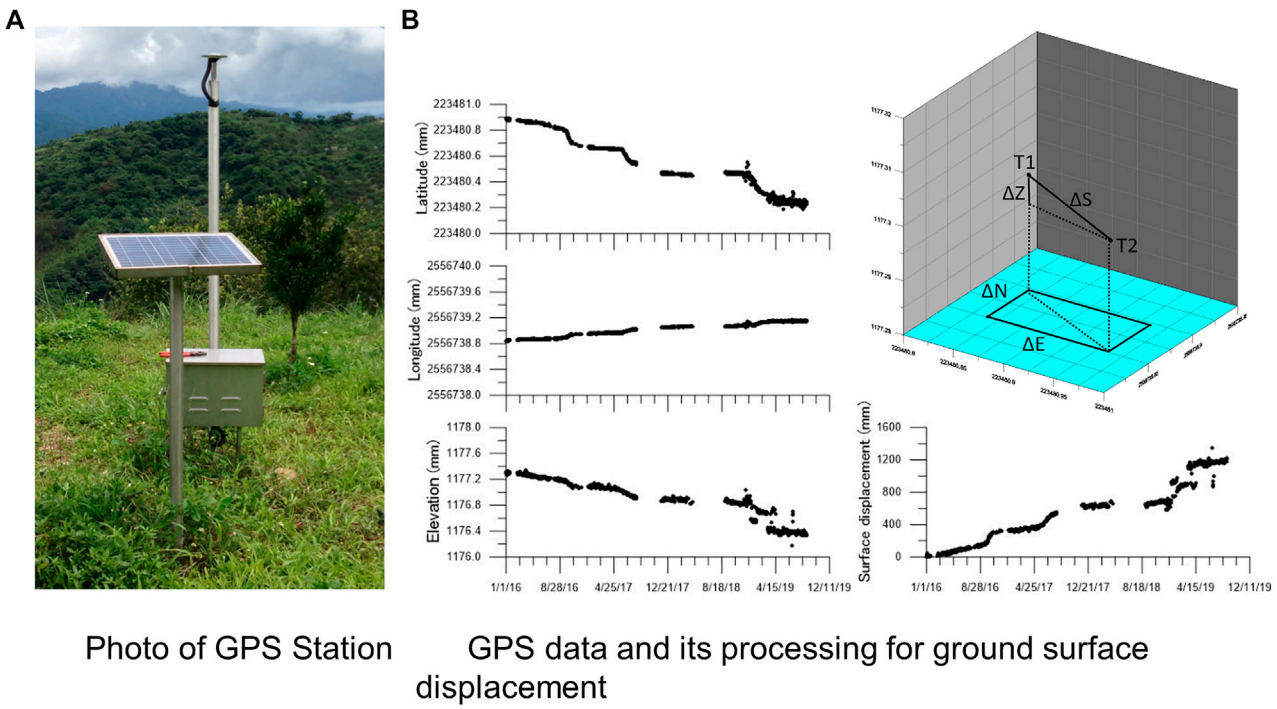


**FIGURE 5 |** GPS observing station and the data processing. **(A)** Photo of GPS station, **(B)** GPS data and its processing for ground surface displacement.

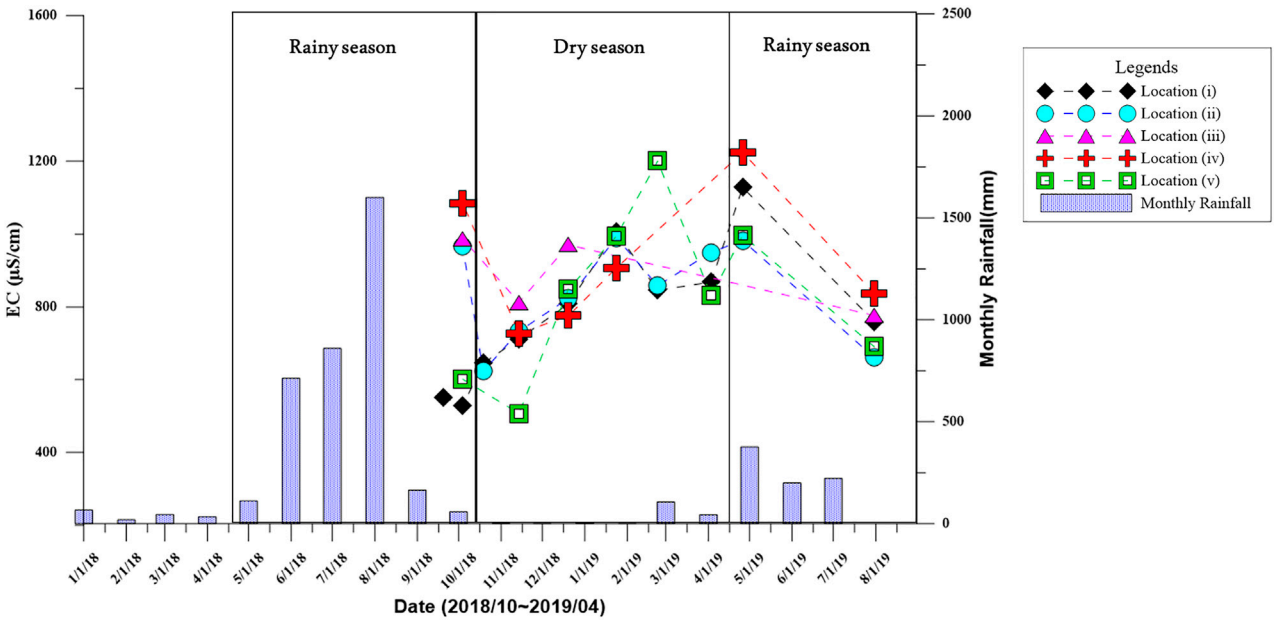


**FIGURE 6 |** Temporal change of EC along the stream.

take water on-site (**Figure 4B**) and measure it with an EC pocket meter, in which the range of measurement is 0–2,000 $\mu$S/cm and the resolution is 1 $\mu$S/cm. For analyzing time change of EC of ZulinPLSL, the evolution of stream EC fixed at the outlet point of the catchment was recorded by an autonomous EC meter; the location is shown in **Figure 4A**.

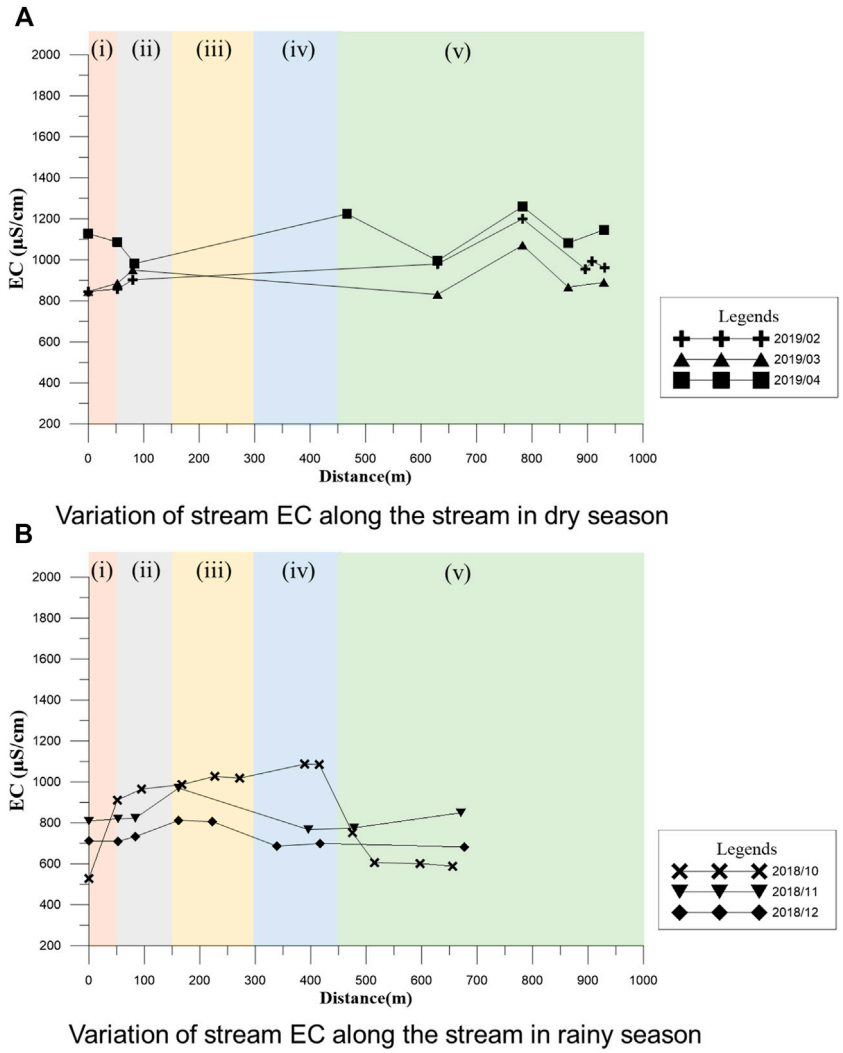


**FIGURE 7 |** Spatial change of EC along the stream. **(A)** Variation of stream EC along the stream in dry season, **(B)** variation of stream EC along the stream in rainy season.

The automatic measurement was installed in the field site, as shown in **Figure 4C**; the range of measurement is 0–20,000 $\mu$S/cm, and the resolution is 0.1 $\mu$S/cm.

### 2.2.2 Rainfall Data

Rainfall data were adopted from an automatic rain gauge. The rainfall data were recorded one time per hour automatically. Daily rainfall and monthly rainfall were obtained from data calculation. Daily rainfall was used to discuss the variation of EC with precipitation. Monthly rainfall was used to clarify the different seasons.

### 2.2.3 GPS Data and Its Processing

The area's surface deformation observation results were collected to present the activity of PLSL. Surface displacement data were from single-frequency GPS monitoring stations installed by the Central Geological Survey in the ZulinPLSL; the location is shown in **Figure 4A**. The observational data from 905 GPS stations were selected due to their obvious surface displacement, and the station is shown in **Figure 5A**. The deformation results were solved every hour with 10 mm resolution. In accordance with daily coordinates (E, N, H) provided by ground adjustment, as shown in **Figure 5B**, the movement distance and cumulative displacement were both calculated. Calculation formulas are in **(Eq. 1)** and **(Eq. 2)**:

$$\Delta S = \sqrt{\Delta E^2 + \Delta N^2 + \Delta Z^2} \text{ and} \quad (1)$$

$$S = \sum \Delta S, \quad (2)$$

where $\Delta S$ is the daily deformation (mm), $\Delta E$ is the daily E coordinate change (mm), $\Delta N$ is the daily N coordinate change

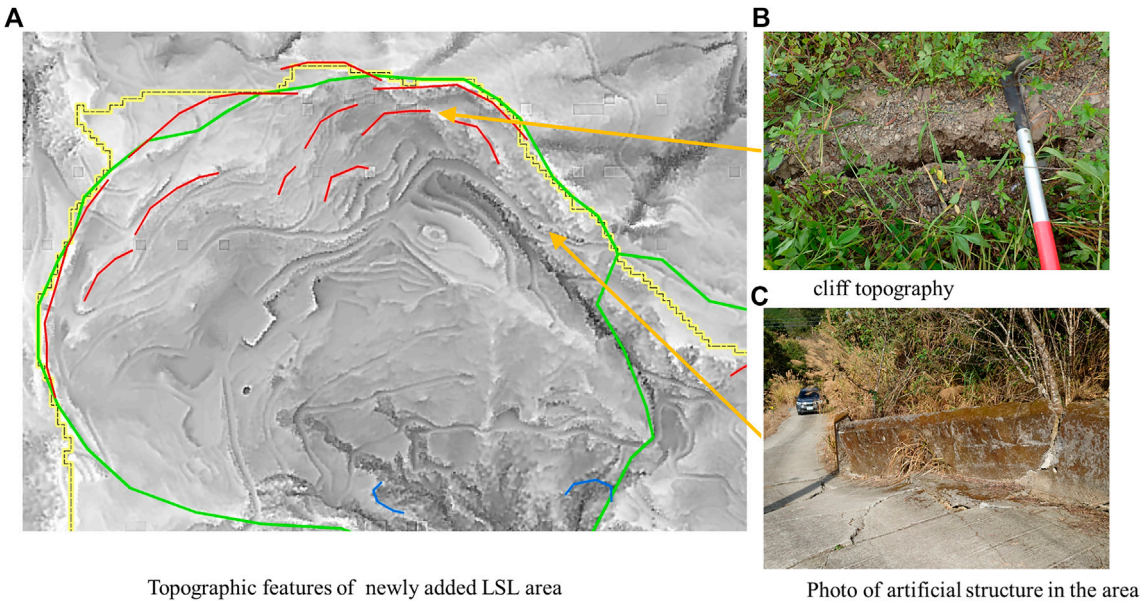


**FIGURE 8 |** Regional PLSL supplementary survey. **(A)** Topographic features of newly added LSL area, **(B)** cliff topography, **(C)** photo of artificial structure in the area.

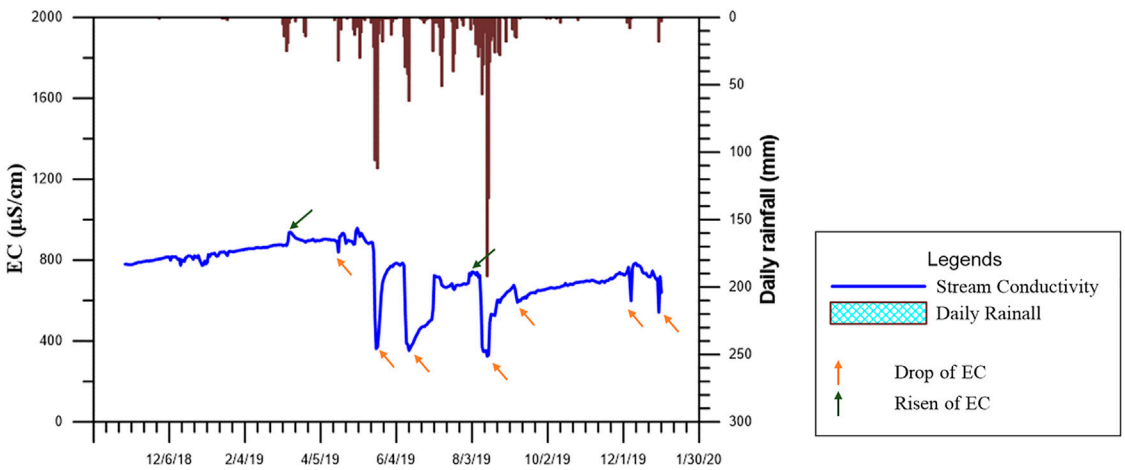


**FIGURE 9 |** Comparison of rainfall and stream EC.

(mm), ΔZ is the daily Z coordinate change (mm), and S: cumulative deformation (mm).

## 3 RESULTS AND DISCUSSION

### 3.1 Temporal and Spatial Changes of Stream EC

The data of stream EC obtained on-site over time with corresponding rainfall data were compared. There are 6 surveys from October 2018 to April 2019. In **Figure 6**, the horizontal axis is time and the vertical axis is conductivity and rainfall. Monthly accumulated rainfall was used to consider seasonal variation in conductivity.

Accordingly, as shown in **Figure 6**, it may be ascertained that dry season stream EC is higher than the wet season, and stream EC continues to increase with time during the dry season, only then gradually decreasing at wet season onset. In the dry season, the mainstream flow relies on groundwater spring. Throughout this period, it is known that stream conductivity is higher. For the wet season, under the influence of rainfall replenishment, the stream water source is not only the original groundwater source but includes increasing rainfall, surface runoff, and other different

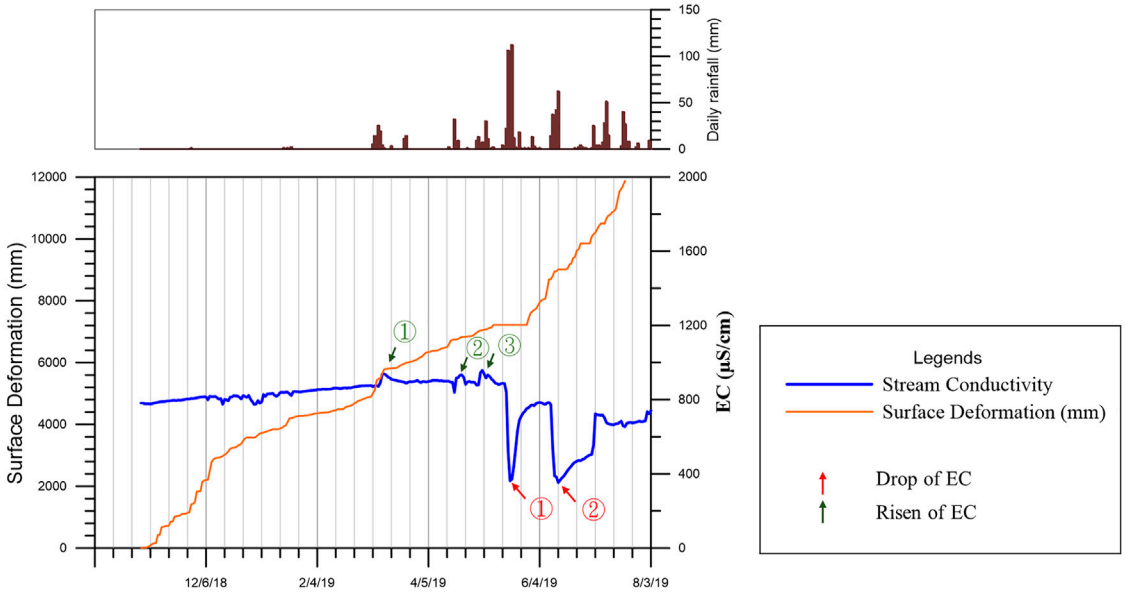


**FIGURE 10 |** Comparison of stream EC and ground surface displacement.

sources. As it is refilled, stream EC is reduced by the increasing amount of water. Therefore, it can be seen for this study area that groundwater conductivity is higher than that of rainwater or surface runoff. Hence, the change in stream EC is indeed related to groundwater, which can be used to indirectly understand the correlation between surface water and groundwater. This result is in agreement with the investigation of stream EC in Japanese by Jitousono et al. (2006) and Jitousono(2014).

In analyzing stream conductivity, cumulative distance was set to 0 at outlet culvert, with cumulative distance increasing to the upstream direction, cf. **Figure 4A** shows stream EC at corresponding locations, with the horizontal axis as distance and the vertical axis as electrical conductivity value. The different symbols represent measurement results at different times. In **Figure 7A**, the stream EC was collected before the rainy season and in **Figure 7B**, after the rainy season.

**Figure 7B** presents that the stream EC changes significantly around the river region 4 and region 5. As shown in **Figure 4A**, the slope toe of PLSL is located between the river region 4 and region 5. This phenomenon demonstrates that upstream stream conductivity increases significantly after passing the PLSL boundary and then decreases as it moves away. Take October 2018 data in **Figure 7B** for example, stream EC at the bottom edge of the river region 5 was 606 μS/cm, while stream EC at the top edge of the river region 4 increased to 1,085 μS/cm.

**Figure 7A** points out that there is another stream EC peak in the river region 5. According to the first peak, which this study pointed out in **Figure 7B** between the river regions 4 and 5, the peak of stream EC exists due to the spring water from PLSL. This evidence in **Figure 7A** indicates that there is another groundwater spring out at this location increasing stream EC. Consider the topographic features, as shown in **Figure 4A**. Thus, a supplementary on-site survey was deployed, as shown in **Figure 8**. The new identified area is the newly added LSL area for this survey. The artificial structure in the area is due to strong subsurface damage, with a highly active east ridge and clear cliff topography, as shown in **Figure 8**, with an exposed new sliding surface. Hence, additional groundwater outflow is possible. From the overall spatial change analysis results, it is seen that using the change points in conductivity can indeed elucidate whether the slope has a PLSL area or whether there is groundwater influx.

## 3.2 Relation Between Stream EC and Rainfall

To clarify the relationship between stream EC variation and rainfall, this study observed the stream EC of the watershed outlet continuously; the comparison is depicted in **Figure 9**. In **Figure 9**, the horizontal axis is time, the vertical axis is the stream EC variation, and the bar graph is daily rainfall. As shown in **Figure 9**, EC dropped significantly after rainfall events and increased afterward. The EC drop could be observed easily after continuous rainfall. According to the concept of stream EC variation response to infiltration, as shown in **Figure 1A**, the amount of infiltration water can dilute the concentration of chemical ions, and so the stream EC decreased after peak of rainfall intensity. After the end of rainfall events, the supply of river came from the slope's spring water. As the concept of stream EC variation response to groundwater, as shown in **Figure 1B**, the stream EC increased due to the spring water from groundwater. This evidence implied that the variation of stream EC could represent the amount of discharge of groundwater in a catchment indirectly.

### 3.3 Relation Between Stream EC and Ground Surface Displacement

In order to evaluate the feasibility of using EC to estimate PLSL activity, this study confirmed the relationship between EC and ground surface displacement. This study collected observational results for ground surface displacement and stream EC in the study area. The comparison is plotted as **Figure 10**. In **Figure 10**, the orange line represents the accumulative displacement amount of the GPS station.

There are two interesting phonemes shown in **Figure 10**. First, the activity of PLSL is positive with the increasing stream EC. In **Figure 10**, green number 1 indicated a steeper change of ground surface displacement, which means the activity of PLSL is faster. Coincidently, a jump of stream EC could be found at the same time. Besides, green numbers 2 and 3 also showed quickly increasing stream EC, and the cumulative displacement also reflected a minor increasing. These results implied that the sudden jump of stream EC could be used to judge the activity of PLSL indirectly. Second, the evolution of stream EC showed different rising speed after red numbers 2 and 3. According to the cumulative displacement, the PLSL was changed to more active after the time point of red number 2. This study considered that the high activity of PLSL might change the pattern of groundwater flow and resulted in a decrease of spring water from the groundwater system. Thus, the concentration of chemical ions in the stream after time point of red number 3 could not be supplied immediately. After the PLSL was maintained in a steady activity, which means the increasing speed of cumulative displacement remained as a fixed value, the groundwater could drain outside slope stably. Thereafter, the stream EC was also kept in a fixed range, which was 700 –800 μS/cm.

## 4 CONCLUSION

This study investigated the ZulinPLSL area exploring seasonal differences in stream conductivity over time. Spatially, EC changes along difference distance from the PLSL were analyzed. Finally, correlations between stream EC, rainfall, and ground surface displacement data were studied. The research results areas follows:

1) The study clearly determined that dry season conductivity is higher than that of wet season. During the wet season, streams are affected by rainfall and overland flow, and EC is lower. During the dry season, conductivity has a continuous upward trend due to deep groundwater continuous outflow, or because of higher proportional groundwater in the stream without rainfall, conductivity is higher.
2) In the ZulinPLSL, it was found that stream conductivity near the PLSL is higher, and stream conductivity upstream and downstream have a downward trend. Moreover, in light of differences in stream conductivity, it can be inferred that there are two groundwater springs or groundwater sources in this area.
3) This study explored relationships between cumulative rainfall, cumulative surface displacement, and EC. Based on the results, the cumulative rainfall and cumulative surface displacement have the same trends as the conductivity rise and drop-stop slope sections.
4) In accordance with the aforementioned research and analysis, measuring stream EC to estimate the activity of PLSL is effective. Hydrological changes and cumulative surface displacements can be elicited from long-term conductivity changes indirectly elucidating the activity level of PLSLs, which could serve as one of the monitoring indicators.
5) Since there are no existing drillings in the study area, continuous groundwater level data could not be obtained. It is suggested that the study area be drilled for further exploring relationships between groundwater level changes, groundwater level flow changes, and EC, which will be significantly useful for predicting occurrence of LSLs.
6) The results of this study implied a potential application for the monitoring of PLSL activity. By the investigation of temporal and spatial stream EC variation, the optimal location for automatic stream EC observation is the outlet point of catchment. The base line of stream EC can be estimated by the recording data in dry season. If there is any abnormal increasing stream EC, it is implied that the PLSL becomes active. This study is a pioneer research, and we expect to advance it in the following study.

## DATA AVAILABILITY STATEMENT

The original contributions presented in the study are included in the article/Supplementary Material; further inquiries can be directed to the corresponding author.

## AUTHOR CONTRIBUTIONS

Conceptualization, Y-JT; methodology, Y-JC, C-HW, K-AH, and W-LL; formal analysis, Y-JC, C-HW, and K-AH; Y-JT, F-TS, and W-LL wrote the manuscript, and all authors contributed to improving the paper. All authors have read and agreed to the published version of the manuscript.

## REFERENCES

Celia, M. A., and Binning, P. (1992). A Mass Conservative Numerical Solution for Two-phase Flow in Porous media with Application to Unsaturated Flow. *Water Resour. Res.*28 (10), 2819–2828. doi:10.1029/92wr01488

Chigira, M. (2014). "Geological and Topographic Detection of Dangerous Slopes on Large Scale Landslides," in Abstract for the 63th annual meeting of SABO Society. Tokyo, Japan, 2014.

Jitousono, T., Shimokawa, E., and Teramoto, Y. (2006). Potnetial Site Prediction of Deep-Seated Landslide on the Western Flank of Mt. Yahazu-Dake, Izumi City, Kagoshima Prefecture, Japan. *J. Jpn. Soc. Erosion Control. Eng.*59 (2), 5–12.

Jitousono, T. (2014). Site Prediction of Potential Deep-Seated Landslides by Using Electric Conductivity of Mountain Stream Water. *J. Jpn. Soc. Erosion Control. Eng.*6 (6), 56–59.

Kirschbaum, D., and Stanley, T. (2018). Satellite-Based Assessment of Rainfall-Triggered Landslide Hazard for Situational Awareness. *Earth's Future*6, 505–523. doi:10.1002/2017EF000715

Lee, W.-L., Tai, Y.-C., Shieh, C.-L., Miyamoto, K., and Lin, Y.-F. (2019). Hydro-mechanical Response with Respect to the Air Ventilation for Water Filtration in Homogeneous Soil. *J. Mt. Sci.*16 (11), 2562–2576. doi:10.1007/s11629-019-5643-0

Lin, C. W., Yi, D. C., and Huang, M. L. (2012). Digital Terrain from Airborne LiDAR—An Effective Tool for Seeking Potential Large-Scale Landslides. *Geo Topic*31, 44–48.

Mantovani, F., Pasuto, A., Silvano, S., and Zannoni, A. (2000). Collecting Data to Define Future hazard Scenarios of the Tessina Landslide. *Int. J. Appl. Earth Observation Geoinformation*2 (1), 33–40. doi:10.1016/s0303-2434(00)85024-2

Marui, H. (2017). "Mitigation of Natural Hazards in Mountain Watersheds of Japan," in *Ecosystem Services of Headwater Catchments* (Cham: Springer), 89–103. doi:10.1007/978-3-319-57946-7_10

Miyamoto, K., and Imaizumi, F. (2012). "A Theoretical Explanation of Triggering Condition of Deep-Seated Landslide," in Proceedings of 3rd International Workshop on Multimodal Sediment Disasters, A-5, Takayama city, Japan, September, 2012, 1–8.

Ray, R. L., and Jacobs, J. M. (2007). Relationships Among Remotely Sensed Soil Moisture, Precipitation and Landslide Events. *Nat. Hazards*43, 211–222. doi:10.1007/s11069-006-9095-9

Stanley, T., and Kirschbaum, D. B. (2017). A Heuristic Approach to Global Landslide Susceptibility Mapping. *Nat. Hazards*87, 145–164. doi:10.1007/s11069-017-2757-y

Terzaghi, K. (1943). *Theoretical Soil Mechanics*. New York: John Wiley & Sons, 11–15.

Trigo, R. M., Zêzere, J. L., Rodrigues, M. L., and Trigo, I. F. (2005). The Influence of the North Atlantic Oscillation on Rainfall Triggering of Landslides Near Lisbon. *Nat. Hazards*36 (3), 331–354. doi:10.1007/s11069-005-1709-0

Van Asch, T. W. J., Buma, J., and Van Beek, L. P. H. (1999). A View on Some Hydrological Triggering Systems in Landslides. *Geomorphology*30, 25–32. doi:10.1016/s0169-555x(99)00042-2

Wei, Z.-l., Lü, Q., Sun, H.-y., and Shang, Y.-q. (2019). Estimating the Rainfall Threshold of a Deep-Seated Landslide by Integrating Models for Predicting the Groundwater Level and Stability Analysis of the Slope. *Eng. Geology.*253, 14–26. doi:10.1016/j.enggeo.2019.02.026

Wei, Z.-l., Wang, D.-f., Sun, H.-y., and Yan, X. (2020). Comparison of a Physical Model and Phenomenological Model to Forecast Groundwater Levels in a Rainfall-Induced Deep-Seated Landslide. *J. Hydrol.*586, 124894. doi:10.1016/j.jhydrol.2020.124894

Weng, C. H., Tsai, Y. J., Shieh, C. L., and Egusa, T. (2018). "Study on Correlation of Electrical Conductivity and Potential Large-Scale Landslide in Taiwan," in 2018 Symposium Proceedings of the INTERPRAENENT, 2018 in the Pacific Rim, Toyama, Japan, October 2018, 110–116.

**Conflict of Interest:** The authors declare that the research was conducted in the absence of any commercial or financial relationships that could be construed as a potential conflict of interest.

**Publisher's Note:** All claims expressed in this article are solely those of the authors and do not necessarily represent those of their affiliated organizations, or those of the publisher, the editors, and the reviewers. Any product that may be evaluated in this article, or claim that may be made by its manufacturer, is not guaranteed or endorsed by the publisher.

frontiers in Earth Science

ORIGINAL RESEARCH
published: 23 March 2022
doi: 10.3389/feart.2021.769061

# Generation and Subsequent Transport of Landslide-driven Large Woody Debris Induced by the 2018 Hokkaido Eastern Iburi Earthquake

*Takashi Koi*[1]*, *Norifumi Hotta*[2], *Yasutaka Tanaka*[1] and *Shin'ya Katsura*[1,3]

[1]Center for Natural Hazards Research, Hokkaido University, Sapporo, Japan, [2]Graduate School of Agricultural and Life Science, The University of Tokyo, Tokyo, Japan, [3]Research Faculty of Agriculture, Hokkaido University, Sapporo, Japan

The earthquake that occurred on 6 September 2018, in the eastern part of the Iburi region of Hokkaido, Japan (the Hokkaido Eastern Iburi Earthquake) caused thousands of shallow landslides in mountain areas. In areas where many landslides occurred, the trees on the slope became large woody debris (LWD) and were supplied to the catchment. Understanding the properties of LWD during the earthquake and its subsequent movement after the earthquake are important to manage the produced LWD and implement disaster prevention measures. This study evaluates the risk of future LWD disasters based on the sequence of LWD generation, its spatial distribution, and LWD relocation linked to temporal fluctuations in rainfall events. The study site is the upper Habiu River catchment (0.37 $km^2$), where multiple shallow earthquake-related landslides occurred. Orthophotos and elevation data acquired before and after the earthquake were used to detect the properties of LWD. To evaluate the risk of an LWD disaster, we examined the correspondence between the hydraulic quantities, including the precipitation for 2 years after the earthquake and the water depth. It was estimated that approximately 7,000 LWD pieces (9,119 $m^3$ $km^{-2}$) were produced during the earthquake. Orthophoto interpretations indicate that over 80% of the LWD produced at the time of the landslide moved from the slope to the channel accompanied by the landslide debris; some of that then flowed down, accumulated, and formed logjams. In the river channel approximately two years after the earthquake, the destruction of logjams and the clear and drastic movement of LWD could not be confirmed. In this catchment, the uneven LWD distribution and the formation of logjams were fixed almost immediately after the landslide at the time of the earthquake; these characteristics are important when considering future actions. The water depth evaluation based on the difference in the excess return period indicate that the degree of risk differs depending on the deposition location in the channel. This suggests that not all LWD in the catchment are dangerous and that a risk assessment focusing on the LWD location can be effective. This study also makes it possible to determine high priority areas for LWD treatment.

**Keywords: large woody debris, shallow landslide, catchment management, disaster mitigation, risk assesment, the 2018 Hokkaido Eastern Iburi earthquake**

OPEN ACCESS

***Edited by:***
*Chong Xu,*
*Ministry of Emergency Management, China*

***Reviewed by:***
*Qiang Zou,*
*Institute of Mountain Hazards and Environment (CAS), China*
*Qingxiang Meng,*
*Hohai University, China*
*Xiaoyi Shao,*
*China Earthquake Administration, China*

***Correspondence:**
*Takashi Koi*
*koi@cen.agr.hokudai.ac.jp*

***Specialty section:***
*This article was submitted to Geohazards and Georisks, a section of the journal Frontiers in Earth Science*

***Received:*** *01 September 2021*
***Accepted:*** *31 December 2021*
***Published:*** *23 March 2022*

***Citation:***
*Koi T, Hotta N, Tanaka Y and Katsura S (2022) Generation and Subsequent Transport of Landslide-driven Large Woody Debris Induced by the 2018 Hokkaido Eastern Iburi Earthquake. Front. Earth Sci. 9:769061. doi: 10.3389/feart.2021.769061*

## INTRODUCTION

In Japan, the current amount of forest accumulation is close to three times that of approximately 50 years ago due to increase of old-growth forests (MAFF, 2018). In mountain areas, large woody debris (LWD) produced by landslides and stream bank erosion, primarily during heavy rainfall events, may flow downstream along with landslide debris or as instream LWD transport during subsequent large flooding events, sometimes with disastrous effects (Ruiz-Villanueva et al., 2014; Lucía et al., 2015; Comiti et al., 2016; De Cicco et al., 2018; Mazzorana et al., 2018). In Japan, LWD generated in the Yosasa River Basin in 1998 blocked bridges in the downstream area and caused widespread flooding (Minami et al., 2000) and, in 2018, a large amount of LWD from a landslide area flowed downstream during a heavy rainfall event in northern Kyushu (Marutani et al., 2017; Moriya et al., 2018).

LWD produced with landslides can be induced not only by heavy rainfall but also by earthquakes. Landslide-driven LWD induced by earthquakes is not expected to move long distances, unlike LWD induced during heavy rainfall events; instead, the LWD remains with the landslide debris and sometimes forms logjam in the catchment. Even though it is unlikely that LWD will cause direct damage in downstream areas during an earthquake, there is a risk that new LWD deposition in the drainage area will float and be transported long distances during subsequent rainfall events. In headwater streams, LWD deposited at river channels has been reported to have moved over the course of a few years (Wohl and Goode, 2008; Dixon and Sear, 2014).

However, the formation of logjams in river channels plays an important role in the formation of the river morphology and ecosystems (Abbe and Montgomery, 1996; Piégay and Gurnell, 1997; Sear et al., 2010) and sediment is accumulated on the upstream side of LWD in river channels, forming step and pool structures (Nakamura and Swanson, 1993; Thompson, 1995; Abe and Nakamura, 1996). LWD captures litter, providing an appropriate environment for aquatic life (Speaker et al., 1984). The formation of step and pool structures and the retention of particle organic matter by LWD improves the growth of fish (Fausch and Northcote, 1992; Riley and Fausch, 1995). In addition, fallen trees in the river channel themselves serve as a source of particle organic matter for mountain streams (Ward and Aumen, 1986). Therefore, removing LWD drastically changes the river morphology and affects fish habitats (Smith et al., 1993; Abe and Nakamura, 1999).

The Intergovernmental Panel on Climate Change (IPCC) reported that, in mid-latitudes of the Northern Hemisphere (30–60°N), where Japan is located, the frequency of heavy precipitation events has increased over the past century (IPCC, 2014). Therefore, in the future, it is expected that a large amount of LWD will be generated and that the relocation of LWD in river channels will become significant during large-scale events. If there is no risk of a large amount of the LWD flowing downstream, it is preferable that the LWD remain in the basin for a long period of time to enable the formation of mountain stream ecosystems. Understanding the LWD production volume, deposition location, and patterns during an earthquake and its subsequent transport after an earthquake are important to properly manage the produced LWD and implement disaster prevention measures.

The earthquake that occurred on 6 September 2018, in the eastern part of the Iburi region of Hokkaido, Japan (the Hokkaido

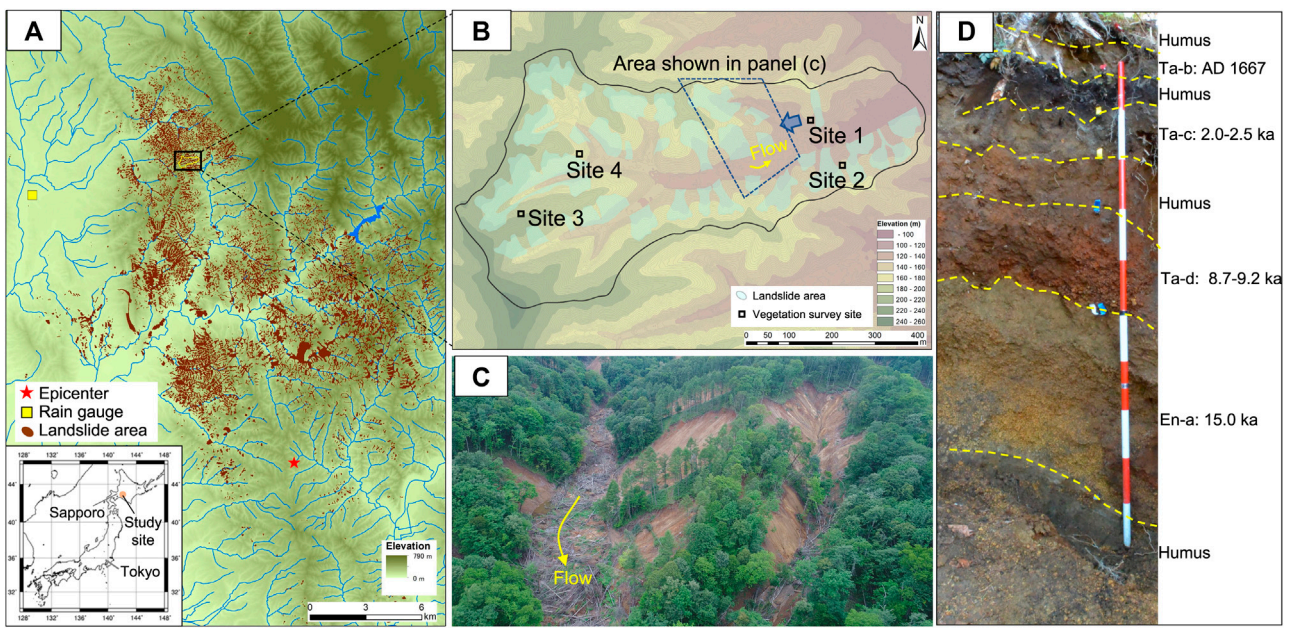


**FIGURE 1 |** Study site description. **(A)** Landslide distribution induced by the 2018 Hokkaido Eastern Iburi Earthquake. **(B)** Drainage of the study site. **(C)** Aerial view of the study site. **(D)** Geological structure of the study site.

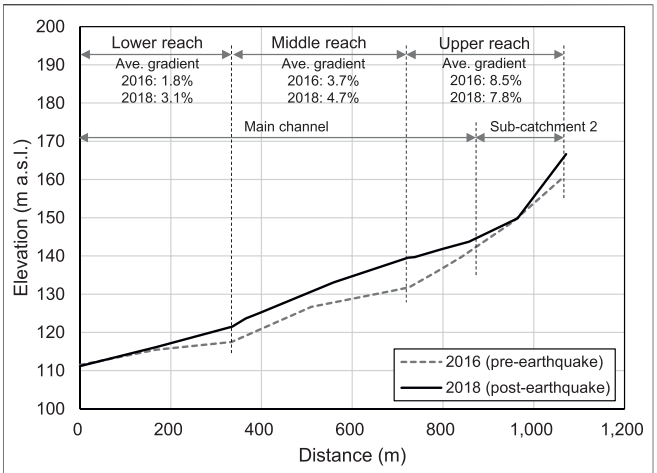


**FIGURE 2 |** Pre- and post-earthquake longitudinal profiles of the river channel Elevation is given in meters above sea level (m a.s.l.).

Eastern Iburi Earthquake, $M_{JMA}$ 6.7) caused thousands of shallow landslides over an area of 400 $km^2$ (Osanai et al., 2019; Zhao et al., 2020). In hilly areas where many landslides occurred, the trees on the slopes became driftwood associated with landslide debris, supplying an extremely large amount of LWD to the catchment. In heavy rainfall events, approximately 66% of the LWD pieces in debris flows are discharged to the catchment outlet (Ishikawa et al., 1989). However, almost all of earthquake-induced LWD is retained in the catchment because of the minimal hydraulic power. In addition, there have been few cases with large amounts of earthquake-generated LWD. Therefore, the generation of LWD by earthquakes and its subsequent movement is not well known. If a large amount of LWD remains in a catchment, as in the case after an earthquake occurrence, the future movement of the LWD may cause damage to bridges or other facilities as a result of driftwood collisions and accumulation and may aggravate flood damage in downstream areas.

This study evaluates the risk of future LWD disasters based on the sequence of LWD generation, its spatial distribution, the temporal fluctuations of rainfall events, and the accompanying relocation of LWD.

# MATERIALS AND METHODS

## Study Site

The study site is the upper Habiu River catchment (0.37 $km^2$) of the Atsuma River system (**Figure 1A,B**). The elevation of the catchment ranges from 111 m to 241 m, the channel length is approximately 1,070 m, and the average channel gradient is 5%. No artificial structures, such as check dams, have been installed in the catchment, and the entire section is a natural river channel. The average annual rainfall at the Abira station of the Automated Meteorological Data Acquisition System (AMeDAS), located approximately 8 km west of the main basin, is 1,053 mm (ranging from 449 mm to 1,615 mm). From mid-December to late March every year, the area is covered with snow. The geology of this catchment is based on Neogene sedimentary rocks, upon which multiple layers of volcanic ejecta from different events are deposited. The entire catchment is a prefectural forest managed by the Hokkaido government and made up of mature broad-leaved forests dominated by Japanese white birch (*Betula platyphylla* var. *japonica Hara*) and Japanese oak (*Quercus mongolica* var. *grosseserrata Rehder et Wilson*), as well as some planted forests of Japanese larch (*Lalix leptolepis Gordon*) and Todo fir (*Abies sachalinensis*). Even though the presence of active faults (earthquake occurrences) approximately 5,000 years ago in this region was noted in surveys of slopes, terrace strata, and river floodplain sediments, no evidence has been found to indicate a large-scale landslide event, such as that caused by the 2018 Hokkaido Eastern Iburi earthquake, for at least the last 10,000 years (Oka, 2019).

Few earthquake-induced landslides occurred near the epicenter of the 2018 Hokkaido Eastern Iburi earthquake (**Figure 1A**), with most landslides occurring in a range of 5–22 km from the epicenter (Zhang et al., 2019). The study site is located approximately 20 km northwest of the epicenter, where shallow landslides were particularly concentrated (**Figure 1A,B**). Because volcanic ejecta is thickly deposited in the areas where many landslides occurred and the distribution of the landslide areas is highly consistent with the distribution of volcanic ejecta, the deposition of volcanic ejecta is thought to be the most important element related to landslide occurrences (Li et al., 2020). At the study site, thick volcanic ejecta from the Shikotsu caldera area is deposited from the surface to a depth of approximately 2 m (**Figure 1D**). Even though a volcanic ejecta layer originating from Mt. Tarumae (Ta-d) has been observed as being a slide surface for landslides in other areas (Zhang et al., 2019; Li et al., 2020), the volcanic ejecta layer that became the slide surface in the study area is a pumice layer (En-a) with a thickness of approximately 80 cm that was ejected from Mt. Eniwa 15,000 years ago. Three layers of volcanic ejecta (Ta-b, c, d) from Mt. Tarumae, which is also a volcano near the Shikotsu caldera, are deposited above En-a (**Figure 1D**). Therefore, the landslide debris produced from the landslide slopes was composed of volcanic ejecta with a maximum grain size of 1–2 cm or less, with almost no coarse gravel with larger grain sizes. According to a survey conducted after the earthquake, the grain size distribution of En-a is 4% gravel, approximately 50% sand, and approximately 40% silt, with the remainder being clay with a 50% grain size of approximately 0.1 mm (Osanai et al., 2019).

## Data Acquisition

It is possible to acquire LWD information from orthophoto images acquired using unmanned aerial vehicles (UAVs) (Tsunetaka et al., 2021). Aerial photographs and elevation data after the earthquake were acquired twice, immediately after the earthquake (15 September 2018) and approximately 2 years after the earthquake (20 October 2020). These data were used to obtain topographic information and to detect LWD generation, movement, deposition during the earthquake, and subsequent movement after the earthquake. Elevation data prior to the earthquake were also acquired on 1 October 2016. The 2016

**TABLE 1 |** Summary of the characteristics of the three reaches.

| | Main channel Sub-catachments | Drainage area [km$^2$] | Chennel length [m] | Averagee bankfull width [m] | Average gradinet [%] | Landslide area [m$^2$] | Landslide ratio [%] | Vegetation type |
|---|---|---|---|---|---|---|---|---|
| Upper reach | Sub-catachment-1 | 0.04 | 164 | 15 | 12.3 | 17,760 | 41 | Hardwood forest Coniferous forest(plantation) |
| | Sub-catachment-2 | 0.05 | 214 | 12 | 10.7 | 19,042 | 42 | Hardwood forest |
| | Sub-catachment-3 | 0.08 | 356 | 17 | 7.7 | 13,693 | 17 | Hardwood forest |
| | Sub-catachment-4 | 0.02 | 95 | 19 | 10.0 | 8,633 | 36 | Hardwood forest |
| | Main channel | 0.01 | 173 | 26 | 3.1 | 631 | 5 | Hardwood forest |
| Middle reach | Sub-catachment-5 | 0.03 | 131 | 16 | 6.0 | 7,300 | 24 | Hardwood forest |
| | Main channel | 0.07 | 349 | 38 | 4.7 | 23,505 | 32 | Hardwood forest Coniferous forest(plantation) |
| Lower reach | Main channel | 0.06 | 336 | 47 | 3.1 | 19,466 | 32 | Hardwood forest Coniferous forest(plantation) |
| Entire catachment | — | 0.37 | 1,079 | — | 5.1 | 110,029 | 30 | — |

data consist of a 5-m grid digital elevation model (DEM) published by the Geospatial Information Authority of Japan (https://fgd.gsi.go.jp/download/menu.php). For the 2018 elevation data, we used a 1-m grid DEM generated from laser profiler data acquired from Hokkaido Prefecture. The 2020 data consist of orthoimage data created using structure from motion technology incorporating photographic UAV (DJI Phantom 4 RTK)-acquired image data, which consist of overlapping vertical aerial photographs.

The hourly rainfall data from 1976 to 2020 were acquired from the AMeDAS Abira station of the Japan Meteorological Agency (https://www.data.jma.go.jp/obd/stats/etrn/). This rainfall station is the closest to the study site. It was confirmed that the rainfall data at the Abira station were more consistent with the storage-type rainfall observation data installed near the study site than data acquired from other rainfall observation stations. Therefore, in this study, the rainfall data at the Abira station were used as is.

## Catchment Topography and Earthquake-Induced Landslides

The topographical information of the basin prior to and after the earthquake and the landslide areas that occurred because of the earthquake were identified using Geographic Information System (GIS) software (ArcGIS) based on the 2016 and 2018 DEMs. The landslide and river channel areas after the earthquake were determined from the contour map created from the 2018 DEM and an interpretation of the orthophoto image data; the landslide area, channel length, channel gradient, and river channel width were then calculated.

The catchment was divided into three categories, the upper, middle, and lower reaches, based on the main channel gradient of the topography prior to the earthquake (i.e., the 2016 elevation data; **Figure 2**). Based on the flow path automatically generated via a topographical analysis by ArcGIS, four sub-catchments were set in the upper reach and one sub-catchment was set in the middle reach, Sub-catchment 2, which has the longest channel length, was treated as the main channel (**Figure 2** and **Table 1**). The landslide area was modeled by interpreting the 2018 and 2020 orthophoto images and creating polygons.

## LWD Properties Associated With the Earthquake

At the study site, LWD generated during the earthquake was left *in situ* without being artificially removed and no planting was carried out on the landslide slopes (**Figure 1C**). The LWD generation during the earthquake and its location for the next approximately 2 years were identified by conducting a field survey, interpreting orthophoto image data, and performing topographical analyses using multiple elevation data. Because branches and leaves remain with the LWD pieces generated during the earthquake and it is difficult to automate the LWD identification, the number of LWD pieces was measured visually by interpreting the orthophoto images, creating a polyline for each LWD piece, and counting the number of polylines on the GIS. The identified LWD pieces were counted based on only their main trunk, not their branches. There are few shadows in the orthophoto images, and the number of LWD pieces was obtained with high accuracy, except in the logjam regions and areas with buried trees; however, all "visible" pieces were identified.

The position and number of LWD pieces generated during the earthquake were separated into slope and river channel categories using the orthophoto image acquired on 20 October 2020. The orthophoto image was created using Structure from Motion software (Pix4D Mapper). The created orthophoto image was read into ArcGIS, the number of LWD pieces was counted, and the LWD lengths were determined. To identify the LWD pieces generated during the earthquake with higher accuracy, we used a 2020 orthophoto image that was taken from a relatively low altitude (height above ground level of 110 m) and has a relatively high resolution; at this time, the leaves had fallen as a result of the death of the driftwood, making it easy to identify the trunks. The 2018 orthophoto image acquired immediately after the

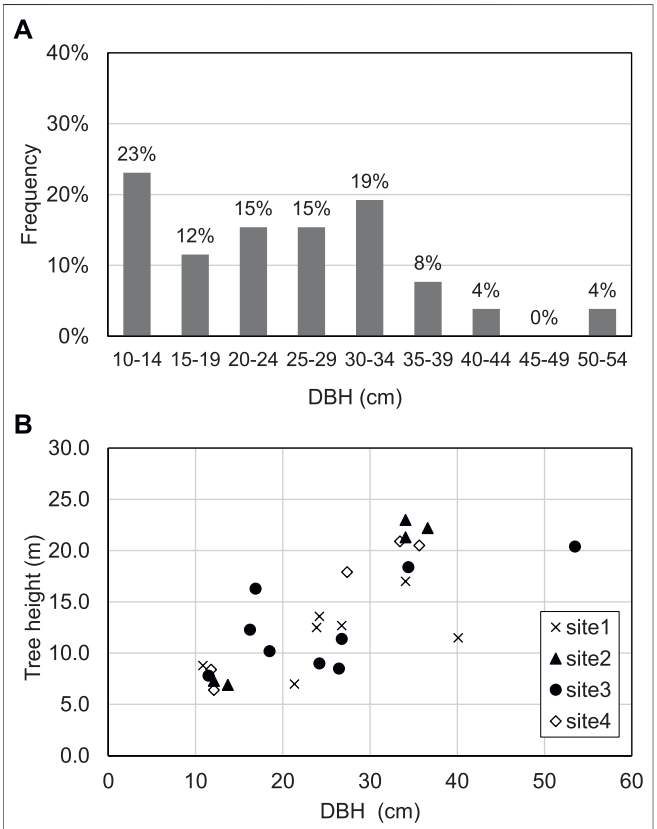


**FIGURE 3 |** Relationship between the diameter at breast height (DBH) of the standing trees and **(A)** the frequency and **(B)** the tree height.

earthquake was used as a supplement. The change in the LWD position after the earthquake was confirmed by comparing the orthophoto image data from 2018 to 2020.

The number and volume of LWD pieces produced by the landslides were estimated by multiplying the standing tree density and the trunk volume obtained from a vegetation survey by the individual landslide areas. The vegetation survey was conducted at four plots (10 m × 10 m) with different tree species and slope orientations: a south-facing slope (broad-leaved forest) and a north-facing slope (plantation coniferous forest) in the downstream area and a south-facing slope (broad-leaved forest) and a north-facing slope (broad-leaved forest) in the upstream area (**Figure 1B**). The vegetation survey targeted standing trees with a diameter at breast height (DBH) of 10 cm or more, which are generally treated as LWD. From the vegetation survey, trees with a DBH of 30 cm or more (maximum 53 cm) accounted for the largest proportion at 35%, followed by DBHs of 10–14 cm at 23% (**Figure 3A**). The height of the standing trees with a DBH of 30 cm or more was approximately 20 m (**Figure 3B**).

The forest stand density was calculated after dividing the region into broad-leaved, coniferous (plantation), and mixed forests according to the vegetation prior to the earthquake; the densities of these sub-regions were 0.07 trees $m^{-2}$, 0.05 trees $m^{-2}$, and 0.06 trees $m^{-2}$, respectively. The density of the standing trees in the mixed forests was the average value of those in the broad-leaved and coniferous forests. The trunk volume was estimated from the DBH and the tree height. The vegetation map published by the Ministry of the Environment was used to determine the vegetation distribution in the basin.

## Hydraulic Values

To evaluate the risk of driftwood disasters, we compared the correspondence between the LWD relocation and the hydraulic quantities, such as the precipitation, peak discharge, and normal flow depth, for the approximately 2-year period following the earthquake. Because the entire channel section is a natural river channel and the presence of boulders cannot be confirmed, the influence of obstacles was not considered.

To determine the hydrological record for the 2 years following the earthquake, the peak discharge was calculated after extracting rainfall amounts of over 5 mm in 24 h. There were 72 extracted events in total. Rainfall during snowfall events was excluded. The return periods (2, 10, 20, 50, and 100 years) of the 1-h and 24-h rainfall were calculated using software for statistical analyses of hydrological data (Hydrological Statistics Utility version 1.5), developed by the Japan Institute of Country-ology and Engineering (JICE), and were estimated from the most compatible distributions, i.e., the Gumbel and square-root exponential-type distributions of the maximum, respectively, using the yearly maximum 1-h and 24-h rainfall from 1976 to 2020. Then, the magnitude of the rainfall events experienced during the 2 years was evaluated by comparing the rainfall record with the rainfall of the *n*-year return period.

Whether or not an LWD piece moves is determined by the drag and friction forces acting on each piece (e.g., Braudrick and Grant, 2000). However, water is significantly involved as a condition for LWD to float and flow, and the magnitude relationship between the water depth and the log diameter is important for log float and flow (Haga et al., 2006; Ruiz-Villanueva et al., 2019). In particular, the necessary condition for a log to travel a long distance occurs when the water depth at the peak discharge is greater than the log diameter (Haga et al., 2002; Haga et al., 2006). Therefore, this study focused on the normal-flow depth at peak discharge as the movement condition for an LWD piece.

Various methods for estimating the peak discharge have been proposed, and the rational formula (e.g., Kadoya and Fukushima, 1976; Hotchkiss and Mccallum, 1995) can estimate the peak discharge from the rainfall record even if a hydrograph is not obtained. This formula is also applicable to small watersheds, such as that of the study site, because it does not consider the influence of the catchment area or the distribution of the rainfall intensity. In this study, the peak discharge ($Q_p$ in $m^3\ s^{-1}$) during a flood event was determined using the rational formula:

$$Q_p = \frac{1}{3.6} C_f R_e A, \tag{1}$$

where $C_f$ is the non-dimensional runoff coefficient, $R_e$ is the effective rainfall intensity [mm $h^{-1}$], and $A$ is the drainage area [$km^2$]. In this study, considering that this catchment is a volcanic area and that the slopes were covered with forest but landslides occurred over

approximately 30% of the entire area, $C_f$ was set to 0.45 according to the standard for the Hokkaido Prefecture. The $C_f$ value changes depending on the surface conditions of a catchment, and it is reported to be approximately 0.35–0.45 in the forests of Japan (Kadoya, 1988). Considering that this study site is covered by forest with many bared landslide areas, $C_f$ = 0.45 is a reasonable value. Discharge during snowmelt was not included.

The normal-flow depth was calculated as an index related to the movement of the driftwood. Here, because the channel gradient and bankfull width differ between the main channel and the sub-catchment in each reach, the normal-flow depth ($h^*$) was calculated from the following formulas based on Manning's formula assuming that the river channel has a trapezoidal cross section (Inoue 2008):

$$h = \left(\frac{nQ}{i^{1/2}B}\right)^{3/5} \tag{2}$$

$$h^* = h\frac{\left(1 + 2\sqrt{m^2+1}\ \frac{h}{B}\right)^{2/5}}{1 + m\frac{h}{B}} \tag{3}$$

where $h$, $h^*$ is the normal flow depth [m], $Q$ is the peak discharge during a rainfall event [$m^3\ s^{-1}$], $i$ is the channel gradient, $B$ is the bankfull width [m], $n$ is Manning's roughness coefficient, and $m$ is the side-slope gradient. The peak discharge was determined by dividing the event peak flow rate by each individual drainage area (i.e., the main channel and the five sub-catchments). The $n$ value is difficult to determine uniformly because it changes significantly, even at the same point, depending on the fluvial topography, riverbed material, and changes in the water depth (Asano et al., 2012). For example, it is estimated to be 0.050–0.100 when there are very large amounts of vegetation in the floodplain (Arcement and Schneider, 1989), while it is estimated to be 0.035–0.100 in a natural river where the river width is larger than 30 m and boulders and brush are present (Chow, 1959). Even though the $n$ value of rivers with large amounts of LWD is not well known, in this study, a value of 0.070, which is generally used in natural mountain watershed rivers in Japan, was adopted.

# RESULTS

## Spatial Density of LWD Induced by the Earthquake

The total number of LWD pieces generated by the landslides during the earthquake was estimated to be 6,972, and the total volume of the LWD generated was estimated to be 3,386 $m^3$ (**Table 2**). The number of LWD pieces generated in the upper reach was the highest at 3,999, while that in the lower reach was the lowest at 1,081. In this catchment, landslides occurred at approximately the same rate throughout the entire catchment area; therefore, there was no significant difference in the number and volume of LWD pieces generated per unit area and the unit number for the entire area was estimated to be 18,435 pieces $km^{-2}$ with an estimated spatial density of 9,119 $m^3\ km^{-2}$.

In Japan, it is estimated that $10^2$–$10^4$ pieces $km^{-2}$ of LWD are induced by heavy rainfall events in comparable catchment areas (Mizuyama et al., 1985; Ishikawa et al., 1989) and the trunk volume has been estimated to be $10^1$–$10^3\ m^3\ km^{-2}$ (Ishikawa et al., 1989). Compared with these values, the number and volume of LWD pieces generated during this earthquake was significantly larger.

The number of LWD pieces deposited around the landslide slopes and in the river channel, as confirmed by the orthophoto images, was 5,733 pieces throughout the entire catchment. The number of LWD pieces deposited in the middle reach was the highest at 2,581, while it was the lowest at 926 in the lower reach (**Table 2**).

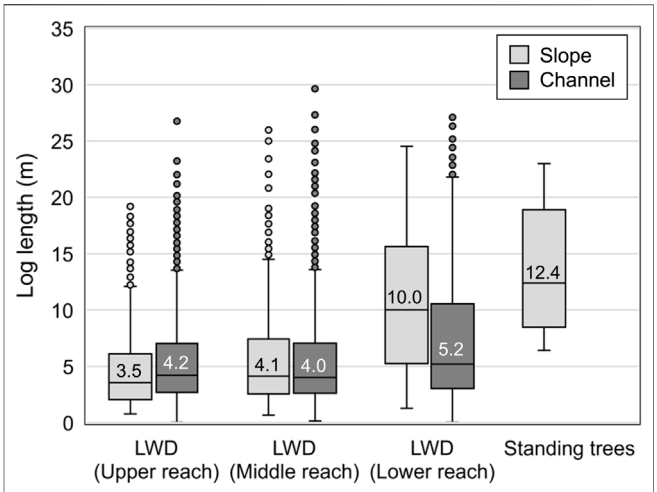


**FIGURE 4 |** Box and whisker plots of the log lengths of the large woody debris (LWD) in the three reaches based on an orthophoto interpretation and that of the standing trees based on a vegetation survey. The line within each box indicates the median value, and the box end lines indicate the 25th and 75th percentiles. The upper and lower whiskers show the maximum and minimum values, respectively, in the range of 1.5 times the median to the quartile interval. The dots indicate outliers, and the numbers indicate the median value.

**TABLE 2 |** Generation and depsition of large woody debris (LWD) within each reach.

| | Drainage area [$km^2$] | Number of generation | Specific LWD number [pieces $km^{-2}$] | Generation volume [$m^3$] | Specific LWD volume [$m^3 km^{-2}$] | Deposition number | | |
|---|---|---|---|---|---|---|---|---|
| | | | | | | Total | slope | channel |
| Upper reach | 0.21 | 3,999 | 19,434 | 1,842 | 8,952 | 2,226 | 711 | 1,511 |
| Middle reach | 0.10 | 1,892 | 18,072 | 947 | 9,042 | 2,581 | 361 | 2,220 |
| Lower reach | 0.06 | 1,081 | 17,800 | 596 | 9,813 | 926 | 203 | 723 |
| Entire area | 0.37 | 6,972 | 18,435 | 3,385 | 9,119 | 5,733 | 1,275 | 4,458 |

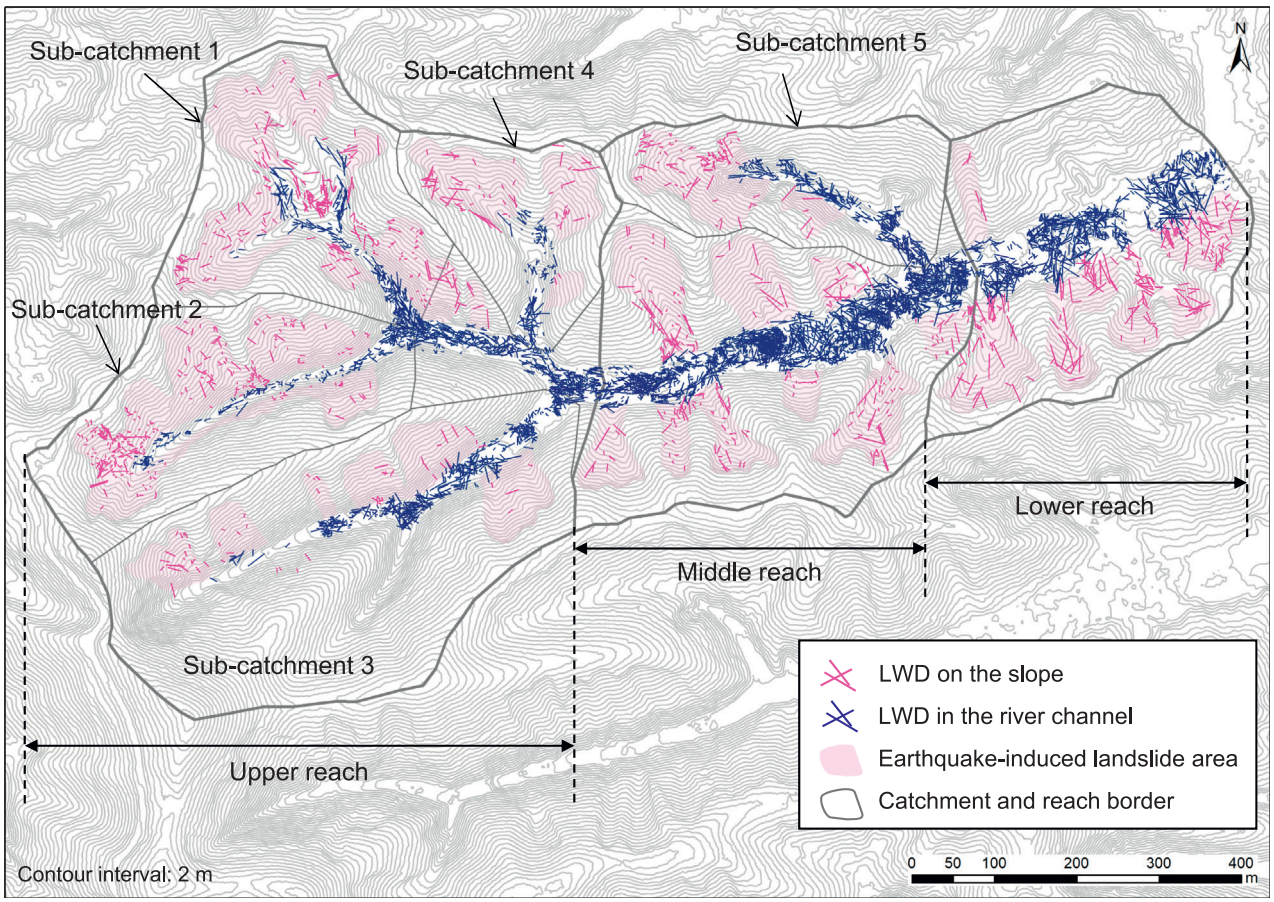


**FIGURE 5 |** Location of LWD generated as a result of the 2018 earthquake. Pink bars indicated pieces of LWD on the stope, and navy blue bars indicate pieces of LWD in the river channel. Light pink areas indicate landslide areas induced by the earthquake.

The median LWD log length was approximately 4.0 m for both the upper and middle reaches on the landslide slope and in the river channel, while for the lower reach, it was significantly longer with values of 10.0 m on the landslide slope and 5.2 m in the river channel (**Figure 4**). In particular, the LWD log length on the lower reach landslide slope was nearly in the same range as the median value (12.4 m) of the standing trees obtained from the vegetation survey.

## LWD Location and Deposition Rate

In this catchment, relatively few pieces of LWD remained on the landslide slope and the location of the LWD was unevenly distributed (**Figure 5**). Some pieces of LWD in the river channel accumulated in a complicated manner and formed logjams around the confluences of the tributaries of the upper reach and in the river channel of the middle reach. There are relatively few pieces of LWD in the upstream regions of the upper reach. Even though LWD is deposited almost evenly throughout the entire river channel in the middle reach, LWD in the lower reach is deposited at the foot of the landslide slopes and there are areas in which LWD is not deposited in the river channel.

In this study, the ratio of the number of LWD pieces deposited on slopes or in river channels to the number of LWD pieces generated at the landslide slope is defined as the LWD deposition rate ($L_{WD}DR$). The number of LWD pieces around the landslide slopes and in the river channels was 5,733 compared with the estimated number of LWD pieces of 6,972 that were generated during the earthquake, making the $L_{WD}DR$ value 82% (the $L_{WD}DR$ value of the landslide slopes was 18% and that of the river channels was 64%; **Figure 6A**). The $L_{WD}DR$ value on the landslide slopes was 18% throughout the entire catchment, which means that more than 80% of the LWD moved from the slopes to the river channels (**Figure 6A**). This tendency at the landslide slopes is similar for the three reaches (18–19%).

Conversely, the $L_{WD}DR$ values of the river channels vary longitudinally. The $L_{WD}DR$ value in the river channel for the entire catchment is 64%, which is significantly different from the values of 38% for the upper reach, 100% or more for the middle reach, and 67% for the lower reach (**Figure 6A**). An $L_{WD}DR$ value of 100% or more means that the count includes pieces of LWD produced outside the reach. The $L_{WD}DR$ values of the five sub-catchments vary widely and is relatively small compared with the reach scale (**Figure 6B**).

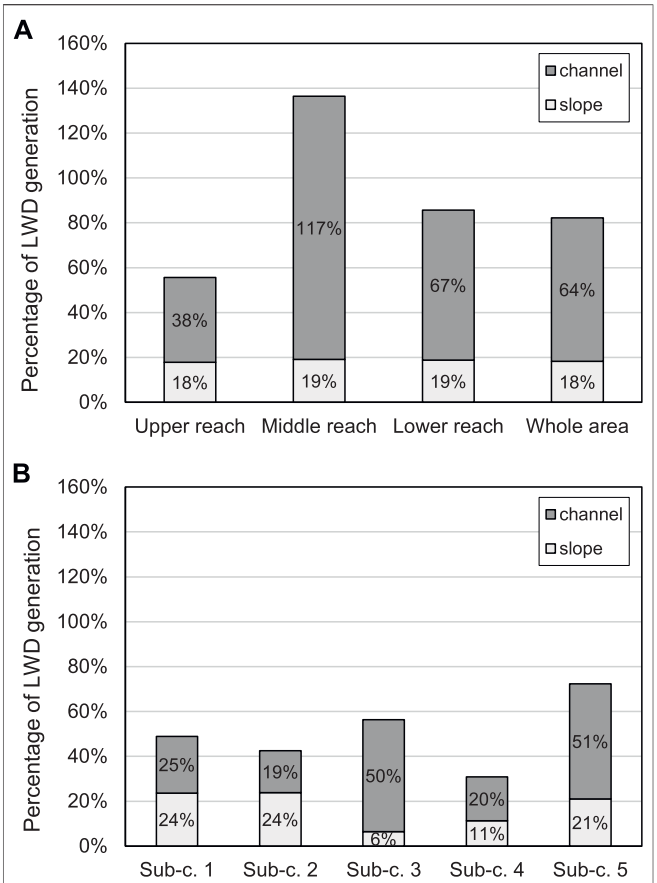


**FIGURE 6 |** Percentage of LWD genelation (LWDDR) within each **(A)** reach and **(B)** sub-catchment.

## Change in the LWD Position After the Earthquake

Comparing the LWD deposits in 2018 and 2020, no clear or drastic change in the LWD position could be confirmed throughout the entire catchment during the approximately 2 years following the earthquake, nor could any destruction of the logjams that formed longitudinally in the river channel be confirmed (**Figure 7A-C**). In the upper-reach sub-catchments, a few pieces of LWD that had deposited without forming a logjam disappeared or appeared 2 years after the earthquake. In sub-catchment 1, it was confirmed that the LWD that had accumulated in the river channel in 2018 was buried under sediment in 2020 (**Figure 8A**). In sub-catchment 2, the disappearance and new appearance (via supply from upstream or the slope) of LWD were confirmed in 2020 (**Figure 8B**). In sub-catchment 3, LWD submerged by the upstream flooding of a logjam was also confirmed (**Figure 8C**).

The above indicates that the distribution of the LWD pieces and the formation of logjams were limited to a very restricted range of the sub-catchments. The uneven distribution of the LWD deposition and the formation of logjams in the catchment were determined by the flow at the time of the landslides triggered by the earthquake, and these deposits remained as they were 2 years later with almost no relocation.

## Rainfall and Discharge Two years After the Earthquake

The hourly rainfall and 24-h rainfall of events from 6 September 2018, when the earthquake occurred, to 20 October 2020, are shown in **Figure 9**. The largest amount of rainfall during this period was 19.5 mm $h^{-1}$ (with a 24-h rainfall of 57 mm) for the 1-h rainfall on 17 August 2019, and 63 mm (with a maximum 1-h rainfall of 9.5 mm $h^{-1}$) for the 24-h rainfall on 23 September 2019. We calculated the rainfall for 2-years, 10-years, 20-years, 50-years, and 100-years return periods and compared it with the maximum value of the 1-h and 24-h rainfall in the 2 years following the earthquake. We found that all the rainfall events recorded during this period were smaller than the rainfall of the 2-years return period (**Figure 9**). Therefore, there were no high-magnitude flood events in this catchment during the 2 years following the earthquake.

A relatively large flood in the last 2 years occurred on 23 September 2019, with an estimated peak discharge of 46.8 $m^3$ $s^{-1}$; the normal flow depth is 0.06–0.07 m for the main channel and 0.02–0.04 m for the sub-catchment (**Table 3**). Pieces of LWD are removed from the riverbed (i.e., via floating) when the water depth increases and the floating limit of the LWD is exceeded (Haga et al., 2006; Ruiz-Villanueva et al., 2019). Haga et al. (2002) focused on the ratio of the $h^*$ of the water depth to the diameter of the LWD and showed that LWD travels longer distances in natural river systems when $h^*$ equals one or more. The LWD in this study is treated as having a diameter of 10 cm or more; therefore, if the water depth exceeds 10 cm, $h^*$ becomes one or more. Because the assumed normal flow depth in actual rainfall events after the earthquake is less than 10 cm, the values of $h^*$ in all three reaches did not exceed 1. The rainfall record for the 2 years following the earthquake suggests that the LWD in the study area is unlikely to float and move a long distance.

# DISCUSSION

## LWD Budget and Dynamics During the Earthquake

In this study, the LWD generated during the earthquake was examined primarily via an orthophoto image acquired in 2020. While a few pieces of the LWD in the upstream river channel were buried in sediment and flooded ponds (**Figure 7A**, **Figure 8A,C**), the LWD position did not significantly change after the earthquake, according to a comparison with the LWD position in 2018. Therefore, the LWD position in 2020 is treated as reflecting the state of production at the time of the 2018 earthquake.

The $L_{WD}$DR value of the entire catchment was estimated at 82%, and the location of the remaining 18% has not been identified. Because there appears to be almost no LWD that flowed out of the catchment, according to the field survey

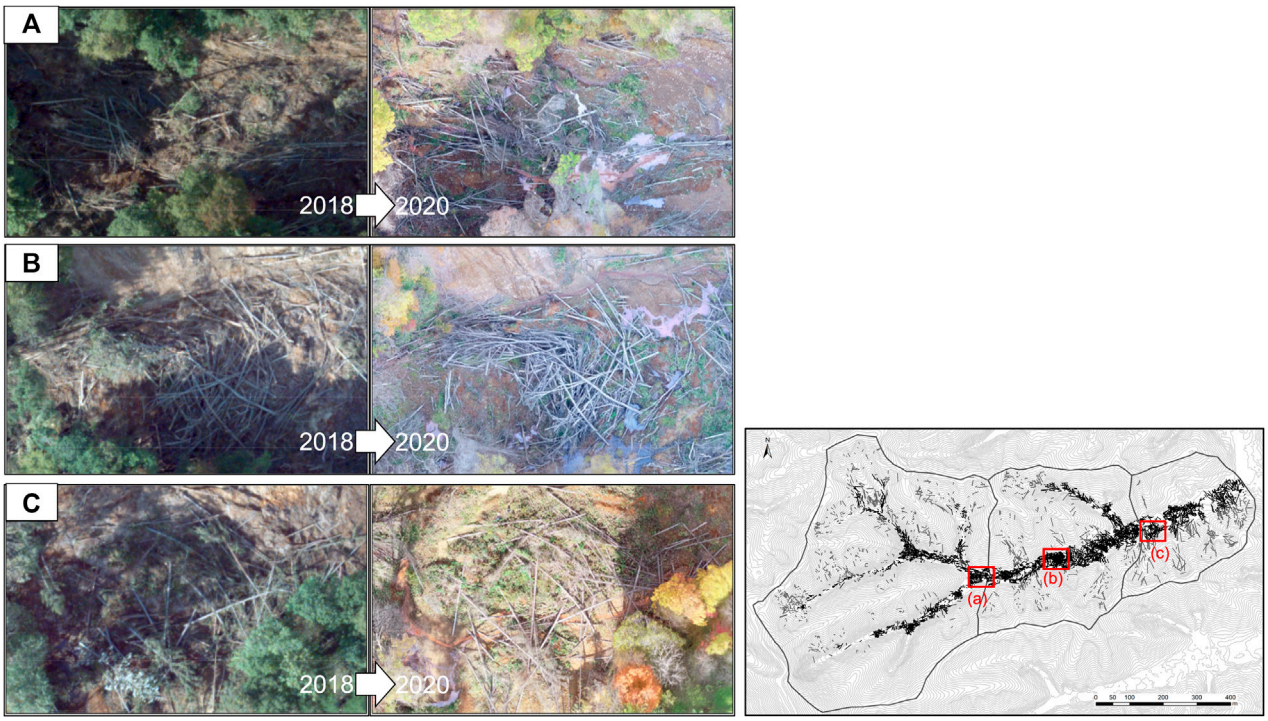


**FIGURE 7 |** Comparison of the LWD locations along the main channel in 2018 and 2020. **(A)** upper reach, **(B)** Middle reach and **(C)** lower reach.

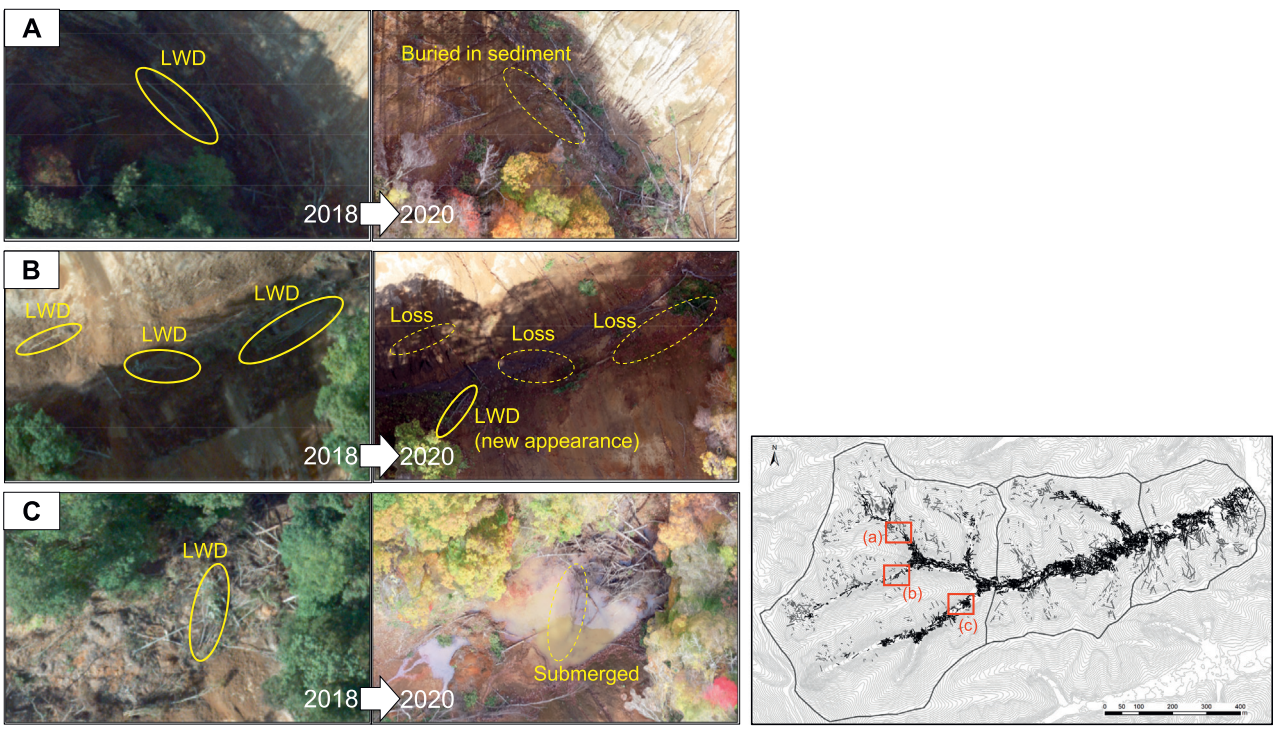


**FIGURE 8 |** Comparison of the LWD locations in the upper stream regions in 2018 and 2020. **(A)** Sub-catchment 1, **(B)** Sub-catchment 2 and **(C)** Sub-catchment 3.

**TABLE 3 |** Characteristics of the hydraulic quantities at the September 23,2019,event.

| Location | | Max.rainfall event in 2 years after the earthquake (Sep. 23,2019) | | |
|---|---|---|---|---|
| | | 24-h Rainfall [mm] | Peak discharge [$m^3$ $sec^{-1}$] | Water depth [m] |
| Upper reach | Sub-catchment 1 | | 0.16 | 0.03 |
| | Sub-catchment 2 | | 0.17 | 0.03 |
| | Sub-catchment 3 | | 0.30 | 0.04 |
| | Sub-catchment 4 | 63 | 0.09 | 0.02 |
| | Main channel | | 0.72 | 0.07 |
| Middle reach | Sub-catchment 5 | | 0.11 | 0.02 |
| | Main channel | | 1.16 | 0.06 |
| Lower reach | Main channel | | 1.39 | 0.07 |

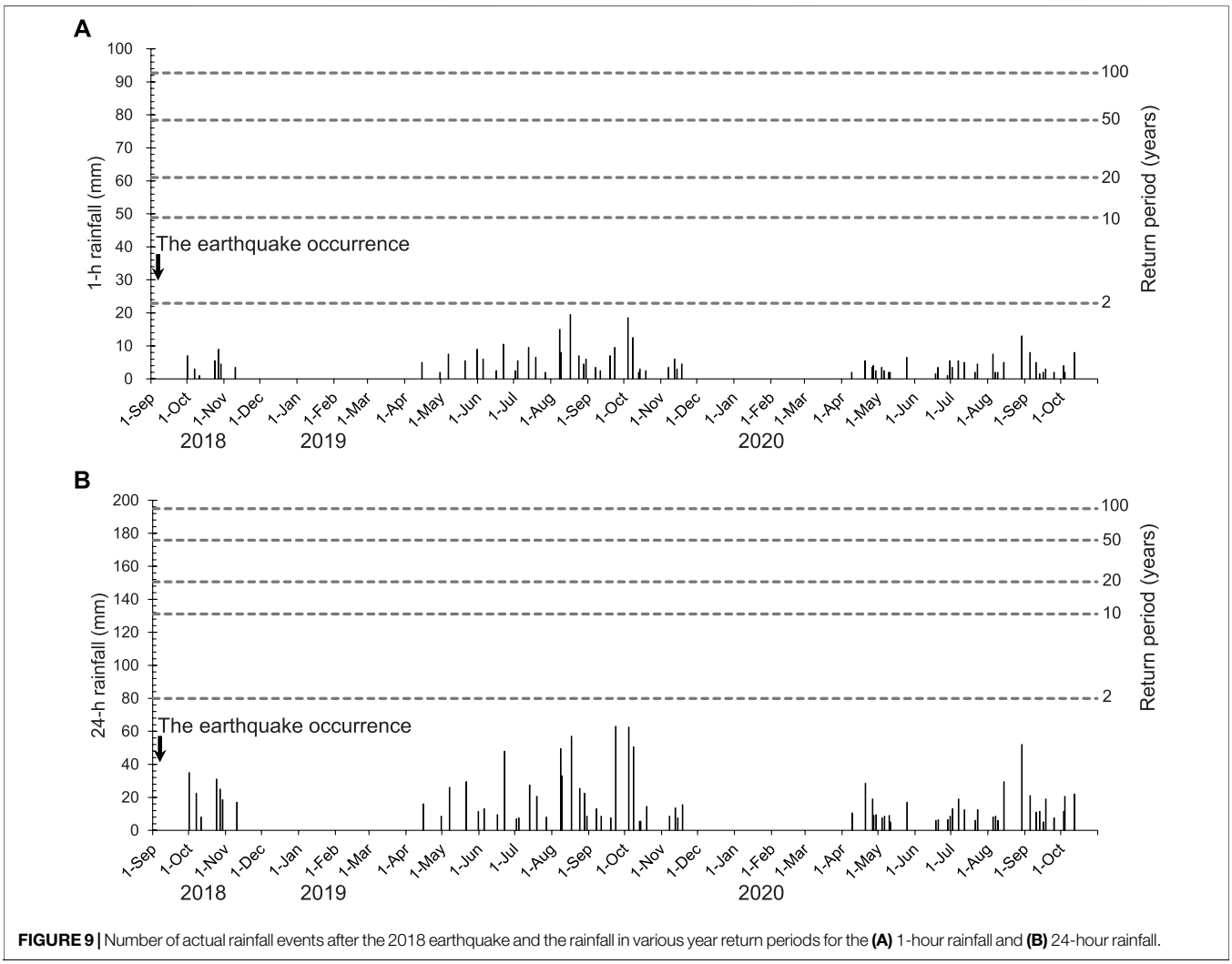


**FIGURE 9 |** Number of actual rainfall events after the 2018 earthquake and the rainfall in various year return periods for the **(A)** 1-hour rainfall and **(B)** 24-hour rainfall.

around the catchment outlet, the unknown LWD is likely present in the catchment. It may be that the LWD on the slope was not extracted because it is in the shadow of the standing trees on the edge of the landslide area; however, because there are almost no logjams or burial of LWD on the slope, the LWD can be extracted with higher accuracy on the slope than in the river channel. Here, assuming that the LWD on the slope was not overlooked, the amount of LWD deposition, having been estimated at 82%, must be the result of overlooked LWD in the river channel.

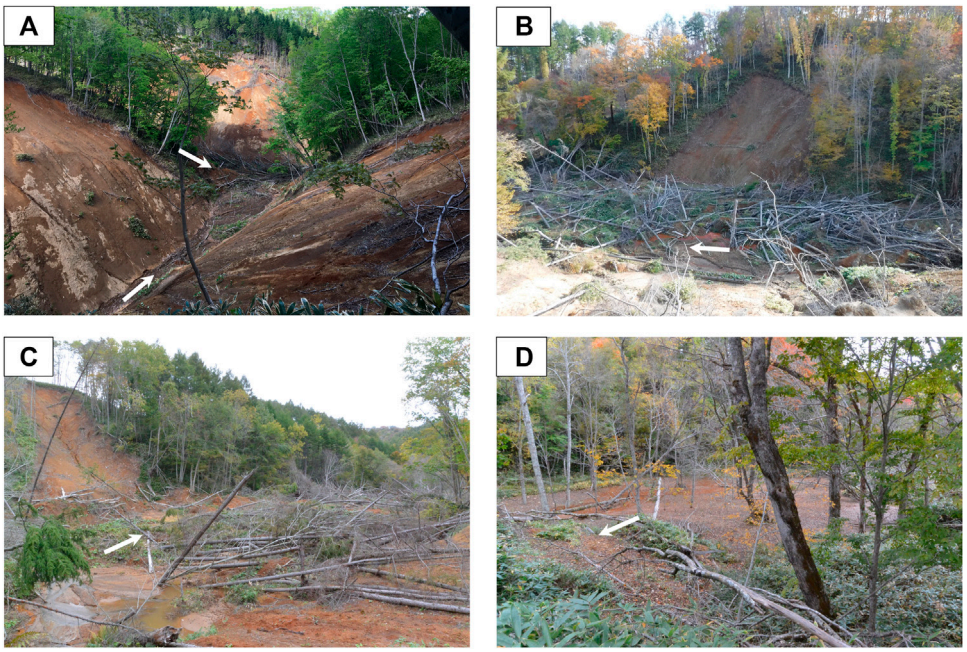


**FIGURE 10 |** Examples of instream LWD deposition after the 2018 earthquake. **(A)** Logjam at the channel junction in the upper reach (photo taken on 26 March 2021). **(B)** Logjam at the channel junction in the middle reach (photo taken on 20 October 2021). **(C)** Logjam at the channel junction in the lower reach (photo taken on 11 October 2019). **(D)** Tree stand on the channel in the lower reach (photo taken on 14 October 2020). The arrows in each photo indicate the flow direction.

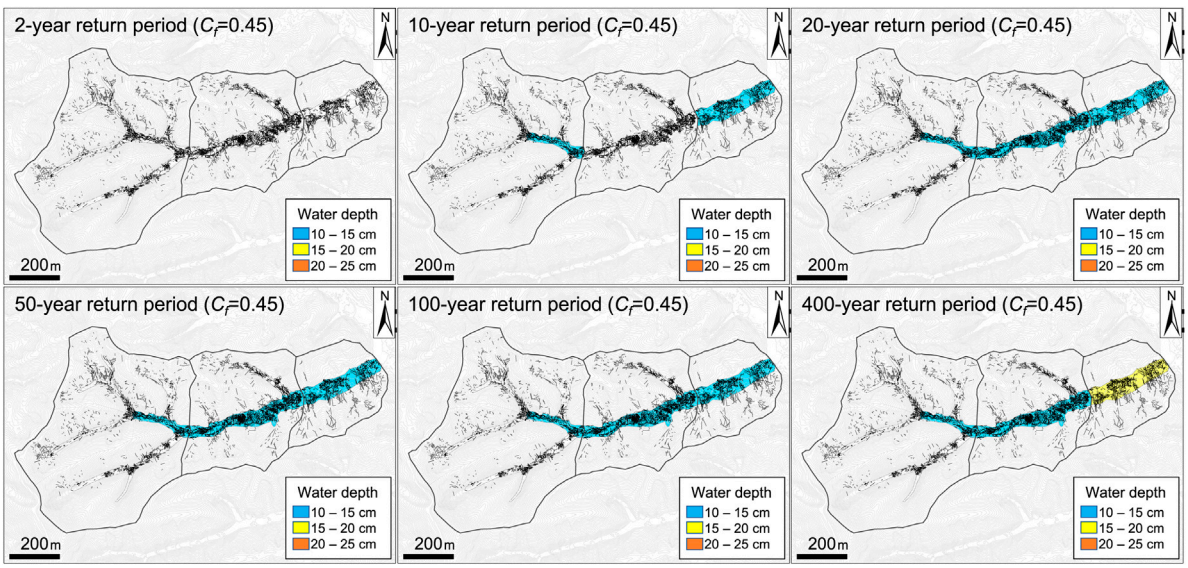


**FIGURE 11 |** Water depths for the various year return periods at the main channel and in the upper stream areas (runoff coefficient $C_f$ = 0.45).

Some of the LWD in the river channel forms logjams, and all of the pieces of LWD inside these logjams may not be discernable in aerial photographs. Especially in the middle reach, LWD is deposited forming logjams throughout the entire main river channel, regardless of the individual landslide locations. In the middle reach, the $L_{WD}DR$ value in the river channel is 117%; this value is even higher if there is no overlooked LWD. In other words, the number of LWD pieces in the middle reach is larger than the production number, suggesting that the LWD generated in the upper

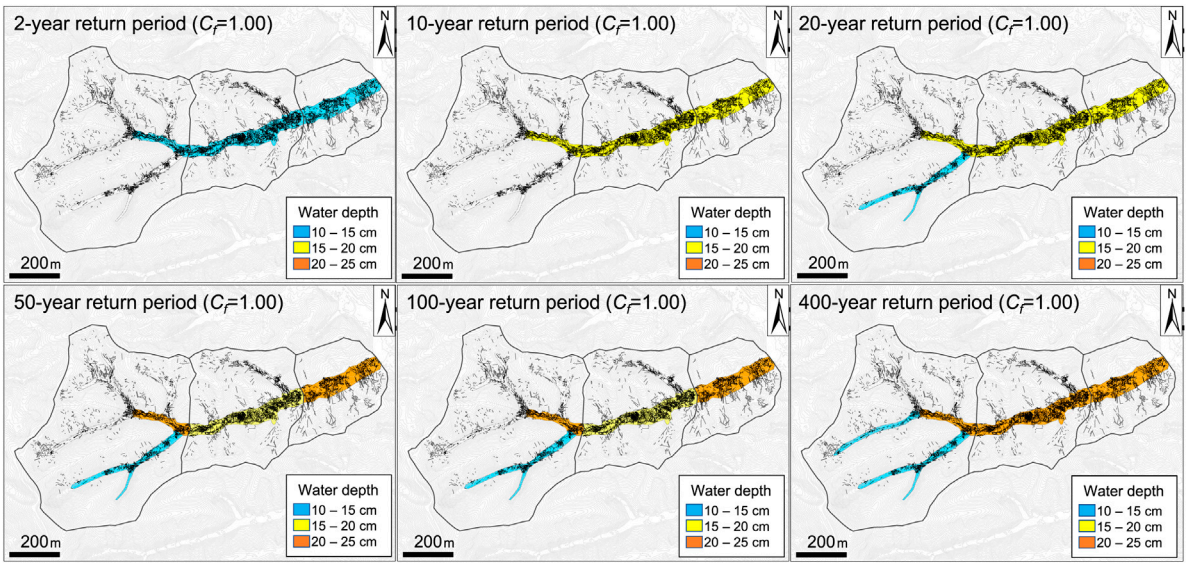


**FIGURE 12 |** Water depths for the various year return periods at the main channel and in the upper stream areas (runoff coefficient $C_f$ = 1.00).

reach flowed down through the river channel and that this LWD is included in the middle reach.

Logjams are formed by the accumulation of LWD during the process of transportation (Abbe and Montgomery, 1996). It is likely that the LWD that reached the river channel from the slope at the time of the landslides in the upper reach passed through the river channel of the steep upper reach and moved to the middle reach section, where the channel gradient is relatively gentle, and then accumulated there. This is consistent with the channel slope having become loose only in the upper reach and riverbed aggradation (up to approximately 10 m) having occurred throughout the entire middle reach section (**Figure 2**), as indicated by comparisons before and after the earthquake.

The $L_{WD}DR$ values in the four sub-catchments of the upper reach were 31–56%, and that of the middle reach was 72%, which is smaller than the $L_{WD}DR$ values of each reach scale, except for sub-catchment 3, which had an $L_{WD}DR$ value of 56% (**Figure 6**). This suggests that part of the LWD produced in each sub-catchment reached the sub-catchment outlet or exited it. Because LWD accumulates at tributary junctions and form logjams, most of the LWD that flowed downstream stopped around the tributary junction. Based on the longest channel length from the headwater to the tributary junction (sub-catchment 2), the LWD flowed up to approximately >200 m down the channel at the time of the earthquake occurrence.

The $L_{WD}DR$ value of the lower reach is 86%. The log length of the LWD in the lower reach is longer than those in the upper and middle reaches (**Figure 4**). In the upper and middle reaches, the driftwood length is relatively short because the LWD broke during the process of flowing with the landslide debris or was buried in the sediment when the flow stopped. Conversely, in the lower reach, the landslide debris was deposited almost directly under the landslide slope (**Figure 5**) and it is possible that it was not affected by damage or burial caused by the flow. Furthermore, because standing trees exist in the river channel near the catchment outlet (**Figure 10D**), it is thought that long-distance movement of landslide debris including LWD did not occur during the earthquake.

The LWD is thought to have moved up to approximately >200 m in the river channel accompanied by landslide debris in the upstream area, despite the landslides occurring without the direct involvement of rainfall. In this area, the volcanic ejecta, which is the soil layer above the sliding surface, is constantly close to saturation (Aoki et al., 2021). Soil tests conducted after the earthquake showed that the natural water content of En-a was close to the liquid limit (Osanai et al., 2019). Furthermore, the liquidity was relatively high because of the arrangement of the movement distance of the landslide debris (Osanai et al., 2019; Zhao et al., 2020). The locations and the condition of the LWD, as confirmed in this study, indicates that the landslide debris was highly fluid and moved a long distance at the time of the earthquake only in steep upper streams.

## Risk Assessment and Catchment Management After LWD Generation

One condition for moving LWD downstream is that the length of the LWD be shorter than the bankfull width (Lienkaemper and Swanson, 1987). In this catchment, the LWD log length is shorter than the width of the river channel (**Table 1** and **Figure 4**); therefore, there is a risk that the LWD will move if there is a large-scale flood in the future, transporting the LWD over long distances. We assume that the LWD moves when $h^*$ becomes one or more, based on Haga et al. (2002), and the hazard is discussed with respect to the abundance ratio of

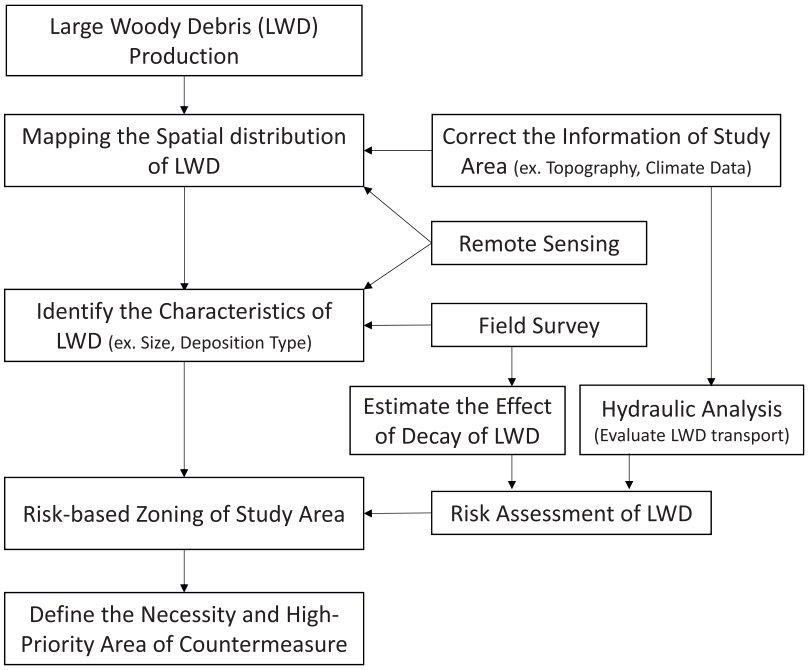


**FIGURE 13 |** Flowchart of the methodology for LWD risk assessment after a event occurrence.

the LWD, which changes according to the assumed water depth for various rainfall magnitudes.

From the comparison of the 2018 and 2020 LWD positions, the movement of the LWD could not be clearly confirmed in the actual 2-years rainfall record (<2-years return period rainfall) after the earthquake; however, the LWD is not expected to travel long distances as a result of the average rainfall that occurs during a given year. Here, we calculated the water depths of the 2-years, 10-years, 20-years, 50-years, 100-years, and 400-years return period rainfall. When there is a large amount of preceding rainfall, the soil moisture in the catchment becomes nearly saturated up to the ground surface and Horton-type surface flows occur. Because the effect of the initial loss of rainfall is small and the runoff rate is high in such a case, the water depth when the runoff coefficient ($C_f$) = 1 was also estimated.

When the water depth is evaluated under normal conditions ($C_f$ = 0.45), a water depth exceeding 10 cm was confirmed to not occur within the 2-years return period (**Figure 11**). In return periods of more than 10 years, the water depth exceeds 10 cm in the main channels, which is a condition for LWD to travel long distances. However, the maximum water depth is 15.1 cm at the lower reach in the 400-years return period and most of the maximum water depths are less than 15 cm. Even if floating occurs, it represents only approximately 23% of all the LWD (**Figure 3**) and there is no danger of movement for most of the LWD. In the five sub-catchments, it is assumed that a water depth exceeding 10 cm does not occur, even on the scale of the 400-years return period rainfall, nor does a situation in which the LWD travels a long distance.

Under the condition that the outflow rate of the catchment is high ($C_f$ = 1.00), the water depth will exceed 10 cm in all main channels, even in the 2-years return period rainfall (**Figure 12**). Furthermore, it is estimated that a water depth of 15–20 cm can be assumed on the scale of the probability of exceeding the 10-years return period rainfall and that 35% of the LWD (**Figure 3**) will move a long distance in the main channel if the LWD pieces float. If the more than 50-years return period rainfall is exceeded, the water depth will reach 20–25 cm. In this case, 50% of the LWD pieces will move a long distance if floating occurs, increasing the risk of LWD transportation. In all of the sub-catchments, the water depth exceeds 10 cm for the more than 20-years return periods but the water depth is less than 15 cm and the risk is minimal, even if LWD movement occurs.

However, even if the water depth is larger than the diameters of the LWD pieces, long-distance movement may not occur. Haga et al. (2002) pointed out that conditions in which the LWD are trapped by obstacles in the channel or buried in gravel also provide great bearing capacity for the LWD. In this catchment, logjams have formed at multiple locations along the river channel and some of the LWD is buried in gravel (**Figure 10A–C**). It is assumed that, because of the deposition and accumulation conditions of the LWD in this catchment, the LWD will not start to move even if the water depth exceeds the floating water depth limit at times of major flooding after the earthquake.

In addition, it has been found that the residence time of driftwood is 80% or more and 50 years or less, with a maximum of 1,400 years, and the longer the residence time of the LWD, the more the decay of a piece of LWD will progress (Hyatt and Naiman, 2001). The LWD supplied to the river channel is subdivided and flows downstream as it decays (Ward and Aumen, 1986; Seo et al., 2015). Even though half of the LWD pieces are expected to move along the main channel

with a rainfall event of the 400-years return period (**Figure 12**), the risk of disaster associated with this movement may be reduced as the wood pieces are subdivided via decay over time.

The LWD did not move in the actual rainfall events in the 2 years following the earthquake. However, some pieces of LWD will likely move during rainfall events with return periods of more than 10 years and it is assumed that there is a risk that this will cause a disaster. However, the risk is smaller in the sub-catchment of the upper stream than in those of the mainstream. In other words, not all LWD in the catchment is uniformly dangerous. A method for assessing the risk associated with LWD at the catchment scale after LWD generation is shown in **Figure 13**. The risk is related to where and how far the LWD was transported and deposited after the landslide occurrence; therefore, risk assessments focusing on these characteristics could be effective. In addition, LWD may decay over time, reducing the disaster risk. These facts indicate that, in disaster risk assessments after LWD generation, it is necessary to examine the spatial distribution of the LWD, including logjams, and to perform zoning according to the degree of risk. These zoning results can then be used to determine locations with a higher priority for countermeasures.

## CONCLUSION

We examined the LWD production, movement, and deposition from landslides generated by the 2018 Hokkaido Eastern Iburi Earthquake and evaluated the future risks associated with LWD movement. Approximately 7,000 pieces (9,119 $m^3\ km^{-2}$) of LWD were generated in this area during the earthquake, and more than 80% of these moved from the slope to the river channel. The LWD that reached the river channel stopped flowing at a maximum of 200 m or more from the upper reach to the middle reach and were accompanied by the landslide debris at the time the landslide occurred. The LWD deposited in the main river channel did not move during the 2 years following the earthquake. This was not simply because there were no high-magnitude flooding events but because logjams formed at multiple locations in the river channel and some of the LWD was buried in gravel and submerged in water ponds. Given these conditions of the LWD deposition, there is currently a low risk of the LWD relocating during future flooding. In this catchment, the uneven LWD distribution and the formation of logjams were fixed almost immediately after the landslide at the time of the earthquake; these facts are important when considering future measures. From the water depth evaluation based on the difference in the excess return period, the degree of risk differs depending on the location of the LWD deposition in the channel. This suggests tha t not all LWD in the catchment is dangerous and that risk assessments focusing on the location of the LWD can be effective. This study makes it possible to determine high priority areas for LWD treatment.

## DATA AVAILABILITY STATEMENT

The original contributions presented in the study are included in the article/Supplementary Material, further inquiries can be directed to the corresponding author.

## AUTHOR CONTRIBUTIONS

TK designed the study, performed the field survey and the GIS analysis, and wrote the first draft of the manuscript. NH provided ideas to refine the study and acquired the aerial survey data using a UAV. YT organized the GIS data to enable a correct analysis. SK conducted the vegetation survey and an evaluation to properly use the rainfall data. All authors contributed to improving the manuscript.

## FUNDING

This work was supported by JSPS KAKENHI grant numbers JP18H03819 and JP18H03957, the River Fund of the River Foundation, and the project "Development of technology for impacts, mitigation and adaptation to climate change in the sectors of agriculture, forestry, and fisheries" of the Agriculture, Forestry, and Fisheries Research Council.

## ACKNOWLEDGMENTS

We are deeply grateful to the Department of Fisheries and Forestry, Hokkaido Government, for providing the aerial survey data just after the earthquake and to the Iburi General Subprefectural Bureau, Hokkaido Government, for providing the local information materials. We thank Martha Evonuk, PhD, from Edanz (https://jp.edanz.com/ac) for editing a draft of this manuscript.

## REFERENCES

Abbe, T. B., and Montgomery, D. R. (1996). Large Woody Debris Jams, Channel Hydraulics and Habitat Formation in Large Rivers. *Regul. Rivers: Res. Mgmt.* 12, 201–221. doi:10.1002/(sici)1099-1646(199603)12:2/3<201::aid-rrr390>3.0.co;2-a

Abe, T., and Nakamura, F. (1996). Pool and Cover Formation by Coarse Woody Debris in a Small Low-Gradient Stream in Northern Hokkaido. *J. Jpn. For. Soc.* 78, 36–42. (in Japanese with English abstract). doi:10.11519/jjfs1953.78.1_36

Abe, T., and Nakamura, F. (1999). Effects of Experimental Removal of Woody Debris on Channel Morphology and Fish Habitat. *Ecol. Civil Eng.* 2 (2), 179–190. doi:10.3825/ece.2.179

Aoki, T., Katsura, S. y., Yoshino, T., Koi, T., Tanaka, Y., and Yamada, T. (2021). "Pressure Head Dynamics on a Natural Slope in Eastern Iburi Struck by the 2018 Hokkaido Earthquake," in *Understanding and Reducing Landslide Disaster Risk. WLF 2020. ICL Contribution to Landslide Disaster Risk Reduction*. Editors V. Vilímek, F. Wang, A. Strom, K. Sassa, P. T. Bobrowsky, and K. Takara (Cham: Springer), 81–86. doi:10.1007/978-3-030-60319-9_7

Arcement, G. J., and Schneider, V. (1989). Guide for Selecting Manning's Roughness Coe†cients for Natural Channels and Flood plains. *US Geol. Surv. Water Supply Paper* 2339, 1–38. doi:10.3133/wsp2339

Asano, Y., Hoshino, S., Uchida, T., and Akiyama, K. (2012). Measuring the Flow and Manning's Roughness Coefficient of Mountain Streams. *Jpn. Soc. Erosion Control. Eng.* 65, 62–68. (in Japanese with English abstract). doi:10.11475/sabo.65.1_62

Braudrick, C. A., and Grant, G. E. (2000). When Do Logs Move in Rivers? *Water Resour. Res.* 36 (2), 571–583. doi:10.1029/1999wr900290

Chow, V. T. (1959). *Open Channel Hydraulic, International Student Edition*. New York: McGraw Hill Book Company, Inc, 680.

Comiti, F., Lucía, A., and Rickenmann, D. (2016). Large wood Recruitment and Transport during Large Floods: a Review. *Geomorphology* 269, 23–39. doi:10.1016/j.geomorph.2016.06.016

De Cicco, P. N., Paris, E., Ruiz-Villanueva, V., Solari, L., and Stoffel, M. (2018). In-channel wood-related Hazards at Bridges: A Review. *River Res. Applic* 34, 617–628. doi:10.1002/rra.3300

Dixon, S. J., and Sear, D. A. (2014). The Influence of Geomorphology on Large wood Dynamics in a Low Gradient Headwater Stream. *Water Resour. Res.* 50, 9194–9210. doi:10.1002/2014WR015947

Fausch, K. D., and Northcote, T. G. (1992). Large Woody Debris and Salmonid Habitat in a Small Coastal British Columbia Stream. *Can. J. Fish. Aquat. Sci.* 49, 682–693. doi:10.1139/f92-077

Haga, H., Kumagai, T. o., Otsuki, K., and Ogawa, S. (2002). Transport and Retention of Coarse Woody Debris in Mountain Streams: An *In Situ* Field experiment of Log Transport and a Field Survey of Coarse Woody Debris Distribution. *Water Resour. Res.* 38, 1. doi:10.1029/2001WR001123

Haga, H., Sakamoto, Y., and Ogawa, S. (2006). Export of Woody Debris from Forested Headwater Catchments. *Mizu Kankyo Gakkaishi* 29 (4), 207–213. doi:10.2965/jswe.29.207

Hotchkiss, R. H., and Mccallum, B. E. (1995). Peak Discharge for Small Agricultural Watersheds. *J. Hydraulic Eng.* 121 (1), 36–48. doi:10.1061/(asce)0733-9429(1995)121:1(36)

Hyatt, T. L., and Naiman, R. J. (2001). The Residence Time of Large Woody Debris in the Queets River, Washington, USA. *Ecol. Appl.* 11 (1), 191–202. doi:10.1890/1051-0761(2001)011[0191:trtolw]2.0.co;2

Inoue, K. (2008). *Illustrated Hydraulics*. Kyoto: Gakugei Publication, 143. (in Japanese).

IPCC (2014). *Climate Change 2014: The Physical Science Basis. Contribution of Working Group/to the Fifth Assessment Report of the Intergovernmental Panel on Climate Change*. Cambridge, United Kingdom and New York, NY, USA: Cambridge University Press, 1535.

Ishikawa, Y., Mizuyama, T., and Fukuzawa, M. (1989). Generation and Flow Mechanisms of Floating Logs Associated with Debris Flow. *J. Jpn. Soc. Eros Control. Eng.* 42 (3), 4–10. (in Japanese with English abstract). doi:10.11475/sabo1973.42.3_4

Kadoya, M., and Fukushima, A. (1976). Concentration Time of Flood in Small or Medium River basin. *Kyoto Univ. Disaster Prev. Res. Inst. Annuals* 19B, 143–152. (in Japanese with English abstract).

Kadoya, M. (1988)., 56. Japan, 1061–1065. (in Japanese, title translated by the author). doi:10.11408/jjsidre1965.56.11_1061Variety of Runoff Characteristics Due to Changes in Land Cover Type*J. Agric. Eng. Soc.*

Li, R., Wang, F., and Zhang, S. (2020). Controlling Role of Ta-D Pumice on the Coseismic Landslides Triggered by 2018 Hokkaido Eastern Iburi Earthquake. *Landslides* 17, 1233–1250. doi:10.1007/s10346-020-01349-y

Lienkaemper, G. W., and Swanson, F. J. (1987). Dynamics of Large Woody Debris in Streams in Old-Growth Douglas-fir Forests. *Can. J. For. Res.* 17, 150–156. doi:10.1139/x87-027

Lucía, A., Comiti, F., Borga, M., Cavalli, M., and Marchi, L. (2015). Dynamics of Large wood during a Flash Flood in Two Mountain Catchments. *Nat. Hazards Earth Syst. Sci.* 15, 1741–1755. doi:10.5194/nhess-15-1741-2015

MAFF (2018). "Annual Report on Forest and Forestry in Japan Fiscal Year 2017 (Summary)," in *(Forestry Agency, Ministry of Agriculture, Forestry and Fisheries, Japan)*. Available at: https://www.maff.go.jp/e/data/publish/index.html#Annual (Accessed August 31, 2021).

Marutani, T., Kaibori, M., Jitousono, T., Mizuno, H., Ohno, H., Shimizu, O., et al. (2017). Sediment-related Disasters by a Heavy Rainfall in the Northern Part of Kyushu-Island, Japan in July 2017. *J. Jpn. Soc. Eros Control. Eng.* 70 (4), 31–42. (in Japanese with English abstract). doi:10.11475/sabo.70.4_31

Mazzorana, B., Ruiz-Villanueva, V., Marchi, L., Cavalli, M., Gems, B., Gschnitzer, T., et al. (2018). Assessing and Mitigating Large wood-related Hazards in Mountain Streams: Recent Approaches. *J. Flood Risk Management* 11, 207–222. doi:10.1111/jfr3.12316

Minami, N., Doi, Y., Osanai, N., Takesaki, S., Nakayama, Y., Nonaka, K., et al. (2000). Report of Woody Debris Disaster at Yosasa River on August 1998 in Tochigi Prefecture, Japan. *J. Jpn. Soc. Eros Control. Eng.* 53 (4), 44–51. (in Japanese with English abstract). doi:10.11475/sabo1973.53.4_44

Mizuyama, T., Ohba, A., and Manzen, H. (1985). Production and Transport of Woody Trash and Logs Associate with Debris Flow Occurrence. *J. Jpn. Soc. Eros Control. Eng.* 38 (1), 1–6. (in Japanese). doi:10.11475/sabo1973.38.1

Moriya, H., Nihei, Y., Hasebe, Y., Mine, K., Sushimoto, K., Yano, S., et al. (2018). Study on driftwood Disaster in Kita River, Fukuoka Prefecture, Due to 2017 Northern Kyushu Flood. *Jjsce B1* 74, 1195–I. (in Japanese with English abstract). doi:10.2208/jscejhe.74.I_119510.2208/jscejhe.74.i_1195

Nakamura, F., and Swanson, F. J. (1993). Effects of Coarse Woody Debris on Morphology and Sediment Storage of a Mountain Stream System in Western Oregon. *Earth Surf. Process. Landforms* 18, 43–61. doi:10.1002/esp.3290180104

Oka, T. (2019). Quaternary Researching the basin of Azuma River and 2018 Hokkaido Eastern Iburi Earthquake. *Nagoya Univ. Chronological Res.* 3, 11–22. (in Japanese with English abstract). doi:10.18999/nagubc.3.11

Osanai, N., Yamada, T., Hayashi, S.-i., Kastura, S. y., Furuichi, T., Yanai, S., et al. (2019). Characteristics of Landslides Caused by the 2018 Hokkaido Eastern Iburi Earthquake. *Landslides* 16, 1517–1528. doi:10.1007/s10346-019-01206-7

Piégay, H., and Gurnell, A. M. (1997). Large Woody Debris and River Geomorphological Pattern: Examples from S. E. France and S. England. *Geomorphology* 19, 99–116. doi:10.1016/S0169-555X(96)00045-1

Riley, S. C., and Fausch, K. D. (1995). Trout Population Response to Habitat Enhancement in Six Northern Colorado Streams. *Can. J. Fish. Aquat. Sci.* 52, 34–53. doi:10.1139/f95-004

Ruiz-Villanueva, V., Díez-Herrero, A., Ballesteros, J. A., and Bodoque, J. M. (2014). Potential Large Woody Debris Recruitment Due to Landslides, Bank Erosion and Floods in Mountain Basins: a Quantitative Estimation Approach. *River Res. Applic.* 30, 81–97. doi:10.1002/rra.2614

Ruiz-Villanueva, V., Mazzorana, B., Bladé, E., Bürkli, L., Iribarren-Anacona, P., Mao, L., et al. (2019). Characterization of wood-laden Flows in Rivers. *Earth Surf. Process. Landforms* 44, 1694–1709. doi:10.1002/esp.4603

Sear, D. A., Millington, C. E., Kitts, D. R., and Jeffries, R. (2010). Logjam Controls on Channel:floodplain Interactions in Wooded Catchments and Their Role in the Formation of Multi-Channel Patterns. *Geomorphology* 116, 305–319. doi:10.1016/j.geomorph.2009.11.022

Seo, J. I., Nakamura, F., Chun, K. W., Kim, S. W., and Grant, G. E. (2015). Precipitation Patterns Control the Distribution and export of Large wood at the Catchment Scale. *Hydrol. Process.* 29, 5044–5057. doi:10.1002/hyp.10473

Smith, R. D., Sidle, R. C., Porter, P. E., and Noel, J. R. (1993). Effects of Experimental Removal of Woody Debris on the Channel Morphology of a forest, Gravel-Bed Stream. *J. Hydrol.* 152, 153–178. doi:10.1016/0022-1694(93)90144-X

Speaker, R., Moore, K., and Gregory, S. (1984). Analysis of the Process of Retention of Organic Matter in Stream Ecosystems. *SIL Proc.* 22, 1835–1841, 1922-2010. doi:10.1080/03680770.1983.11897582

Thompson, D. M. (1995). The Effects of Large Organic Debris on Sediment Processes and Stream Morphology in Vermont. *Geomorphology* 11, 235–244. doi:10.1016/0169-555x(94)00064-x

Tsunetaka, H., Mtibaa, S., Asano, S., Okamoto, T., and Kurokawa, U. (2021). Comparison of Length and Dynamics of wood Pieces in Streams Covered with Coniferous and Broadleaf Forests Mapped Using Orthophotos Acquired by an Unmanned Aerial Vehicle. *Prog. Earth Planet. Sci.* 8, 22. doi:10.1186/s40645-021-00419-6

Ward, G. M., and Aumen, N. G. (1986). Woody Debris as a Source of Fine Particulate Organic Matter in Coniferous Forest Stream Ecosystems. *Can. J. Fish. Aquat. Sci.* 43, 1635–1642. doi:10.1139/f86-202

Wohl, E., and Goode, J. R. (2008). Wood Dynamics in Headwater Streams of the Colorado Rocky Mountains. *Water Resour. Res.* 44, W09429. doi:10.1029/2007WR006522

Zhang, S., Li, R., Wang, F., and Iio, A. (2019). Characteristics of Landslides Triggered by the 2018 Hokkaido Eastern Iburi Earthquake, Northern Japan. *Landslides* 16, 1691–1708. doi:10.1007/s10346-019-01207-6

Zhao, B., Wang, Y., Feng, Q., Guo, F., Zhao, X., Ji, F., et al. (2020). Preliminary Analysis of Some Characteristics of Coseismic Landslides Induced by the Hokkaido Iburi-Tobu Earthquake (September 5, 2018), Japan. *Catena* 189, 104502. doi:10.1016/j.catena.2020.104502

**Conflict of Interest:** The authors declare that the research was conducted in the absence of any commercial or financial relationships that could be construed as a potential conflict of interest.

**Publisher's Note:** All claims expressed in this article are solely those of the authors and do not necessarily represent those of their affiliated organizations, or those of the publisher, the editors and the reviewers. Any product that may be evaluated in this article, or claim that may be made by its manufacturer, is not guaranteed or endorsed by the publisher.

# Advantages of publishing in Frontiers

**OPEN ACCESS**
Articles are free to read for greatest visibility and readership

**FAST PUBLICATION**
Around 90 days from submission to decision

**HIGH QUALITY PEER-REVIEW**
Rigorous, collaborative, and constructive peer-review

**TRANSPARENT PEER-REVIEW**
Editors and reviewers acknowledged by name on published articles

**Frontiers**
Avenue du Tribunal-Fédéral 34
1005 Lausanne | Switzerland

**Visit us:** www.frontiersin.org
**Contact us:** frontiersin.org/about/contact

**REPRODUCIBILITY OF RESEARCH**
Support open data and methods to enhance research reproducibility

**DIGITAL PUBLISHING**
Articles designed for optimal readership across devices

**FOLLOW US**
@frontiersin

**IMPACT METRICS**
Advanced article metrics track visibility across digital media

**EXTENSIVE PROMOTION**
Marketing and promotion of impactful research

**LOOP RESEARCH NETWORK**
Our network increases your article's readership